

1                   **Jet-Track Correlation Studies of the Quark Gluon Plasma**

2                   BY

3                   HALLIE CAUSEY TRAUGER

4                   M.Ed. University of Illinois at Chicago, 2015

5                   M.S. University of Illinois at Chicago, 2014

6                   B.A. University of Chicago, 2010

7                   THESIS

8                   Submitted in partial fulfilment of the requirements

9                   for the degree of Doctor of Philosophy in Physics

10                  in the Graduate College of the University of Illinois at Chicago, 2017

11                  Chicago, IL

12                  DEFENSE COMMITTEE:

13                  Olga Evdokimov, Chair and Advisor

14                  David Hofman

15                  Zhenyu Ye

16                  Misha Stephanov

17                  Julia Velkovska, Vanderbilt University

*19 For my students, with the hope that they, too, may enjoy the privilege of following their curiosity  
20 and passions wherever these may lead.*

21

## ACKNOWLEDGEMENTS

22 Thanks go here...

23

HCT

## CONTRIBUTION OF AUTHORS

- 25 - Note previous publications (HIN-14-016, HIN-15-011, HIN-16-020)
- 26 - Describe CMS authorship policy
- 27 - Outline general CMS inputs (reconstruction etc.) that contributed to work
- 28 - Outline aspects that are my own work (and others' contributions to these as well, esp. Run 2)

## CONTENTS

30	<b>1 Introduction</b>	<b>1</b>
31	<b>2 The quark gluon plasma</b>	<b>2</b>
32	2.1 Predictions and early evidence for the quark gluon plasma . . . . .	2
33	2.2 Thermodynamics of the quark gluon plasma . . . . .	4
34	2.3 Time-evolution of heavy ion collisions . . . . .	5
35	2.4 Characterizing collision geometry and event centrality . . . . .	7
36	2.5 Kinematic variables and coordinates . . . . .	9
37	2.6 Collective behavior in the QGP . . . . .	10
38	<b>3 Jets as probes of the quark gluon plasma</b>	<b>13</b>
39	3.1 Measuring suppression of high- $p_T$ particles and jets . . . . .	14
40	3.2 Jet fragmentation function and jet shape measurements . . . . .	18
41	3.3 Dijet asymmetry and momentum balance studies . . . . .	20
42	<b>4 Models of jet energy loss in the quark gluon plasma</b>	<b>24</b>
43	4.1 Survey of theoretical models of jet quenching mechanisms . . . . .	24
44	4.2 Quenching model comparisons to high- $p_T$ jet observables . . . . .	27
45	4.3 Theoretical motivations for detailed jet-track correlation studies . . . . .	38
46	<b>5 The Large Hadron Collider and the CMS detector</b>	<b>40</b>
47	5.1 The Large Hadron Collider . . . . .	40
48	5.2 The CMS detector . . . . .	41
49	5.3 Trackers in the CMS detector . . . . .	41
50	5.4 Calorimeters in the CMS detector . . . . .	43
51	5.5 The CMS trigger system . . . . .	44
52	<b>6 Track reconstruction and correction</b>	<b>46</b>
53	6.1 Track reconstruction in pp collisions . . . . .	46
54	6.2 Track reconstruction in PbPb collisions . . . . .	47
55	6.3 High purity tracks . . . . .	48
56	6.4 Tracking efficiency and fake rate evaluation and correction . . . . .	49
57	<b>7 Jet reconstruction and correction</b>	<b>51</b>
58	7.1 Jet reconstruction with the anti- $k_t$ algorithm . . . . .	51
59	7.2 Underlying event subtraction in PbPb data . . . . .	53
60	7.3 Jet energy corrections . . . . .	54
61	<b>8 Data and Monte Carlo samples</b>	<b>56</b>
62	8.1 Data samples and event selection . . . . .	56
63	8.2 Collision centrality determination and classes . . . . .	57
64	8.3 Monte Carlo simulation . . . . .	57
65	8.4 Jet selection and dijet asymmetry classes . . . . .	62
66	8.5 Track selection and classes . . . . .	62
67	8.6 Summary of analysis bins . . . . .	64

68	<b>9 Jet-track correlation measurements</b>	<b>65</b>
69	9.1 Analysis procedure . . . . .	65
70	9.2 Jet-track correlation pair-acceptance correction . . . . .	66
71	9.3 Separation of correlations into long range and short-range components . . . . .	66
72	9.4 Residual Jet Fragmentation Function correction . . . . .	70
73	9.5 Background fluctuation bias correction . . . . .	74
74	9.6 Evaluation of systematic uncertainties . . . . .	81
75	<b>10 Discussion of results</b>	<b>84</b>
76	10.1 Inclusive jet particle density correlation results . . . . .	84
77	10.2 Dijet correlation results at 2.76 TeV . . . . .	95
78	10.3 Jet shapes at 2.76 TeV and 5.02 TeV . . . . .	104
79	10.4 Decomposition of hemisphere momentum balance in dijet events at 2.76 TeV . . . . .	108
80	10.5 Theory implications of these results . . . . .	120
81	<b>11 Conclusion</b>	<b>121</b>
82	<b>References</b>	<b>122</b>
83	<b>Appendices</b>	<b>128</b>
84	A Jet kinematics . . . . .	128
85	B Background fitting details . . . . .	142
86	C Pair acceptance and event decomposition systematic uncertainties . . . . .	146
87	D Correlation widths and related uncertainty . . . . .	148
88	<b>Vita</b>	<b>152</b>

**LIST OF TABLES**

90      I	Summary of data samples and number of selected events . . . . .	56
91      II	Summary of Monte Carlo samples and generated events at 2.76 TeV . . . . .	59
92      III	Summary of Monte Carlo samples and generated events at 5.02 TeV . . . . .	61
93      IV	Summary of data selections and analysis bins . . . . .	64
94      V	Systematic uncertainties for particle density correlation studies at 2.76 TeV . . . . .	82
95      VI	Systematic uncertainties for particle density correlation studies at 5.02 TeV . . . . .	83
96      VII	Systematic uncertainties for balanced and unbalanced dijets in transverse momentum distribution studies at 2.76 TeV . . . . .	83
97		

## LIST OF FIGURES

99	1	QCD coupling constant $\alpha_s$ . . . . .	3
100	2	QCD phase diagram . . . . .	6
101	3	Glauber model illustration . . . . .	8
102	4	Dihadron correlation in $\Delta\eta - \Delta\phi$ . . . . .	11
103	5	Fits to dihadron $\Delta\phi$ distributions to extract flow coefficients . . . . .	12
104	6	Flow coefficients $v_2$ and $v_3$ by centrality and $p_T$ . . . . .	12
105	7	Illustration of QCD cross section factorization . . . . .	14
106	8	Charged particle $R_{AA}$ at 200 GeV and 2.76 TeV . . . . .	16
107	9	Charged particle $R_{AA}$ at 2.76 and 5.02 TeV . . . . .	16
108	10	Jet $R_{AA}$ at 2.76 TeV . . . . .	17
109	11	Jet fragmentation function in 2.76 TeV PbPb and pp data . . . . .	18
110	12	Jet shape measurement in 2.76 TeV PbPb and pp data . . . . .	19
111	13	Illustration of dijet asymmetry . . . . .	20
112	14	Dijet asymmetry and in 2.76 TeV PbPb and pp data . . . . .	21
113	15	Hemisphere momentum balance in dijet events as a function of $A_J$ . . . . .	22
114	16	Radial distribution of hemisphere momentum balance as a function of $\Delta r$ for unbalanced dijets . . . . .	23
115	17	Temperature dependence of $\hat{q}$ from different quenching models . . . . .	25
116	18	Model comparisons to charged particle $R_{AA}$ at 5.02 TeV . . . . .	28
117	19	Simulated dependence of jet $R_{AA}$ on $R$ at 2.76 TeV from JEWEL . . . . .	29
118	20	Simulated dependence of jet $R_{AA}$ on $R$ at 2.76 TeV with the coupled jet-fluid model . . . . .	30
119	21	Predicted jet $R_{AA}$ as a function of $p_T$ at 2.76 TeV from SCET <sub>G</sub> . . . . .	30
120	22	Calculated jet $R_{AA}$ as a function of $p_T$ at 2.76 TeV from the hybrid model . . . . .	31
121	23	Simulated jet shape ratio $\rho(\Delta r)_{\text{PbPb}}/\rho(\Delta r)_{\text{pp}}$ at 2.76 TeV from JEWEL . . . . .	32
122	24	Calculated jet shapes in PbPb and pp and their ratio at 2.76 TeV from the coupled jet-fluid model . . . . .	33
123	25	Calculated jet shapes in PbPb and pp at 2.76 TeV from the coupled jet-fluid model, extended to $\Delta r = 1$ . . . . .	33
124	26	Calculated jet shape ratio $\rho(\Delta r)_{\text{PbPb}}/\rho(\Delta r)_{\text{pp}}$ at 2.76 TeV with SCET <sub>G</sub> . . . . .	34
125	27	Calculated jet shape ratio $\rho(\Delta r)_{\text{PbPb}}/\rho(\Delta r)_{\text{pp}}$ at 2.76 TeV from the hybrid model for a range of values of broadening parameter $K$ . . . . .	34
126	28	Calculated jet shape ratio $\rho(\Delta r)_{\text{PbPb}}/\rho(\Delta r)_{\text{pp}}$ at 2.76 TeV from the hybrid model with and without the medium backreaction . . . . .	35
127	29	Simulated JFF ratio PbPb/pp at 2.76 TeV from JEWEL . . . . .	36
128	30	Calculated JFF ratio PbPb/pp at 2.76 TeV from the hybrid model . . . . .	37
129	31	Simulated dijet asymmetry parameter $A_J$ in pp and PbPb at 2.76 TeV from JEWEL . . . . .	37
130	32	Missing- $p_T$ as a function of $A_J$ hybrid model . . . . .	39
131	33	CMS detector perspective drawing . . . . .	42
132	34	Diagram of CMS trackers . . . . .	43
133	35	Diagram of the HCAL . . . . .	44
134	36	Tracking efficiency correction example . . . . .	50
135	37	Closure with and without JFF-JEC for quark and gluon jets. . . . .	55
136	38	Centrality distribution for PYTHIA+HYDJET reweighted to the distribution of PbPb data. . . . .	59
137	39	Vertex z distribution for PYTHIA+HYDJET reweighted to the distribution of PbPb data. . . . .	59

145	40	Vertex z distribution for PYTHIA reweighted to the distribution of pp data. . . . .	60
146	41	Illustration of the pair-acceptance correction procedure . . . . .	67
147	42	Illustration of the event decomposition procedure without $\Delta\phi$ fitting . . . . .	68
148	43	Illustration of the event decomposition procedure with $\Delta\phi$ fitting . . . . .	69
149	44	Jet fragmentation function bias corrections for particles with $1 < p_T^{\text{trk}} < 2$ GeV . . .	71
150	45	Jet fragmentation function bias corrections for particles with $2 < p_T^{\text{trk}} < 3$ GeV . . .	71
151	46	Jet fragmentation function bias corrections for particles with $3 < p_T^{\text{trk}} < 4$ GeV . . .	72
152	47	Jet fragmentation function bias corrections for particles with $4 < p_T^{\text{trk}} < 8$ GeV . . .	72
153	48	Integrated yield attributed to jet fragmentation function bias as a function of $p_T^{\text{trk}}$ . .	73
154	49	Integrated yield attributed to jet fragmentation function bias as a function of centrality	73
155	50	Background fluctuation bias corrections for particles with $1 < p_T^{\text{trk}} < 2$ GeV . . . . .	75
156	51	Background fluctuation bias corrections for particles with $2 < p_T^{\text{trk}} < 3$ GeV . . . . .	75
157	52	Background fluctuation bias corrections for particles with $3 < p_T^{\text{trk}} < 4$ GeV . . . . .	76
158	53	Background fluctuation bias corrections for particles with $4 < p_T^{\text{trk}} < 8$ GeV . . . . .	76
159	54	Integrated yield attributed to background fluctuation bias as a function of $p_T^{\text{trk}}$ . . .	77
160	55	Data-driven check of integrated yields attributed to background fluctuation bias . . . . .	78
161	56	Data-driven check of correlated $\Delta\eta$ yields attributed to background fluctuation bias	79
162	57	Comparison of background selection bias effect for quark verus gluon jets . . . . .	80
163	58	Inclusive jet $\Delta\eta$ correlations for tracks with $1 < p_T^{\text{trk}} < 2$ GeV at 2.76 TeV . . . . .	85
164	59	Inclusive jet $\Delta\phi$ correlations for tracks with $1 < p_T^{\text{trk}} < 2$ GeV at 2.76 TeV . . . . .	86
165	60	Inclusive jet $\Delta\eta$ correlations for tracks with $2 < p_T^{\text{trk}} < 3$ GeV at 2.76 TeV . . . . .	87
166	61	Inclusive jet $\Delta\phi$ correlations for tracks with $2 < p_T^{\text{trk}} < 3$ GeV at 2.76 TeV . . . . .	88
167	62	Inclusive jet $\Delta\eta$ correlations for tracks with $3 < p_T^{\text{trk}} < 4$ GeV at 2.76 TeV . . . . .	89
168	63	Inclusive jet $\Delta\phi$ correlations for tracks with $3 < p_T^{\text{trk}} < 4$ GeV at 2.76 TeV . . . . .	90
169	64	Inclusive jet $\Delta\eta$ correlations for tracks with $4 < p_T^{\text{trk}} < 8$ GeV at 2.76 TeV . . . . .	91
170	65	Inclusive jet $\Delta\phi$ correlations for tracks with $4 < p_T^{\text{trk}} < 8$ GeV at 2.76 TeV . . . . .	92
171	66	Inclusive jet $\Delta\eta$ correlations at 5.02 TeV . . . . .	92
172	67	Inclusive jet $\Delta\phi$ correlations at 5.02 TeV . . . . .	93
173	68	Inclusive jet distribution of charged particles as a function of $\Delta r$ at 5.02 TeV . . . .	93
174	69	Integrated inclusive jet charged particle yields at 2.76 and 5.02 TeV . . . . .	94
175	70	Dijet $\Delta\eta$ correlations for tracks with $1 < p_T^{\text{trk}} < 2$ GeV at 2.76 TeV . . . . .	96
176	71	Dijet $\Delta\phi$ correlations for tracks with $1 < p_T^{\text{trk}} < 2$ GeV at 2.76 TeV . . . . .	97
177	72	Integrated charged particle yields for inclusive, leading, and subleading jets . . . . .	98
178	73	Leading jet $\Delta\eta$ correlation widths as a function of $p_T^{\text{trk}}$ at 2.76 TeV . . . . .	100
179	74	Leading jet $\Delta\phi$ correlation widths as a function of $p_T^{\text{trk}}$ at 2.76 TeV . . . . .	101
180	75	Subleading jet $\Delta\eta$ correlation widths as a function of $p_T^{\text{trk}}$ at 2.76 TeV . . . . .	102
181	76	Subleading jet $\Delta\phi$ correlation widths as a function of $p_T^{\text{trk}}$ at 2.76 TeV . . . . .	103
182	77	Inclusive jet shape at 5.02 TeV, shown differentially in $p_T^{\text{trk}}$ . . . . .	105
183	78	Leading jet shape at 2.76 TeV, shown differentially in $p_T^{\text{trk}}$ . . . . .	106
184	79	Subleading jet shape at 2.76 TeV, shown differentially in $p_T^{\text{trk}}$ . . . . .	107
185	80	Dijet subleading-to-leading hemisphere momentum balance for balanced dijets . . . . .	110
186	81	Dijet subleading-to-leading hemisphere momentum balance for unbalanced dijets . . . . .	111
187	82	Jet peak subleading-to-leading momentum balance for balanced dijets . . . . .	112
188	83	Jet peak subleading-to-leading momentum balance for unbalanced dijets . . . . .	113
189	84	long-range subleading-to-leading momentum balance for balanced dijets . . . . .	115
190	85	long-range subleading-to-leading momentum balance for unbalanced dijets . . . . .	116
191	86	Integrated transverse momentum in the long-range $\Delta\phi$ -correlated distribution as a function of track- $p_T$ . . . . .	117

193	87	Relative contributions from jet peaks and long-range asymmetry to the double difference PbPb–pp, subleading-leading in total hemisphere transverse momentum for central collisions . . . . .	118
194			
195	88	Relative contributions from jet peaks and long-range asymmetry to the double difference PbPb–pp, subleading-leading in total hemisphere transverse momentum for peripheral collisions . . . . .	119
196			
197	89	Distribution of transverse momentum, pseudorapidity, and azimuthal distribution of all jet selections for Pythia data compared to PYTHIA simulation. . . . .	128
198			
199	90	Transverse momentum distribution of all jet selections for PbPb data at 2.76 TeV compared to PYTHIA+HYDJET simulation. . . . .	129
200			
201	91	Pseudorapidity distribution of all jet selections for PbPb data at 2.76 TeV compared to PYTHIA+HYDJET simulation. . . . .	130
202			
203	92	Azimuthal angle distribution of all jet selections for PbPb data at 2.76 TeV compared to PYTHIA+HYDJET simulation for each collision centrality bin. . . . .	131
204			
205	93	Distribution of pseudorapidity distribution of all jet selections for PbPb data compared to PYTHIA+HYDJET simulation for each collision centrality bin. . . . .	132
206			
207	94	Transverse momentum distribution for PbPb data compared to PYTHIA+HYDJET simulation for each collision centrality bin. . . . .	132
208			
209	95	Jet $\eta$ distribution for PbPb data compared to PYTHIA+HYDJET simulation for each collision centrality bin. . . . .	132
210			
211	96	Jet $\phi$ distribution for PbPb data compared to PYTHIA+HYDJET simulation for each collision centrality bin. . . . .	133
212			
213	97	Jet $p_T$ , $\eta$ , and $\phi$ for all pp dijets and for pp dijets with $A_J$ : $0 < A_J < 0.11$ . . . . .	134
214			
215	98	Jet $p_T$ , $\eta$ , and $\phi$ for all pp dijets and for pp dijets with $A_J$ : $0.11 < A_J < 0.22$ . . . . .	135
216			
217	99	Jet $p_T$ , $\eta$ , and $\phi$ for all pp dijets and for pp dijets with $A_J$ : $0.22 < A_J < 0.33$ . . . . .	136
218			
219	100	Jet $p_T$ , $\eta$ , and $\phi$ for all pp dijets and for pp dijets with $A_J$ : $A_J > 0.33$ . . . . .	137
220			
221	101	Jet $p_T$ , $\eta$ , and $\phi$ for all PbPb dijets and for PbPb dijets with $0 < A_J < 0.11$ . . . . .	138
222			
223	102	Jet $p_T$ , $\eta$ , and $\phi$ for all PbPb dijets and for PbPb dijets with $0.11 < A_J < 0.22$ . . . . .	139
224			
225	103	Jet $p_T$ , $\eta$ , and $\phi$ for all PbPb dijets and for PbPb dijets with $0.22 < A_J < 0.33$ . . . . .	140
226			
227	104	Jet $p_T$ , $\eta$ , and $\phi$ for all PbPb dijets and for PbPb dijets with $A_J > 0.33$ . . . . .	141
228			
229	105	Dijet background fits (preliminary step) . . . . .	142
230			
231	106	Leading jet background fits . . . . .	143
232			
233	107	Subleading jet background fits . . . . .	144
234			
235	108	Inclusive jet background fits . . . . .	145
236			
237	109	Pair acceptance uncertainty determination . . . . .	146
238			
239	110	Background subtraction uncertainty determination . . . . .	147
240			
241	111	Width determination for PbPb leading jets . . . . .	148
242			
243	112	Width determination for pp leading jets . . . . .	149
244			
245	113	Width determination for PbPb subleading jets . . . . .	150
246			
247	114	Width determination for pp subleading jets . . . . .	151
248			

## LIST OF ABBREVIATIONS

ADS/CFT	Anti-deSitter/Conformal Field Theory
AMY	Arnold-Moore-Yaffe
AMPT	A Multiphase Transport Model
ASW	Armesto-Salgado-Widemann
BDMPS-Z	Baier-Dokshitzer-Mueller-Peigné-Schiff-Zakharov
BNL	Brookhaven National Laboratory
CERN	Conseil Européen pour la Recherche Nucléaire
CMS	Compact Muon Solenoid
DGLAP	Dokshitzer-Gribov-Lipatov-Altarelli-Parisi
ECAL	Electromagnetic Calorimeter
$E_T$	Transverse Energy
GLV	Gyulassy-Lévai-Vitev
HCAL	Hadronic Calorimeter
HF	Hadronic Forward
HLT	High Level Trigger
HT-BW	Higher Twist Berkeley-Wuhan
HT-M	Higher Twist Majumder
JEC	Jet Energy Correction
JES	Jet Energy Scale
JFF	Jet Fragmentation Function
LBT	Linear Boltzman Transport
LHC	Large Hadron Collider
MC	Monte Carlo
PbPb	Lead-lead (collision data)
PDF	Parton Distribution Function
pPb	Proton-lead (collision data)
pp	Proton-proton (collision data)
pQCD	Perturbative Quantum Chromodynamics
$p_T$	Transverse Momentum
QCD	Quantum Chromodynamics
QGP	Quark Gluon Plasma
RHIC	Relativistic Heavy Ion Collider
SCET <sub>G</sub>	Soft Collinear Effective Theory with Glauber Gluons
UE	Underlying Event
UrQMD	Ultrarelativistic Quantum Molecular Dynamics

**SUMMARY**

## 1 INTRODUCTION

## 2 THE QUARK GLUON PLASMA

### 237 2.1 Predictions and early evidence for the quark gluon plasma

238 Quantum chromodynamics (QCD) describes the interactions of the quarks and gluons (together  
 239 known as partons) via the strong nuclear force. The strength of the QCD interactions, described  
 240 by the QCD coupling constant  $\alpha_s(Q)$  decreases as distances between strongly interacting partons  
 241 decreases and their exchanged momentum  $Q$ :

$$\alpha_s(Q) \propto \frac{1}{\ln(\frac{Q^2}{\Lambda_{QCD}})}, \quad (1)$$

242 where  $\Lambda_{QCD} \approx 0.2$  GeV gives the QCD scale. Figure 1 shows the dependence of  $\alpha_s$  on momentum  
 243 scale  $Q$ . In the regime where separations between partons are relatively large (small  $Q$ ),  $\alpha_s$  is large,  
 244 leading to the observed confinement of quarks and gluons in composite particles called hadrons, most  
 245 commonly baryons (comprised of 3 quarks, including protons and neutrons) and mesons (comprised  
 246 of 2 quarks). In the large  $Q$  regime, however—accessed via large baryon chemical potential  $\mu_B$  or  
 247 large temperature  $T$ —the strength of the coupling constant  $\alpha_s$  decreases, in a phenomenon known as  
 248 asymptotic freedom. Asymptotic freedom both permits the accurate approximation of high-energy  
 249 hadron interactions using perturbation theory (pQCD), and implies the deconfinement of quarks  
 250 and gluons. This phase of deconfined quarks and gluons, known as the quark gluon plasma (QGP),  
 251 was originally conceived as a gas of color-charged quarks and gluons, analogous to the plasma of  
 252 photons and electrons previously studied in quantum electrodynamics. In collider studies, this  
 253 suggests the possibility of a phase transition anticipated between the hadron gas phase present  
 254 under ordinary matter conditions, and the QGP phase present at sufficiently great  $\mu_B$  or  $T$  [1, 2].

255 In the early 1980s, relativistic nuclear collisions were suggested as a means of producing  
 256 sufficient temperatures and densities to induce a quark-gluon plasma and probe the transition  
 257 between the QGP and ordinary matter. Efforts were also made to anticipate key experimental  
 258 signatures of the short-lived possible QGP, relying in many cases on the anticipation that the QGP  
 259 would behave according to a hydrodynamic description of a system in at least partial thermal  
 260 equilibrium. Proposed signatures included enhancements of strange (heavy) quarks, unusual event  
 261 structures, greater rates of direct dilepton and photon production [4]. The first heavy ion collisions

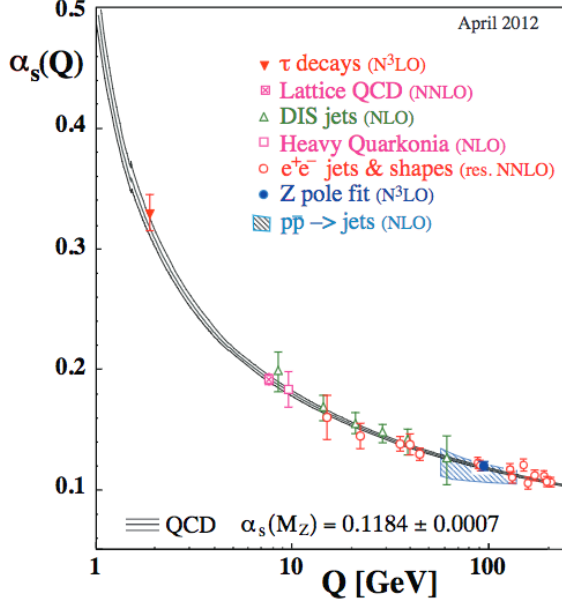


Figure 1. Momentum scale dependence of QCD coupling constant  $\alpha_s$ , from Ref. [3].

began with fixed-target experiments at the Super Proton Synchrotron (SPS) at CERN in the mid-1980s, colliding nuclei including gold and lead at energies from 40 GeV to 160 GeV through the 1990s. Analysis of the hadron yields in these collisions showed an apparent chemical equilibrium of quarks and gluons at about 170 MeV and enhancement (as anticipated) both of strangeness (via kaon/pion ratios, and  $J/\psi$  production rates). In the early 2000, a CERN press release cited these results in declaring that “a common assessment of the collected data leads us to believe that a new state of matter has indeed been created...[that] features many of the characteristics of the theoretically predicted quark-gluon plasma” [5].

Shortly after the SPS announcement, the first gold-gold collisions began at the Relativistic Heavy Ion Collider (RHIC) at Brookhaven National Laboratory, beginning an era of high-energy heavy ion collisions that would later be complimented by a parallel program at the Large Hadron Collider at CERN. Through data collection and analysis by experiments at each of these colliders over the ensuing nearly two decades, the field has gradually shifted from searches for signatures of QGP formation in heavy ion collisions, to detailed characterizations of its properties and evolution. In 2005, the four experimental collaborations at RHIC (BRAHAMS, PHENIX, PHOBOS, and STAR) published coordinated white papers [6, 7, 8, 9] summarizing the assembled evidence that

278 results from gold-gold collisions could not be explained by models of ordinary hadronic matter–  
 279 most notably in signatures of collective behavior (see Sec. 2.6) and in suppression of particles with  
 280 relatively high transverse momentum (see Sec. 3). Beginning in 2010, heavy ion studies at the LHC  
 281 by the ALICE, ATLAS, and CMS Collaborations (and more recently by the LHCb Collaboration)  
 282 have complimented the RHIC access to a wide range of center-of-mass-energies in the 7.7 GeV to  
 283 200 GeV range with measurements at 2.76 TeV and 5.02 TeV.

## 284 2.2 Thermodynamics of the quark gluon plasma

285 The existence of a plasma phase of hadronic matter and a number of the properties of this phase can  
 286 also be inferred directly from thermodynamic considerations of hadronic matter. In free space, the  
 287 density of states of hadrons as a function of resonance mass  $m$  increases exponentially, following  
 288 the Hagedorn spectrum

$$\rho(m) = m^{\frac{5}{2}} e^{\frac{m}{T_0}}, \quad (2)$$

289 where  $T_0 \approx m_\pi \approx 140$  MeV. [10, 11]. When taking into account the finite size of hadrons (with  
 290 radii on the order of 1 fm), this suggests an upper limit or critical temperature  $T_c \approx 150 - 200$   
 291 MeV above which quark and gluon deconfinement occurs. The pressure and energy density of  
 292 this plasma phase are both, to first order in the ideal gas, proportional to  $T^4$ , with higher order  
 293 corrections introduced by the non-zero effective (“thermal”) quark and gluon masses. Defining  
 294 a color-dependent constant  $c$  and a “bag pressure”  $B$  (named after the MIT model of hadrons  
 295 as “bags” of quarks and gluons) that takes into account the difference between quark and gluon  
 296 ground states and the vacuum, pressure may be expressed to first order as:

$$P = cT^4 - B, \quad (3)$$

297 and energy density  $\epsilon$  may be expressed to first order as:

$$\epsilon = 3cT^4 + B. \quad (4)$$

298 Interaction effects due differences between the ground state and the vacuum may be captured by  
299 “interaction measure”  $\Delta = (\epsilon - 3P)/T^4$ . Lattice QCD studies show a sharp rise in energy density  
300 from the low-density hadronic state at the critical temperature  $T_c$ , saturating to constant values  
301 at larger  $T$ . These values are about 10% less than those expected for an ideal massless gas due  
302 to the higher order thermal mass corrections. The interaction measure remains non-zero above  
303  $T_c$ , indicative of differences between the vacuum and the QCD ground state or possibly of color  
304 resonance states in the QGP. [11, 12]

305 Figure 2 gives a schematic illustration of the QCD phase diagram as a function of baryon  
306 chemical potential and temperature based on thermodynamic considerations and lattice QCD stud-  
307 ies. While chiral symmetry is spontaneously broken for non-zero quark masses, asymptotic freedom  
308 implies chiral symmetry at sufficiently large temperatures and a phase transition between the two  
309 (hadronic and quark gluon plasma) phases, which is first-order at sufficiently large  $\mu_B$  with sin-  
310 gularities in thermodynamic functions. Below a certain critical point value of  $\mu_B$  (and at critical  
311 temperature  $T_c$ ), however, the transition is a cross-over without singular behavior, and lattice  
312 QCD simulations have demonstrated such cross-over behavior for the limit  $\mu_B = 0$ . This suggests  
313 the existence of a tricritical point on the phase boundary between confined and deconfined QCD  
314 phases. [11, 12, 13] The beam energy scan program at RHIC probes center-of-mass energies ranging  
315 from 7.2 to 200 GeV to probe temperatures around the predicted values for  $T_c$ ; at LHC energies  
316 2.76 TeV and 5.5 TeV initial QGP temperatures are estimated in the 300 - 700 MeV range, well  
317 above the critical temperature. [14]

318 **2.3 Time-evolution of heavy ion collisions**

319 Connecting predictions and simulations of QGP behavior to experimental results requires the de-  
320 scription and analysis of several different sequential phases of heavy ion collisions [11, 15]:

- 321 1. **Initial state** – Nuclei A and B (lorentz-contracted into two flat discs) approach each other  
322 with impact parameter  $b$  and nucleon distributions  $\rho A(r)$  and  $\rho B(r)$ , establishing a set of  
323 initial conditions with implications for the later evolution of the medium.
- 324 2. **Pre-equilibrium** – Initially after nuclei collide (before thermalization time  $\tau_0$ ), nucleons  
325 interact dynamically as the QGP begins to form. Various models – including IP-Glasma,

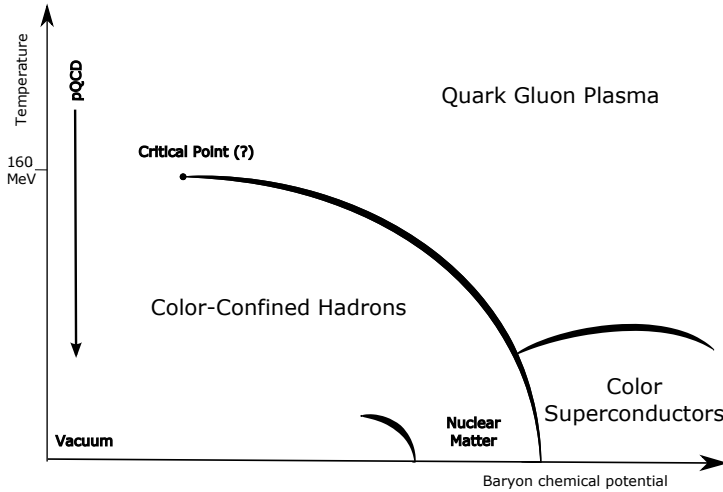


Figure 2. Schematic phase diagram of strongly interacting matter as a function of baryon chemical potential  $\mu_B$  and temperature  $T$ .

326       A Multiphase Transport Model (AMPT), Ultrarelativistic Quantum Molecular Dynamics  
 327       (UrQMD), and models based on the Anti-deSitter/Conformal Field Theory (ADS/CFT) cor-  
 328       respondence – attempt to capture these dynamics.

329       **3. Hydrodynamic expansion** – After thermalization time  $\tau_0$  local thermodynamic equilib-  
 330       rium is achieved, producing an expanding medium whose properties can be described with  
 331       ideal fluid dynamics with sheer viscosity to energy-density ratio  $\eta/s \approx 1.6$  at RHIC and the  
 332       LHC [16].

333       **4. Hadronization (“freeze-out”)** – Quarks and gluons recombine into hadrons in the phase  
 334       transition back from deconfined to confined QCD matter. As the medium expands, it reaches  
 335       sufficiently low densities and temperatures that thermal equilibrium is lost, and quark and  
 336       gluon recombination stops. Chemical freeze-out occurs when particle number changing pro-  
 337       cesses end; kinetic freeze-out occurs later, when the ratio of the expansion rate to the collision  
 338       rate among particles drops to the point that collisions no longer occur.

339       **5. Free-streaming** – recombined hadrons move through the beam pipe vacuum and are mea-  
 340       sured by the detector. Experimental results can only directly access these final distributions  
 341       of particles, from which inferences are made about the other collision stages.

342 Each stage of this QGP time evolution may be accessed via various experimental observables.  
343 Vacuum-like hadronization is well-modeled by parton shower simulations in Monte Carlo genera-  
344 tors such as PYTHIA and HERWIG that capture proton-proton collision dynamics. Heavy ion colli-  
345 sions, however, present the challenge of defining a freeze-out hypersurface at which hydrodynamic  
346 evolution terminates, and hadronization begins. This hypersurface occurs at the phase transition  
347 boundary, and may be experimentally accessed via the yields of hadron species in the final state  
348 (as particle numbers do not change during the free-streaming stage) [11]. Initial collision geometry  
349 may be described via Glauber Models and nuclear parton distribution functions (PDFs) of the  
350 incoming partons, as discussed in Sec. 2.4. Signatures of initial collision anisotropy and collective  
351 hydrodynamic evolution may be observed as “collective flow” via particle correlations (Sec. 2.6).  
352 Pre-equilibrium dynamics are particularly difficult to access, but probes including the medium mod-  
353 ifications to high- $p_T$  jets presented in this analysis provide possibilities for distinguishing between  
354 the different theoretical models.

#### 355 2.4 Characterizing collision geometry and event centrality

356 In heavy ion events there is a wide range of possible collision geometries: at one extreme the nuclei  
357 may collide head-on (referred to as a “central” collision, with impact parameter  $b = 0$ ), while at  
358 the other they may barely graze each other (referred to as a “peripheral” collision). The initial  
359 geometry, size, and evolution of the QGP formed in these events may vary considerably based on  
360 these initial collisions. At the most basic level, events may vary in both the number of participating  
361 nucleons ( $N_{\text{part}}$ ), and in the number of binary nucleon-nucleon collisions ( $N_{\text{coll}}$ ) occurring in the  
362 event. While it is not possible to directly measure  $b$ ,  $N_{\text{part}}$ , or  $N_{\text{coll}}$  in a heavy ion experiment, it is  
363 possible to measure the total energy deposited in calorimeters at very forward rapidities along the  
364 beam line direction. The total energy deposited in these forward calorimeters is directly related to  
365 the number of “spectator” nucleons that do not collide in the event, and therefore inversely related  
366 to  $N_{\text{part}}$ . By dividing the total experimental event sample into “centrality classes” (ranging from  
367 0% “most central” to 100% “most peripheral”) by total energy deposited at forward rapidity and  
368 mapping this classification to a simulated sample, it is possible to map events to Monte Carlo  
369 simulation and extract mean values for  $N_{\text{part}}$  and  $N_{\text{coll}}$  [17].

370 Glauber Models allow for the characterization of event parameters based on modeling of  
 371 collision geometry. In the simplest “optical limit” of such models, it is assumed that individual  
 372 nucleons accelerated to very high momenta move relatively independently and linearly, and deflec-  
 373 tion and shadowing effects are neglected. These assumptions reduce the problem to one of only  
 374 collision geometry, take the inelastic nucleon-nucleon cross-section  $\sigma_{NN}^{\text{inel}}$  and the density of nucleons  
 375 in each colliding nucleus  $\rho_A(r)$  and  $\rho_B(r)$  to calculate a “nuclear overlap function”  $T_{AB}$ , defined  
 376 as:

$$T_{AB} = \int d^2\vec{s} \int dz_A \rho_A(\vec{s}, z_A) \int dz_B \rho_B(\vec{s} - \vec{b}, z_B), \quad (5)$$

377 where the integrals  $\int dz_A \rho_A(\vec{s}, z_A)$  and  $\int dz_B \rho_B(\vec{s} - \vec{b}, z_B)$  define the probability of finding a nucleon  
 378 at locations  $(\vec{s}, z_A)$  and  $(\vec{s} - \vec{b}, z_B)$ , respectively with the geometry shown in Fig. 3.

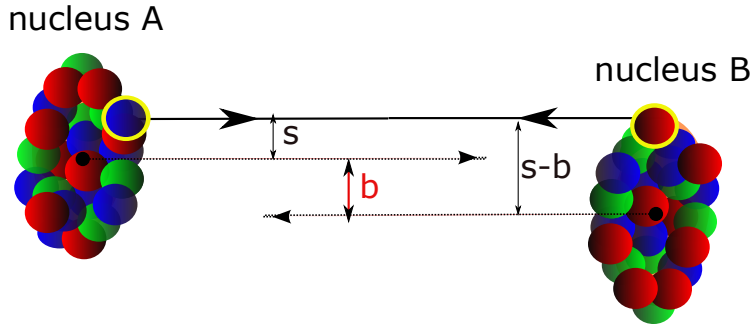


Figure 3. Schematic illustration of Glauber Model geometry for a nucleus-nucleus collision, showing impact parameter  $\vec{b}$  between the two nuclei and locations of two representative colliding nuclei.

379 The resulting total number of collisions is then given by:

$$N_{\text{coll}}(b) = \sigma_{NN}^{\text{inel}} T_{AB}(b). \quad (6)$$

380 For example for minimum bias collisions at LHC energy 2.76 TeV  $\sigma_{NN} = 65$  mb,  $\sigma_{\text{PbPb}} = 7660$   
 381 mb,  $\langle T_{\text{PbPb}} \rangle = \int d^2b T_{\text{PbPb}} / \int d^2b = 5.65 \text{ mb}^{-1}$ , and  $\langle N_{\text{coll}}(b) \rangle = 367$  [17, 18]. The optical limit  
 382 calculations described above are able to reasonably capture collision parameters, but are limited  
 383 by their neglect of effects including nuclear shadowing and diffraction. Glauber Monte Carlo sim-

384 ulations are able to re-introduce some of these effects, thereby better capturing the nuclear cross  
385 section [17, 19].

386 **2.5 Kinematic variables and coordinates**

387 In high-energy colliders the  $z$  axis is defined parallel to the colliding beams, with  $x$  and  $y$  axes  
388 spanning a transverse plane perpendicular to the beam axis. Because the colliding nuclei are  
389 accelerated to nearly the speed of light, it is necessary to use relativistic coordinates starting from  
390 the energy-momentum relationship:

$$E^2 = p_x^2 c^2 + p_y^2 c^2 + p_z^2 c^2 + M^2 c^4 \quad (7)$$

391 for a particle with rest mass  $M$ . The azimuthal coordinate in the transverse plane is then simply  
392 given by:

$$\phi = \tan^{-1} \left( \frac{p_y}{p_x} \right) \quad (8)$$

393 With incoming particles colliding with very large  $p_z$ , the outgoing direction of collision products is  
394 characterized by their rapidity  $y$ , a generalization of velocity defined by:

$$y = \ln \sqrt{\frac{E + p_z c}{E - p_z}}, \quad (9)$$

395 The rapidity is defined such that particles which emerge perpendicular to the beam axis (with  
396  $p_z = 0$ ) have  $y = 0$ , while  $y \rightarrow \infty$  toward the beam line. In practice, however, the outgoing  
397 particle's rest mass  $M$  and energy  $E$  are generally unknown, while the total momentum  $\vec{p}$  can be  
398 measured in detectors. In ultrarelativistic collisions, where  $\vec{p}^2 \gg M^2 c^2$ , we instead measure the  
399 pseudorapidity  $\eta$  defined by:

$$\eta = \ln \left( \frac{|\vec{p}| + p_z}{|\vec{p}| - p_z} \right) \quad (10)$$

400 Pseudorapidity may also be calculated from the polar angle  $\theta$  with respect to the beam pipe,

$$\eta = -\ln \left( \tan \left( \frac{\theta}{2} \right) \right) \quad (11)$$

401 As is clear from this representation, particles perpendicular to the beampipe with  $\theta = \pi/2$  corre-  
402 spond to rapidity  $\eta = 0$ , while particles with  $\theta = \pi/4$  correspond to  $\eta \approx 0.88$ .

403 In general throughout this document, energies and measurements are presented in natural  
404 units with  $\hbar = c = 1$  (momenta, for example, are given in MeV or GeV rather than MeV/c or  
405 GeV/c). Azimuthal angle  $\phi$  is measured in radians.

406 **2.6 Collective behavior in the QGP**

407 In any nucleus-nucleus collision, the initial collision region will exhibit some azimuthal anisotropy—  
408 both due to the elliptical overlap region for collisions with impact parameter  $b > 0$ , and due to local  
409 variations in the nuclear densities  $\rho A$  and  $\rho B$ . As the medium thermalizes and hydrodynamically  
410 expands, this spatial anisotropy translates into anisotropy in momentum space or “collective flow”  
411 of the expanding medium. This correlation is retained through the hadronization and free-streaming  
412 phases, and is ultimately detectable via modulation in the distribution of particles with respect to  
413 the reaction plane ( $\psi_{RP}$ , the plane spanned by the impact parameter  $\vec{b}$  and the beam direction).  
414 This may be expanded in a Fourier series,

$$\frac{dN}{d\phi} = \frac{N}{2\pi} \left( 1 + 2 \sum_n v_n \cos(n(\phi - \psi_{RP})) \right), \quad (12)$$

415 using Fourier coefficients  $v_1$ ,  $v_2$ ,  $v_3$ , etc. (sometimes referred to as “harmonic flow coefficients”)  
416 to model the  $\Delta\phi$  correlation between particles and the reaction plane. These coefficients may be  
417 interpreted as corresponding to different geometric anisotropies in the initial state:  $v_1$  refers to  
418 “directed flow” which arises as colliding nucleons are repelled perpendicular to the beam direction  
419 in the reaction plane. Elliptic flow coefficient  $v_2$  refers to the elliptical anisotropy arising from the  
420 overlap of two roughly circular nuclei, while  $v_3$  (“triangular flow”) and higher coefficients refer to  
421 more complex initial geometries arising from fluctuations in the nucleon densities [20].

422 The azimuthal direction of the reaction plane  $\psi_{RP}$  cannot be directly experimentally mea-  
423 sured, but may be estimated based on event-by-event particle distributions in the detector. Al-  
424 ternatively, flow may be measured by considering two-particle correlations measuring  $\Delta\phi_{\text{trig,assoc}}$   
425 between trigger and associated particles. In this case, the Fourier decomposition of the  $\Delta\phi_{\text{trig,assoc}}$   
426 distribution becomes

$$\frac{1}{N_{\text{trig}}} \frac{dN^{\text{pair}}}{d\Delta\phi_{\text{trig,assoc}}} = \frac{N_{\text{assoc}}}{2\pi} \left( 1 + 2\sum_n V_n \cos(n(\Delta\phi_{\text{trig,assoc}})) \right), \quad (13)$$

427 Here the combined flow coefficients  $V_n$  are found to be factorizable into coefficients for the trigger  
 428 and associated hadrons, i.e.  $V_n = v_{n,\text{trig}} \times v_{n,\text{assoc}}$  [21, 22]. To measure collective flow through this  
 429 two-particle method, two dimensional correlations in  $\Delta\eta - \Delta\phi$  are constructed between trigger and  
 430 associated hadrons, as shown in Fig. 4 from CMS study [22]. These distributions are projected over  
 431 the large  $\Delta\eta$  region (in this case  $|\Delta\eta| < 2$  to capture long range correlations, and are fit in  $\Delta\phi$  with  
 432 the Fourier function shown above to extract flow coefficients  $V_1$ ,  $V_2$ , and  $V_3$ , from which  $v_1$ ,  $v_2$ , and  
 433  $v_3$  may be calculated. These studies find centrality- and  $p_T$ -dependent flow coefficients through  $v_3$ ,  
 434 with  $v_3$  present substantially smaller than  $v_2$ . As expected from simple geometrical considerations,  
 435 values of  $v_2$  and  $v_3$  are greatest for mid-central collisions in which collision anisotropy is greatest,  
 436 and peak as a function of  $p_T$  in the 2-3 GeV range, as shown in Fig. 6.

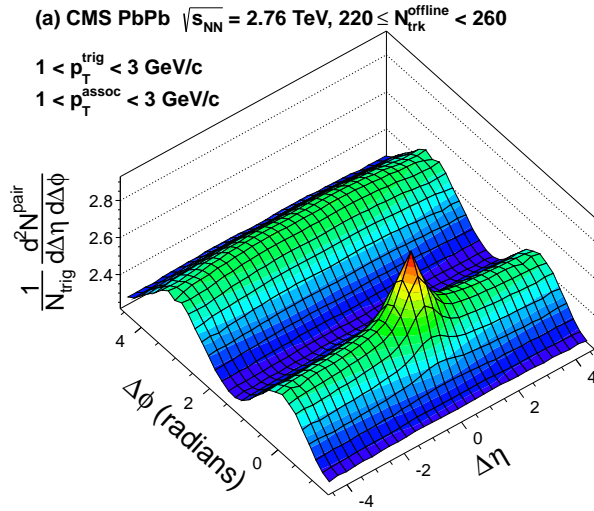


Figure 4. Illustration of dihadron correlation in  $\Delta\eta - \Delta\phi$  for  $1 < p_T^{\text{trig}} < 3$  GeV and  $1 < p_T^{\text{assoc}} < 3$  GeV in central PbPb collisions at 2.76 TeV from Ref. [22]

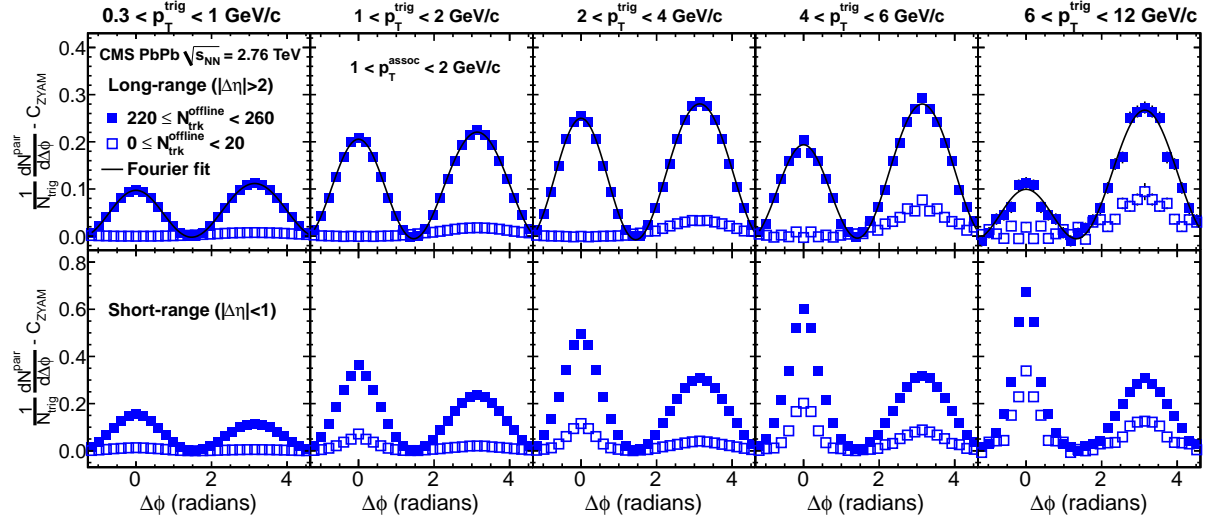


Figure 5. Fourier fits to dihadron  $\Delta\phi$  distributions for  $1 < p_T^{\text{assoc}} < 2$  GeV as a function of  $p_T^{\text{trig}}$  in central PbPb collisions at 2.76 TeV from Ref. [22]

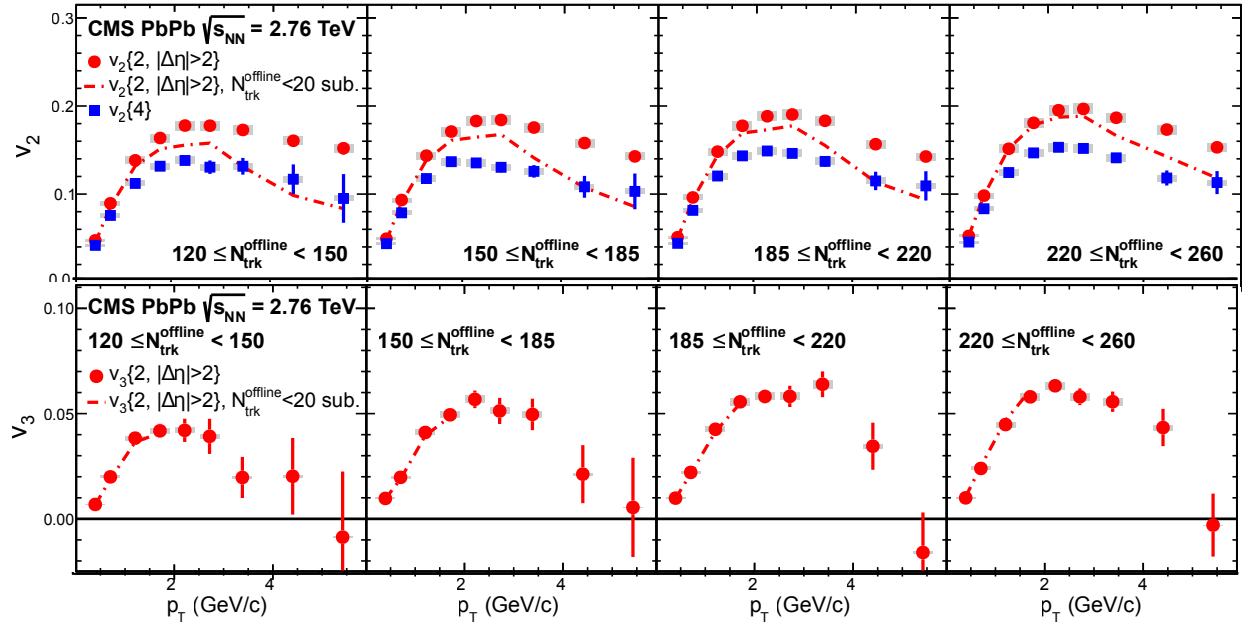


Figure 6. Flow coefficients  $v_2$  and  $v_3$  by centrality and  $p_T$  at 2.76 TeV from Ref. [22]

### 3 JETS AS PROBES OF THE QUARK GLUON PLASMA

438 Hard scatterings in heavy ion collisions can provide powerful probes of the quark gluon plasma.  
 439 Because of asymptotic freedom, high-energy parton-parton processes can be accurately character-  
 440 ized via pQCD, and have been thoroughly studied experimentally in hadron-hadron collisions. In  
 441 heavy ion collisions, the initial parton-parton interaction should by causality behave the same as a  
 442 parton-parton interaction in hadron-hadron collisions. After the collision, however, outgoing par-  
 443 tons traverse the quark gluon plasma, providing the opportunity to study medium properties by  
 444 comparing heavy ion results to expectations inferred from hadron-hadron “vacuum” reference data.  
 445 These studies are facilitated by the “factorization theorem” in pQCD, which states that the cross  
 446 section  $\sigma_{AB \rightarrow h}^{\text{hard}}$  of hadron  $h$  produced in the hard process  $A + B \rightarrow h$ ) can be decomposed into  
 447 contributions from:

- 448 • The perturbative cross section of the parton hard scattering  $\sigma_{ab \rightarrow c}^{\text{hard}}$
- 449 • The initial parton distribution functions (PDFs) of partons in the colliding nuclei A and B  
 450 ( $f_{a/A}$  and  $f_{b/B}$  for partons of flavor  $a$  and  $b$ )
- 451 • The fragmentation function  $\mathcal{D}_{c \rightarrow h}$  describing the probability that parton  $c$  fragments into  
 452 hadron  $h$  with momentum fraction  $z = p_h/p_c$

453 The total cross section may be represented, schematically, as:

$$d\sigma_{AB \rightarrow h}^{\text{hard}} = f_{a/A}(x_a, Q^2) f_{b/B}(x_b, Q^2) \times d\sigma_{ab \rightarrow c}^{\text{hard}}(x_a, x_b, Q^2) \times \mathcal{D}_{c \rightarrow h}(z, Q^2), \quad (14)$$

454 Each contribution to  $d\sigma_{AB \rightarrow h}$  can be experimentally determined, and in hadron-hadron collisions  
 455  $\sigma_{ab \rightarrow c}^{\text{hard}}$ , fragmentation functions, and PDFs should each be universal. Figure 7 illustrates this  
 456 factorization for hard-scattering interaction  $A + B \rightarrow h$ . The final state parton branching is  
 457 given by the Dokshitzer-Gribov-Lipatov-Altarelli-Parisi (DGLAP) equations that encode the QCD  
 458 radiation probabilities for a parton propagating in the vacuum.

459 The partonic cross section  $\sigma_{ab \rightarrow c}^{\text{hard}}$  furthermore should not, by causality, depend on the pres-  
 460 ence or absence of the QGP. Medium modifications may enter at two phases in this process: first,  
 461 via energy loss by parton  $c$  passing through the medium, and second via possible medium-induced

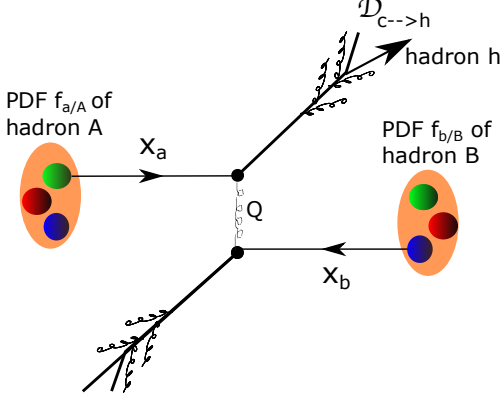


Figure 7. Illustration of the QCD hard-scattering  $A + B \rightarrow h$ .

462 changes to fragmentation functions  $\mathcal{D}_{c \rightarrow h}$ . Parton energy loss is attributed to two primary mech-  
 463 anisms: collisional energy loss from scatterings with partons in the medium, and medium induced  
 464 radiation roughly analogous to electromagnetic ionization in a medium [23, 24]. This medium-  
 465 induced parton energy loss implies an observable reduction of medium properties can also be fur-  
 466 ther probed by comparing measurements of jet substructure in heavy ion collisions compared to pp  
 467 reference data (Sec. 3.2), and by studying modifications to  $p_T$  balance in back-to-back dijet events  
 468 (Sec. 3.3).

### 469 3.1 Measuring suppression of high- $p_T$ particles and jets

470 One observable to probe parton energy loss in the medium is to compare yields of both particles  
 471 with relatively high transverse momentum ( $p_T$ ), and of reconstructed jets (collections of particles  
 472 clustered in an effort to reconstruct the original parton energy – see Sec. 7). This reduction in jet  
 473 yields compared to expectations from “vacuum” reference or scaled binary collisions can be studied  
 474 as both a signature of the presence of the QGP, and an observable to distinguish between models  
 475 of interactions within the QGP (see Sec. 3.1).

476 Since by pQCD factorization the partonic cross-section  $\sigma_{ab \rightarrow c}$  should be independent, in the  
 477 absence of the quark gluon plasma, the nuclear inclusive cross section would be expected to scale  
 478 with the number of participating nucleons, i.e.

$$479 d\sigma_{AB \rightarrow h}^{\text{hard}}(b) = \langle T_{AB}(b) \rangle \sigma_{\text{pp}}^{\text{hard}} \quad (15)$$

479 where  $T_{AB}(b)$  parameterizes the probability of nucleon-nucleon interactions for a given impact  
 480 parameter for nuclei A and B colliding with impact parameter  $b$  as discussed in Sec. 2.4. A com-  
 481 parison of actual hadron (or jet) yields compared to this expectation can therefore give information  
 482 about parton interactions with the medium, as characterized by the nuclear modification factor  
 483  $R_{AA}$  defined as the ratio of the observed yield in heavy ion data to the expectation from binary  
 484 scaled pp data:

$$R_{AA}(p_T, \eta) = \frac{d^2\sigma_{AA}/dp_T d\eta}{\langle T_{AB}(b) \rangle d^2\sigma_{pp}/dp_T d\eta} \quad (16)$$

485 Consistent with quenching expectations, RHIC measurements of  $R_{AA}$  in gold-gold collisions  
 486 showed substantial suppression of a factor of 70-80% for  $p_T > 4$  GeV [6, 7, 8, 9]. Comparisons of  
 487 RHIC measurements to early LHC results showed similar qualitative features, but greater suppres-  
 488 sion at low- $p_T$  at the LHC, despite the more slowly falling pp spectrum at the LHC, as shown in  
 489 Fig. 8. Measurements at the LHC have also found that  $R_{AA}$  rises with  $p_T$  for charged particles with  
 490  $p_T > 7$  GeV, and have shown no significant center-of-mass energy differences when comparing  $R_{AA}$   
 491 at 2.76 TeV and 5.02 TeV, as shown in Fig. 9. The  $p_T$  dependence of  $R_{AA}$  is generally driven by  
 492 three factors: the kinematic constraints on jet energy loss (model-specific details will be discussed  
 493 in Sec. 4), the fact that  $R_{AA}$  takes the ratio of two steeply falling spectra the scattered partons, one  
 494 shifted by energy loss and one un-shifted, and the effects of nuclear shadowing and anti-shadowing  
 495 in the nuclear PDFs [24, 25].

496 Studies of high- $p_T$  tracks make use of the fact that such tracks are likely to originate from  
 497 outgoing partons in hard-scattering interactions, providing an indirect look at energy loss by the  
 498 parton used as a probe of the QGP. To more directly reconstruct parton energy, we may instead  
 499 consider reconstructed jets, defined as the collection of (spatially grouped) particles resulting from  
 500 the fragmentation of a high- $p_T$  quark or gluon. Jet reconstruction, described in detail in Sec. 7,  
 501 groups detector deposits to reconstruct a jet energy, and uses Monte Carlo simulation to reconstruct  
 502 a “true” jet energy of the original parton. Quenching studies with reconstructed jets therefore can  
 503 offer a more direct look at energy loss in the medium by comparing measured energy in jets in  
 504 heavy ion collisions to those in proton-proton collisions. Measurements of jet  $R_{AA}$  at the LHC

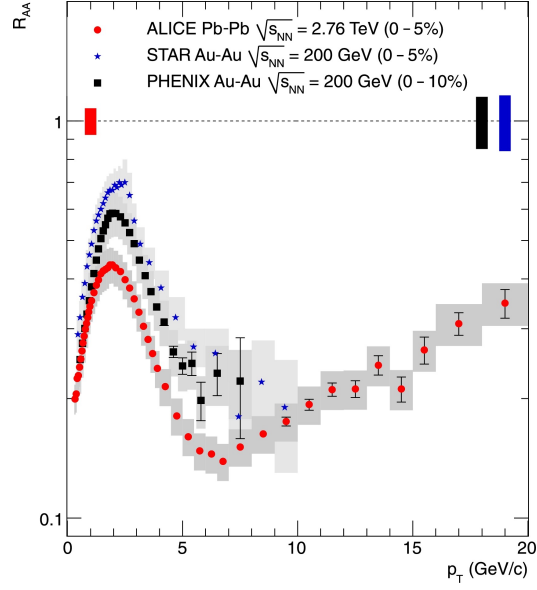


Figure 8. Measurements of charged particle  $R_{AA}$  from the STAR and PHENIX Collaborations at 200 GeV at RHIC, compared to ALICE results from the LHC at 2.76 TeV from Ref. [26].

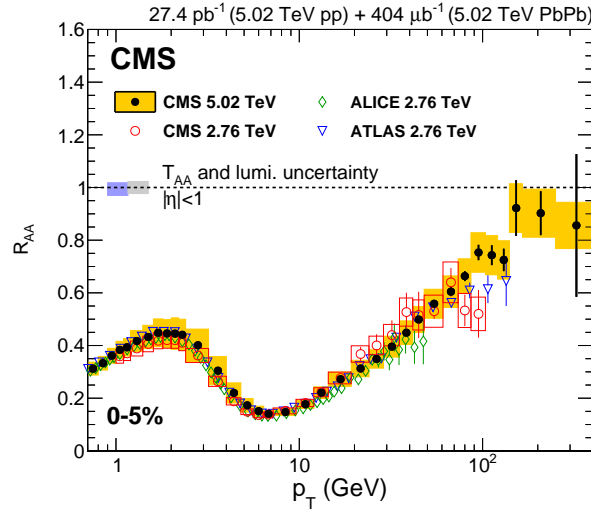


Figure 9. Measurements of charged particle  $R_{AA}$  at LHC energies 2.76 TeV and 5.02 TeV from Ref. [27].

reported in Refs. [28, 29] show suppression by a factor of approximately 40-60% in most central PbPb collisions, with weak dependence on jet  $p_T$  as shown in Fig. 10.

Jet  $R_{AA}$  measurements capture parton energy loss by measuring the reduction in yields in the presence of the QGP. To connect jet  $R_{AA}$  to charged particle  $R_{AA}$  measurements, it is necessary

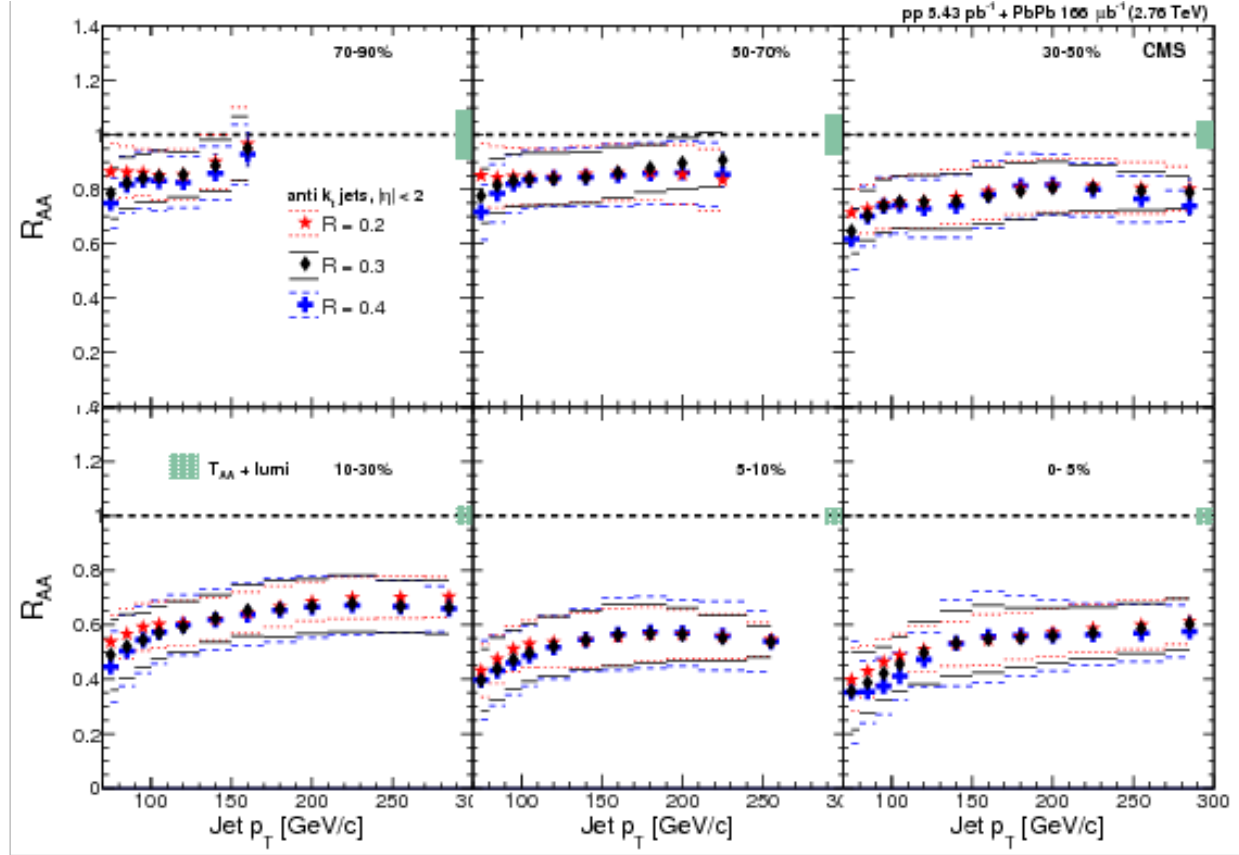


Figure 10. Jet  $R_{AA}$  at 2.76 TeV from Ref. [29].

509 to also consider trends in jet fragmentation patterns with jet- $p_T$ . High- $p_T$  jets are more likely to  
 510 originate from quarks than from gluons, and therefore exhibit “harder” fragmentation patterns—  
 511 i.e. higher- $p_T$  jets fragment into relatively fewer particles each with more  $p_T$  compared to jets  
 512 at lower- $p_T$ . Jets with softer fragmentation are also expected to exhibit greater modification in  
 513 the QGP, as low- $p_T$  fragmentation products rescatter in the medium. The highest- $p_T$  tracks, for  
 514 which  $R_{AA}$  is the smallest, are associated with those jets that have not only the highest- $p_T$ , but  
 515 also the hardest fragmentation. The high- $p_T$  sector of jet  $R_{AA}$  measurements at LHC energies,  
 516 however, still includes significant contributions from jets reconstructed from softer particles that  
 517 exhibit significant suppression.

518 **3.2 Jet fragmentation function and jet shape measurements**

519 Measurements of jet  $R_{AA}$  quantify the overall reduction in numbers of high- $p_T$  jets passing a certain  
 520 momentum threshold, providing an indication of the magnitude of jet energy loss in different  $p_T$   
 521 regions. As discussed above, this measurement can constrain the possible mechanisms of jet energy  
 522 loss. To further constrain models of jet energy loss, additional observables aim to capture the details  
 523 of jet fragmentation and its modification in the quark gluon plasma. One such measurement is the  
 524 jet fragmentation function, which captures the  $p_T$  distribution of tracks carrying jet momentum,  
 525 parameterized via the variables  $z$  and  $\zeta$ :

$$z = \frac{p_{||}^{\text{track}}}{p_{||}^{\text{jet}}}, \zeta = \frac{1}{\ln(z)}, \quad (17)$$

526 where  $p_{||}^{\text{track}}$  refers to the component of the track  $p_T$  along the jet axis. Jet fragmentation function  
 527 measurements from CMS shown in Fig. 11 show a centrality-dependent modification to fragmen-  
 528 tation function in PbPb relative to pp data, with a depletion in the mid- $\zeta$  range, balanced by an  
 529 enhancement at large  $\zeta$ , in the region corresponding to low- $p_T$  tracks. This shows a redistribu-  
 530 tion of energy within the jet cone toward softer particle production in the presence of the medium, con-  
 531 sistent with predictions of parton energy loss corresponding to a suppression of high- $p_T$  particles  
 532 (model details will be discussed in Sec. 4).

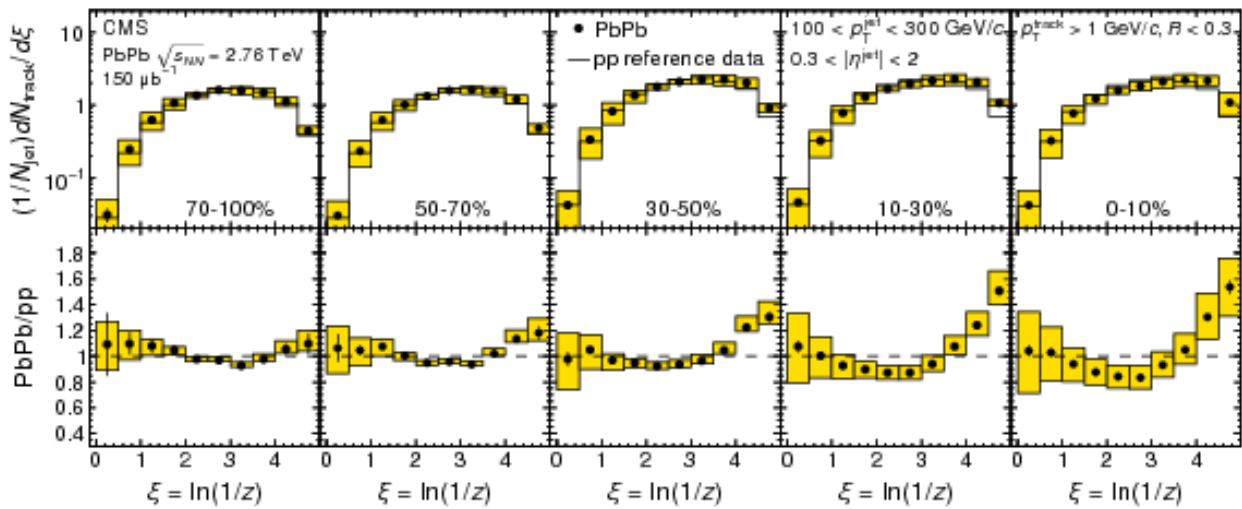


Figure 11. Jet fragmentation function for jets with  $100 < p_T < 300$  GeV in 2.76 TeV PbPb and pp data from Ref. [30].

533 In addition to characterizing the  $p_T$  spectrum of jet constituents, the distribution of  $p_T$   
 534 with respect to the jet axis can also help to constrain fragmentation scenarios. This distribution,  
 535 known as the jet shape, is defined within the jet cone as:

$$\rho(\Delta r) = \frac{1}{\delta r} \frac{1}{N_{\text{jet}}} \sum_{\text{jets}} \frac{\sum_{\text{tracks} \in [r_a, r_b]} p_T^{\text{track}}}{p_T^{\text{jet}}}, \quad (18)$$

536 where  $r_a$  and  $r_b$  correspond to the inner and outer radii, respectively, of an annulus of width  $\delta r = 0.5$   
 537 around the jet axis. The first jet shape measurement from CMS, shown in Fig. 12 (measured with  
 538 particles with  $p_T > 1$  GeV), shows a spatial redistribution of energy from small radii ( $\Delta r \approx 0.1$ )  
 539 to larger radii ( $\Delta r > 0.2$ ) from the jet axis. This is qualitatively consistent with predictions of  
 540 energy redistribution into particles that are both relatively soft ( $p_T < 3$  GeV, as observed in jet  
 541 fragmentation function measurements), and recovered at relatively large angles from the jet axis.  
 542 In this way, the study of jet shape modifications *within* the jet cone motivate extension of these  
 543 measurements to larger angles from the jet axis to quantify the distribution and  $p_T$  composition of  
 544 particles at angles larger than  $\Delta r = 0.3$ .

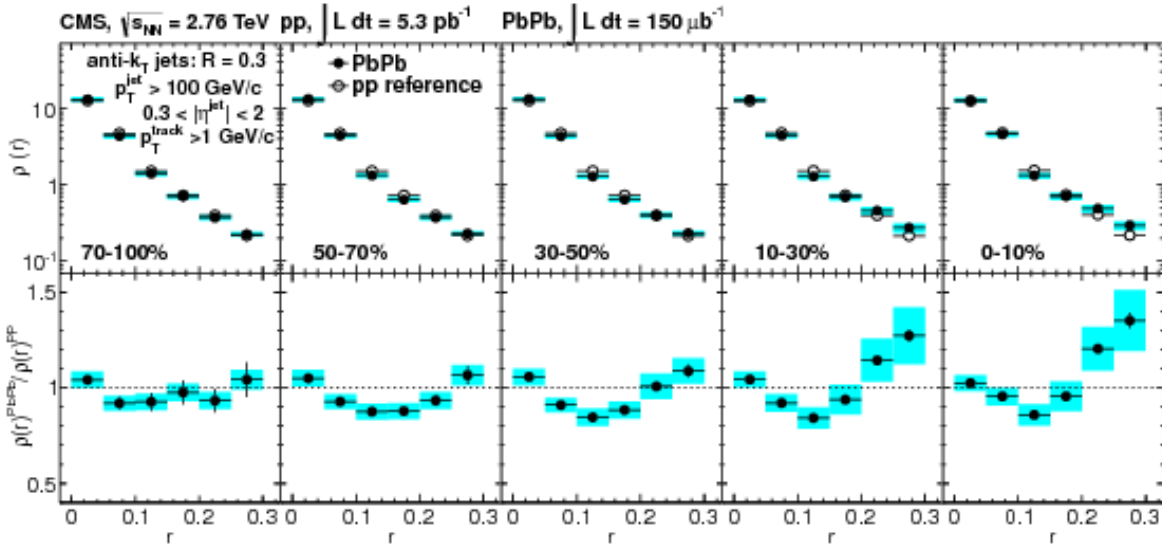


Figure 12. Jet shape measurement in 2.76 TeV PbPb and pp data from Ref. [31].

545 **3.3 Dijet asymmetry and momentum balance studies**

546 Additional possibilities for exploration of medium properties follow from the consideration of “di-  
547 jets,” jets that are back-to-back in azimuthal angle ( $\Delta\phi_{\text{jets}} \approx \pi$ ). As the incoming collision partici-  
548 pants each begin with  $p_T \approx 0$  GeV, the total  $p_T$  of outgoing partons immediately after the collision  
549 must also be 0. If both partons experience either no energy loss (as in the vacuum) or approximately  
550 equal energy loss (i.e. by experiencing roughly equal path-lengths through the medium), the mea-  
551 sured  $p_T$  of each jet in the dijet pair would be approximately equal. If, however, the hard-scattering  
552 occurs toward the surface of the QGP, the jet with a longer path-length through the medium might  
553 be expected to experience substantially more energy loss, leading to a  $p_T$  asymmetry in the dijet  
554 pair as illustrated in Fig. 13. This expectation was probed via studies of di-hadron correlations  
555 with high- $p_T$  particle triggers ( $4 < p_T < 6$  GeV by STAR at RHIC,  $8 < p_T < 15$  GeV by ALICE  
556 at the LHC) showed results consistent with the expectation. These studies showed the substantial  
557 suppression (even disappearance, in the STAR studies) of yields of particles with  $p_T > 2$  GeV in  
558 the region opposite the trigger hadron in azimuth [32, 33], consistent with path-length dependent  
559 jet quenching and a surface bias in trigger particles.

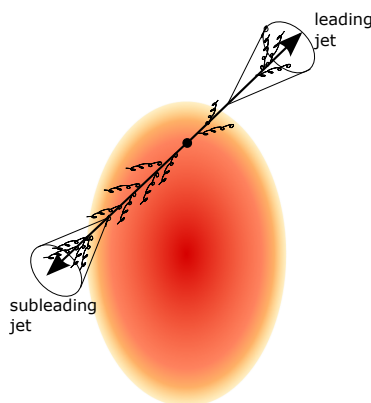


Figure 13. A “back-to-back” pair of dijets separated by  $\Delta\phi = \pi$ , with a highest- $p_T$  leading jet  
experiencing less quenching in the medium, and a more-quenched subleading jet with a longer path  
length through the medium.

560 The large kinematic reach of hard probes at the LHC allows for dijet studies at much higher  
561  $p_T$ . The first of these studies measured the “dijet imbalance” between the highest- $p_T$  (“leading

562 jet,” with  $p_{T,1}$ ) and second-highest- $p_T$  jets (“subleading jet,” with  $p_{T,2}$  in the event, parameterized  
563 as:

$$A_J = \frac{p_{T,1} - p_{T,2}}{p_{T,1} + p_{T,2}} \quad (19)$$

564 These studies, by the ATLAS and CMS Collaborations [34, 35] showed a centrality-dependent shift  
565 in the  $A_J$  in PbPb collisions, with greater dijet asymmetry in central PbPb data than in pp or in  
566 peripheral PbPb collisions. In pp and peripheral PbPb collisions, asymmetric dijet events are those  
567 in which some  $p_T$  is carried by a third jet, and the  $A_J$  distribution is steeply falling. In central PbPb  
568 collisions, however, there are expected to be two contributions to the sameple of asymmetric dijet  
569 events: not only three-jet events, but also dijet events in which the subleading jet is substantially  
570 quenched. As shown Fig. 14, this effect is evident in the shift toward larger values of  $A_J$  in central  
571 PbPb collisions.

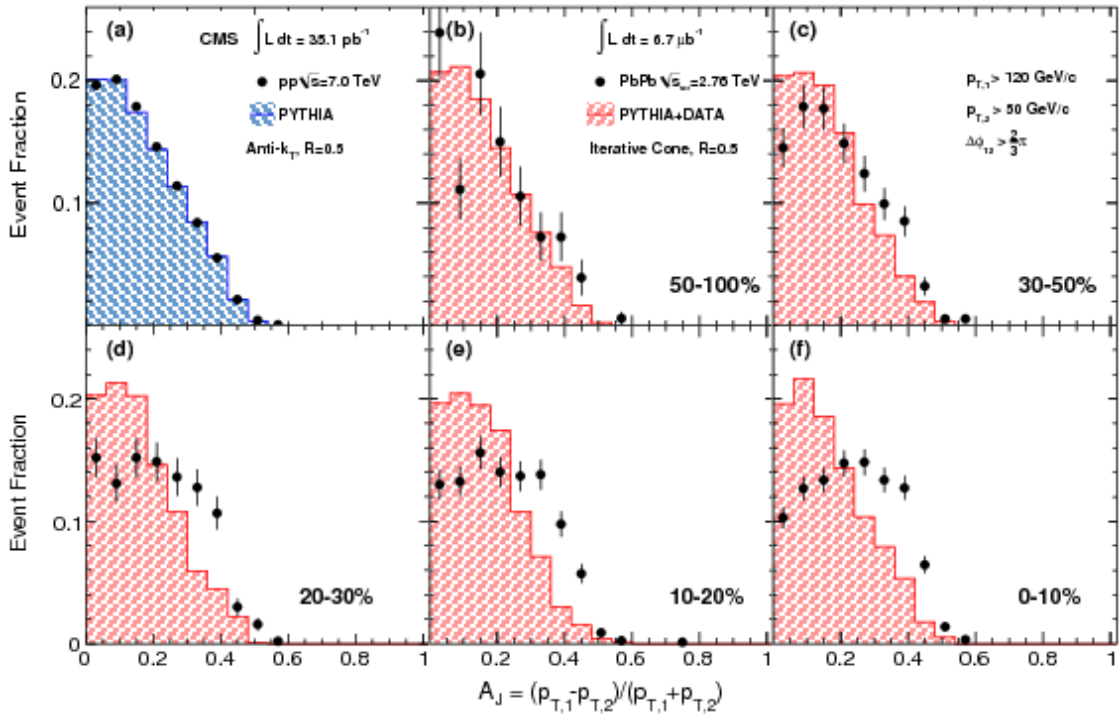


Figure 14. Dijet asymmetry in 2.76 TeV PbPb and pp data for jet selection  $p_{T,1} > 120$  GeV,  
 $p_{T,2} > 50$  GeV, and  $\Delta\phi_{1,2} > 2\pi/3$  from Ref. [35].

572 The transverse momentum difference between the leading and subleading jets may be con-  
573 ceptualized as “missing- $p_T$ ” from the subleading jet, which must by momentum conservation be

recovered somewhere in the hemisphere of the event surrounding the subleading jet axis. One way  
 to capture this momentum balance is by comparing the total  $p_T$  carried by tracks in different  $p_T$   
 classes in the subleading relative to the leading hemisphere. This balance is shown in the top row  
 Fig. 15, for  $\langle p_T^{\parallel} \rangle$  defined as the projection of each track's  $p_T$  projected in  $\phi$  onto the dijet axis (i.e.  
 the average of the leading and subleading jet axes) [36]. In pp and peripheral PbPb data, this  
 balance shows the depletion of tracks with  $p_T > 8$  GeV in the subleading relative to the leading  
 hemisphere balanced primarily by tracks with  $2 < p_T < 8$  GeV, consistent with the localization  
 of these tracks in additional jets for unbalanced dijets in this scenario. The magnitude of the  
 “missing- $p_T$ ” balancing distribution increases with growing  $A_J$  by construction. Comparing PbPb  
 to pp distributions (differences shown in the bottom row of Fig. 15), the balancing distribution in  
 unbalanced (large  $A_J$ ) events in central PbPb data shows larger contributions from soft particles  
 with  $p_T < 2$  GeV and smaller contributions from particles with  $p_T > 4$  GeV, indicating that the  
 more of the balancing  $p_T$  distribution in the subleading side is carried by soft quenching products  
 rather than additional jets.

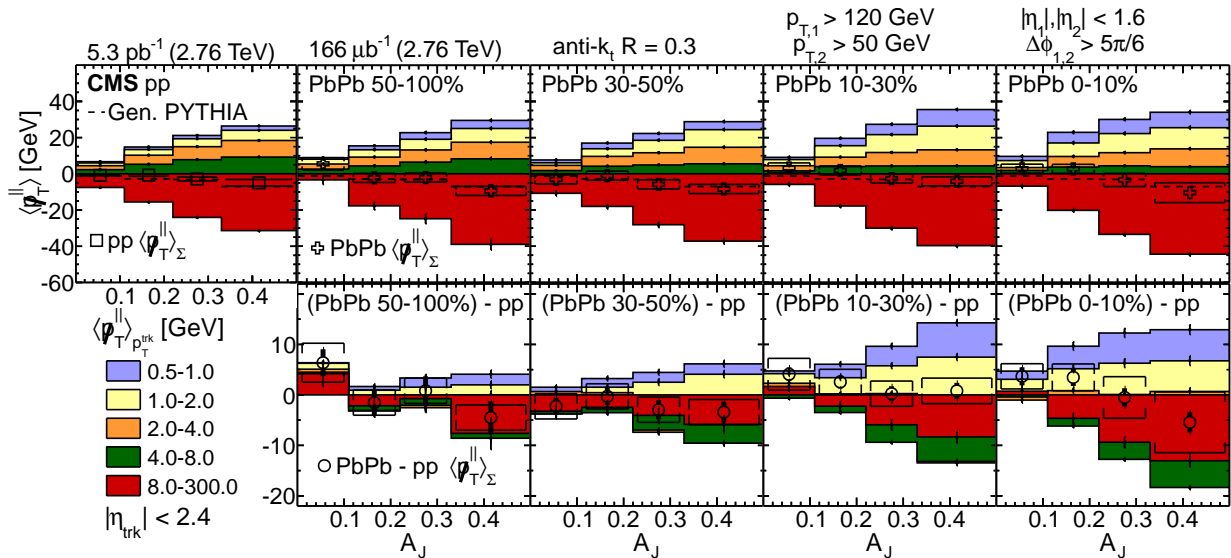


Figure 15. Top row: hemisphere  $p_T$  momentum balance in dijet events as a function of  $A_J$ , taking the total difference  $\langle p_T^{\parallel} \rangle$  in the subleading hemisphere minus that in the leading hemisphere from Ref. [36] in pp and PbPb data. Bottom row: Differences PbPb - pp.

Dijet momentum balance studies therefore show evidence of redistribution of jet energy  
 from harder to softer particles via jet quenching, and greater quenching of the subleading than

leading jets. As discussed above, the angular distribution of quenching products relative to the jet axis is also highly relevant for constraining models of interactions between the jet and the medium. This measurement is shown in Fig. 16 for unbalanced dijets with  $A_J > 0.22$ . Comparing the radial distribution with respect to the dijet axis shows that in this unbalanced dijet sample in central PbPb events, more  $p_T$  is recovered in lower- $p_T$  particles extending to large angles from the jet axis. It is important to note that this measurement shows overall hemisphere differences in the radial  $p_T$  distribution, combining the effects of quenching to the subleading jet, quenching to the leading jet, and also any azimuthal asymmetry in the underlying event (as would arise if the direction of the dijet axis coupled to odd underlying event flow terms such as  $v_3$ ). Isolating and further studying each of these contributions will be a major goal of this analysis, as discussed in Sec. 4.3.

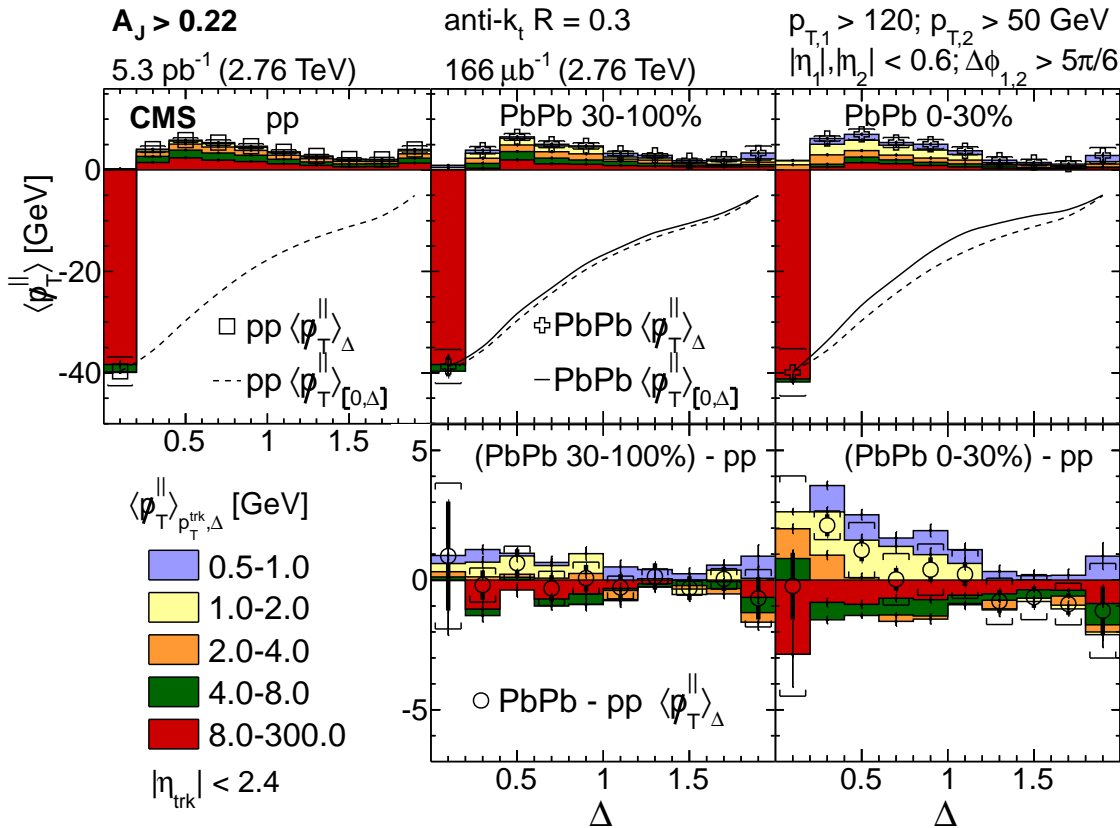


Figure 16. Top row: hemisphere  $p_T$  momentum balance in dijet events with  $A_J > 0.22$  as a function of  $\Delta r$ , taking the total difference  $\langle \vec{p}_T^{\parallel} \rangle_{\Delta}$  in the subleading hemisphere minus that in the leading hemisphere from Ref. [36] in pp and PbPb data. Bottom row: Differences PbPb - pp.

600      **4 MODELS OF JET ENERGY LOSS IN THE QUARK GLUON PLASMA**

601    A range of theoretical models of jet quenching have been developed to specifically account for the  
602    energy loss of a propagating probe through the quark gluon plasma. In general, models characterize  
603    collisional energy loss mechanisms (i.e. jet energy loss via elastic interactions with the medium),  
604    radiative energy loss by the propagating parton, and in some cases a medium response in the form  
605    of a “plasma wave” or back reaction. Some prominent examples of specific quenching models are  
606    surveyed briefly in Sec. 4.1. Some relevant comparisons to data are shown in Sec. 4.2, and then  
607    Sec. 4.3 summarizes goals of the present analysis in the context of the current state of jet quenching  
608    models.

609      **4.1 Survey of theoretical models of jet quenching mechanisms**

610    Jet quenching models consider a range of different conceptual pictures and mathematical formalisms  
611    to account for parton energy loss in the QGP and to predict experimental observables such as  $R_{AA}$ ,  
612    jet substructure, and dijet momentum balance. In all cases, one or more controlling parameters  
613    are fit or varied to experimental data (in many cases based on  $R_{AA}$ ), and other observables are  
614    then extracted. One example of such a parameter (used directly in the Higher Twist approach  
615    and calculable in other approaches) is the jet transport parameter  $\hat{q}$  that measures the average  
616    squared transverse momentum per unit path length  $\lambda$  transferred to the medium from the parton  
617    via collisional and/or elastic energy loss:

$$\hat{q} = \frac{\langle p_T^2 \rangle_{\text{med}}}{\lambda}. \quad (20)$$

618    Several models, discussed briefly and qualitatively below, have shown notable convergence in values  
619    of  $\hat{q}$  obtained via different approaches, as illustrated in Fig. 17 [37] from the JET Collaboration.  
620    These correspond to approximate values for temperature-scaled  $\hat{q}$  of  $4.6 \pm 1.2$  at RHIC and  $3.7 \pm 1.4$   
621    at the LHC. The brief summaries of these models included below are adapted from the more detailed  
622    descriptions in Refs. [19, 37, 38].

- 623      • **Higher Twist** – The “Higher Twist” approach treats medium modification to jets as an  
624      extension of pQCD factorization, suppressed by powers of the hard scattering momentum scale

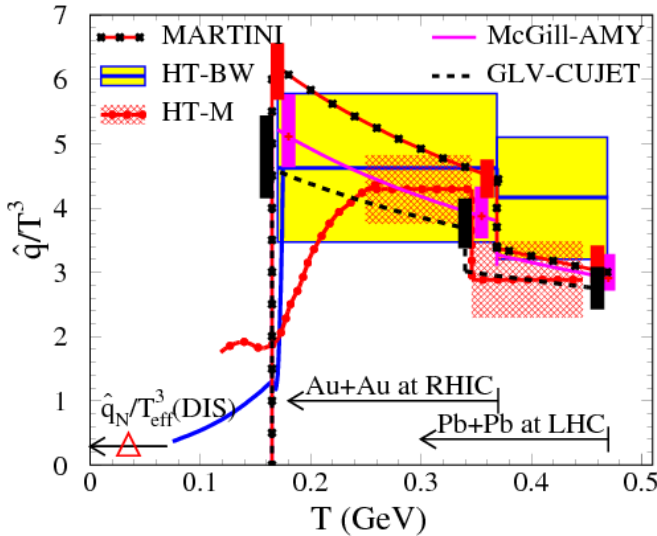


Figure 17. Temperature dependence of  $\hat{q}/T^3$  for a 10 GeV jet from different quenching models, analyzed by the JET Collaboration in Ref. [37].

625  $Q^2$ . These modifications involve “higher-twist” processes in which multiple partons interact  
626 coherently, in medium-induced splitting functions depend on medium properties via transport  
627 parameter  $\hat{q}$ . The Higher Twist Majumder (HT-M) approach extends the Higher Twist  
628 Berkeley Wuhan (HT-BW) model to include multiple gluon scatterings via modifications to  
629 the DGLAP vacuum evolution equations.

- 630 • **Arnold-Moore-Yaffe (AMY)** – The AMY approach treats the quark gluon plasma with  
631 a finite temperature field theory, with equilibrated particles with thermal mass  $gT$  and jet  
632 virtuality comparable to this thermal mass scale. With this approach, there is no hard scale  
633 for the jet, and vacuum-like jet fragmentation is not directly handled. Predictions are carried  
634 out by solving thermal QCD rate equations for parton distribution functions, either with  
635 collinearized interaction equations in the McGill implementation, or via full Monte Carlo  
636 simulation based on PYTHIA 8 in the MARTINI implementation.

- **Gyulassy-Lévai-Vitev (GLV)** – The GLV approach (expanded to include thermal mass and heavy quark effects as DGLV and implemented in the CUJET Monte Carlo framework) treats the medium as a collection of partially screened scattering centers. GLV starts from the hard radiation spectrum and also includes multiple soft gluon emissions. Scatterings in this model are governed by the ratio of the jet path length through the medium to the scattering length  $L/\lambda$ . Calculations are carried out as expansions in powers of  $L/\lambda$ , with the leading order corresponding to low opacity (or “thin medium”) and higher orders corresponding to additional scatterings in a denser or thicker QGP.
  - **Baier-Dokshitzer-Mueller-Peigné-Schiff-Zakharov (BDMPS-Z) and Armesto-Salgado-Wiedemann (ASW)** – The BDMPS-Z and ASW approaches compute energy loss via multiple soft scatterings in the medium. Similar to GLV, these approaches model the QGP as a collection of scattering centers with which an outgoing parton interacts. These interactions are encoded via quenching weights (modeled with Poisson distributions) that capture the probability that a parton loses a fraction of energy  $\epsilon$  due to  $n$  gluon emissions. JEWEL and YAJEM are both full Monte Carlo implementations of this approach.
  - **Linear Boltzman Transport (LBT)** – The LBT approach handles inelastic scattering in the medium via the Boltzmann equation, and also incorporates medium-induced gluon radiation with a spectrum taken from the Higher-Twist formalism. In this approach, collision kernels are taken from pQCD, while medium evolution is modeled with hydrodynamic simulation. Explicit calculation of  $\hat{q}/T^3$  yields results consistent with those shown in Fig. 17 [39, 40].
- In addition to the family of models with consistent jet transport coefficients summarized above, other diverse models have shown some success in capturing observables of jet suppression and structure modification in the medium, as will be discussed in Sec. 4.2.
- **Soft Collinear Effective Theory with Glauber Gluons (SCET<sub>G</sub>)** – The development of SCET in proton-proton physics was motivated by the inability of pQCD (due to infrared divergences) to handle interactions between propagating partons and low-energy particles traveling in the same direction as the parton. SCET is able to handle multiple soft energy scales via power-counting formalism at a range of energy scales. To apply SCET to studies

665 of QGP interactions, it is extended to include interactions in the medium with Glauber  
666 gluons, which are gluons with transverse momentum that is much larger than their momentum  
667 collinear with the parton. In SCET<sub>G</sub> medium interactions via Glauber gluons are modeled  
668 as background color fields that mediate interactions between the propagating parton and the  
669 QGP [41, 42, 43].

670 • **Strong/Weak Hybrid Model from AdS/CFT** – The strong/weak hybrid model assumes  
671 that the initial jet fragmentation occurs as in the vacuum (considering, as in HT, jets with  
672 virtuality scales much larger than the medium), so that interactions occur via modifications  
673 to the energy loss of partons within the jet. Predictions about this parton energy loss are  
674 derived from gauge-string duality modeling QCD as a  $\mathcal{N} = 4$  supersymmetric Yang-Mills  
675 theory. Here the propagating parton is treated as dual to a string falling into a black hole,  
676 and its rate of energy loss is computed via holography as a function of its initial energy and  
677 stopping distance in a medium of temperature T. [44, 45, 46]. Recent developments to this  
678 model have incorporated a “back reaction” in the hydrodynamic medium response to the jet  
679 taking the form of both a wake in the plasma and a Mach cone carrying energy through the  
680 plasma in the direction of the jet at large angles [47].

681 • **Coupled Jet-Fluid Model** – In this model, the full jet parton shower is coupled to the  
682 hydrodynamic flow of the medium. Modeled jet modifications include longitudinal energy  
683 loss, transverse momentum broadening, and medium-induced partonic splittings. In addition,  
684 the energy deposited in the medium by the parton shower of the jet is treated as a source  
685 terms for jet-induced changes to the evolution of the medium. In simulation, this results in  
686 a Mach cone shock wave induced by a jet propagating faster than the speed of sound in the  
687 medium. [48].

## 688 4.2 Quenching model comparisons to high- $p_T$ jet observables

689 Comparisons to various experimental observables can help to validate or challenge these diverse  
690 models of jet quenching, and the models outlined above have each shown some successes in this re-  
691 gard. A wide range of models have captured the  $p_T$  dependence of charged particle suppression fac-  
692 tor  $R_{AA}$  (illustrated in Fig. 18, particularly in the high- $p_T$  sector where radiative energy loss is likely

to dominate. Recently, however, there have been increasing efforts to accurately capture quenching dynamics via reconstructed jets, including capturing jet  $R_{AA}$  (discussed in Sec. 4.2.1), jet fragmentation functions (Sec. 4.2.3), jet shapes (Sec. 4.2.2), and dijet momentum balance (Sec. 4.2.4). To summarize the state of the theoretical field in capturing these observables, the discussion below will focus on four diverse models that represent very different approaches to jet quenching and that each offer recent predictions for several different observables: BDMPS as implemented in JEWEL, SCET<sub>G</sub>, the Hybrid model, and the Coupled Jet-Fluid model.

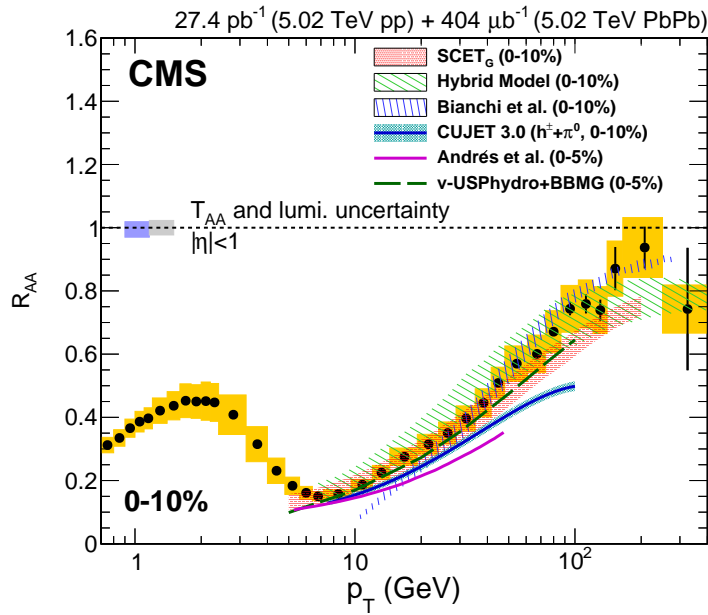


Figure 18. Model comparisons to charged particle  $R_{AA}$  in 0-10% central PbPb data at 5.02 TeV from Ref. [27].

#### 4.2.1 Quenching model comparisons: jet $R_{AA}$

In JEWEL the background is treated as ensemble of partons, and interactions between a propagating jet and this medium may be handled in several ways; in the predictions considered here, thermal partons produced in jet-medium interactions will be retained in the jet and hadronized with other jet partons. In considering the JEWEL predictions with this method, it is important to note that this is a limiting case, in which these partons then do not interact further with the medium. This approach can accurately capture the nearly flat  $p_T$  dependence of jet  $R_{AA}$  observed by the ATLAS and CMS Collaborations. As shown in Fig. 19, it also exhibits a dependence in  $R_{AA}$  on jet cone

708 radius parameter  $R$ , as larger cone sizes capture additional jet-related particles redistributed to  
709 larger angles from the jet axis (in PbPb relative to pp) via interactions with the medium [49].

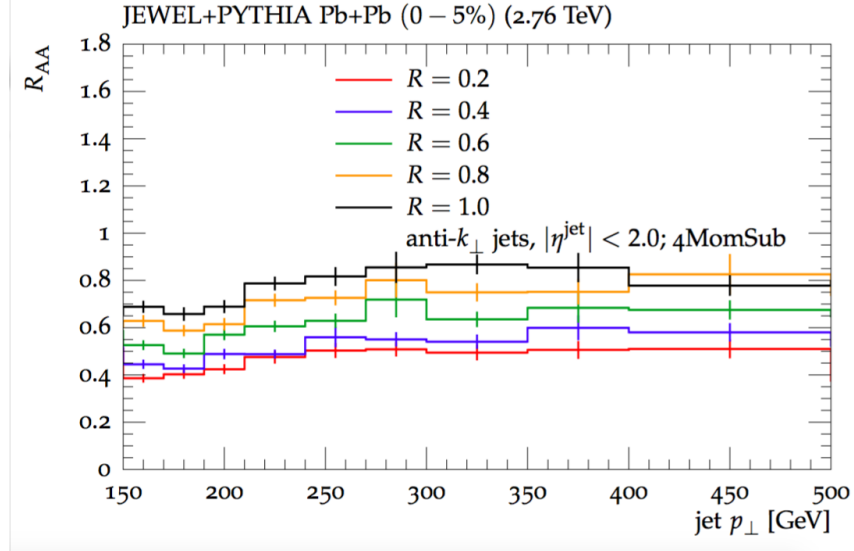


Figure 19. Simulated dependence of jet  $R_{AA}$  on jet reconstruction parameter  $R$  at 2.76 TeV from JEWEL in Ref. [49].

710 Similar to the JEWEL simulation, the calculations of  $R_{AA}$  from the coupled jet-fluid model,  
711 shown in Fig. 20 suggests greater dependence on jet reconstruction parameter  $R$  than is evident  
712 in the CMS measurement (although calculations are consistent within the large uncertainties on  
713 the measurement). In this calculation, about 10% of the suppression obtained with parton shower  
714 modifications alone is recovered when hydrodynamic response is also included, bringing calculated  
715  $R_{AA}$  closer to the experimentally measured  $p_T$  dependence when this coupled fluid evolution is  
716 taken into account.

717 Calculations of jet  $R_{AA}$  with SCET<sub>G</sub> explicitly parameterize the effects of initial state energy  
718 loss, also known as “cold nuclear matter” (CNM) effects, with parameter  $\mu_{\text{CNM}}$ . Varying this  
719 parameter changes the calculated values of  $R_{AA}$  substantially with larger values better capturing  
720 ATLAS and CMS measurements as shown in Fig. 21, suggesting the relevance of initial state  
721 effects in overall jet suppression. It is important to note that in these calculations radiative but not  
722 collisional energy loss is taken into account. Like JEWEL and the coupled jet-fluid model, SCET<sub>G</sub>  
723 also suggests significant  $R_{AA}$  dependence on jet reconstruction parameter  $R$ , with less suppression  
724 for larger values of  $R$  as “lost” energy is recovered at relatively large angles [42].

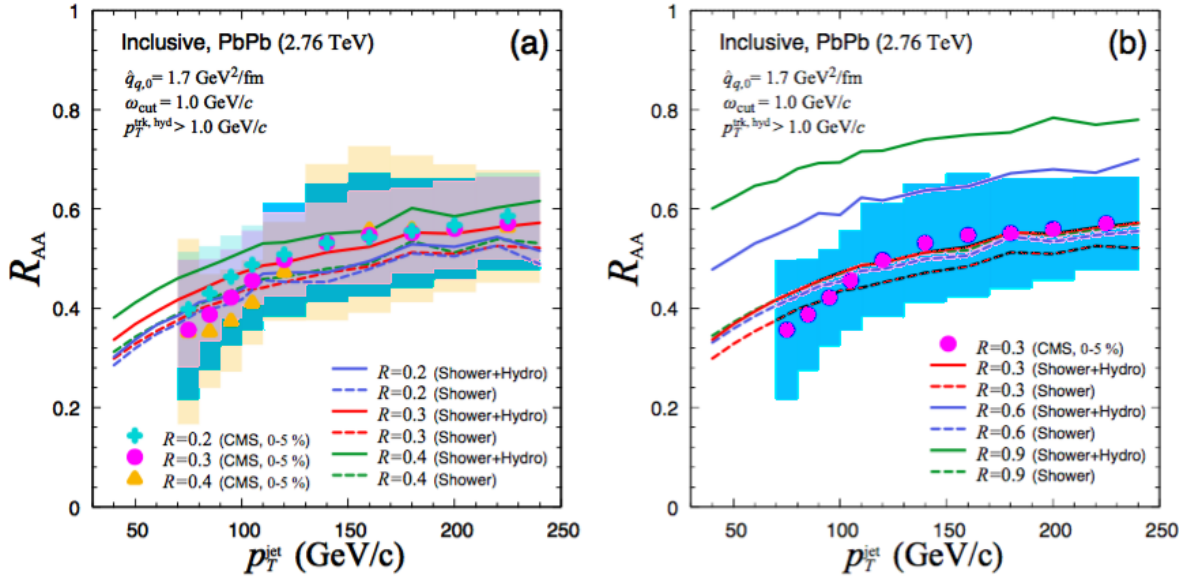


Figure 20. Simulated dependence of jet  $R_{AA}$  on jet reconstruction parameter  $R$  at 2.76 TeV from the coupled jet-fluid model, compared to CMS data at  $R = 0.2, 0.3, 0.4$  in Ref. [48].

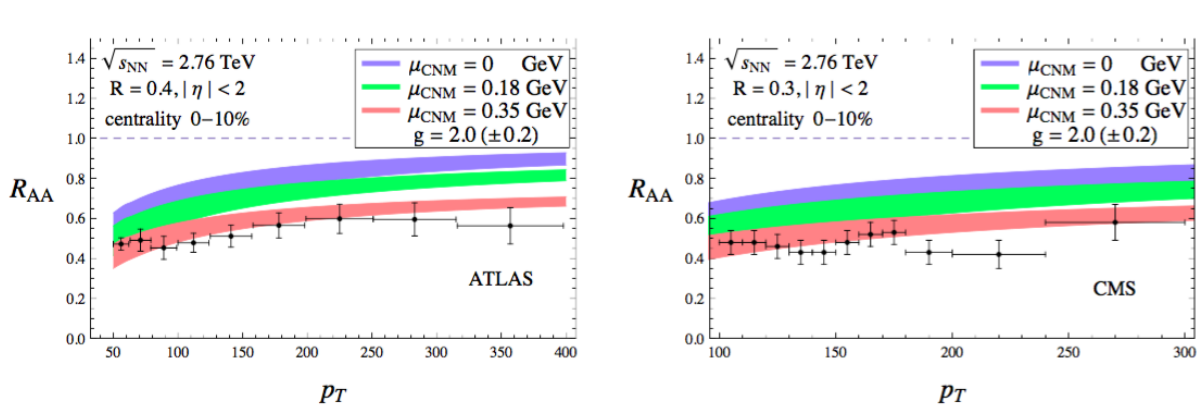


Figure 21. Predicted jet  $R_{AA}$  as a function of  $p_T$  at 2.76 TeV from  $\text{SCET}_G$ , shown for several values of initial state energy loss parameter  $\mu_{\text{CNM}}$  in Ref. [42].

In the strong/weak hybrid model derived from the AdS/CFT correspondence, the theory-dependent constant  $K = \hat{q}/T^3$  is defined to capture jet broadening in the medium. Comparisons of this model to data aim to constrain possible values of  $K$ , which are expected to be between 5 and 20 (although a much wider range of possible is considered in calculations). However, as Fig. 22 demonstrates in comparing model predictions, at several different jet radii  $R$ , for the rather extreme cases  $K = 0$  and  $K = 40$ , observables including  $R_{AA}$  are in fact rather insensitive to the

value of  $K$ . This is likely due to the fact that broad jets are more quenched than narrow jets by the plasma, so that the PbPb jet sample ends up dominated by jets with hard fragmentation. For these jets made up of few (or only one) parton transverse momentum “kicks” from the medium used to introduce broadening in this model end up only changing the jet axis direction rather than broadening the jet. The hybrid model predicts only weak dependence on jet reconstruction radius parameter  $R$  similar to the CMS measurement, although in this case the model uncertainties and experimental uncertainties are both large [47].

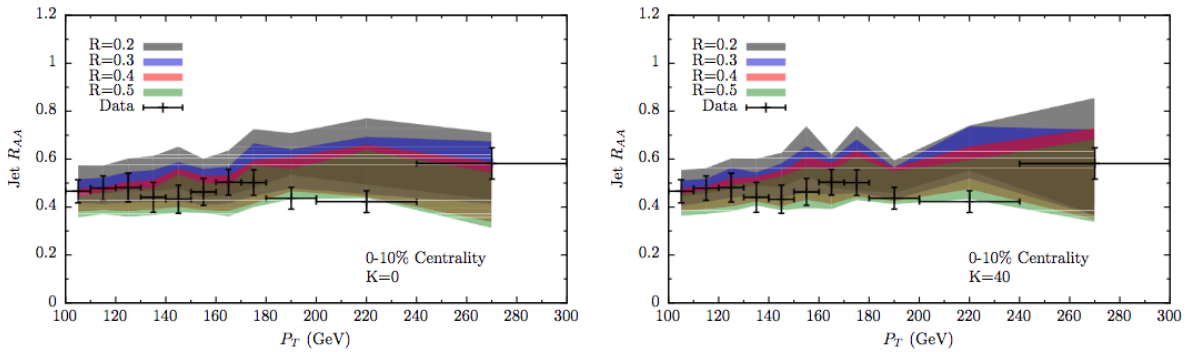


Figure 22. Calculated jet  $R_{AA}$  as a function of  $p_T$  at 2.76 TeV from the strong/weak hybrid model for broadening parameters  $K = 0$  (left, corresponding to no broadening) and  $K = 40$  (right, corresponding to extreme broadening) and a range of values of radius parameter  $R$  in Ref. [47].

#### 738 4.2.2 Quenching model comparisons: jet shapes

The JEWEL simulation of the jet shape observables accurately captures the redistribution of  $p_T$  from small to larger angles only with the inclusion of recoil effects from the medium as shown in Fig. 23. This larger-angle enhancement is driven by the soft ( $p_T < 3$  GeV) particles, and is completely absent in simulation without recoil effects, suggesting that these soft recoil particles drive the energy redistribution to larger angles from the jet axis. Taken with the jet radius dependence of  $R_{AA}$  also found by JEWEL to much larger radii than the  $R = 0.3$  measurement and simulation shown in Fig. 23, this interpretation motivates the extension of  $p_T$ -differential measurements of jet shape to larger angles from the jet axis.

In the coupled jet-fluid model, accounting for modifications to the parton shower only captures the jet modifications to jet shape  $\rho(\Delta r)$  fairly well at small angles from the jet axis, but

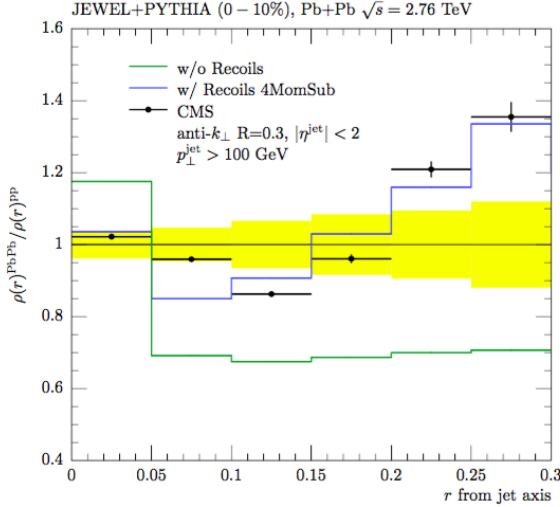


Figure 23. Simulated jet shape ratio  $\rho(\Delta r)_{\text{PbPb}}/\rho(\Delta r)_{\text{pp}}$  at 2.76 TeV from JEWEL in Ref. [49].

as the angle grows the relevance of the hydrodynamic response becomes increasingly evident, as shown in Fig 24. This is consistent with the qualitative idea that medium modifications may make the inner cone of the jet more narrowly collimated, while hydrodynamic response and medium transport results in broadening evident in a long and soft “tail” to the jet extending to large angles in  $\Delta r$  from the jet axis. The expectation in considering excitations that evolve with the medium is that these should in fact extend to significantly larger angles than the previously measured  $\Delta r$ , as shown in Fig 25.

Considerations of jet shape ratio  $\rho(\Delta r)_{\text{PbPb}}/\rho(\Delta r)_{\text{pp}}$  with SCET<sub>G</sub> separately consider CNM effects, effects arising from cross section suppression  $R_{AA}$  (with no direct modification to shape), and modifications to the parton shower in the medium. As Fig. 26 shows, CNM effects alone show little deviation from 1, implying that CNM effects do not change the relative fraction of quark jets to gluon jets much (as quark and gluon jets have significantly different shapes, so changes in the quark jet to gluon jet ratio would be evident in the jet shape ratio). Accounting for the overall cross section suppression shown in  $R_{AA}$  calculations above but assuming no changes to individual jet shapes in PbPb versus pp collisions results in narrowing of the jet cone, as shown in red in Fig. 26, due to the fact that broader gluon jets experience greater suppression, leaving a larger relative contribution from narrower quark jets. Adding in the jet-by-jet modifications to the parton shower captures the enhancement at relatively large  $\Delta r$  observed in CMS measurements.

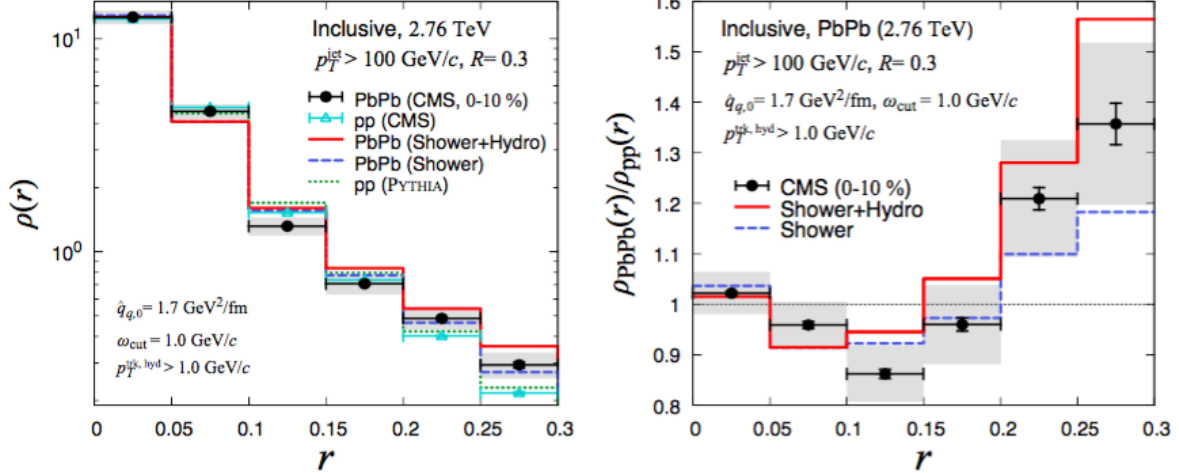


Figure 24. Calculated jet shapes in PbPb and pp at 2.76 TeV from the coupled jet-fluid model from Ref. [48].

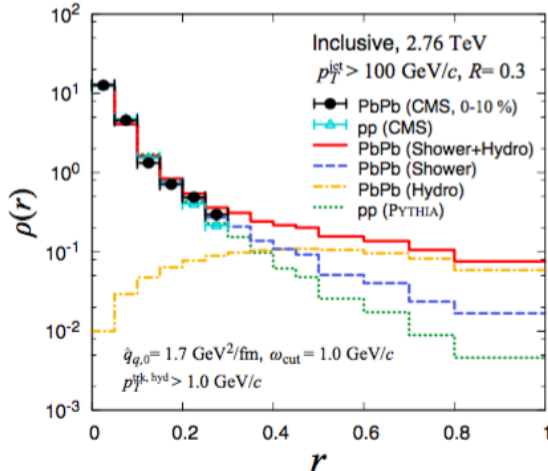


Figure 25. Calculated jet shapes in PbPb and pp at 2.76 TeV, extended to  $\Delta r = 1$  from the coupled jet-fluid model from Ref. [48].

767 In this case, broadening is captured by modifications to radiative energy loss via glauber gluon  
768 interactions, without directly accounting for collisional energy loss effects [42].

769 When hybrid model calculations of jet shape are carried out with a variety of broadening  
770 parameters  $K$  but without taking into account a back-reaction in the medium, all exhibit a narrow-  
771 ing within the jet cone as shown in Fig. 27. As discussed above with the hybrid model calculations  
772 of  $R_{AA}$ , this is likely due to the fact that broader jets are more likely to be quenched, leaving

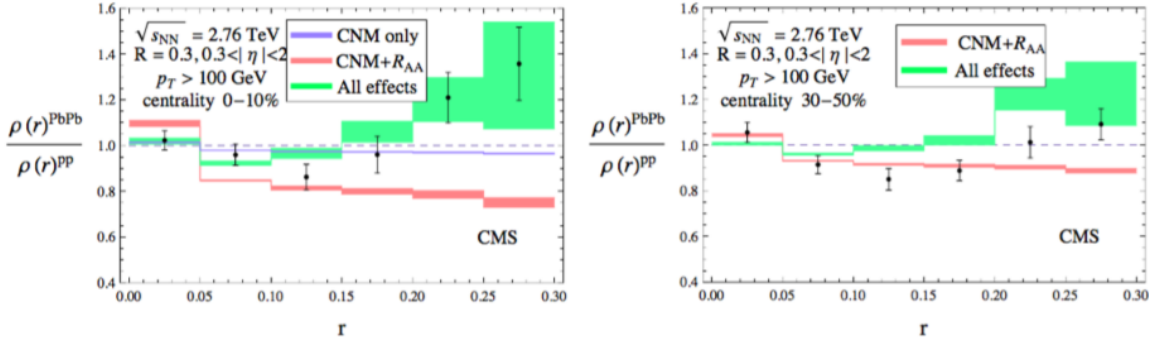


Figure 26. Calculated jet shape ratio  $\rho(\Delta r)_{\text{PbPb}}/\rho(\Delta r)_{\text{pp}}$  at 2.76 TeV with SCET<sub>G</sub>, showing contributions from cold nuclear matter, from jet suppression  $R_{AA}$ , and from medium modifications to the parton shower, in Ref. [42].

773 behind a narrower jet sample. Again as with the  $R_{AA}$  calculation, little dependence on broadening  
 774 parameter  $K$  is evident, since for these jets with hard fragmentation the transverse momentum  
 775 kicks in the medium only change the jet direction and the jet shape is constructed with respect to  
 776 the reconstructed jet axis rather than the original parton direction. For any choice of  $K$ , including  
 777 unrealistically large values corresponding to extreme broadening, the model in this form does not  
 778 capture the soft enhancement at large  $\Delta r$  from the jet axis [47].

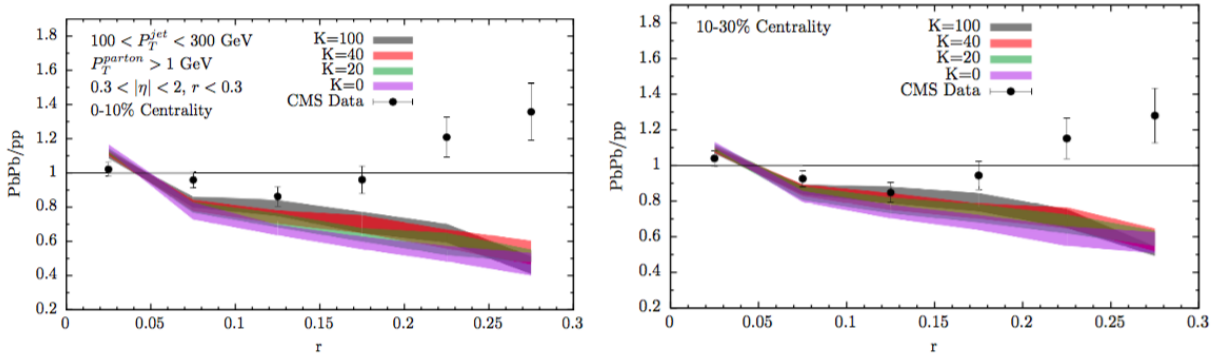


Figure 27. Calculated jet shape ratio  $\rho(\Delta r)_{\text{PbPb}}/\rho(\Delta r)_{\text{pp}}$  at 2.76 TeV from the strong/weak hybrid model for a range of values of broadening parameter  $K$  in Ref. [47].

779 In order to begin to account for this feature, the hybrid model must incorporate a “back-  
 780 reaction” in the medium in the form of a plasma wake and/or a Mach cone carrying momentum  
 781 through the medium in the same direction as the jet. This is implemented in the model as per-

782 turbations in the medium dependent on the kinematics of the jet and the momentum it loses as  
 783 it passes through the medium. Figure 28 compares hybrid model jet shape calculations with and  
 784 without this backreaction to CMS data. With the backreaction implemented, the model exhibits  
 785 a slight reversal in the narrowing trend at large  $\Delta r$  in central PbPb data relative to pp data that  
 786 comes closer to experimental results, although even with this backreaction it is still far from cap-  
 787 turing the large  $\Delta r$  enhancement in PbPb relative to pp observed by CMS and captured by other  
 788 models. This suggests the relevance of including a medium response in the jet shape calculation,  
 789 but that the current implementation of this response substantially underestimates the effect, which  
 790 the authors speculate may be due to under-estimation of the momentum deposited in the medium  
 791 by the jet, over-thermalization of this deposited energy, or greater removal of backreaction effects  
 792 via background subtraction than is applied to data [47].

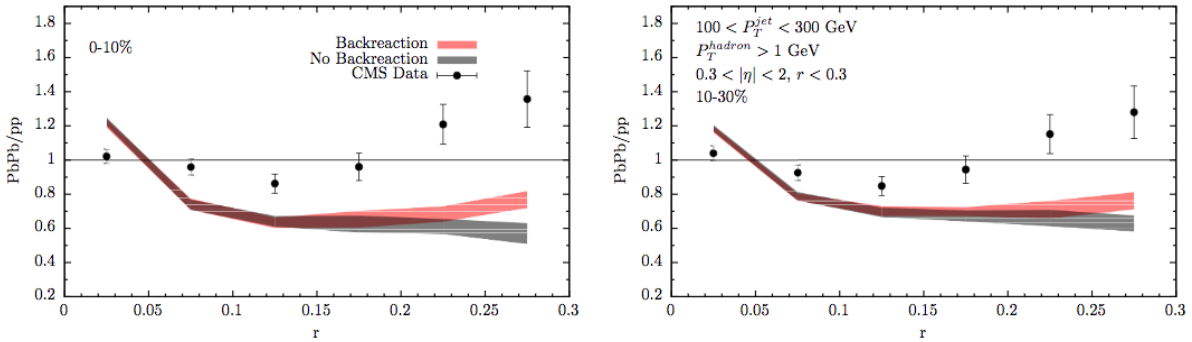


Figure 28. Calculated jet shape ratio  $\rho(\Delta r)_{\text{PbPb}}/\rho(\Delta r)_{\text{pp}}$  at 2.76 TeV from the strong/weak hybrid model, comparing calculations with and without the plasma backreaction from Ref. [47].

### 793 4.2.3 Quenching model comparisons: jet fragmentation functions

794 Fragmentation function measurements capture the  $p_T$  distribution of constituent hadrons (or tracks)  
 795 in a jet defined by a particular radius  $R$ . In JEWEL, track-by-track background subtraction is  
 796 not possible, so while jet  $p_T$  is background-subtracted the fragmentation function measurement is  
 797 carried out with all tracks. Figure 29 shows ATLAS and CMS JFF measurements compared to  
 798 JEWEL with and without medium recoil. As expected due to the lack of background subtraction,  
 799 the simulation with recoil included overshoots the low- $p_T$  (high- $\zeta$ ) enhancement observed in PbPb  
 800 relative to pp. Without recoil, however, JEWEL shows suppression rather than enhancement in this

region, supporting the interpretation of this soft enhancement as due to medium response to the propagating jet [49].

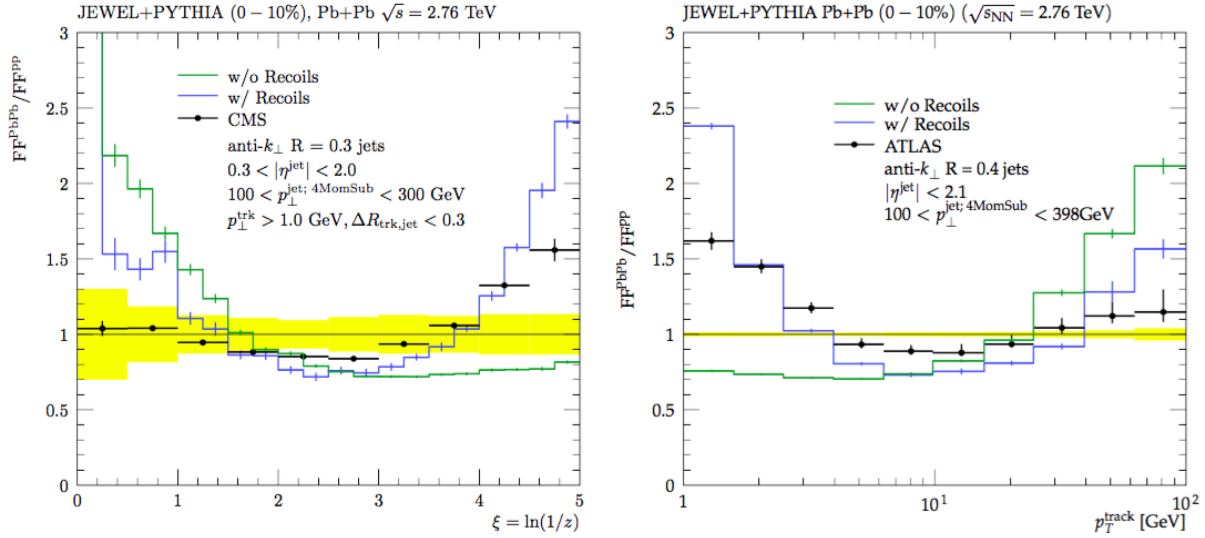


Figure 29. Simulated jet fragmentation function ratio PbPb/pp at 2.76 TeV from JEWEL in Ref. [49].

In the hybrid model before the implementation of the backreaction, energy lost by the jet is assumed to thermalize completely so that it loses all correlation to the jet axis. The calculated jet fragmentation function modification PbPb/pp in this scenario (for  $K = 0$ ) is shown in the gray band in Fig 30. Like the JEWEL simulation without recoil, the hybrid model in this scenario misses the enhancement of low- $p_T$  particles (corresponding to large  $\zeta = 1/\ln(z)$ ) in the fragmentation function measurement. When the backreaction is included in the calculation, the model comes qualitatively closer to the shape of the  $\zeta$ -dependence of the fragmentation function, capturing the rising trend toward large  $\zeta$  that corresponds to low- $p_T$  enhancement. As with the jet shapes calculation, however, while the inclusion of the backreaction improves the qualitative correspondence between the shape of the trend from the model calculation and the shape of the data, even with the backreaction quantitative agreement is not achieved [47].

#### 4.2.4 Quenching model comparisons: dijet asymmetry

Dijet asymmetry studies include both measurements of the distribution of asymmetry parameter  $A_J$ , and studies to capture the balancing distribution of  $p_T$  “missing” from the subleading jet.

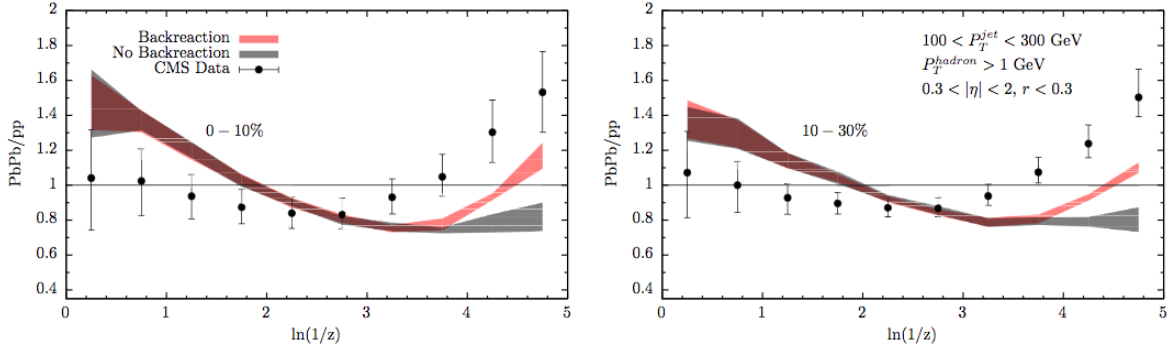


Figure 30. Calculated jet fragmentation function ratio  $\text{PbPb}/\text{pp}$  at 2.76 TeV from the strong/weak hybrid model comparing calculations with and without the plasma backreaction from Ref. [47].

817 In JEWEL simulations of the  $A_J$  distribution, shown in Fig. 31, little effect is shown from adding  
 818 medium response (“recoils”), and this serves to slightly reduce the  $A_J$  modifications observed with  
 819 medium-induced fragmentation but without the inclusion of recoil partons into medium-modified  
 820 jets [49].

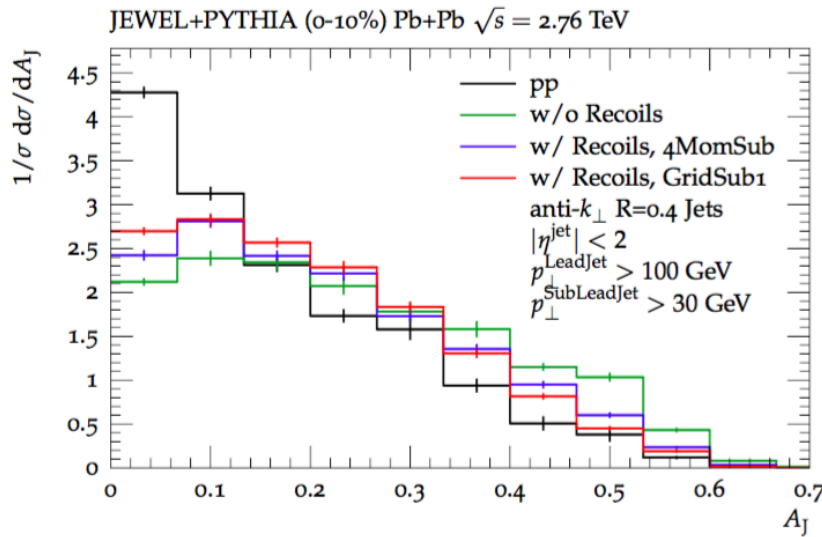


Figure 31. Simulated dijet asymmetry parameter  $A_J$  in pp and PbPb at 2.76 TeV from JEWEL in Ref. [49].

821 The hybrid model compares simulation to CMS measurements of the “balancing” distri-  
 822 bution of track- $p_T$  in the subleading (plotted positive) versus the leading (plotted negative) hemi-

sphere. Experimental results (discussed in Sec. 3.3) are shown again in the bottom panel of Fig. 32 for reference. Without the backreaction (shown in the top panel of Fig. 32), the hybrid model captures the energy loss by the subleading jet, as evident in the large high- $p_T$  depletions, but none of the soft enhancements in unbalanced dijets evident in PbPb data. With the backreaction implemented, the hybrid model qualitatively captures the soft enhancement, but yields fewer particles with  $2 < p_T < 4$  GeV and somewhat more particles with  $p_T < 2$  GeV than the data. Comparisons between the hybrid model and CMS data for the  $\Delta r$  distribution of the balancing transverse momentum in the subleading jet hemisphere shows this same behavior: without the backreaction none of the balancing excesses of soft particles in the subleading jet hemisphere relative to the leading jet hemisphere are recovered, while adding the backreaction captures the general momentum balancing distribution while missing some particles in the  $2 < p_T < 4$  GeV range [47].

### 4.3 Theoretical motivations for detailed jet-track correlation studies

Recent theory developments have included increasingly robust treatment of soft physics, and increasingly detailed treatment of jet substructure and predictions of medium reactions to propagating jets including at large angles from the jet axis. These approaches are accompanied by increasing interest in observables that are sensitive to the details of jet-medium interaction, and in particular to the angular distributions of jet fragmentation particles and to a possible Mach cone or other medium response at potentially large angles from the jet axis. In both JEWEL simulation and the strong/weak hybrid model, a “back reaction” or recoil in the medium is needed to properly capture both the enhancement of low- $p_T$  particles in jet fragmentation functions, and the large angle enhancement in the PbPb jet shape. The SCET<sub>G</sub> model, on the other hand, captures jet shape modifications via glauber gluon interactions but without an explicit recoil effect, while coupled jet-fluid model is able to capture jet shape coupled parton shower modification and hydrodynamic evolution. Measurements in pp and a range of PbPb centralities that are both differential in track- $p_T$  and extend to large angles from the jet axis can offer the potential to help distinguish between these quite different pictures of jet-medium interactions.

Toward that end, the results from the CMS Collaboration discussed in this analysis use correlations between jets and charged particles to extend jet shape measurements to large angles from the jet axis and provide detailed characterization of jet peak in separate dimensions  $\Delta\eta$  and

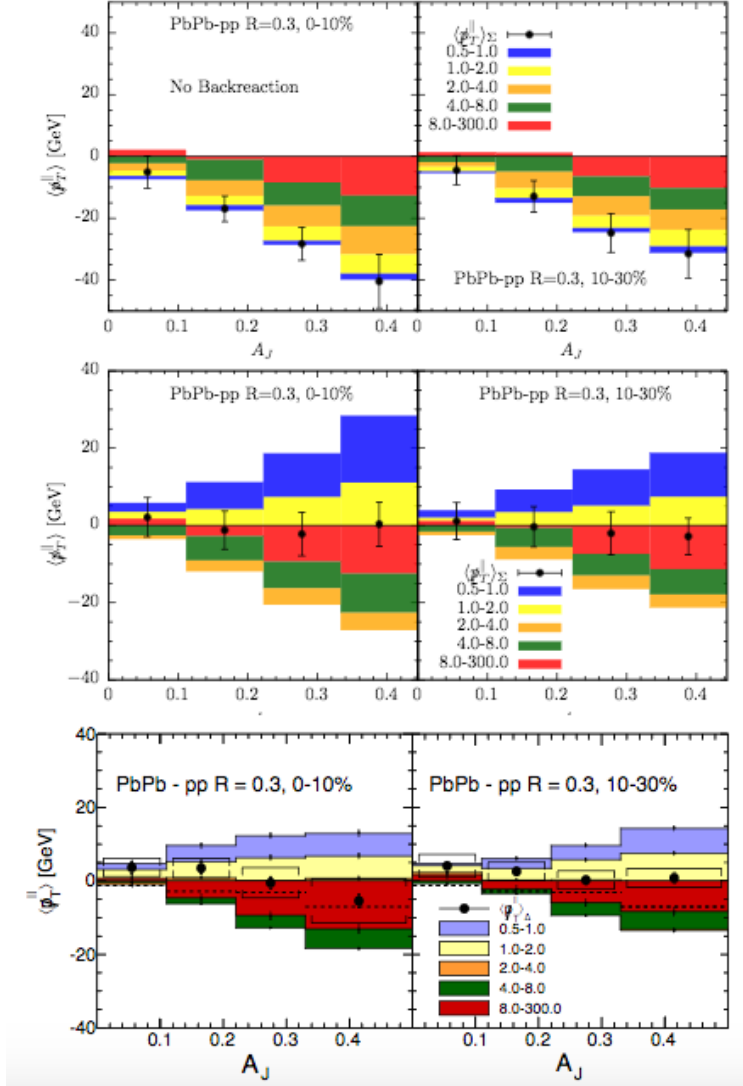


Figure 32. Calculated jet shape ratio  $\rho(\Delta r)_{\text{PbPb}}/\rho(\Delta r)_{\text{pp}}$  at 2.76 TeV from the strong/weak hybrid model in Ref. [47].

852  $\Delta\phi$ . In addition to measurements for an inclusive selection of high- $p_T$  jets, dijet correlation studies  
853 are carried out for leading and subleading jets as a function of  $A_J$ . These studies can help to  
854 connect measurements of dijet asymmetry and event-wide momentum balance to studies of jet  
855 modifications at small angles, clarifying the interpretation of transverse momentum distributions  
856 in heavy ion events compared to a “vacuum” reference of pp dijet data.

## 5 THE LARGE HADRON COLLIDER AND THE CMS DETECTOR

### 858 5.1 The Large Hadron Collider

859 The Large Hadron Collider (LHC), located at CERN near Geneva, is the largest and highest-  
 860 energy particle accelerator in the world. It consists of two counter-rotating particle beam line in  
 861 a tunnel 26.7 km in circumference, located between 45 m and 170 m underground [50]. During  
 862 standard operation, the LHC collides beams of protons accelerated and focused using a series  
 863 of superconducting magnets, cooled to below 2 K using supercritical helium. Particle beams are  
 864 brought together for collisions at in experimental detectors at four points in the accelerator ring: the  
 865 ATLAS, CMS, ALICE, and LHCb detectors. In addition to the proton-proton (pp) data collected  
 866 at center-of-mass energies  $\sqrt{S_{NN}} = 7$  TeV, 8 TeV, and 13 TeV, the LHC has also been operated  
 867 for heavy ion physics by colliding with fully-stripped lead nuclei ( $^{182}\text{Pb}^{82+}$ ) in lead-lead (PbPb)  
 868 and proton-lead (pPb) collisions. Heavy ion runs at the LHC have included PbPb data and pp  
 869 “reference” runs at  $\sqrt{S_{NN}} = 2.76$  TeV (2011 and 2013, respectively) and 5.02 TeV (2015) and pPb  
 870 data at  $\sqrt{S_{NN}} = 5.02$  TeV (2013 and 2016) and 8.16 TeV (2016). This analysis relies on PbPb  
 871 data at 2.76 TeV and 5.02 TeV, and corresponding pp reference data at the same center-of-mass  
 872 energies.

873 In peak proton-proton operation, the LHC collides 2,808 bunches each containing approx-  
 874 imately  $10^{11}$  protons with a minimum bunch spacing of 25 ns, for a maximum luminosity of  
 875  $10^{34}\text{cm}^{-2}\text{s}^{-1}$  delivered to the high-luminosity detectors (ATLAS and CMS). The lead-lead per-  
 876 formance target of  $10^{27}\text{cm}^{-2}\text{s}^{-1}$  delivered via 592 bunches of  $10^7$  lead ions was slightly exceeded  
 877 during the 2015 PbPb run. At this high-intensity frontier, it is common during nominal pp data  
 878 collection and possible in PbPb data collection that multiple distinct proton-proton collisions may  
 879 occur within a recorded event in a phenomenon known as “pile-up.” However, pile-up is relatively  
 880 rare in PbPb collisions due to the lower luminosities, and in the present analysis only one primary  
 881 vertex will be considered (with products of any other possible interactions removed via background  
 882 subtraction procedures).

883 **5.2 The CMS detector**

884 The CMS detector is named for the Compact Muon Solenoid at its heart: a superconducting magnet  
885 with magnetic field of 3.8 T, length of 13 m, diameter of 6 m, and weight 14,000 tons. Inside  
886 of this solenoid, the detector includes silicon pixel and strip detectors for particle tracking (see  
887 Sec. 5.3 for a detailed explanation), and electromagnetic and hadronic calorimeters (see Sec. 5.4).  
888 Calorimeters within the solenoid volume are complemented by additional calorimetry outside of the  
889 solenoid that provides coverage in the very forward direction close to the beam line, including the  
890 hadronic forward (HF) calorimeter in the region  $3.0 < |\eta| < 5.2$  used in this analysis for centrality  
891 determination, and the Zero Degree and CASTOR calorimeters in the even more forward region.  
892 The CMS detector also includes an extensive muon system outside of the solenoid volume, consisting  
893 of aluminum drift tubes in the barrel region, cathode strip chambers in the forward region, and a  
894 complementary system of resistive plate chambers (not discussed in detail here as muons are not of  
895 primary relevance to this analysis). Full details about the CMS detector may be found in Ref. [51],  
896 and a perspective drawing of the CMS detector from this report is shown in Fig. 33.

897 In the CMS detector, the  $+z$  axis is defined to be horizontal, pointing to the West along  
898 the beam line direction. The  $x$  axis is horizontal, pointing to the South toward the center of the  
899 LHC. The  $+y$  axis is vertical, pointing upward. The azimuthal angle  $\phi = \tan^{-1}(\frac{y}{x})$  is defined in  
900 the  $x$ - $y$  plane such that  $\phi = 0$  is the  $+x$  axis. Pseudorapidity  $\eta = -\ln(\tan(\frac{\theta}{2}))$  is defined to have the  
901 same sign as the  $+z$  axis. Pseudorapidity coverage in the CMS detector ranges from  $\eta = 0$  at the  
902  $y$ -axis, to  $|\eta| > 8.3$  in Zero Degree Calorimeter approaching the  $+/z$  axis.

903 **5.3 Trackers in the CMS detector**

904 The CMS tracking system consists of a small silicon pixel detector for precise measurement near  
905 the interaction point (with three layers with radii 4.4 cm to 10.2 cm), surrounded by a large silicon  
906 strip detector with layers to a radius of 110 cm. In both detectors, a cylindrical tracker “barrel” is  
907 complemented by “endcap” disks that together provide full azimuthal coverage and pseudorapidity  
908 coverage in the range  $|\eta| < 2.5$ . The pixel detector consists of 66 million pixels in 1440 modules.  
909 It provides three-dimensional measurements of “hits,” or interactions of particles with tracker  
910 materials, with a transverse resolution  $10\mu\text{m}$  and longitudinal resolution  $20 - 40\mu\text{m}$  (and a third

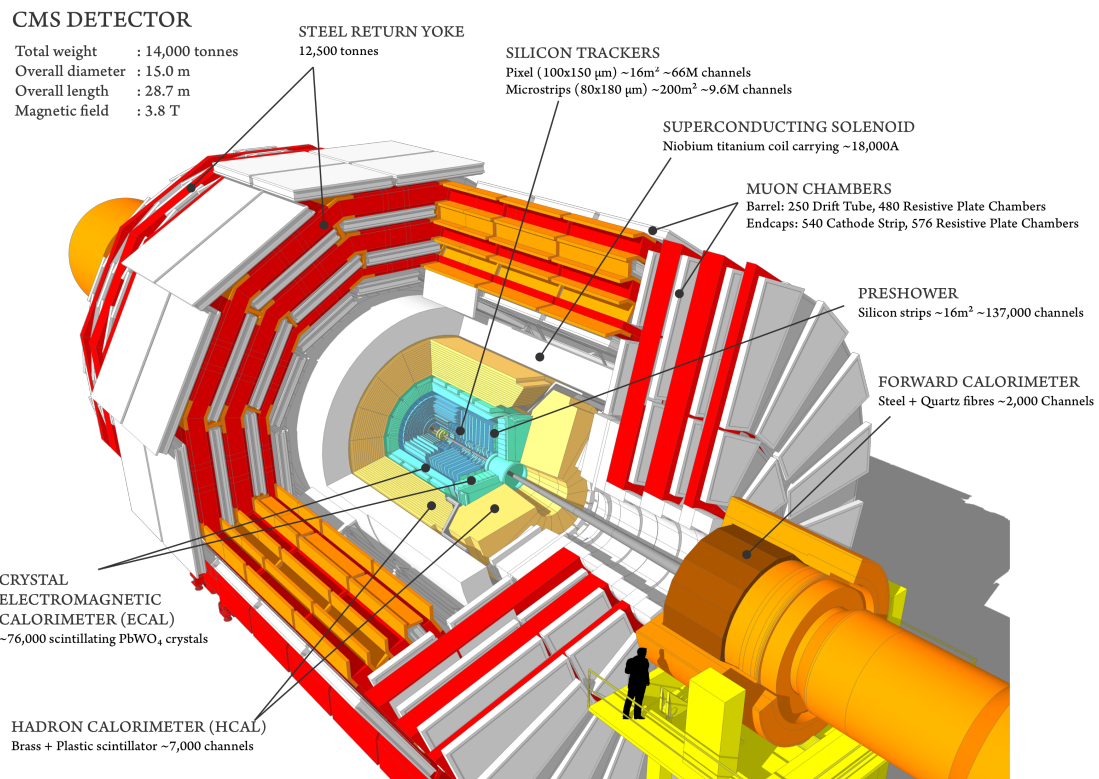


Figure 33. Perspective rendering of the CMS detector, showing component sub-detectors with a human included for scale perspective [52].

coordinate provided by the pixel plane). The silicon strip detector consists of 9.3 million strips in 15,148 modules, organized in four components: Tracker Inner Barrel (TIB) and Disks (TID), Tracker Outer Barrel (TOB, covering the region  $r > 55$  cm), and Tracker End Caps (TEC, covering the region  $124 < |z| < 282$  cm). Figure 34 shows a diagram of the pixel and strip detectors, which have total length 5.8 m and diameter 2.5 m [53]. Track reconstruction and tracking efficiency will be discussed in detail in Sec. 6.

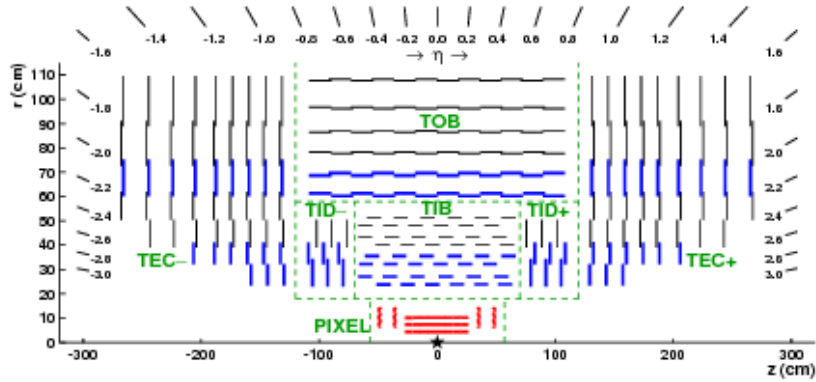


Figure 34. Diagram of CMS pixel and silicon strip detectors in the  $r - z$  plane [53].

#### 917 5.4 Calorimeters in the CMS detector

This analysis relies on electromagnetic and hadronic calorimeters for the energy measurements used as inputs for the reconstruction of high- $p_T$  jets. The ECAL, which measures the energy of charged particles, consists of 75 848 lead tungstate ( $\text{PbWO}_4$ ) crystal scintillators, organized in 5 arrays, covering  $|\eta| < 1.48$  in a barrel region and  $1.48 < |\eta| < 3.0$  in the endcap region. Light from the scintillators is captured with avalanche photodiodes in the barrel region, and vacuum phototriodes in the endcap region. A preshower detector system in front of the ECAL is used to assist in the identification of neutral pions and electrons [51]. ECAL energy resolution ranges from about 1-2.5% (depending  $|\eta|$  and photon conversion) in the barrel region, and from 2.5-4% in the endcap region. [54].

Hadrons pass through the ECAL and are stopped by the HCAL, a hermetic detector which records their energy using a system of scintillator tiles embedded with wavelength-shifting fibers.

929 The HCAL has three regions, as shown in Fig. 35: barrel (HB), endcap (HE), and an outer region  
 930 (HO) outside of the solenoid, necessitated by the fact that the HB is volume-limited by the solenoid  
 931 diameter. In the barrel region  $|\eta| < 1.74$ , the HCAL cells have widths of 0.087 in pseudorapidity  
 932 and 0.087 in  $\phi$ , while for  $|\eta| > 1.74$  the coverage of the towers increases progressively to a maximum  
 933 of 0.174 in  $\Delta\eta$  and  $\Delta\phi$ . HCAL towers are mapped onto ECAL towers within the barrel region, and  
 934 their summed energies are used to determine the location, energy, and axis of jets, as described  
 935 below in Sec. 7. The HCAL is complimented in the forward region by the HF calorimeters, which  
 936 each consist quartz fibers in the  $\pm z$  directions organized in 432 readout towers in the region  $3.0 <$   
 937  $|\eta| < 5.2$  [51]. In this analysis, only jets from the barrel region of the calorimeters will be included,  
 938 while the HF detector is used for the determination of PbPb event centrality as described in Sec. 8.2.



Figure 35. Diagram of the HCAL [51].

## 939 5.5 The CMS trigger system

940 The collision rate at the LHC is so high that it is impossible to store and process every event  
 941 that occurs in the CMS detector. A two-level online trigger system is therefore used to select events  
 942 of interest. Furthermore, data selected with loose trigger requirements (for example “zero bias”  
 943 data with no selection criteria and “minimum bias” criteria consisting of minimal requirements to  
 944 demonstrate the presence of a collision event) may also need to be further “prescaled” to limit  
 945 the rate of recorded events by a specified factor. The trigger system consists of a first (L1) trigger  
 946 consisting of programmable electronics that use information from the calorimeter and muon systems

947 of the detector to select events to record. The L1 trigger operates with an interval of approximately  
948  $4\mu$  s, with a maximum rate of 100 kHz. The next trigger level, the High Level Trigger (HLT), consists  
949 of a processor farm that allows for more sophisticated event selection based on the reconstruction of  
950 physics objects. Reconstruction is performed in a series of steps, or a “HLT path,” chosen to apply  
951 selection in order of increasing reconstruction complexity, so as to minimize processing time [55].  
952 This analysis will rely primarily on two kinds of triggers: minimum bias data, and jet-triggered  
953 data samples selected by requiring the presence of an online reconstructed jet with  $p_T > 80$  GeV  
954 ( $p_T > 100$  GeV for 5.02 TeV PbPb data). No prescale is applied for the jet-triggered data samples  
955 used in this analysis.

## 6 TRACK RECONSTRUCTION AND CORRECTION

### 957 6.1 Track reconstruction in pp collisions

958 Standard track reconstruction in CMS occurs in the following steps, summarized here and described  
 959 in detail in Ref. [53]:

- 960     • **Hit reconstruction** – In the pixel tracker, zero-suppression is performed by setting an ad-  
 961       justable threshold, equivalent charge to 3200 for each pixel. Pixel hits are reconstructed as  
 962       clusters of adjacent pixels, requiring a minimum charge equivalent of 4000 electrons (compared  
 963       to at least 21,000 electrons deposited by a typical ionizing particle). In the strip detector,  
 964       zero-suppression is performed by subtracting the baseline pedestal and noise from the signal,  
 965       and clusters are seeded with channels which contain charge at least three times that of the  
 966       pedestal. Adjacent strips are added to the cluster if their charge is more than twice that of  
 967       the pedestal, and the cluster is kept if its total charge is at least five times larger than the  
 968       combined strip noise. Cluster position in the strip detector is determined from the charge-  
 969       weighted average of strip positions, corrected for Lorentz drift. The average efficiency for hit  
 970       reconstruction in both the pixel and strip detectors (excluding 2.4% of pixel modules and  
 971       2.3% of strip modules known to be defective) is > 99 %.
- 972     • **Track seed generation** – Track reconstruction begins by first running a fast track and  
 973       vertex reconstruction using the pixel tracker only to reconstruct the beamspot position and  
 974       the location of primary vertices in the event. After this, track reconstruction is carried out in  
 975       six iterations, each of which begins with “seeds” that define the trajectories and uncertainties  
 976       of potential tracks. The first set of seeds are pixel triplets, produced from corresponding sets  
 977       of three pixel hits (on a helical track trajectory) with weak constraints on compatibility with  
 978       the beam spot to require that the tracks correspond to promptly produced particles. In later  
 979       iterations, additional information from vertex reconstruction and the silicon strip detector is  
 980       incorporated in seed generation.
- 981     • **Track finding** – The seeds generated in the step above are used as starting points for  
 982       track-finding based on the Kalman filter method, implemented in four steps for each tracker  
 983       layer. First, track parameters at the starting level are extrapolated, assuming a perfectly

984 helical track trajectory (neglecting multiple scatterings, energy loss, and non-uniformity in  
985 the magnetic field), to determine the locations of interception in other pixel layers. The second  
986 step is a search for tracker modules consistent with the interception locations determined in  
987 the previous step. In the third step, hits from mutually exclusive module groups (i.e. groups  
988 of modules for which it is not possible that one track could pass through more than one of  
989 the grouped modules) are used to update and refine hit locations (including the possibility of  
990 adding “ghost” hits where a particle failed to produce a hit due to module inefficiency) and to  
991 calculate the Lorentz drift in the silicon bulk. Finally, in the fourth and last step, new track  
992 candidates are formed by adding one compatible hit from each of the module groupings, and  
993 trajectories are updated combining this added hit with the original track path extrapolation.  
994 All track candidates at a given level are then extrapolated to the next compatible layer and  
995 the procedure repeated through five iterations.

- 996 • **Track fitting** – Finally, the track trajectory is refitted to reduce possible biases (due, for  
997 example, to the beam spot constraint introduced in initial seed finding), and to remove  
998 outlying hits falsely associated to a track.

999 After tracks are reconstructed according to this procedure, the track sample both includes a contri-  
1000 bution from “fake” tracks (that do not correspond to the trajectory of an ionizing particle), which  
1001 is reduced by requiring certain selection criteria as discussed in Sec. 6.3. The collection also suffers  
1002 from detector and reconstruction inefficiencies, which are corrected in this analysis according to  
1003 the procedure described in Sec. 6.4.

## 1004 6.2 Track reconstruction in PbPb collisions

1005 In PbPb collision data, dedicated track reconstruction is necessary due to the dramatically greater  
1006 multiplicity in PbPb compared to pp collisions. This heavy ion tracking occurs in the following  
1007 steps, and is detailed in Refs. [56] and [57]:

- 1008 • **Hit reconstruction** – Tracker hits are reconstructed following the same basic procedure  
1009 applied in pp collisions.
- 1010 • **Track seed generation** – First, primary vertex positions are reconstructed using only a  
1011 collection of pixel hits, extrapolated to the region near the beam spot. In PbPb data pileup

1012       is negligible, so there is generally only one primary vertex reconstructed in each event. Initial  
1013       track seeds are then constructed from pixel triplets only. To reduce combinatorial back-  
1014       grounds, seeds are restricted to those pointing to a region within 2 mm of the primary vertex,  
1015       and further selections are applied on track  $p_T$ , goodness-of-fit ( $\chi^2$ ), and compatibility between  
1016       the seed trajectory and the primary vertex.

1017       • **Track finding** – Track trajectories are propagated through the tracker following a procedure  
1018       similar to that outlined above for pp data. The track seeding and finding procedure is repeated  
1019       through three iterations. In the second and third iterations, hits belonging unambiguously to  
1020       a previously identified tracks are first removed, and then reconstruction is repeated using pixel  
1021       triplet and pixel pair seeds (in the 2nd and 3rd iterations, respectively). Tracks identified in  
1022       these later iterations are merged into first-iteration tracks, with duplicates removed based on  
1023       hit matching.

1024       

### 6.3 High purity tracks

1025       The track reconstruction procedures described above for pp and PbPb collision data give track  
1026       collections with significant “fake rates,” or fraction of reconstructed tracks that cannot be associated  
1027       with a particle. This fake rate is reduced with a series of quality selections, defined in three levels:  
1028       “loose” criteria define the minimum to keep tracks in track collections, “tight” criteria are somewhat  
1029       more stringent (sacrificing some lost efficiency for a lower fake rate), and finally “high purity”  
1030       criteria are most strict and are those applied for most CMS analyses, including those reported  
1031       here. Track quality in each case is set with flags for each track, and criteria in each case are  
1032       applied separately at each iterative tracking step. The precise criteria for high purity tracks at  
1033       each iterative pass are defined in Refs. [53, 56, 57], and include the following types of selections,  
1034       imposed as a function of  $p_T$  and  $\eta$ :

- 1035       • Requirements on the number of hits on the track trajectory ( $N_{\text{hit}}$ )  
1036       • Requirements on the minimum layers in which the track has an associated hit ( $N_{\text{layers}}$ , and  
1037       on the maximum intercepted layers in which the track has no assigned hits  
1038       • A minimum imposed on the goodness-of-fit of the track ( $\chi^2/\text{Ndof}/N_{\text{layers}}$  or  $\chi^2/N_{\text{hit}}$ )

- 1039     • A maximum on relative track- $p_T$  uncertainty  
 1040     • Maxima on longitudinal and transverse impact parameters ( $d_z$  and  $d_{xy}$ ) with respect to the  
 1041       primary vertex position and beam spot

1042 In pp data, criteria are optimized by the quality metric  $Q(\rho) = s/\sqrt{s + \rho b}$ , where  $s$  = selected  
 1043 (“real”) tracks,  $b$  = selected fake tracks, and parameter  $\rho \approx 10$  weights the metric toward min-  
 1044 imizing the fake rate. In PbPb data from Run 2, optimization is performed via the output of a  
 1045 multivariate analysis tool (MVA), as detailed in Ref. [57].

1046 **6.4 Tracking efficiency and fake rate evaluation and correction**

1047 Tracking efficiency for charged particles in pp collisions ranges from approximately 80% at  $p_T \approx 0.5$  GeV  
 1048 to 90% or better at  $p_T \approx 10$  GeV and higher. Track reconstruction is more difficult in the heavy-ion  
 1049 environment due to the high track multiplicity, and tracking efficiency for PbPb collisions ranges  
 1050 from approximately 30% at 0.5 GeV to about 70% at 10 GeV. Tracking efficiencies are evaluated  
 1051 using PYTHIA and PYTHIA+HYDJET Monte Carlo simulation, by comparing track distributions as  
 1052 generated to those after MC samples are passed through GEANT detector simulation and recon-  
 1053 structed with the algorithms used to reconstruct data. Corrections are derived as a function of  
 1054 centrality,  $p_T$ ,  $\eta$ ,  $\phi$ , and local charged particle density. Tracking efficiency closure and systematic  
 1055 uncertainty is evaluated in pythia and pythia+hydjet, comparing generated track  $p_T$ ,  $\eta$ , and  $\phi$  dis-  
 1056 tributions to reconstructed distributions before and after correction. For illustration, examples of  
 1057 these closure checks for 5.02 TeV PYTHIA simulation are shown in Fig. 36. Additional 5% residual  
 1058 systematic uncertainty is conservatively assigned for possible differences between MC and data that  
 1059 might affect tracking performance.

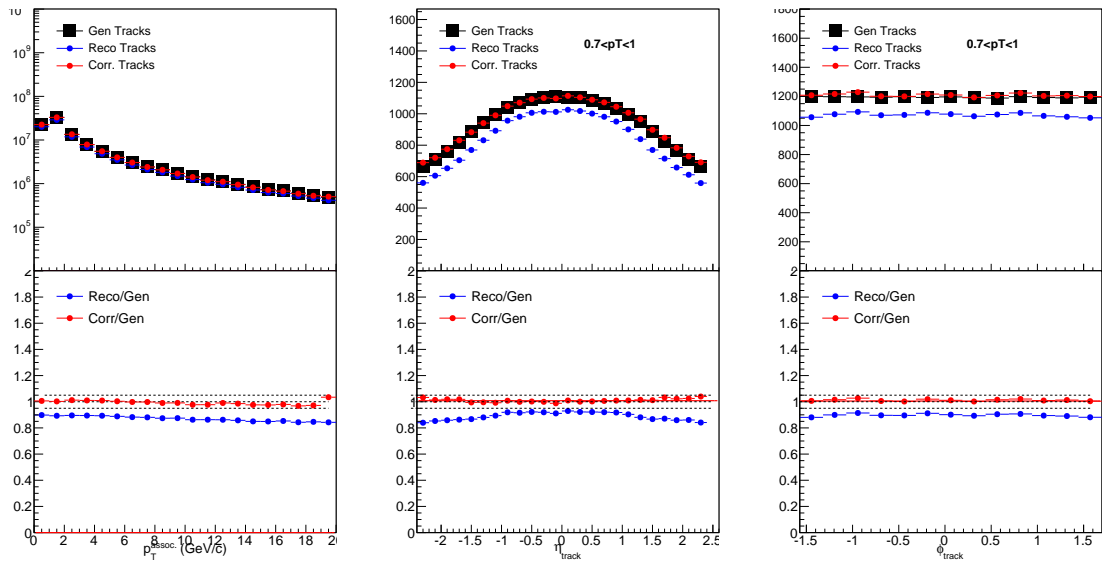


Figure 36. Tracking efficiency correction closure for PYTHIA simulation at 5.02 TeV, comparing tracking generated tracks to uncorrected and corrected reconstructed tracks, as a function of track  $p_T$  and of pseudorapidity, and azimuth for the lowest  $p_T^{\text{trk}}$  bin.

## 7 JET RECONSTRUCTION AND CORRECTION

### 1061 7.1 Jet reconstruction with the anti- $k_t$ algorithm

1062 The goal in jet reconstruction is to identify clusters of hadrons originating from a fragmenting high-  
 1063 energy parton. In high- $p_T$  jet studies in pp collisions, the general locations of jets in an event may  
 1064 be qualitatively obvious via large energy deposits in calorimeters; however, there is no clear single  
 1065 standard of how jet boundaries should be drawn. In practice, jets are defined by the algorithms  
 1066 used to find and determine their direction. These algorithms fall in two primary categories: “cone  
 1067 algorithms,” which define jets within specific conical regions (based on the fact that hadronization  
 1068 has little effect total momentum flow), and “sequential recombination algorithms,” which iteratively  
 1069 identify and cluster pairs of closest particles to form jets that are not necessarily conical. [58, 59, 60].  
 1070 Several properties are desireable, from theoretical and experimental perspectives, in jet finding:

- 1071     • Straightforward implementation for both theoretical calculations and jet-finding and recon-  
 1072         struction in experimental measurements
- 1073     • Cross-sections that are finite in perturbation theory
- 1074     • Infrared and collinear (IRC) safety – the property that a soft collinear emission in a parton  
 1075         splitting should not modify the overall collection of hard (high- $p_T$ ) jets in the event, in  
 1076         particular avoiding the possibility of non-cancelling divergences in perturbation calculations
- 1077     • Soft resilience – clustering jets that are reasonably regular and not overly sensitive to soft  
 1078         particles, a property motivated by the finite resolution of experimental detectors.

1079 Heavy ion jet studies in CMS use the anti- $k_t$  algorithm, a soft-resilient, IRC safe, and straightforward  
 1080 sequential recombination algorithm [59], implemented in the FastJet framework [60]. The anti- $k_t$   
 1081 algorithm clusters entities (calorimeter towers, particles, or partially clustered pseudo-jets)  $i$  and  
 1082  $j$  based on the distance measures  $d_{ij}$  between the two particles and  $d_{iB}$  between the particle and  
 1083 beam, with the measures defined as:

$$d_{ij} = \min(k_{ti}^{-2}, k_{tj}^{-2}) \frac{(\Delta R_{ij})^2}{R^2}, \quad (21)$$

$$d_{iB} = k_{ti}^{-2}, \quad (22)$$

1084 where  $k_{ti}$  refers to the transverse momentum of particle  $i$ ,  $\Delta R_{ij}$  refers to the spatial distance  
 1085 (in rapidity and azimuth) between the two particles, and radius parameter  $R$  is a reconstruction  
 1086 parameter. The name anti- $k_t$  derives from the negative exponent for  $k_t$  (in contrast to other  
 1087 sequential recombination algorithms), which enables IRC safety and soft resilience by making jet  
 1088 shape sensitivity to a particle inversely correlated to the particle's transverse momentum. With  
 1089 this low sensitivity to soft particles, the anti- $k_t$  algorithm results in a collection of mostly circular  
 1090 jets (except in the case of jets separated by less than  $2R$ , in which each jet has a radius of  $\pi R^2$ ).  
 1091 The choice of parameter  $R$  is a trade-off between capturing more fragmentation products (as can  
 1092 extend as far as  $\Delta R_{ij} = 0.8$  in pp collisions), and limiting the influence of background particles  
 1093 in jet reconstruction. In heavy ion experimental studies, where background levels are very high,  
 1094 typical choices of  $R$  range from 0.2 to 0.5.

1095 With the CMS detector, jets may be clustered from ECAL and HCAL information only  
 1096 (“calorimeter jets”) or from information from the full detector, using the particle flow (PF) algo-  
 1097 rithm. The PF algorithm improves jet energy resolution (JER) substantially at low- $p_T$  (at 10 GeV  
 1098 JER is 15% for PF jets versus 40% for calorimeter jets) with improvements decreasing for higher- $p_T$   
 1099 jets (at 100 GeV PF jet JER is 8% versus 12% for calorimeter jets, falling to a difference of 4%  
 1100 versus 5% at 1 TeV). For jet-track correlation studies, however, the resolution improvements that  
 1101 the particle flow algorithm offers come at the cost of enhancing sensitivity to tracking biases in the  
 1102 jet-track correlation signal, since low- $p_T$  tracks are included in jet reconstruction. In this analysis,  
 1103 calorimeter jets are used to avoid these auto-correlation effects, and because we will consider jets  
 1104 with  $p_T > 120$  GeV for which calorimeter jet energy resolution is adequate. Jets are reconstructed  
 1105 with anti- $k_t$  radius  $R = 0.3$  for 2.76 TeV data (“ak3Calo” jets), and with radius  $R = 0.4$  for 5.02  
 1106 TeV data (“ak4Calo” jets). In pp data at 2.76 TeV and 5.02 TeV the contribution to the jet energy  
 1107 from the underlying event (UE) is negligible (less than 1 GeV), so no underlying event subtraction  
 1108 is employed.

1109 **7.2 Underlying event subtraction in PbPb data**

1110 In PbPb collisions it is necessary to subtract contributions from the large underlying event in order  
1111 to recover the true jet energy. There are a variety of methods used for underlying event subtraction,  
1112 of which the following two are relevant for this analysis.

1113 **7.2.1 Noise/pedestal subtraction**

1114 In most CMS high- $p_T$  jet analyses, including 5.02 TeV PbPb data studies here, underlying event  
1115 subtraction is performed using a variant of an iterative noise/pedestal subtraction technique [61].  
1116 This algorithm occurs in the following steps:

- 1117 • First, the mean “pedestal” energy in calorimeter cells as a function of energy  $\eta$  ( $P(\eta)$ ) is  
1118 calculated along with its dispersion.
- 1119 • The pedestal function  $P(\eta)$  is subtracted from all cells.
- 1120 • Cells with non-physical negative energy entries are then set to zero.
- 1121 •  $\langle E_{\text{cell}} \rangle + \langle \sigma(E_{\text{cell}}) \rangle$  is subtracted from each cell to compensate for the elimination of negative  
1122 energy cells.
- 1123 • Jets are clustered from the pedestal-subtracted cells using the anti- $k_t$  algorithm.
- 1124 • The pedestal function  $P(\eta)$  is then re-derived using only cells that are not a part of clustered  
1125 jets, and the algorithm is repeated.

1126 After this underlying event subtraction is applied, the anti- $k_t$  algorithm with radius parameter  
1127  $R = 0.4$  is then employed for jet reconstruction (“akPu4Calo jets”).

1128 **7.2.2 HF/Voronoi subtraction**

1129 For 2.76 TeV PbPb data a different algorithm, designed to eliminate the threshold and possible  
1130 resulting bias from the noise/pedestal technique, is employed [56]. This algorithm uses information  
1131 from the HF detector to model and subtract the underlying event using Voronoi decomposition  
1132 (“HF/Voronoi” algorithm) in the following steps:

- 1133     • The distribution of underlying  $E_T$  as a function of  $\eta$  and  $\phi$  is modeled using singular value  
 1134       decomposition (SVD) training ( $dE_T/d\eta/\phi$  with Voronoi parameters  $v_1 \dots v_4$ ) to extrapolate the  
 1135       UE distribution from the HF calorimeter at large  $\eta$  to the central analysis region ( $|\eta| < 1.6$ ).  
 1136     • The modeled UE distribution is subtracted from all calorimeter cells.  
 1137     • Each calorimeter cell is associated with its nearest neighbors, and energy is redistributed  
 1138       between neighboring in an “equalization” procedure used to eliminate non-physical negative  
 1139        $E_T$  entries (optimized to minimize energy transfers).
- 1140   After Voronoi subtraction and equalization, the anti- $k_t$  algorithm is employed with radius parameter  
 1141    $R = 0.3$  to cluster (“akVs3Calo”) jets.

1142   **7.3 Jet energy corrections**

1143   Jet reconstruction as described above gives spatial coordinates and  $p_T$  for each jet as measured by  
 1144   the detector. Our goal in jet studies, however, is to reconstruct the true total parton or particle  
 1145   energy. This is achieved through jet energy corrections (JEC) that establish a mapping between  
 1146   measured energy (which does not, for example, include neutrinos produced in jet fragmentation)  
 1147   and “true” jet energies. This mapping is complicated by nonlinearity in detector response. Ini-  
 1148   tial corrections are derived as a function of  $p_T$  and  $\eta$  using dijet QCD samples of PYTHIA and  
 1149   PYTHIA+HYDDET Monte Carlo, spatially matching reconstructed jets to generated particles, and  
 1150   comparing generated versus reconstructed jet energy for these matched jets. These “MC truth”  
 1151   corrections are applied to measured jet energies to return a collection of jets that, on average,  
 1152   capture the kinematic distribution of the partons before fragmentation.

1153   These corrections do not, however, fully account for the non-linearity of calorimeter re-  
 1154   sponse. In particular, in an effect particularly relevant for jet-track correlation studies, the jet  
 1155   energy scale depends on jet fragmentation. Given two jets with identical parton energy, the jet  
 1156   with softer fragmentation (i.e. jets with a higher fraction low- $p_T$  particles) will be on average re-  
 1157   constructed with lower energy than the jet with harder fragmentation. When combined with a jet  
 1158   selection threshold, this non-linearity results in a bias that systematically underestimates the jets  
 1159   with soft fragmentation in the analysis sample. An additional fragmentation-function dependent  
 1160   jet energy correction (JFF-JEC) is therefore applied after initial jet energy corrections in order to

1161 reduce this bias (detailed in Ref. [56]). These JFF-JEC are derived using the number of particle flow  
 1162 candidates ( $N_{\text{PF}}$ ) in the jet with  $p_T > 2$  GeV, with this threshold chosen to reduce the influence  
 1163 of soft fluctuations in the underlying event. Correction tables are derived as a function of  $N_{\text{PF}}$ , jet  
 1164  $p_T$ , and PbPb event centrality in PYTHIA and PYTHIA+HYDJET simulation, and are applied to jets  
 1165 after the JECs described above. Finally, iterative residual corrections are applied as a function of  
 1166 jet  $p_T$ . The application of JFF-JECs reduces the overall quark/gluon non-closure, as illustrated for  
 1167 PbPb data in Fig. 37, and slightly improves jet energy resolution overall.

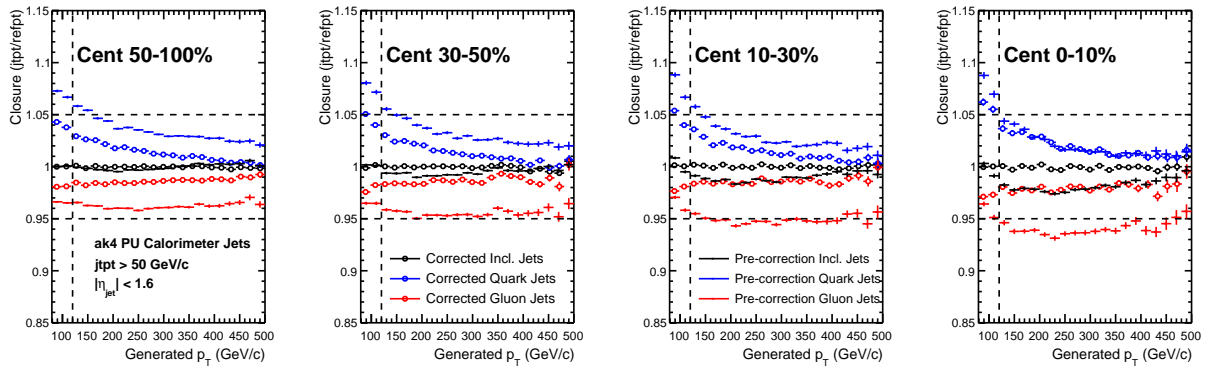


Figure 37. Closure with and without JFF-JEC for quark and gluon jets.

## 8 DATA AND MONTE CARLO SAMPLES

### 1169 8.1 Data samples and event selection

1170 This analysis is based on PbPb and pp data collected with the CMS detector at 2.76 TeV and 5.02  
 1171 TeV during Run 1 and Run 2 of the CERN LHC. Studies at 2.76 TeV use  $166 \mu\text{b}^{-1}$  of PbPb data  
 1172 collected in 2011, and  $5.3 \text{ pb}^{-1}$  of pp data collected in 2013. Studies at 5.02 TeV use  $404 \mu\text{b}^{-1}$  of  
 1173 PbPb data and  $25 \text{ pb}^{-1}$  of pp data, both collected in 2015. Online collision selection was performed  
 1174 using the CMS HLT described in Sec. 5.5 to obtain a minimum bias sample of PbPb collision events,  
 1175 and to obtain samples of PbPb and pp data with the requirement that events contain at least one  
 1176 high- $p_{\text{T}}$  jet (with  $p_{\text{T}} > 80 \text{ GeV}$  for pp data and 2.76 TeV PbPb data,  $p_{\text{T}} > 100 \text{ GeV}$  for 5.02 TeV  
 1177 PbPb data). These jet triggers are fully efficient for offline-reconstructed jets with  $p_{\text{T}} > 120 \text{ GeV}$ .  
 1178 Total numbers of selected events are summarized in Table I.

TABLE I. Summary of data samples and number of selected events

Dataset	Number of selected events
2.76 TeV PbPb MinimumBias	1.01 M
2.76 TeV PbPb Jet-triggered ( $p_{\text{T}} > 80 \text{ GeV}$ )	1.25 M
2.76 TeV pp Jet-triggered ( $p_{\text{T}} > 80 \text{ GeV}$ )	1.27 M
5.02 TeV PbPb MinimumBias	764 k
5.02 TeV PbPb Jet-triggered ( $p_{\text{T}} > 100 \text{ GeV}$ )	3.35 M
5.02 TeV pp Jet-triggered ( $p_{\text{T}} > 80 \text{ GeV}$ )	2.66 M

1179 A number of quality cuts are applied, as is standard for CMS analyses to remove detector  
 1180 noise backgrounds, ultra-peripheral collisions, beam gas events, and events with exceptionally large  
 1181 pixel occupancy. These selection criteria have shown to have negligible impact on dijet analyses [62,  
 1182 63], and are as follows in PbPb and pp collisions:

- 1183 • Vertex- $z$  position within 15 cm of the center of the detector ( $|v_z| < 15$ )
- 1184 • Primary vertex filter – a requirement that events include a reconstructed primary vertex filter  
 1185 with at least two tracks, requiring the presence of inelastic hadronic scattering and removing  
 1186 beam-gas events and ultra-peripheral collisions

- Beam-scraping filter – a requirement of pixel clusters compatible with the primary vertex.  
 In pp, this requires that if there are more than 10 tracks, at least 25% of tracks must be highPurity (see Sec. 6)
  - HB/HE noise filter – a filter to exclude events exhibiting uncharacteristic calorimeter noise [64]
  - PbPb data only: HF coincidence filter – at least 3 GeV recorded in at least each of at least three hadronic forward calorimeter towers on each side of the interaction point
- These cleaning cuts are applied to both minimum bias and jet-triggered data samples. Additional event selection will later be applied to obtain samples of high- $p_T$  jets and dijet events, as discussed in Sec. 8.4 below.

## 8.2 Collision centrality determination and classes

The variable centrality is used to parameterize the degree of overlap of the colliding nuclei. In CMS, centrality is determined using total transverse energy ( $E_T$ ) in the HF calorimeter towers, in the region  $4.0 < |\eta| < 5.2$ . The distribution of total  $E_T$  in all events is used to divide the total minimum bias event sample into centrality bins, each containing 0.5% of the total events. The resulting centrality distribution is flat in minimum bias data by construction. In jet-triggered data, however, requiring the presence of a high- $p_T$  jet results in a larger fraction of more central collisions (in which hard-scatterings are more likely). The collisions defined as “most central” (centrality = 0%) are those with the greatest  $E_T$ , corresponding to collisions in which the nuclei collided head-on. In contrast, the collisions defined as “least central” or “most peripheral” (centrality = 100%) are those in which the nuclei barely overlapped at all. To observe how jet modifications evolve with changing centrality, this analysis considers four centrality classes: 0-10% (most central), 10-30%, 30-50%, and 50-100%.

## 8.3 Monte Carlo simulation

Monte Carlo (MC) simulation is used in this analysis to evaluate and correct for jet reconstruction performance and tracking efficiency for both pp and PbPb data. Simulation of pp data and of the hard processes in PbPb data are performed using the PYTHIA (version 6, tune Z2 [65]) event generator. In order to have reasonable event samples in all jet  $p_T$  ranges, different samples are

1214 produced with various cut-off values of  $\hat{p}_T$ , which are then combined using their respective cross-  
1215 sections as weights. To simulate CMS detector output for MC events, GEANT4 detector simulation  
1216 is used [66]. Jet and track reconstruction performance and efficiency for pp data is evaluated by  
1217 comparing observables in PYTHIA samples as generated to the same observables after they have  
1218 been passed through the detector simulation and the same reconstruction procedures applied to  
1219 pp data. For the relevant jet kinematics observables relevant to this analysis, PYTHIA reasonably  
1220 reproduces pp data.

1221 For PbPb data, the underlying event is simulated using HYDJET (Drum5 tune) [67], which  
1222 combines hydrodynamics with “mini-jets” produced with quenched PYTHIA input. Hard processes  
1223 are generated using PYTHIA, and are directly embedded in this HYDJET sample (referred to as  
1224 PYTHIA+HYDJET simulation), with no medium quenching effects applied to the embedded jets.  
1225 This PYTHIA+HYDJET sample is used to evaluate the reconstruction effects of the presence of the  
1226 heavy ion collision environment, *other* than the jet-medium interactions that are our objects of  
1227 study. As for PYTHIA simulation of pp data, comparing PYTHIA+HYDJET samples that have been  
1228 passed through the detector and reconstructed chain to the generated Monte Carlo allows for the  
1229 evaluation of jet and track reconstruction performance.

### 1230 8.3.1 Monte Carlo centrality and vertex-z reweighting

1231 Simulated PYTHIA+HYDJET samples are generated minimum bias, and therefore must be reweighted  
1232 to match the bias toward more central events induced by requiring the presence of a high- $p_T$   
1233 jets discussed in Sec. 8.2. Reweighting factors are calculated for each 0.5%-wide centrality bin,  
1234 and applied to the PYTHIA+HYDJET sample overall to match the PbPb centrality distribution.  
1235 Similarly, another reweighting procedure is performed to match the distributions of the position of  
1236 the primary interaction along the beam direction in MC and data for both pp and PbPb collisions.  
1237 Figures 38-40 illustrate the necessity and effects of these reweighting procedures.

### 1238 8.3.2 Monte Carlo samples at 2.76 TeV

1239 Tables II and III summarize the PYTHIA and PYTHIA+HYDJET samples used in this analysis by  $\hat{p}_T$ ,  
1240 with respective numbers of generated events and cross-sections used for combining samples.

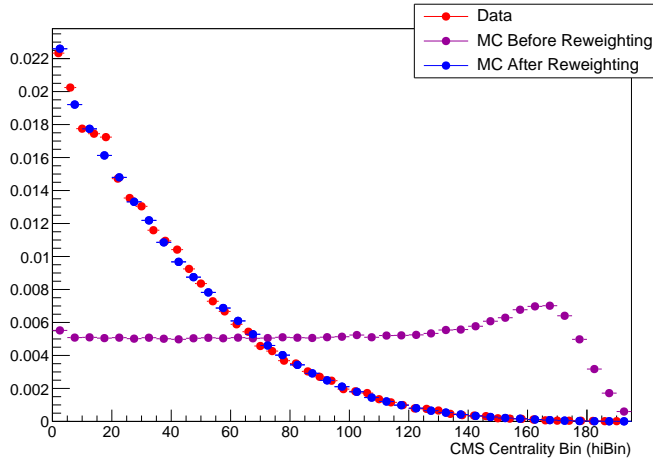


Figure 38. Centrality distribution for PYTHIA+HYDGET reweighted to the distribution of PbPb data.

TABLE II. Summary of Monte Carlo samples and generated events at 2.76 TeV

Generator	Process	Cross section (mb)	Number of events
PYTHIA+HYDGET	$\hat{p}_T > 50$ GeV	$1.025 \times 10^{-3}$	395k
PYTHIA+HYDGET	$\hat{p}_T > 80$ GeV	$9.865 \times 10^{-5}$	368k
PYTHIA+HYDGET	$\hat{p}_T > 120$ GeV	$1.129 \times 10^{-5}$	367k
PYTHIA+HYDGET	$\hat{p}_T > 170$ GeV	$1.465 \times 10^{-6}$	392k
PYTHIA+HYDGET	$\hat{p}_T > 220$ GeV	$2.837 \times 10^{-7}$	181k
PYTHIA+HYDGET	$\hat{p}_T > 280$ GeV	$2.837 \times 10^{-7}$	50k
PYTHIA	$\hat{p}_T > 80$ GeV	$9.865 \times 10^{-5}$	104k
PYTHIA	$\hat{p}_T > 120$ GeV	$1.129 \times 10^{-5}$	975k
PYTHIA	$\hat{p}_T > 170$ GeV	$1.465 \times 10^{-6}$	69k

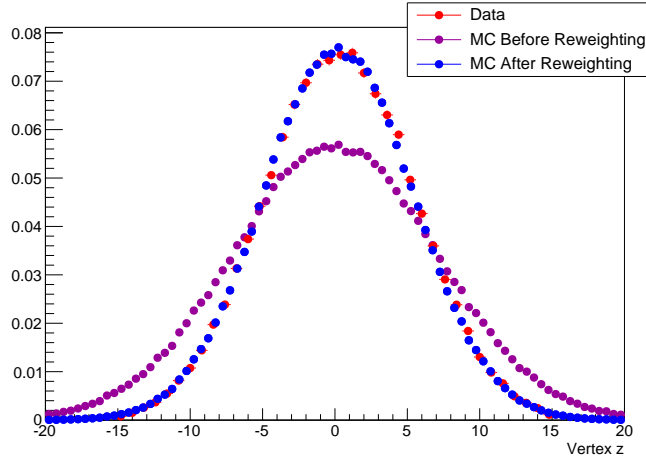


Figure 39. Vertex z distribution for PYTHIA+HYDGET reweighted to the distribution of PbPb data.

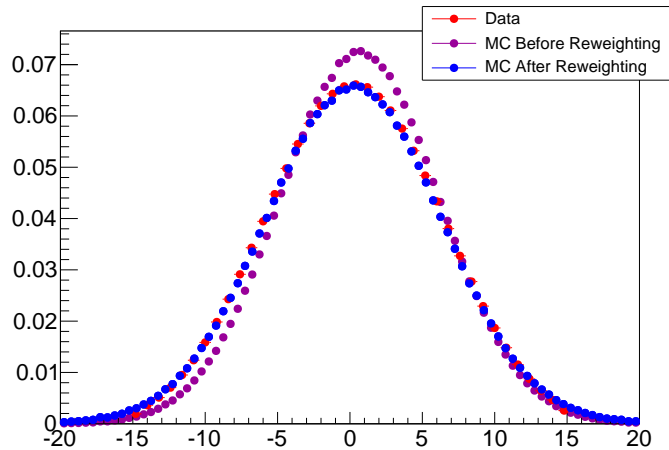


Figure 40. Vertex z distribution for PYTHIA reweighted to the distribution of pp data.

<sup>1241</sup> **8.3.3 Summary of Monte Carlo samples at 5.02 TeV**

TABLE III. Summary of Monte Carlo samples and generated events at 5.02 TeV

Generator	Process	Cross section (mb)	Number of events
PYTHIA+HYDJET	$\hat{p}_T > 80 \text{ GeV}/c$	$4.412 \times 10^{-4}$	499k
PYTHIA+HYDJET	$\hat{p}_T > 120 \text{ GeV}/c$	$6.147 \times 10^{-5}$	496k
PYTHIA+HYDJET	$\hat{p}_T > 170 \text{ GeV}/c$	$1.018 \times 10^{-5}$	498k
PYTHIA+HYDJET	$\hat{p}_T > 220 \text{ GeV}/c$	$2.477 \times 10^{-6}$	200k
PYTHIA+HYDJET	$\hat{p}_T > 280 \text{ GeV}/c$	$6.160 \times 10^{-7}$	200k
<hr/>			
PYTHIA	$\hat{p}_T > 80 \text{ GeV}/c$	$4.412 \times 10^{-4}$	500k
PYTHIA	$\hat{p}_T > 120 \text{ GeV}/c$	$6.147 \times 10^{-5}$	500k
PYTHIA	$\hat{p}_T > 170 \text{ GeV}/c$	$1.018 \times 10^{-5}$	499k
PYTHIA	$\hat{p}_T > 220 \text{ GeV}/c$	$2.477 \times 10^{-6}$	200k
PYTHIA	$\hat{p}_T > 280 \text{ GeV}/c$	$6.160 \times 10^{-7}$	200k

1242 **8.4 Jet selection and dijet asymmetry classes**

1243 Jet selection in this analysis is restricted to the pseudorapidity region  $|\eta_{\text{jet}}| < 1.6$  to ensure stable  
1244 reconstruction performance in the calorimeter barrel region. A requirement is also imposed that  
1245 the highest- $p_T$  track contains no less than 1% and no more than 98% of the total jet  $p_T$ . In the  
1246 jet selection referred to as “inclusive jets” for analysis at both 2.76 TeV and 5.02 TeV, all jets with  
1247  $p_{T,\text{jet}} > 120$  GeV are considered. In this selection, it is possible to select more than one jet from  
1248 the same event, provided that each jet satisfies the inclusive selection criteria.

1249 In addition to the inclusive jet selection, a “dijet” selection of events containing two back-  
1250 to-back high- $p_T$  jets is also analyzed for the 2.76 TeV data sample. Events are included in this  
1251 sample based on the criteria that they contain highest- $p_T$  “leading” jet with  $p_{T,1} > 120$  GeV and a  
1252 second-highest- $p_T$  “subleading” jet with  $p_{T,2} > 50$  GeV with relative azimuthal separation between  
1253 the two jets  $\Delta\phi_{1,2} > \frac{5\pi}{6}$ . This dijet sample is subdivided into a sample of relatively “balanced”  
1254 dijets, with similar  $p_{T,1}$  and  $p_{T,2}$  and a sample of relatively “unbalanced” dijets in which the leading  
1255 jet has a much larger  $p_T$  than the subleading jet based on asymmetry parameter  $A_J$ . The balanced  
1256 selection is defined as those events for which  $A_J < 0.22$ , while the unbalanced selection is defined  
1257 as those events for which  $A_J > 0.22$ . The dividing value  $A_J = 0.22$  is chosen for consistency with  
1258 previous CMS analyses [35, 36]. In this analysis, 52% of central PbPb events are balanced, while  
1259 67% of pp events are balanced. Jet kinematics for all jet samples (broken down by asymmetry for  
1260 2.76 TeV dijet data) are shown in Appendix A.1 for 2.76 TeV data and in Appendix A.2 for 5.02  
1261 TeV data.

1262 **8.5 Track selection and classes**

1263 Tracks, reconstructed as described in Sec. 6 are required to satisfy the following criteria:

- 1264 •  $|\eta_{\text{trk}}| < 2.4$  – restricts to the barrel region of the tracker  
1265 •  $0.5 < p_{T}^{\text{trk}} < 300$  GeV – excludes very low- $p_T$  tracks where reconstruction performance is not  
1266 stable  
1267 • High Purity criteria – see Sec. 6.3

- 1268     • Distance of closest approach (DCA) in x-y plane and in z less than 3 times the DCA error –  
 1269       reduces fraction of tracks not associated with a primary vertex
- 1270     • Relative  $p_T^{\text{trk}}$  error less than 30% (10% for 5.02 TeV PbPb data) – removes tracks with very  
 1271       poor resolution (has a negligible effect on efficiency as CMS resolution is generally good)
- 1272   For 5.02 TeV PbPb data, the following additional criteria are also applied to reduce the contribution  
 1273   from misidentified tracks [57]:
- 1274     • Exclude tracks with fewer than 11 tracker hits
- 1275     • Require that for each track the chi-squared over number of degrees of freedom ( $\chi^2/\text{Ndof}$ ) of  
 1276       the track fit, also divided by the number of tracker layers (nLayer) hit as the track passed  
 1277       through the detector, is less than 0.15, i.e.  $\chi^2/\text{Ndof}/\text{nLayer} < 0.15$ .
- 1278     • For tracks with  $p_T > 20$  GeV (the kinematic region in which misreconstruction is difficult to  
 1279       access with Monte Carlo), calorimeter matching is applied: since high- $p_T$  tracks eventually  
 1280       deposit their energy in a calorimeter after passing through the tracker, tracks are required  
 1281       to be associated with calorimeter transverse energy  $E_T = (E_{\text{ECAL}} + E_{\text{HCAL}})/\cosh(\eta_{\text{trk}})$ , such  
 1282       that  $E_T > 0.5p_T^{\text{trk}}$
- 1283   After these selection criteria are applied, tracking efficiency corrections are applied as described  
 1284   in Sec. 6.4. Tracks in this analysis are considered in the following classes: 0.5–1 GeV, 1–2 GeV,  
 1285   2–3 GeV, 3–4 GeV, 4–8 GeV, 8–12 GeV, 12–16 GeV, 16–20 GeV, and above 20 GeV. Not all bins  
 1286   are considered in every analysis, and for 5.02 TeV studies the lowest- $p_T^{\text{trk}}$  bin is 0.7–1 GeV.

<sup>1287</sup> **8.6 Summary of analysis bins**

<sup>1288</sup> Table IV summarizes the key kinematic selections and bins for the three components to this analysis.

<sup>1289</sup> In all cases, identical selection is applied to PbPb and pp data. Event, jet, and track quality cuts

<sup>1290</sup> are not included in this table.

TABLE IV. Summary of data selections and analysis bins

Variable	2.76 TeV Inclusive	5.02 TeV Inclusive	2.76 TeV Dijets
PbPb Centrality	0-10%, 10-30%, 30-50%, 50-100%	0-10%, 10-30%, 30-50%, 50-100%	0-10%, 10-30%, 30-50%, 50-100%
Jet Selection	$ \eta_{\text{jet}}  < 1.6$ $p_T > 120 \text{ GeV}$	$ \eta_{\text{jet}}  < 1.6$ $p_T > 120 \text{ GeV}$	$ \eta_{\text{jet}}  < 1.6$ $p_{T,1} > 120 \text{ GeV}$ $p_{T,2} > 50 \text{ GeV}$ $\Delta\phi_{1,2} > \frac{5\pi}{6}$
$A_J$ Bins	–	–	$A_J < 0.22$ , $A_J > 0.22$
Track $\eta$	$ \eta_{\text{trk}}  < 2.4$	$ \eta_{\text{trk}}  < 2.4$	$ \eta_{\text{trk}}  < 2.4$
$p_T^{\text{trk}}$ Bins	1-2 GeV, 2-3 GeV, 3-4 GeV, 4-8 GeV	0.7-1 GeV, 1-2 GeV, 2-3 GeV, 3-4 GeV, 4-8 GeV	0.5-1 GeV, 1-2 GeV, 2-3 GeV, 3-4 GeV, 4-8 GeV, 8-300 GeV

1291

## 9 JET-TRACK CORRELATION MEASUREMENTS

1292 

### 9.1 Analysis procedure

1293 Measurements in this analysis are carried out by considering correlations between high- $p_T$  jets and  
 1294 tracks in PbPb and pp collisions. Jets are selected within  $\eta < 1.6$  and  $p_T$  above a particular  
 1295 threshold. For each jet, the relative separation in pseudorapidity ( $\Delta\eta = \eta_{\text{track}} - \eta_{\text{jet}}$ ) and azimuth  
 1296 ( $\Delta\phi = \phi_{\text{track}} - \phi_{\text{jet}}$ ) is measured between the jet and all charged-hadron tracks within  $\eta < 2.4$ . For  
 1297 each jet-track pair, these measurements are recorded in a two-dimensional  $\Delta\eta - \Delta\phi$  correlation in  
 1298 a particular track transverse momentum ( $p_T^{\text{trk}}$ ) and centrality class. Each correlation is normalized  
 1299 by dividing by the number of jets in the sample ( $N_{\text{jets}}$ ), resulting in a signal pair distribution,  
 1300  $S(\Delta\eta, \Delta\phi)$ , that gives the per-jet yield of tracks and their relative distance from the jet:

$$S(\Delta\eta, \Delta\phi) = \frac{1}{N_{\text{jets}}} \frac{d^2N^{\text{same}}}{d\Delta\eta d\Delta\phi}. \quad (23)$$

1301 This procedure results in a two dimensional measurement of the distribution of charged  
 1302 tracks with respect to the jet axis. The same procedure may also be repeated, weighting each track  
 1303 by its  $p_T^{\text{trk}}$ , in order to obtain a distribution of transverse momentum with respect to the jet axis.  
 1304 These particle density and  $p_T^{\text{trk}}$  correlations form the basis for all results discussed in this analysis.  
 1305 From this point, several additional corrections and other steps are necessary to isolate jet-related  
 1306 effects from long range and uncorrelated backgrounds. These additional steps are as follows:

- 1307     • A correction for jet-track pair acceptance effects;
- 1308     • Separation of correlations into short-range jet peaks and and long range components;
- 1309     • Monte Carlo-based corrections for biases related to jet reconstruction.

1310 After these steps, a range of different observables may be extracted to characterize the multiplicity  
 1311 and distribution of tracks and  $p_T^{\text{trk}}$  at both small and large angles from the jet axis.

1312 **9.2 Jet-track correlation pair-acceptance correction**

1313 This analysis considers  $\Delta\eta$  jet-track separations as large as  $\Delta\eta = 2.5$ . With finite  $\eta$  acceptance for  
1314 both jets and tracks ( $|\eta_{\text{jet}}| < 1.6$  and  $|\eta_{\text{track}}| < 2.4$ , tracks that fall within  $\Delta\eta = 2.5$  of a jet may be  
1315 outside the tracking acceptance. This pair acceptance effect results in trapezoidal correlations that  
1316 fall with rising  $|\Delta\eta|$  as tracks are “lost” outside of the acceptance. This effect is purely geometric,  
1317 and may be corrected by reproducing this pair acceptance geometry. This is done by creating a  
1318 “mixed event” correlation in which jets in the sample are correlated to tracks within  $|\eta| < 2.4$  from  
1319 randomly selected events in a minimum bias PbPb sample, matched in vertex- $z$  position (within 0.5  
1320 cm) and centrality (within 2.5%). This reproduces the pair acceptance geometry from the signal  
1321 correlations:

$$ME(\Delta\eta, \Delta\phi) = \frac{1}{N_{\text{jets}}} \frac{d^2N^{\text{mix}}}{d\Delta\eta d\Delta\phi}, \quad (24)$$

1322 is constructed to account for pair-acceptance effects, with  $N^{\text{mix}}$  denoting the number of mixed-event  
1323 jet-track pairs. The mixed event correction is normalized to unity at  $\Delta\eta=0$ , where the jet and track  
1324 are colinear in  $\eta$  and therefore have perfect pair acceptance, with the normalization factor  $ME(0, 0)$ .  
1325 Dividing the signal correlation  $S(\Delta\eta, \Delta\phi)$ , defined in Equation 23, by this normalized mixed event  
1326 correlation  $ME(\Delta\eta, \Delta\phi)/ME(0, 0)$  yields the corrected per-jet correlated yield distribution, as  
1327 illustrated in Figure 41:

$$\frac{1}{N_{\text{jets}}} \frac{d^2N}{d\Delta\eta d\Delta\phi} = \frac{ME(0, 0)}{ME(\Delta\eta, \Delta\phi)} \times S(\Delta\eta, \Delta\phi). \quad (25)$$

1328 **9.3 Separation of correlations into long range and short-range components**

1329 After correlations are corrected for pair-acceptance effects, in each correlation we are left with a  
1330 well-defined jet peak sitting at  $\Delta\eta = 0$ ,  $\Delta\phi = 0$  on top of a large combinatoric and long range  
1331 correlated background. For most measurements, it is necessary to isolate this jet peak in order to  
1332 distinguish jet-related effects from eventwise correlations. In order to achieve this, we note that the  
1333 long range correlation is independent of  $\Delta\eta$  at distances larger than  $\Delta\eta = 1.5$  from the jet. This  
1334 “sideband” region ( $1.5 < |\Delta\eta| < 3.0$ ) is used to model the underlying event, capturing both the

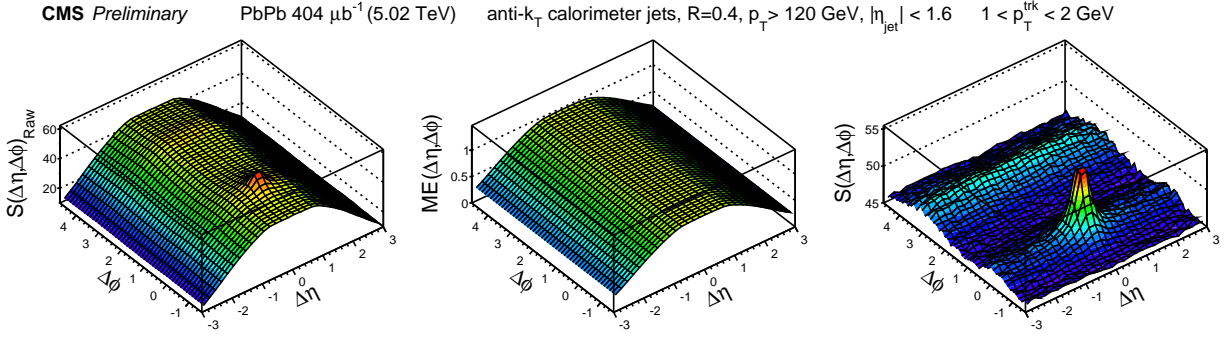


Figure 41. Illustration of the pair-acceptance correction procedure: left panel shows signal correlation  $S(\Delta\eta, \Delta\phi)$ , and center panel shows mixed event correlation  $ME(\Delta\eta, \Delta\phi)$ . Dividing the signal correlation by the normalized mixed event correlation yields the corrected per-jet correlated yield distribution shown in the right panel.

level of the combinatoric background in the event, and also the long range “flow” correlations in the event. The assumption of rapidity-independence of the flow harmonics is based on the CMS study [68], which shows no appreciable variation of the elliptic flow for charged particles above 1 GeV in the pseudorapidity interval of  $\Delta\eta < 3.0$  relevant for this study. As long range correlations depend only on  $\Delta\phi$ , the sideband region is projected into  $\Delta\phi$  to obtain a one-dimensional model of the underlying event. To subtract this long range correlation in 2D, this distribution may be either directly re-propagated into  $\Delta\phi$  (as shown in Figure 42), or may be fit in  $\Delta\phi$  before repropagation in a smoothing procedure as shown in Fig. 43. When aiming to simply remove the long range correlated background, we fit long range correlations function modeling harmonic flow plus a term to capture the (Gaussian or sharper) “away-side” peak opposite the jet in relative azimuth:

$$B(\Delta\phi) = B_0(1+2V_1 \cos(\Delta\phi)+2V_2 \cos(2\Delta\phi)+2V_3 \cos(3\Delta\phi))+A_{AS} \exp\left(-\left(\frac{|\Delta\phi-\pi|}{\alpha}\right)^\beta\right), \quad (26)$$

In this case, the fit is performed only as a smoothing procedure to model the background under the near-side jet peak.; as only the jet peak within  $|\Delta\phi| < \frac{\pi}{2}$  is studied, the fit to the away-side peak is not relevant to the analysis. Furthermore, no physics conclusions can be extracted from the  $V_n$  terms in this fit, which are used only to establish a reasonable functional form for smooth modeling of the background distributions.

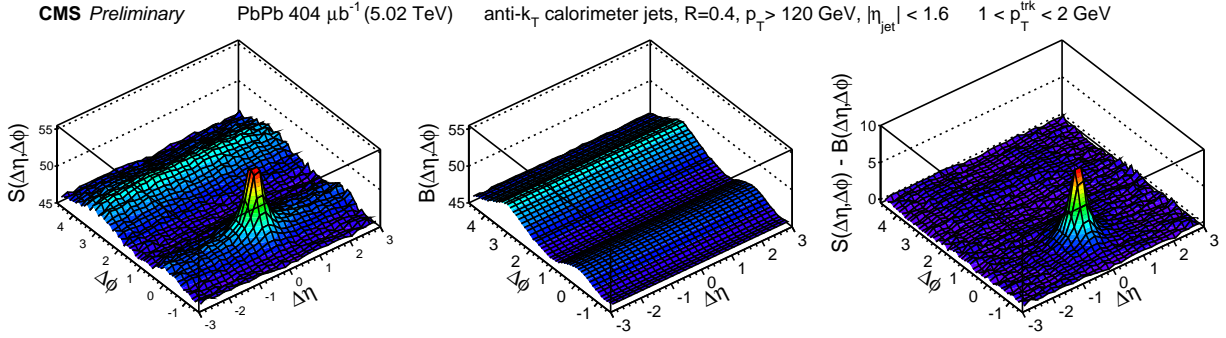


Figure 42. Illustration of the event decomposition procedure without  $\Delta\phi$  fitting: left panel shows the acceptance-corrected correlation, middle panel shows the projected and re-propagated long range distribution, and right panel shows the background-subtracted jet peak.

The long range correlations in the underlying event are in themselves interesting objects of study, however, as they contain information about the collective behavior of particles in the event as a whole, and the extent to which the distribution of high- $p_T$  jets in the event couple to this collective flow. To further study the long range correlations, we may apply the well-established harmonic flow decomposition method used to study two-particle correlations [69] to correlations between jets and tracks. In dijet studies, more accurate information about long range flow correlations can furthermore be obtained by making use of the fact that for our dijet selection and a given value of  $\Delta\eta$  the region  $-\frac{\pi}{2} < \Delta\phi < \frac{\pi}{2}$  of the leading correlation is by definition equivalent to the region  $\frac{\pi}{2} < \Delta\phi < 3\frac{\pi}{2}$  of the subleading correlation. This provides a full  $2\pi$  distribution of the long range correlated underlying event under both the leading and subleading jet peaks. We can then perform a single fit to the combined background. Here we fit with harmonic flow terms only:

$$B(\Delta\phi)^{\text{Dijet}} = B_0(1 + 2V_1 \cos(\Delta\phi) + 2V_2 \cos(2\Delta\phi) + 2V_3 \cos(3\Delta\phi)), \quad (27)$$

In this fit, we find that terms through  $V_3$  are necessary to describe the low- $p_T$ , central background, while at higher- $p_T$  only  $V_1$ ,  $V_2$ . From this combined fit, we extract parameters  $V_1$ ,  $V_2$ , and  $V_3$ . Then, to better constrain the background under the signal and minimize the effects of random background fluctuations, we apply the factorization relation of overall Fourier harmonic  $V_2 = v_2^{\text{jet}} \times v_2^{\text{trk}}$  [70, 21]. The values of  $v_2^{\text{trk}}$  for charged particles are determined in Ref. [69], while the fit parameter  $v_2$  is expected to be independent of  $p_T^{\text{trk}}$  ranges for a given centrality class. The

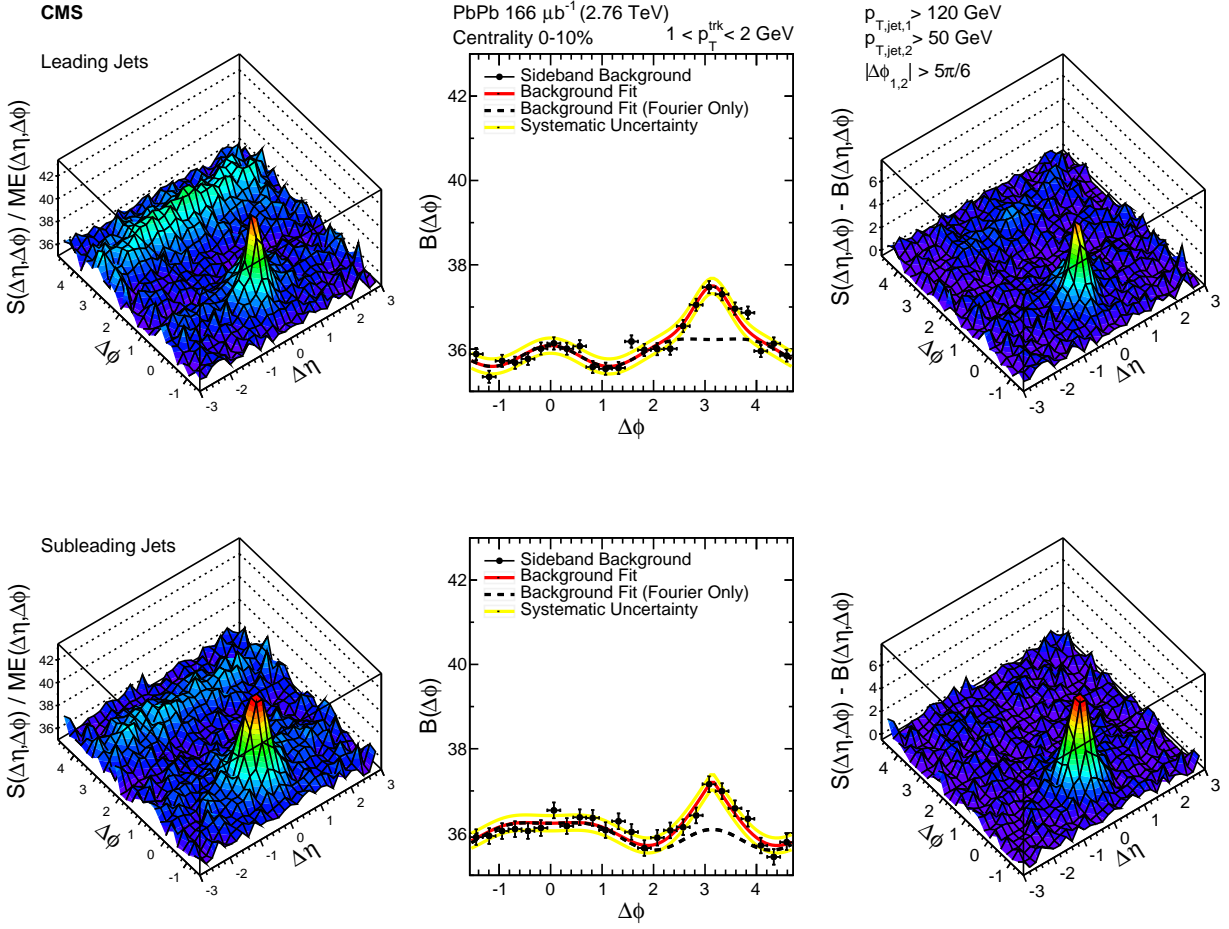


Figure 43. Illustration of the event decomposition procedure with  $\Delta\phi$  fitting: left panel shows the acceptance-corrected correlation, middle panel shows the projected and fit long range distribution, and right panel shows the background-subtracted jet peak.

average value of  $v_2^{\text{jet}}$  from each  $p_T^{\text{trk}}$  range is calculated, and used to fix the  $V_2$  parameter on the second iteration of the fit. Both the combined dijet fit with  $B(\Delta\phi)^{\text{Dijet}}$  and the final  $B(\Delta\phi)$  fits are shown in Appendix B. Through this process, we characterize the underlying event and note that the distribution of jets as well as tracks couples to the flow modulation of the underlying event. This has immediate consequences for studies of momentum balance between leading and subleading hemispheres of the event: as there are non-zero contributions from odd harmonics to the long-range correlated backgrounds, we cannot expect flow cancellation when directly subtracting hemishpere  $p_T^{\text{trk}}$  distributions.

1375 For jet peak studies the underlying event is a background to subtracted to isolate jet peaks.  
1376 After this is done, either by direct subtraction or by subtracting the fit and re-propagated back-  
1377 ground, we are left with isolated 2D jet peaks. Before extracting observables, we must carefully  
1378 consider and correct for reconstruction biases affecting these correlated yields. Before correlations  
1379 are constructed, both tracks and jets are corrected for detector efficiencies and other reconstruction  
1380 effects, as discussed in detail in Sec. 6 and Sec. 7, respectively. There are two additional effects,  
1381 however, in which jet biases are coupled to the multiplicity of low- $p_T$  tracks: a bias against recon-  
1382 structing jets with soft fragmentation that arises from nonlinearity in calorimeter response (reduced  
1383 but not eliminated by the JFF-JEC described in Sec. 7.3), and a bias toward selecting jets that  
1384 sit on upward (soft) fluctuations in the background resulting in excess low- $p_T$  yields around the jet  
1385 axis. Both effects are studied and corrections obtained by carrying out the full analysis in Monte  
1386 Carlo simulation, and corrections are applied to the data correlations after background subtraction.

#### 1387 9.4 Residual Jet Fragmentation Function correction

1388 Jets with harder fragmentation are more likely to be successfully reconstructed than jets with softer  
1389 fragmentation, resulting in a bias toward the selection of jets with fewer associated tracks in both  
1390 pp and PbPb data for all track- $p_T$  selections studied. This bias is partially resolved by the jet  
1391 fragmentation function-dependent jet energy corrections described in Sec. 7. Following the method  
1392 used in [36], corrections are derived for this bias and for the related possible effect of "jet swapping"  
1393 between leading, subleading, and additional jets by comparing correlated per-trigger particle yields  
1394 for all reconstructed jets versus all generated jets. This correction is derived for each jet selection in  
1395 PYTHIA-only simulation, and also in PYTHIA embedded and reconstructed in a HYDJET underlying  
1396 event, excluding HYDJET tracks from the correction determination. For illustration, the derivation  
1397 and magnitude of these corrections for inclusive jets at 2.76 TeV are shown in Figs. 44–47.

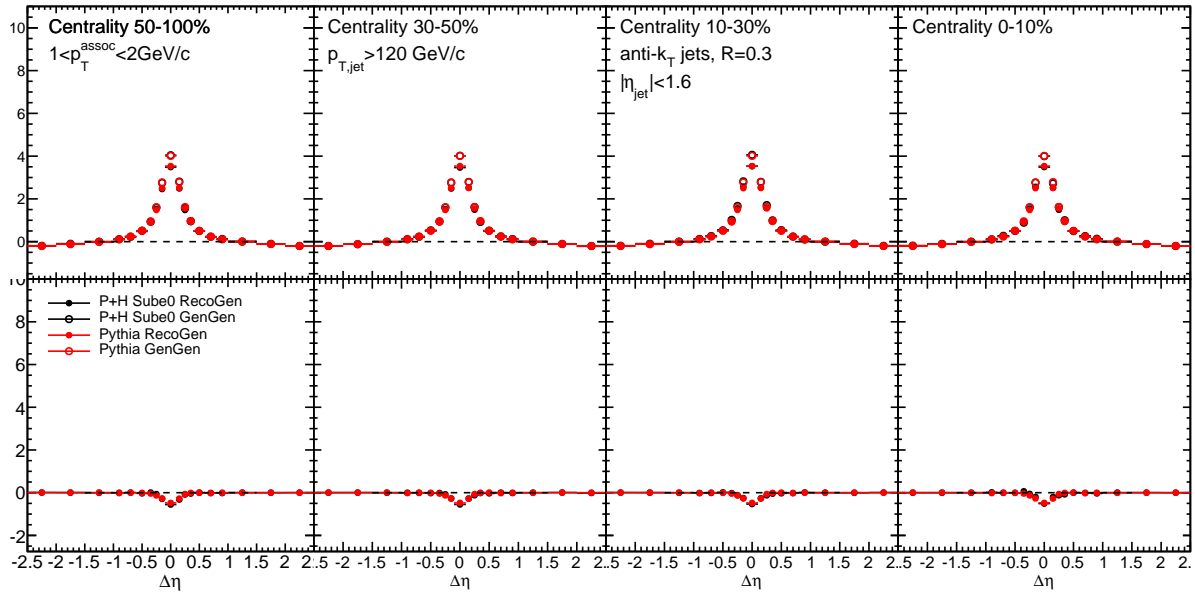


Figure 44.  $\Delta\eta$  jet fragmentation function bias corrections derived by comparing correlations between reconstructed vs. generated jets and generated PYTHIA events, with and without embedding into the HYDJET heavy ion environment, for particles  $1 < p_T^{\text{trk}} < 2 \text{ GeV}$ .

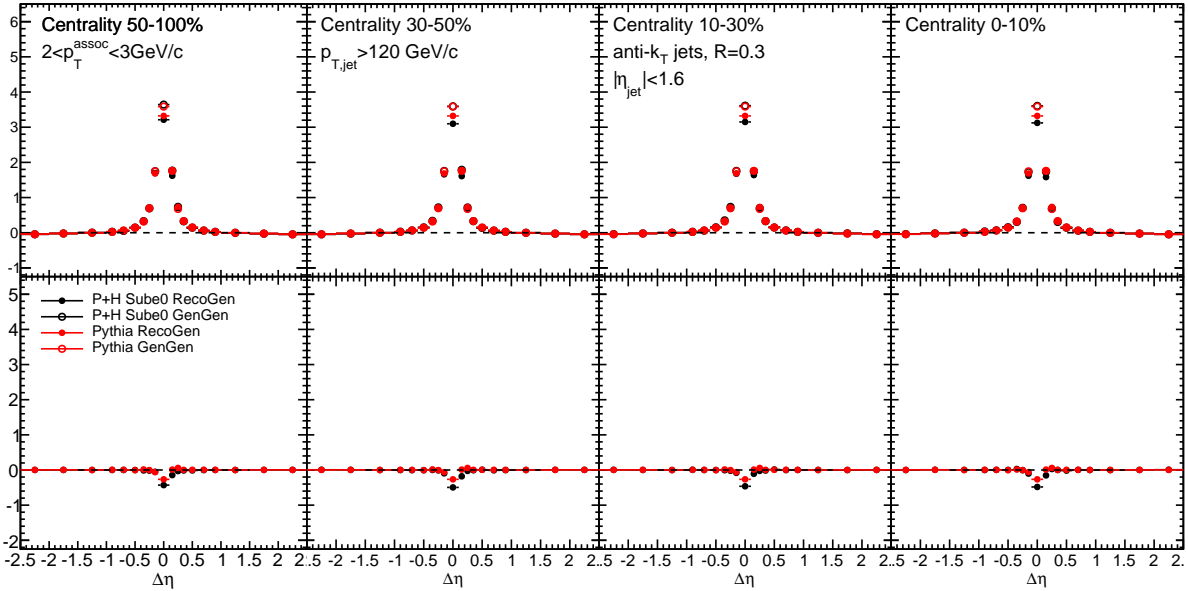


Figure 45.  $\Delta\eta$  jet fragmentation function bias corrections derived by comparing correlations between reconstructed vs. generated jets and generated PYTHIA events, with and without embedding into the HYDJET heavy ion environment, for particles  $2 < p_T^{\text{trk}} < 3 \text{ GeV}$ .

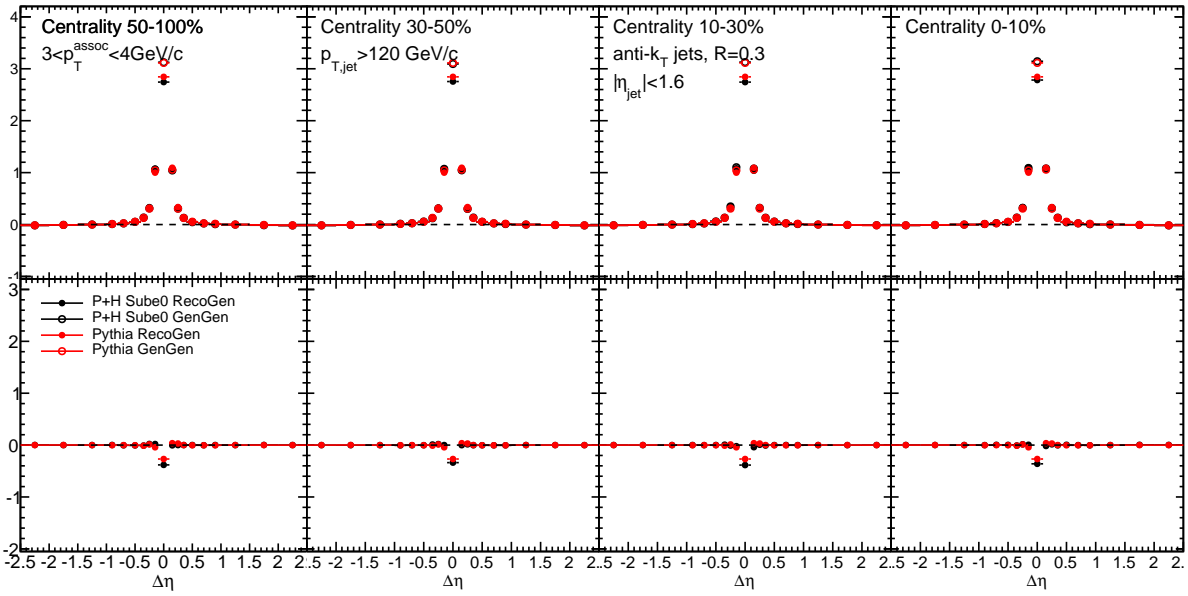


Figure 46.  $\Delta\eta$  jet fragmentation function bias corrections derived by comparing correlations between reconstructed vs. generated jets and generated PYTHIA events, with and without embedding into the HYDJET heavy ion environment, for particles  $3 < p_T^{\text{trk}} < 4 \text{ GeV}$ .

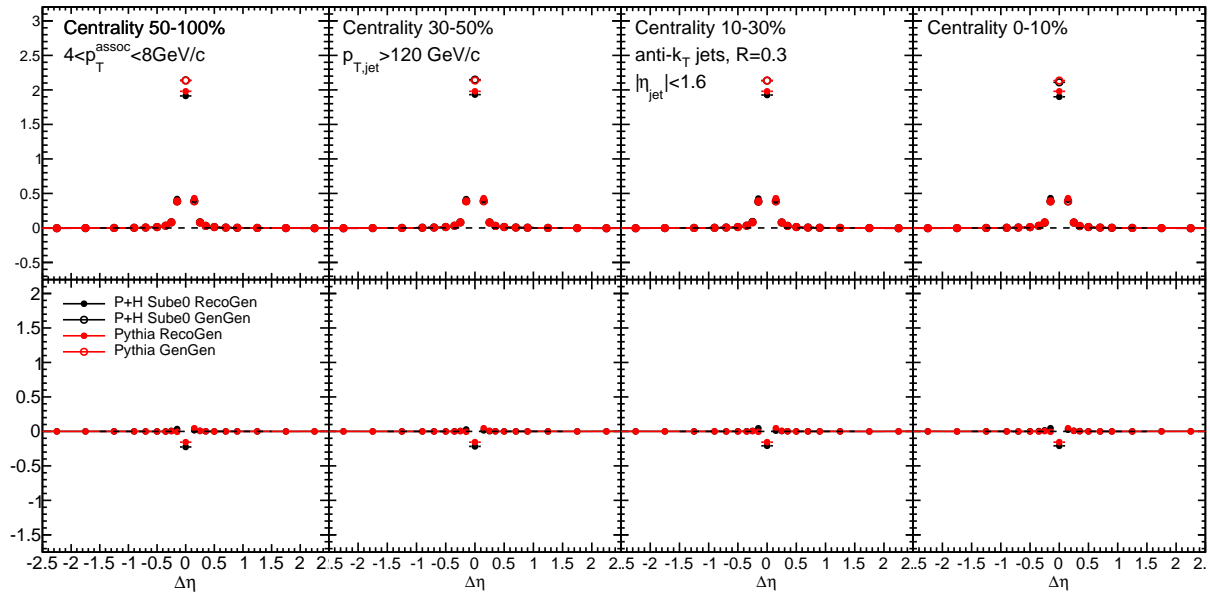


Figure 47.  $\Delta\eta$  jet fragmentation function bias corrections derived by comparing correlations between reconstructed vs. generated jets and generated PYTHIA events, with and without embedding into the HYDJET heavy ion environment, for particles  $4 < p_T^{\text{trk}} < 8 \text{ GeV}$ .

To assess the overall effect of these corrections, the integrated yield of these corrections is  
 shown as a function of transverse momentum and centrality is shown for inclusive, leading, and  
 subleading jets as a function of  $p_T^{\text{trk}}$  in Fig. 48 and as a function of PbPb centrality in Fig. 49.  
 The correction magnitude shows little centrality dependence, and is very similar for pure PYTHIA  
 simulation and PYTHIA embedded into HYDJET.

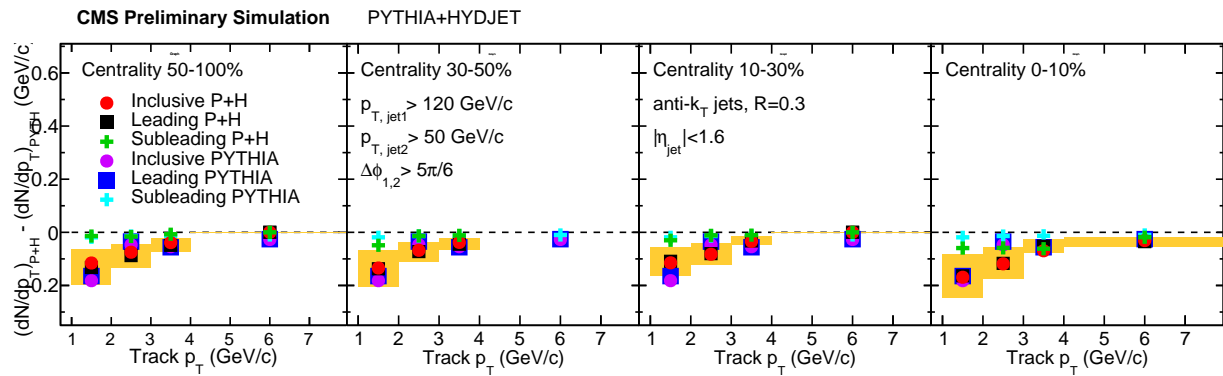


Figure 48. Integrated yield attributed to jet fragmentation function bias in jet reconstruction for PYTHIA alone and embedded into HYDDET, shown as a function of  $p_T^{\text{trk}}$  for each centrality class.

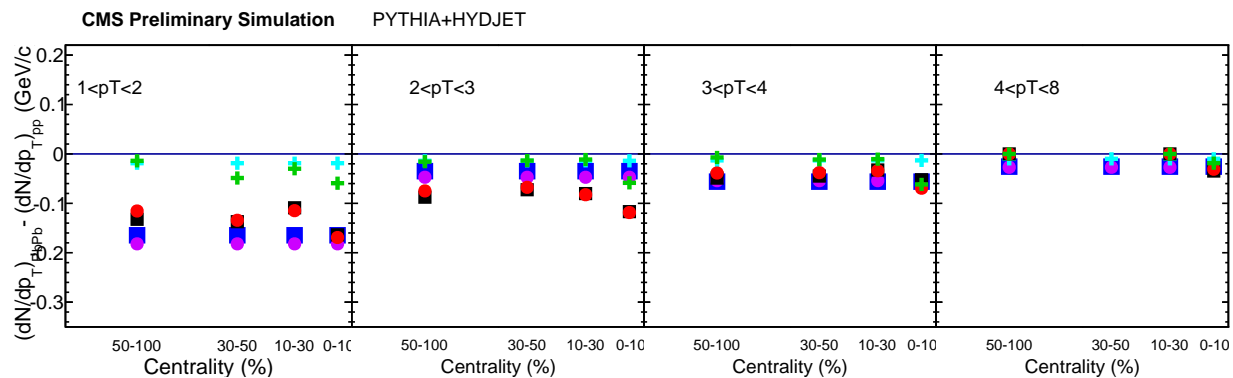


Figure 49. Integrated yield attributed to jet fragmentation function bias in jet reconstruction for PYTHIA alone and embedded into HYDDET, shown as a function of centrality for each associate track  $p_T$  range.

1403 **9.5 Background fluctuation bias correction**

1404 In central PbPb collisions background levels are very high, and naturally fluctuate throughout  
1405 the event. As discussed in Section 7, the process of jet reconstruction in PbPb collisions includes  
1406 background subtraction that accounts for the general distribution of energy in the event. However,  
1407 small, local variations in background levels remain (on the order of 5 GeV within a radius of  $R =$   
1408 0.3). These are reconstructed into the jet, raising or lowering the measured jet energy depending  
1409 on whether the jet sits on an upward or a downward fluctuation in the background. As a result,  
1410 jets with “true”  $p_T$  slightly below the 120 GeV selection threshold that sit on upward background  
1411 fluctuations will be included in the sample, while jets sit on downward will be excluded. Because  
1412 the jet spectrum is steeply falling, it is much more common for a lower- $p_T$  jet (on an upward  
1413 fluctuation) to be included in the sample than for a higher- $p_T$  jet to be excluded. This results in  
1414 the systematic inclusion of tracks from background fluctuations in the peak of tracks observed about  
1415 the jet axis, resulting in a contribution to the initially measured jet peak that must be accurately  
1416 quantified and subtracted.

1417 To estimate and subtract the contribution to the excess yield due to background fluctuation  
1418 bias in jet reconstruction to the measured excess yield, we perform simulations in PYTHIA+HYDJET  
1419 samples with reconstructed jets (but generated tracks, as the tracking efficiency uncertainty is  
1420 analyzed separately), and construct correlations excluding particles generated with the embedded  
1421 PYTHIA hard-scattering process. As the PYTHIA+HYDJET simulation does not include interactions  
1422 between the PYTHIA hard process and the medium, this procedure by construction isolates the  
1423 contribution to the jet peak that is attributable to the background fluctuation bias. The resulting  
1424 corrections are illustrated in Fig. 50 - Fig. 53 for inclusive jets at 2.76 TeV. These correlations show  
1425 a diminishing effect with increasing particle transverse momentum. We subtract the gaussian fit  
1426 to these correlations bin-by-bin from the data results, and also assign the half its magnitude as  
1427 systematic uncertainty to the final measurements. To assess the overall effect of these corrections,  
1428 the integrated yield of these corrections is shown in Fig. 54 as a function of transverse momentum  
1429 and centrality is shown for inclusive, leading, and subleading jets at 2.76 TeV.

1430 Considering that the background fluctuation bias effect in many ways mimics the jet peak  
1431 signal, it is particularly important to validate this correction and confirm both that its origin

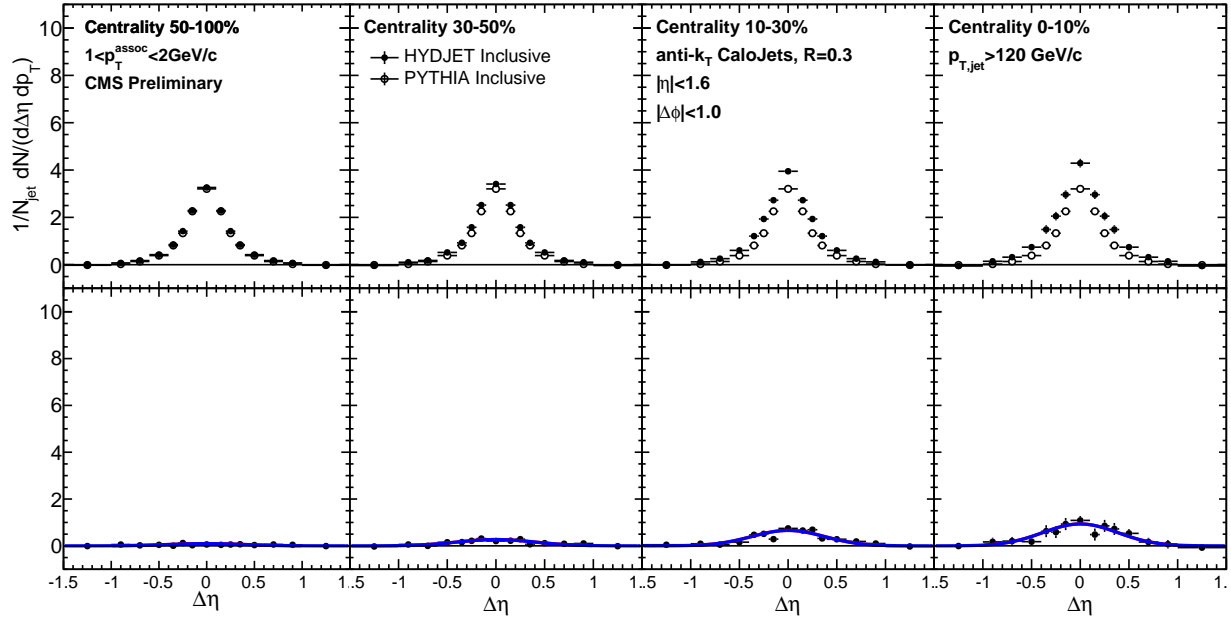


Figure 50.  $\Delta\eta$  background fluctuation bias correction for inclusive jets derived by constructing correlations in PYTHIA+HYDJET between reconstructed jets and only those tracks simulated as part of the heavy ion underlying event rather than the embedded PYTHIA hard process, for particles  $1 < p_T^{\text{trk}} < 2 \text{ GeV}$

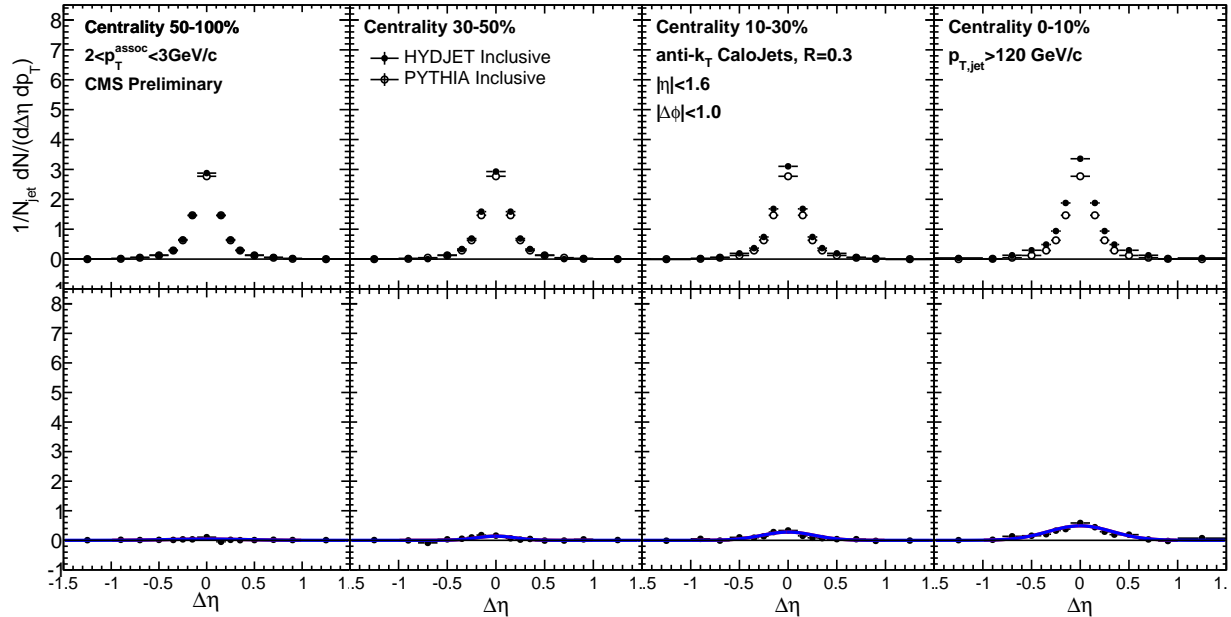


Figure 51.  $\Delta\eta$  background fluctuation bias correction for inclusive jets derived by constructing correlations in PYTHIA+HYDJET between reconstructed jets and only those tracks simulated as part of the heavy ion underlying event rather than the embedded PYTHIA hard process, for particles  $2 < p_T^{\text{trk}} < 3 \text{ GeV}$

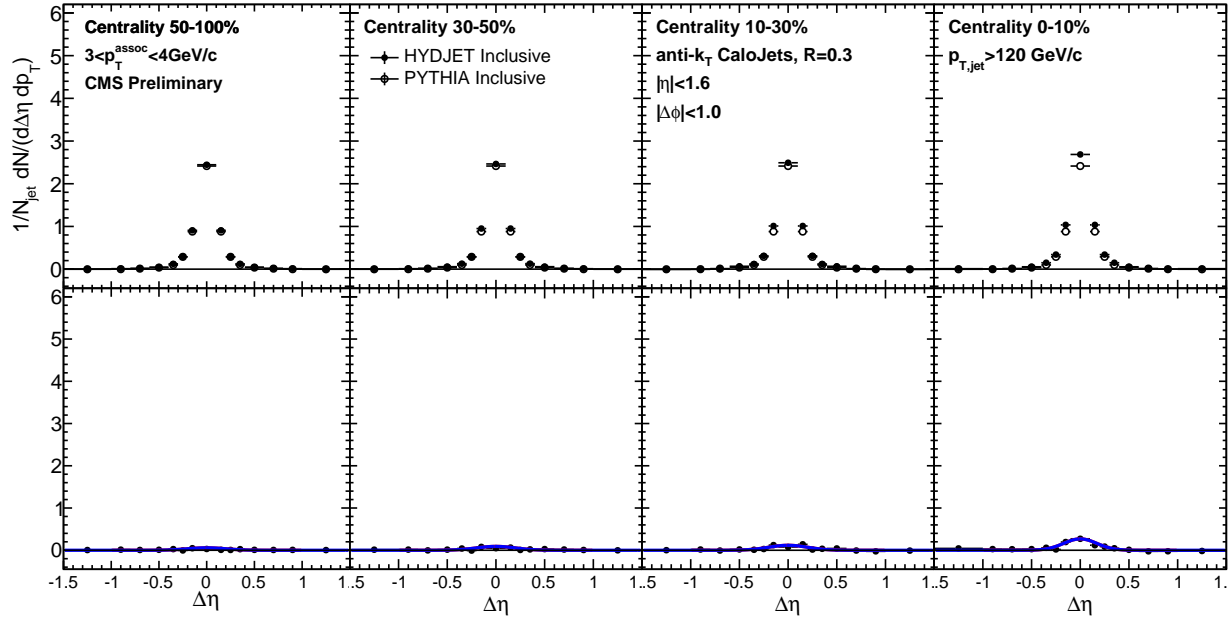


Figure 52.  $\Delta\eta$  background fluctuation bias correction for inclusive jets derived by constructing correlations in PYTHIA+HYDJET between reconstructed jets and only those tracks simulated as part of the heavy ion underlying event rather than the embedded PYTHIA hard process, for particles  $3 < p_T^{\text{trk}} < 4 \text{ GeV}$

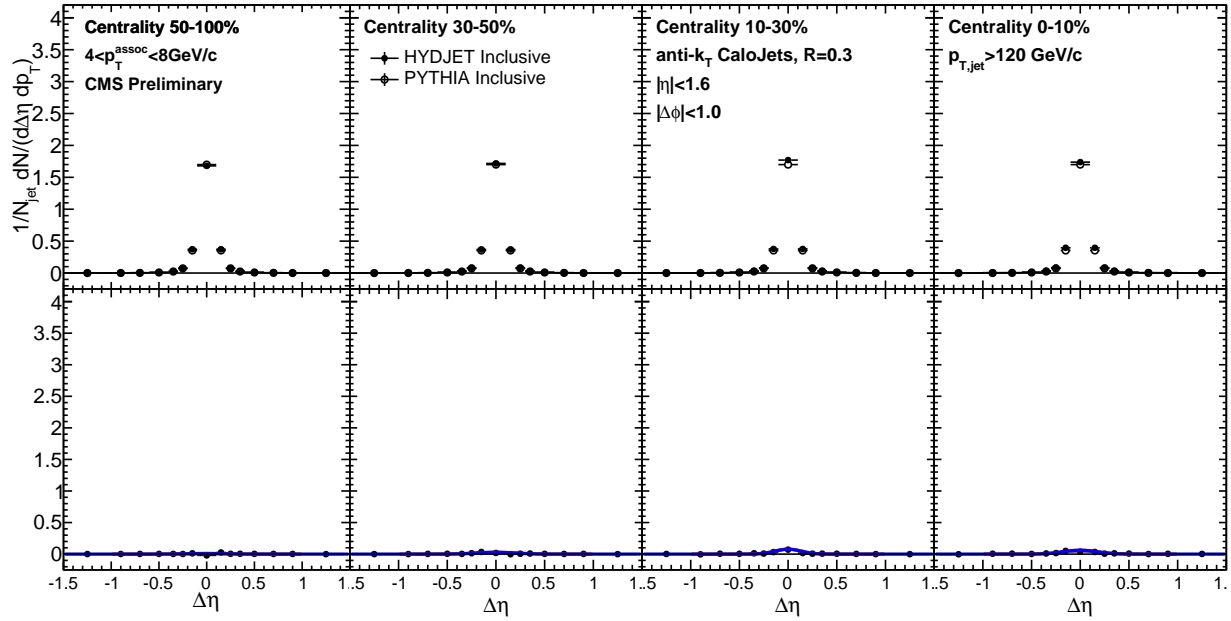


Figure 53.  $\Delta\eta$  background fluctuation bias correction for inclusive jets derived by constructing correlations in PYTHIA+HYDJET between reconstructed jets and only those tracks simulated as part of the heavy ion underlying event rather than the embedded PYTHIA hard process, for particles  $4 < p_T^{\text{trk}} < 8 \text{ GeV}$

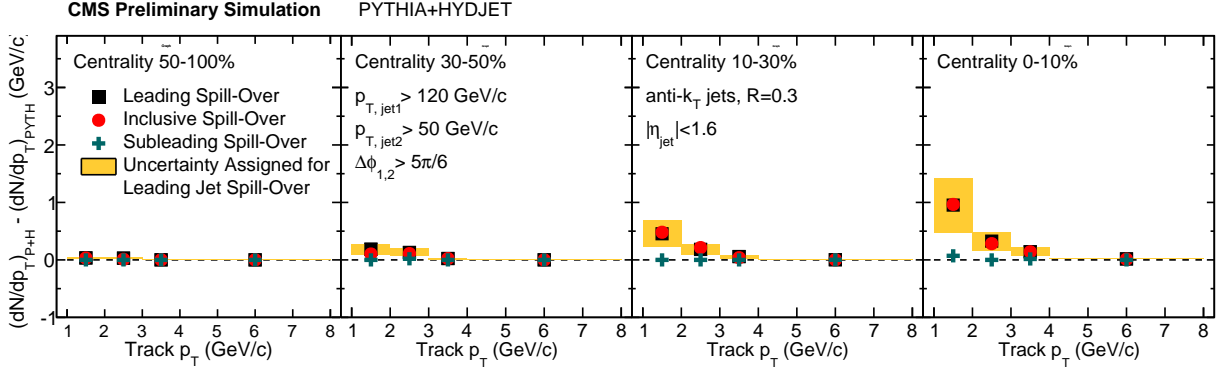


Figure 54. Integrated yield attributed to background fluctuation bias in the selection of inclusive and leading jets, shown as a function of associate track  $p_T$  for each centrality class.

is well-understood and that the HYDJET simulation used to derive it reproduces the background fluctuations in data closely enough to accurately obtain corrections. To check this, we extract a direct estimate of the effect from data using a “pseudo-embedding” of pp jets into a minimum bias PbPb data sample. The goal of this study is to verify that we recover a similar magnitude of excess yield as we attribute based on our more detailed PYTHIA+HYDJET simulations. Here we approximate the effect by adding the total transverse momentum in a circle of radius  $R = 0.3$  around all jets with  $p_T > 90$  GeV, and considering the total deviation up or down of this  $(\Sigma p_T)_{\text{cone}}$  from the average total transverse momentum  $\langle (\Sigma p_T)_{\text{cone}} \rangle$ . First, we may directly compare the average  $p_T$  and fluctuations in  $p_T$  in these random cones between data and Monte Carlo. We find that our Monte Carlo approximately reproduces the data: in data  $\langle (\Sigma p_T)_{\text{cone,data}} \rangle = 10.0$  GeV, with  $\sigma((\Sigma p_T)_{\text{cone,data}}) = 4.9$  GeV, while in Monte Carlo  $\langle (\Sigma p_T)_{\text{cone,MC}} \rangle = 11.9$  GeV, with  $\sigma((\Sigma p_T)_{\text{cone,data}}) = 5.6$  GeV.

We then use these random cones to adjust jet energy and re-select jets: we add the deviation up or down of this  $(\Sigma p_T)_{\text{cone}}$  to each embedded pp jets with this adjusted  $p_T$ . We then fill  $\Delta\eta - \Delta\phi$  correlations to all jets that pass our nominal  $p_T > 120$  GeV jet selection cut. We apply this technique to both our PYTHIA+HYDJET sample and a minimum-bias PbPb data sample to measure the charged particle yield associated with the embedded jet axis as a result of the jet fluctuation bias. As Fig. 55–56 show, this data pseudo-embedding recovers the same magnitude of excess yield due to background fluctuation bias as our nominal Monte Carlo studies, but artificially confines this

1451 effect to a  $R = 0.3$  cone by construction, due to the artificially simple jet reconstruction procedure.

1452 This gives confidence that the origin and magnitude of the effect are well-understood.

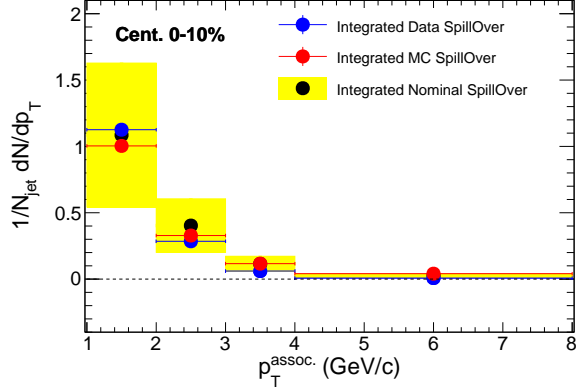


Figure 55. Total integrated magnitude of background fluctuation bias as simulated with pp jets embedded in Minimum Bias events (blue points) compared to the effect as simulated with PYTHIA jets into minimum bias HYDJET and to nominal corrections obtained with full PYTHIA+HYDJET simulation. Nominal systematic errors of +/- 50% as assigned in this analysis are shown as yellow systematic error bars on nominal (full MC simulation) points.

1453 The background fluctuation bias could also be sensitive to the same calorimeter nonlinearity  
1454 bias that necessitates fragmentation-jet energy corrections. To study this question and validate the  
1455 uncertainty associated with this correction, we separately study the effect for quark jets and gluon  
1456 jets, as shown in Figure 57. This study is limited by statistics, but deviations (or fluctuations) in  
1457 the bias for quark versus gluon jets are within the 50% systematic uncertainty assigned.

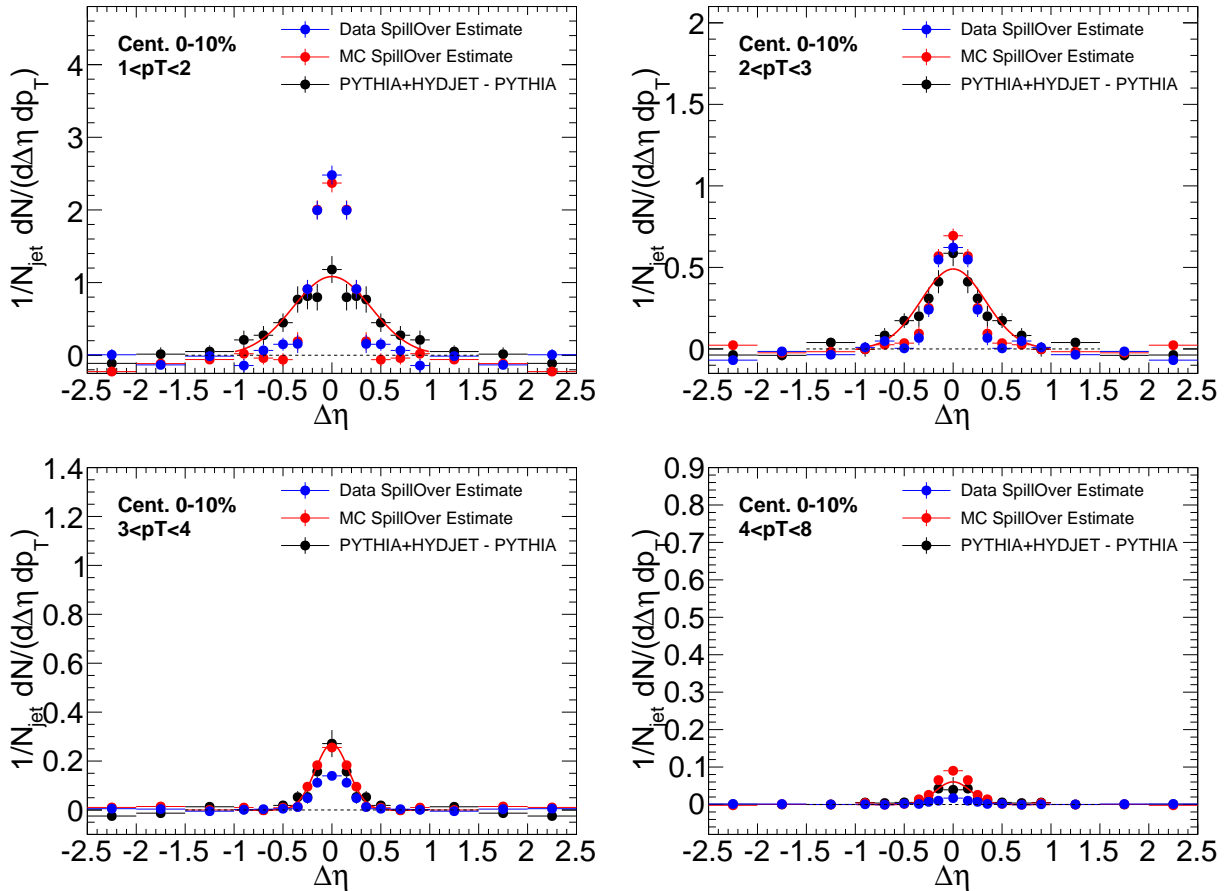


Figure 56. Correlated yield  $\Delta\eta$  due to background fluctuation bias as simulated with pp jets embedded in Minimum Bias events (blue points) compared to the effect applying the same technique with PYTHIA jets in HYDJET minimum bias events, as well as in full PYTHIA+HYDJET simulation (black points with red fit line).

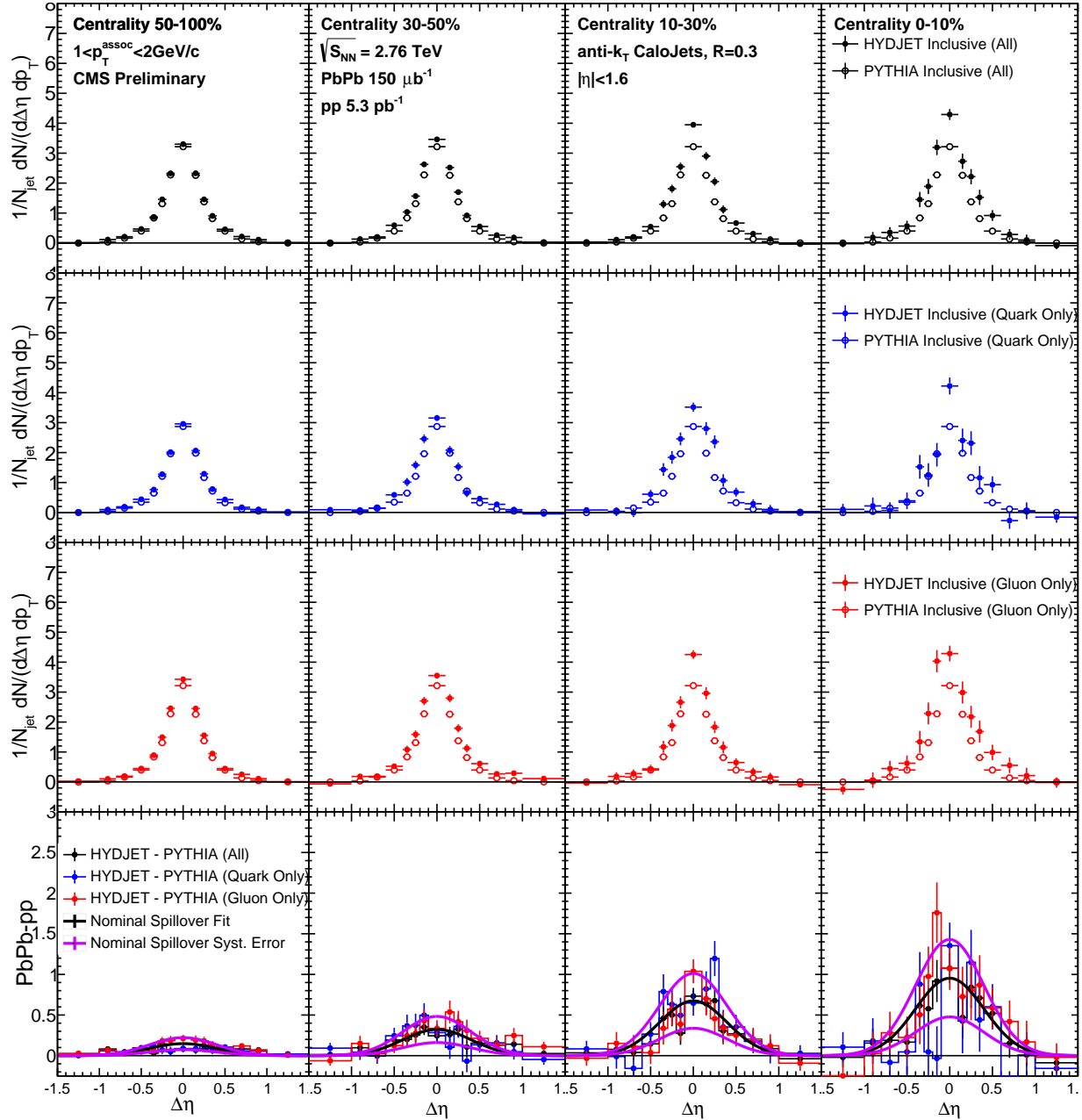


Figure 57. Comparison of magnitude of background selection bias effect for quark and gluon jets versus our nominal sample. Jet selection is inclusive in all cases.

1458 **9.6 Evaluation of systematic uncertainties**

1459 A number of sources of systematic uncertainty have been discussed in presenting jet and track  
1460 reconstruction and the jet-track correlation analysis procedure. To estimate the total systematic  
1461 uncertainty in these measurements, these contributions are added in quadrature. A brief summary  
1462 of all systematic uncertainty contributions, together with the procedure used to estimate their  
1463 magnitude follows. The contributions from each source (relative to jet peak signal) are summarized  
1464 in Tables [V](#)–[VII](#).

1465 **9.6.1 Systematic uncertainties related to jet reconstruction**

1466 Jet reconstruction-related sources of systematic uncertainty in this analysis include the two recon-  
1467 struction biases as discussed above, as well uncertainty associated with the jet energy scale (JES)  
1468 evaluation. We consider three sources of uncertainty on the JES: (1) differences in calorimeter  
1469 response for quark versus gluon jets, meaning that medium-induced changes in jet flavor could  
1470 result in either over-correction or under-correction of jet energy and a resulting bias in jet selection  
1471 (evaluated via Monte Carlo non-closure for quark and gluon jets); (2) possible differences between  
1472 data and simulation; (3) uncertainty due to quenching effects not included in our HYDJET simula-  
1473 tion. To evaluate how each of these sources of JES uncertainty affects final correlations, we vary jet  
1474 selection threshold by the combined uncertainty, and then quantify the resulting differences in the  
1475 final correlations as a measure of the combined residual JES uncertainty. Since all the measured  
1476 correlations are studied per-reconstructed jets, the jet reconstruction efficiency does not contribute  
1477 to the systematic uncertainty of this measurement.

1478 **9.6.2 Systematic uncertainties related to tracking and tracking efficiency corrections**

1479 The tracking efficiency correction uncertainty is estimated from the ratio of corrected reconstructed  
1480 yields and generated yields by using generator level charged particles as a “truth” reference. To ac-  
1481 count for the possible track reconstruction differences in data and simulation, a residual uncertainty  
1482 in track reconstruction efficiency and fake rate corrections is also estimated.

1483 **9.6.3 Systematic uncertainty associated with pair acceptance correction and event  
1484 decomposition**

1485 Uncertainty arising from pair-acceptance effects is estimated by considering the sideband asymme-  
 1486 try after dividing by the mixed-event background. Each sideband region of the final  $\Delta\eta$  distribution  
 1487 ( $-2.5 < \Delta\eta < -1.5$  and  $1.5 < \Delta\eta < 2.5$ ) is separately fit with a horizontal line after background  
 1488 subtraction. The greater of these two deviations from zero is assigned as systematic error. Un-  
 1489 certainties resulting from the background subtraction are determined by considering the average  
 1490 point-to-point deviation in two parts of the sideband region ( $1.5 < |\Delta\eta| < 2.0$  and  $2.0 < |\Delta\eta| < 2.5$ )  
 1491 after background subtraction. The derivations of both of these sources of uncertainty are illustrated  
 1492 in Appendix C. In PbPb data this background subtraction uncertainty is greatest for the most cen-  
 1493 tral events (0–10%) and the lowest track  $p_T$  bin where the background is most significant compared  
 1494 to the signal level, and decreases for less central collisions and for higher  $p_T$  tracks ( $p_T^{\text{trk}} > 2$  GeV).

1495 **9.6.4 Summary of systematic uncertainties**

1496 The contributions to total systematic uncertainty from each of the sources described above are given  
 1497 in Tables V–VII. Table V gives uncertainty evaluations for correlation studies at 2.76 TeV, while  
 1498 Table VI gives the same for studies at 5.02 TeV. Finally, Table VII gives uncertainty evaluations  
 1499 for balanced ( $A_J < 0.22$ ) and unbalanced ( $A_J > 0.22$ ) dijet events in momentum balance studies  
 1500 at 2.76 TeV.

TABLE V. Systematic uncertainties in the measurement of the jet-track correlations in PbPb and pp collisions at 2.76 TeV, as percentage of the total measured correlated yield. The numbers presented in this table summarize the range of values of systematic uncertainty (as a function of  $p_T^{\text{trk}}$ ) for different centrality bins.

Source	0–10%	10–30%	30–50%	50–100%	pp
Background fluctuation bias	3–12%	2–7%	1–5%	0–1%	–
Jet fragmentation function bias	0–2%	0–2%	0–2%	0–2%	0–2%
Residual jet energy scale	3%	3%	3%	3%	3%
Tracking efficiency uncertainty	4%	4%	4%	4%	3 %
Residual track efficiency corr.	5%	5%	5%	5%	5%
Pair acceptance corrections	5–9%	5–9%	4–8%	2–6%	2–3%
Background subtraction	2–5%	2–5%	2–5%	2–5%	1–2%
Total	9–17%	9–14%	8–13%	8–10%	7–8%

TABLE VI. Systematic uncertainties in the measurement of the jet track correlations in PbPb and pp collisions at 5.02 TeV. The numbers presented in this table summarize typical range of systematic uncertainty as a function of collision centrality. The upper limits of the cited values correspond to uncertainties at lowest  $p_T^{\text{trk}}$ , and uncertainties decrease with rising  $p_T^{\text{trk}}$ .

Source	0–10%	10–30%	30–50%	50–100%	ppRef
Background fluctuation bias	0–10%	0–5%	0–2%	0–1%	–
Background fluctuation bias residual	0–2%	0–3%	0–1%	0–1%	–
JFF bias	3–5%	3–4%	3–4%	3–4%	3%
Residual JES	4%	4%	4%	4%	4%
Tracking efficiency uncertainty	1%	1%	1%	1%	1%
Residual tracking efficiency	5%	5%	5%	5%	5%
Pair-acceptance corrections	1–5%	1–4%	1–4%	1–4%	1–2%
Event decomposition	1–9%	0–4%	0–4%	0–3%	0–3%
Total	7–16%	7–11%	7–9%	7–9%	7–8%

TABLE VII. This table summarizes the systematic uncertainties in the measurement of the  $p_T^{\text{trk}}$  correlations in PbPb and pp collisions at 2.76 TeV. Upper and lower limits are shown as a function of collision centrality. Upper values correspond to the uncertainties at lowest  $p_T^{\text{trk}}$ .

Source	0–30%	30–50%	50–100%	pp
Balanced jet selection ( $A_J < 0.22$ ):				
Background fluctuations	1–8%	1–3%	0–1%	–
JFF bias and jet swapping	0–2%	0–2%	0–2%	0–2%
Residual JES	3%	3%	3%	3%
Tracking efficiency	4%	4%	4%	3 %
Residual track efficiency corr.	5%	5%	5%	5%
Pair acceptance corrections	5–9%	4–8%	2–6%	2–3%
Event decomposition	2–5%	2–5%	2–5%	1–2%
Total	9–15%	8–13%	8–10%	7–8%
Unbalanced jet selection ( $A_J > 0.22$ ):				
Background fluctuations	1–10%	1–5%	0–2%	–
JFF bias and jet swapping	0–2%	0–2%	0–2%	0–2%
Residual JES	3%	3%	3%	3%
Tracking efficiency	4%	4%	4%	3 %
Residual track efficiency corr.	5%	5%	5%	5%
Pair acceptance corrections	5–9%	4–8%	2–6%	2–3%
Event decomposition	2–5%	2–5%	2–5%	1–2%
Total	9–16%	8–13%	8–10%	7–8%

## 10 DISCUSSION OF RESULTS

1502 Jet-track correlation studies can produce measurements of the density of particles (in each  $p_T^{\text{trk}}$   
 1503 class) with respect to the jet axis and can also, by creating correlations weighted per-track by  
 1504 its  $p_T^{\text{trk}}$ , produce measurements of the distribution of  $p_T^{\text{trk}}$  in the event as a whole. Both types of  
 1505 measurements are presented here, for inclusive selections of jets with  $p_T > 120$  GeV at 2.76 TeV  
 1506 and 5.02 TeV, and for high- $p_T$  dijet events at 2.76 TeV. First, particle density correlation results are  
 1507 presented in Secs. 10.1- 10.2. Next,  $p_T^{\text{trk}}$  distributions are used to extract measurements of jet shapes  
 1508 (the transverse momentum profiles of jets) in Sec. 10.3. Finally, in Sec. 10.4,  $p_T^{\text{trk}}$  distributions are  
 1509 used to decompose and analyze the hemisphere momentum balance in dijet events.

1510 **10.1 Inclusive jet particle density correlation results**

1511 Particle density correlation studies allow for the detailed characterization of jet fragmentation,  
 1512 and of medium-induced modifications to jet fragmentation in PbPb data (as a function of collision  
 1513 centrality) compared to pp data. The analysis procedure described in Sec. 9 results in fully-corrected  
 1514 2D jet peaks in  $\Delta\eta - \Delta\phi$ , which may then be projected to obtain the distribution of particles in  
 1515 each  $p_T^{\text{trk}}$  class as a function of  $\Delta\eta$  or  $\Delta\phi$ . The top panels of Figs. 58-65 show these  $\Delta\eta$  and  
 1516  $\Delta\phi$  distributions (projected over  $|\Delta\phi| < 1$  and  $|\Delta\eta| < 1$ , respectively) for 2.76 TeV pp data and  
 1517 PbPb data in each  $p_T^{\text{trk}}$  range from 1-2 GeV (Fig. 58-59) up to 4-8 GeV (Fig. 64-65). The bottom  
 1518 panels of these figures show the differences PbPb–pp for illustration of medium modifications to jet  
 1519 fragmentation patterns. In both the  $\Delta\eta$  and  $\Delta\phi$  dimensions, centrality-dependent excesses of soft  
 1520 (low- $p_T^{\text{trk}}$ ) particles are evident. These exhibit the greatest modifications in the most central PbPb  
 1521 collisions, decreasing with centrality until the most peripheral collisions show little modification  
 1522 when compared to pp data. These excesses decrease with increasing  $p_T^{\text{trk}}$ , until in the 4-8 GeV  
 1523 range the enhancements evident at lowest- $p_T^{\text{trk}}$  reverse to possible slight depletion. In both  $\Delta\eta$  and  
 1524  $\Delta\phi$  dimensions, the soft excesses exhibit a gaussian-like distribution around the jet axis, while also  
 1525 extending to large angles  $\Delta\eta = 1$  and  $\Delta\phi = 1$  at lowest  $p_T^{\text{trk}}$ .

1526 Figures 66 and 67 show the corresponding  $\Delta\eta$  and  $\Delta\phi$  distributions at 5.02 TeV. Here,  
 1527 the distribution of particles in each  $p_T^{\text{trk}}$  class are stacked (with lowest- $p_T^{\text{trk}}$  particles on top), and  
 1528 pp data shown separately at left. Again the differences PbPb–pp are shown in bottom panels to

illustrate the medium modifications, and exhibit similar qualitative trends to those described above  
 for 2.76 TeV results. Results may also be presented as a function of radial distance from the jet axis  
 $\Delta r = \sqrt{\Delta\eta^2 + \Delta\phi^2}$ . Figure 68 presents charged particle yields, differentially in  $p_T^{\text{trk}}$ , as a function  
 of  $\Delta r$ . For comparison, the bottom row of each plot shows the difference, PbPb minus pp. This  
 shows the particles contributing to a jet fragmentation function measurement within a given radius  
 from a jet, and illustrates the radial dependence of modifications extending to at least  $\Delta r = 1$ .

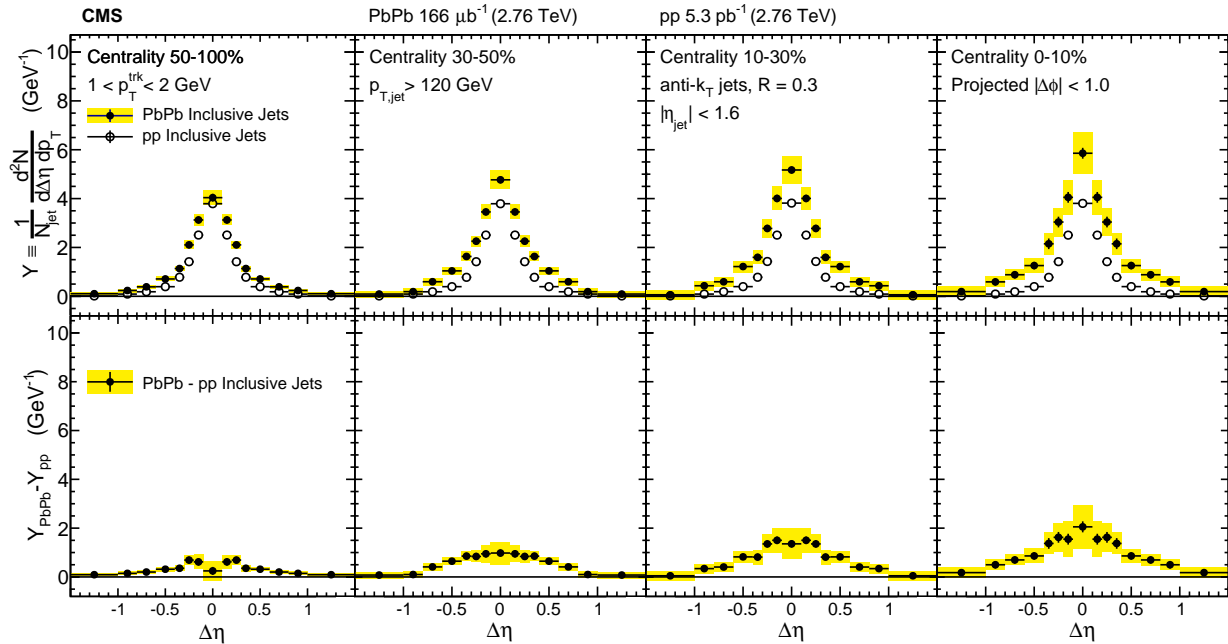


Figure 58. Symmetrized  $\Delta\eta$  distributions (projected over  $|\Delta\phi| < 1$ ) of background-subtracted particle yields correlated to PbPb and pp inclusive jets with  $p_T > 120$  GeV are shown in the top panels for tracks with  $1 < p_T^{\text{trk}} < 2$  GeV. The difference in PbPb and pp per-jet yields is shown in the bottom panels. The total systematic uncertainties are shown as shaded boxes, and statistical uncertainties are shown as vertical bars (often smaller than the symbol size).

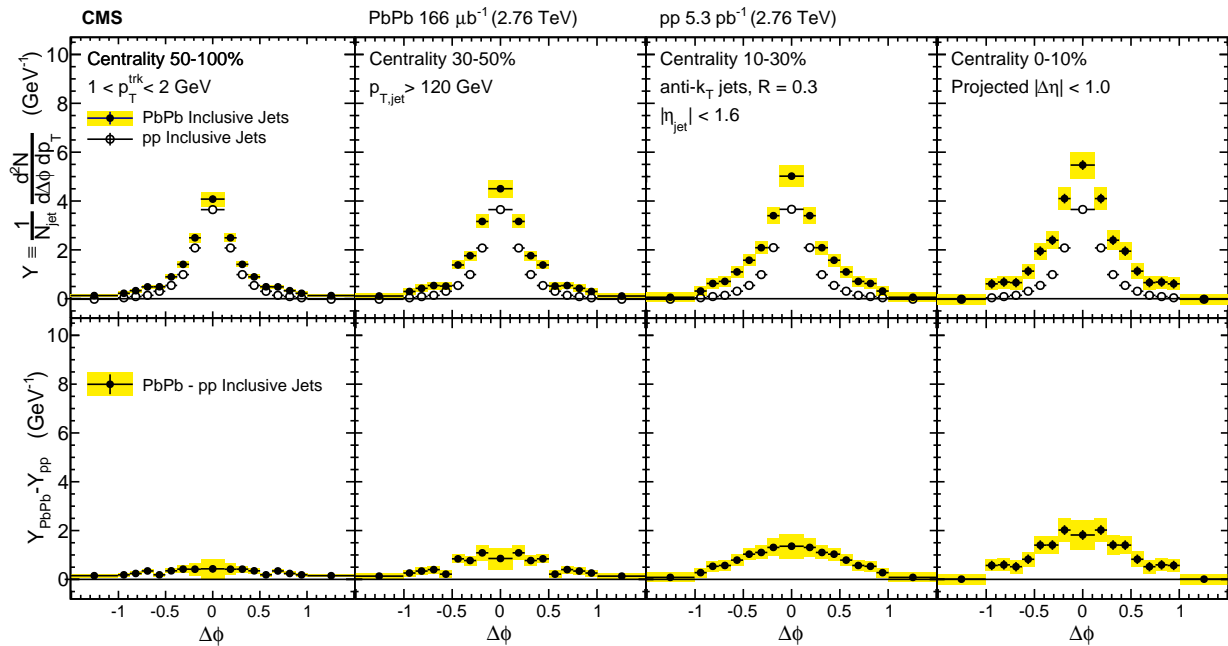


Figure 59. Symmetrized  $\Delta\phi$  distributions (projected over  $|\Delta\eta| < 1$ ) of background-subtracted particle yields correlated to PbPb and pp inclusive jets with  $p_{\text{T}} > 120 \text{ GeV}$  are shown in the top panels for tracks with  $1 < p_{\text{T}}^{\text{trk}} < 2 \text{ GeV}$ . The difference in PbPb and pp per-jet yields is shown in the bottom panels. The total systematic uncertainties are shown as shaded boxes, and statistical uncertainties are shown as vertical bars (often smaller than the symbol size).

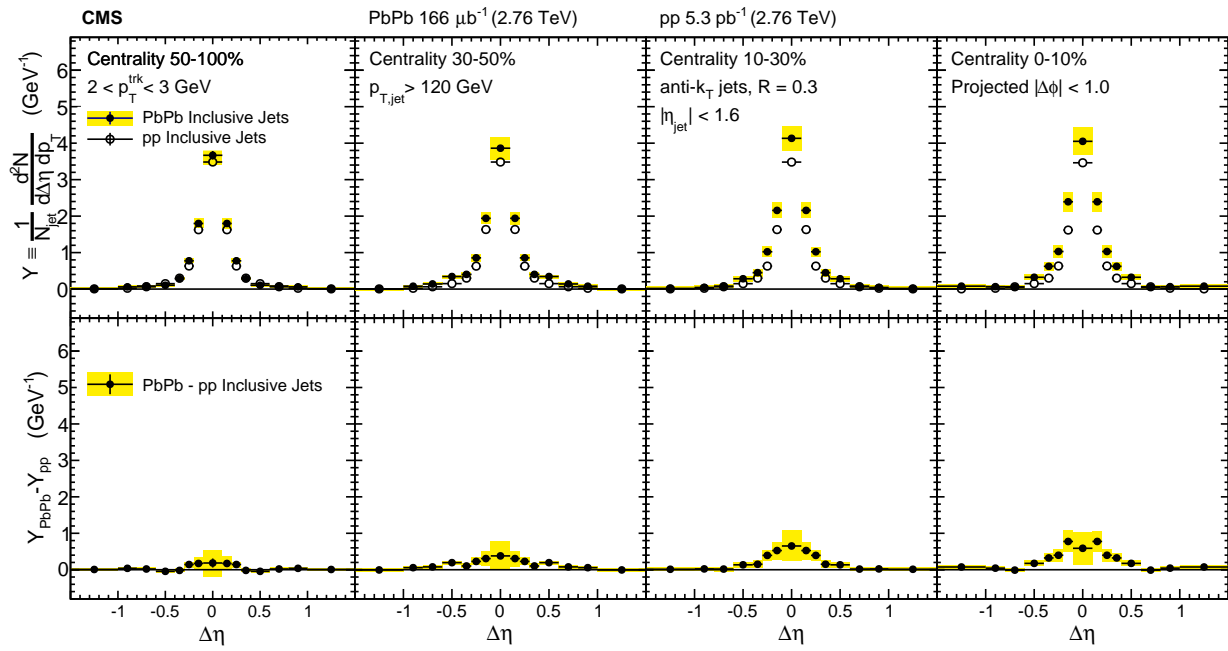


Figure 60. Symmetrized  $\Delta\eta$  distributions (projected over  $|\Delta\phi| < 1$ ) of background-subtracted particle yields correlated to PbPb and pp inclusive jets with  $p_{\text{T}} > 120 \text{ GeV}$  are shown in the top panels for tracks with  $2 < p_{\text{T}}^{\text{trk}} < 3 \text{ GeV}$ . The difference in PbPb and pp per-jet yields is shown in the bottom panels. The total systematic uncertainties are shown as shaded boxes, and statistical uncertainties are shown as vertical bars (often smaller than the symbol size).

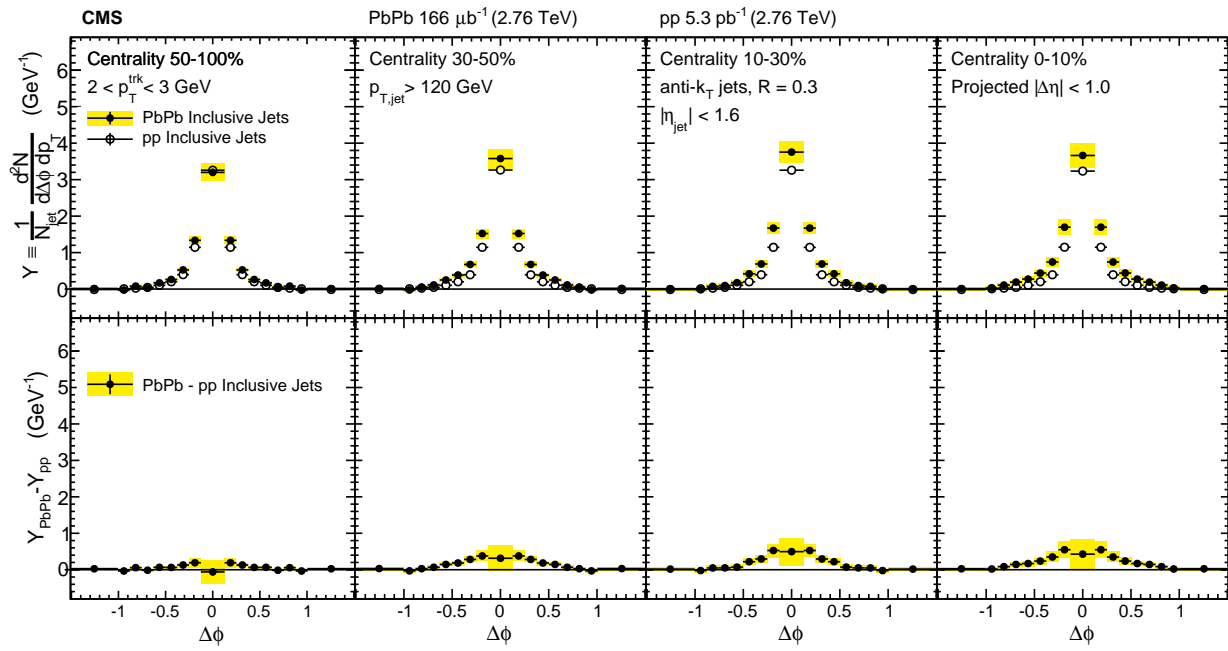


Figure 61. Symmetrized  $\Delta\phi$  distributions (projected over  $|\Delta\eta| < 1$ ) of background-subtracted particle yields correlated to PbPb and pp inclusive jets with  $p_{\text{T}} > 120 \text{ GeV}$  are shown in the top panels for tracks with  $2 < p_{\text{T}}^{\text{trk}} < 3 \text{ GeV}$ . The difference in PbPb and pp per-jet yields is shown in the bottom panels. The total systematic uncertainties are shown as shaded boxes, and statistical uncertainties are shown as vertical bars (often smaller than the symbol size).

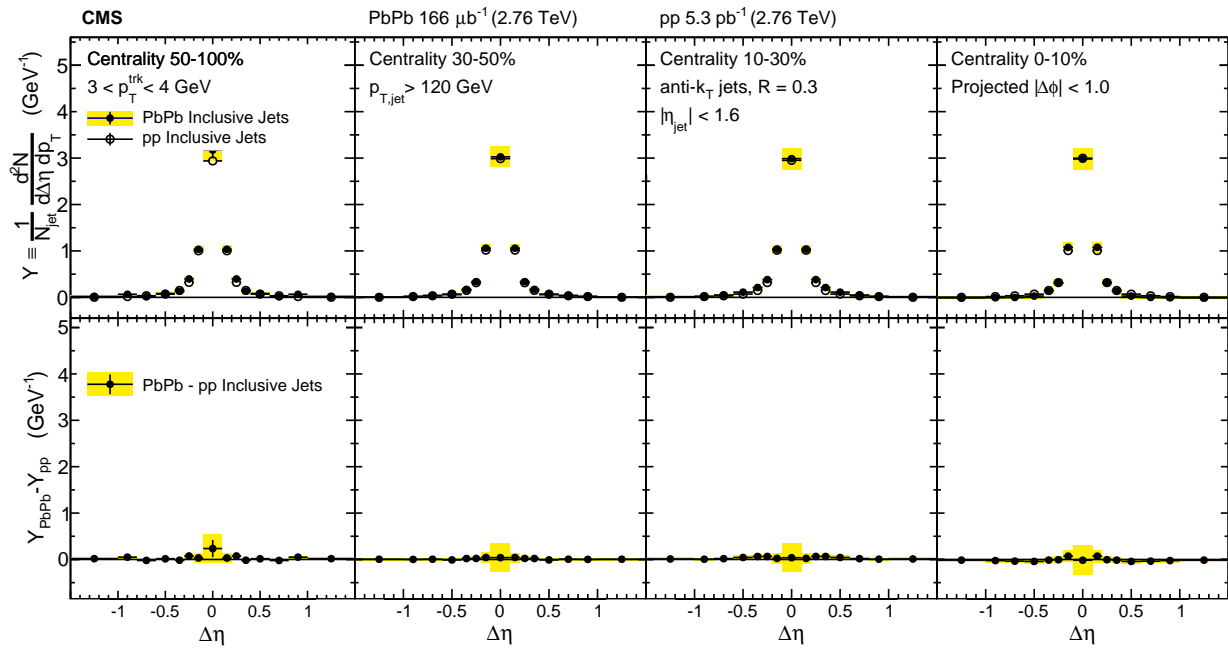


Figure 62. Symmetrized  $\Delta\eta$  distributions (projected over  $|\Delta\phi| < 1$ ) of background-subtracted particle yields correlated to PbPb and pp inclusive jets with  $p_T > 120 \text{ GeV}$  are shown in the top panels for tracks with  $3 < p_T^{\text{trk}} < 4 \text{ GeV}$ . The difference in PbPb and pp per-jet yields is shown in the bottom panels. The total systematic uncertainties are shown as shaded boxes, and statistical uncertainties are shown as vertical bars (often smaller than the symbol size).

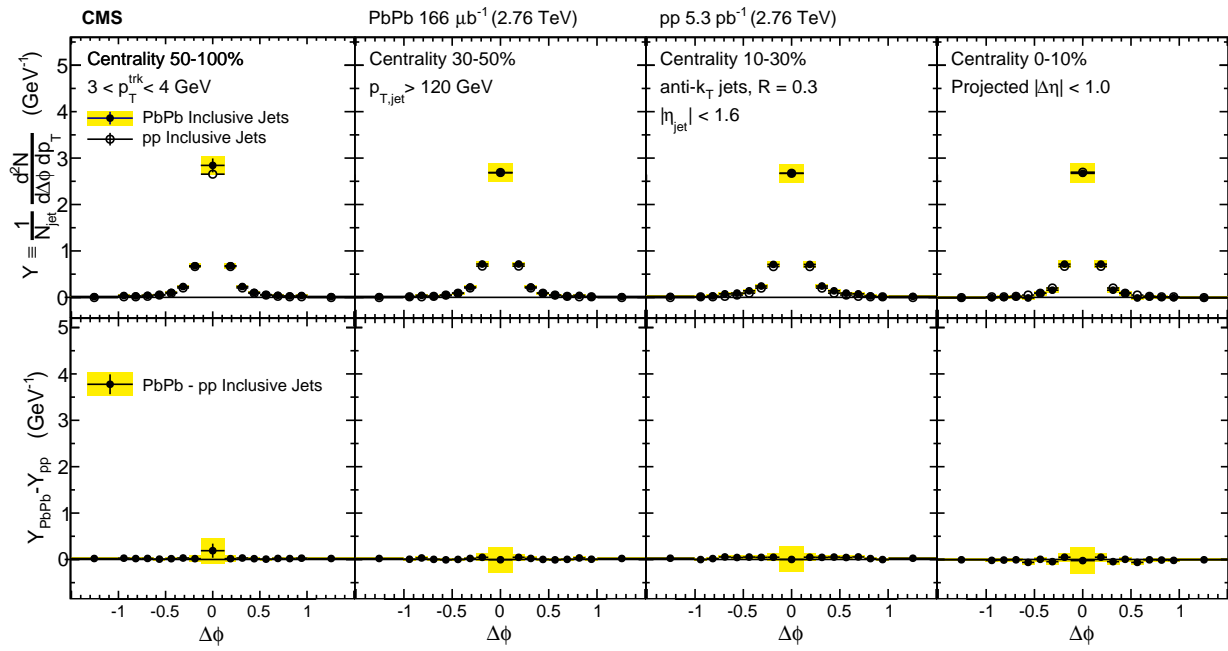


Figure 63. Symmetrized  $\Delta\phi$  distributions (projected over  $|\Delta\eta| < 1$ ) of background-subtracted particle yields correlated to PbPb and pp inclusive jets with  $p_T > 120 \text{ GeV}$  are shown in the top panels for tracks with  $3 < p_T^{\text{trk}} < 4 \text{ GeV}$ . The difference in PbPb and pp per-jet yields is shown in the bottom panels. The total systematic uncertainties are shown as shaded boxes, and statistical uncertainties are shown as vertical bars (often smaller than the symbol size).

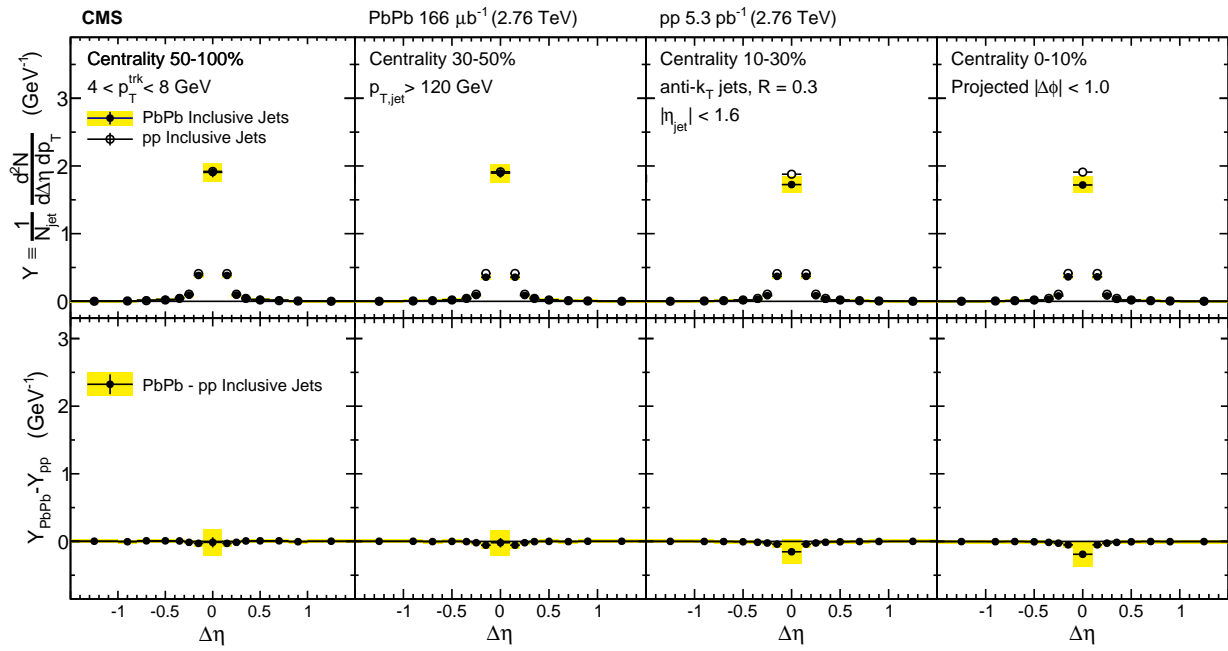


Figure 64. Symmetrized  $\Delta\eta$  distributions (projected over  $|\Delta\phi| < 1$ ) of background-subtracted particle yields correlated to PbPb and pp inclusive jets with  $p_T > 120 \text{ GeV}$  are shown in the top panels for tracks with  $4 < p_T^{\text{trk}} < 8 \text{ GeV}$ . The difference in PbPb and pp per-jet yields is shown in the bottom panels. The total systematic uncertainties are shown as shaded boxes, and statistical uncertainties are shown as vertical bars (often smaller than the symbol size).

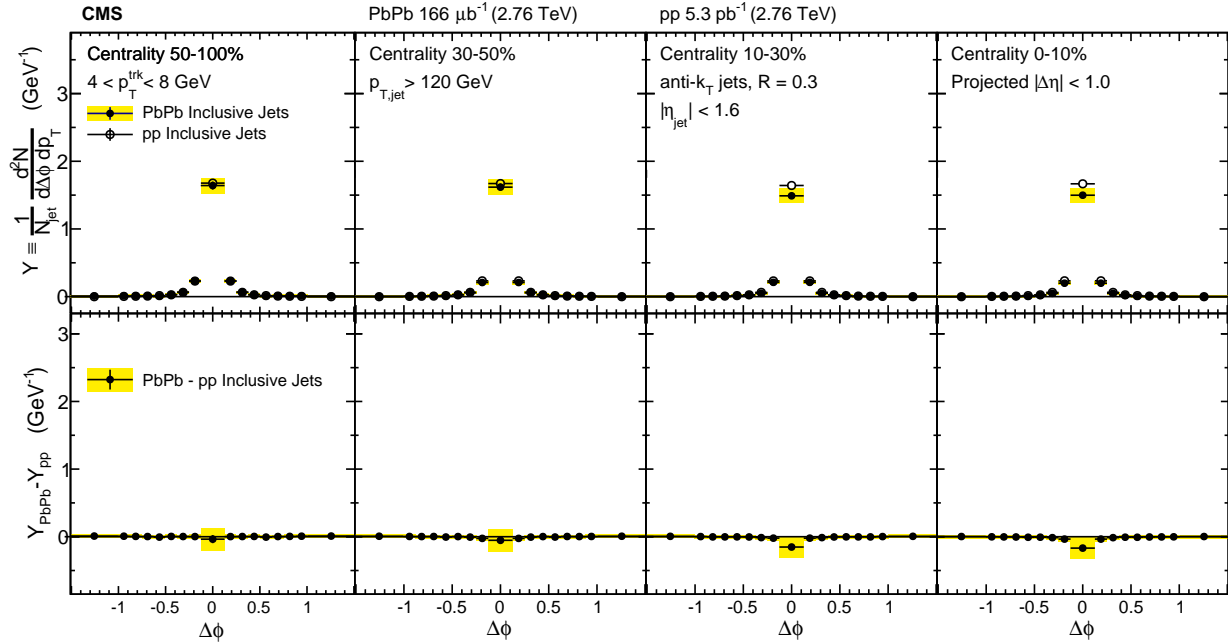


Figure 65. Symmetrized  $\Delta\phi$  distributions (projected over  $|\Delta\eta| < 1$ ) of background-subtracted particle yields correlated to PbPb and pp inclusive jets with  $p_T > 120$  GeV are shown in the top panels for tracks with  $4 < p_T^{\text{trk}} < 8$  GeV. The difference in PbPb and pp per-jet yields is shown in the bottom panels. The total systematic uncertainties are shown as shaded boxes, and statistical uncertainties are shown as vertical bars (often smaller than the symbol size).

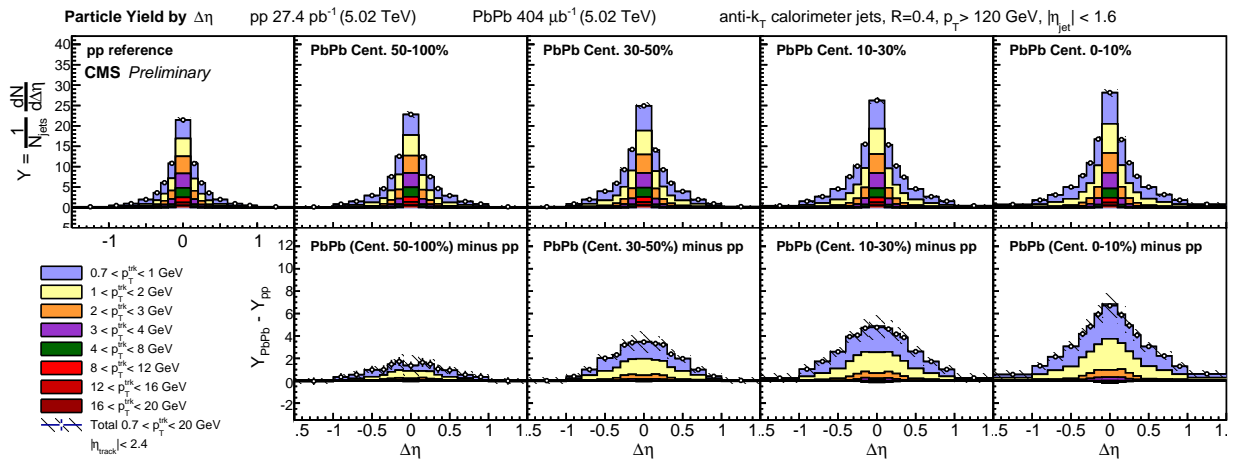


Figure 66. Top row: distributions of charged particle yields correlated to jets with  $p_T > 120$  GeV as a function of  $\Delta\eta$  (projected over  $|\Delta\phi| < 1$ ), shown differentially for all  $p_T^{\text{trk}}$  bins for pp, peripheral PbPb, and central PbPb data. Bottom row: PbPb minus pp difference in these distributions. Hatched lines on  $p_T^{\text{trk}}$ -inclusive points show total systematic uncertainties.

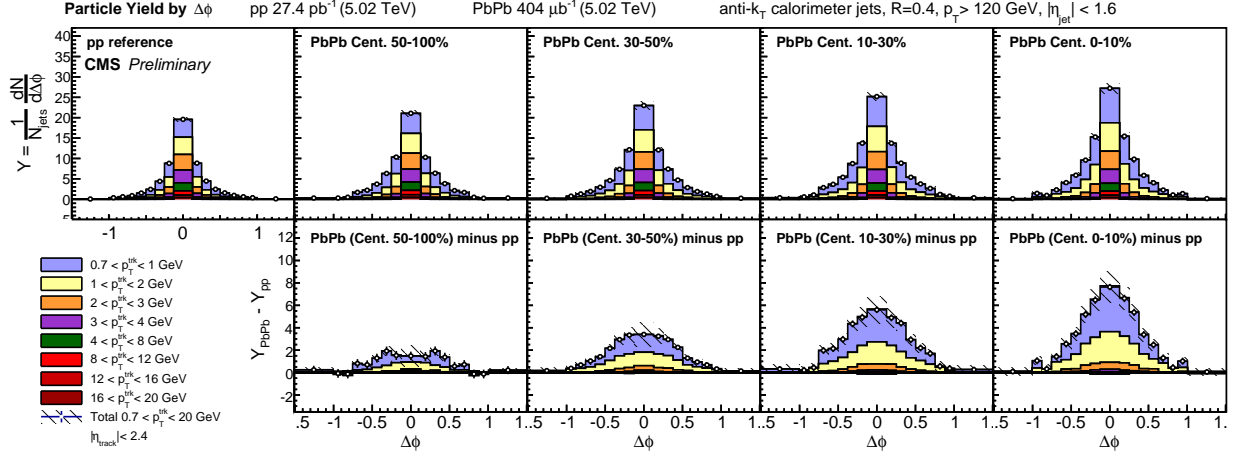


Figure 67. Top row: distributions of charged particle yields correlated to jets with  $p_T > 120$  GeV as a function of  $\Delta\phi$  (projected over  $|\Delta\eta| < 1$ ), shown differentially for all  $p_T^{\text{trk}}$  bins for pp, peripheral PbPb, and central PbPb data. Bottom row: PbPb minus pp difference in these distributions. Hatched lines on  $p_T^{\text{trk}}$ -inclusive points show total systematic uncertainties.

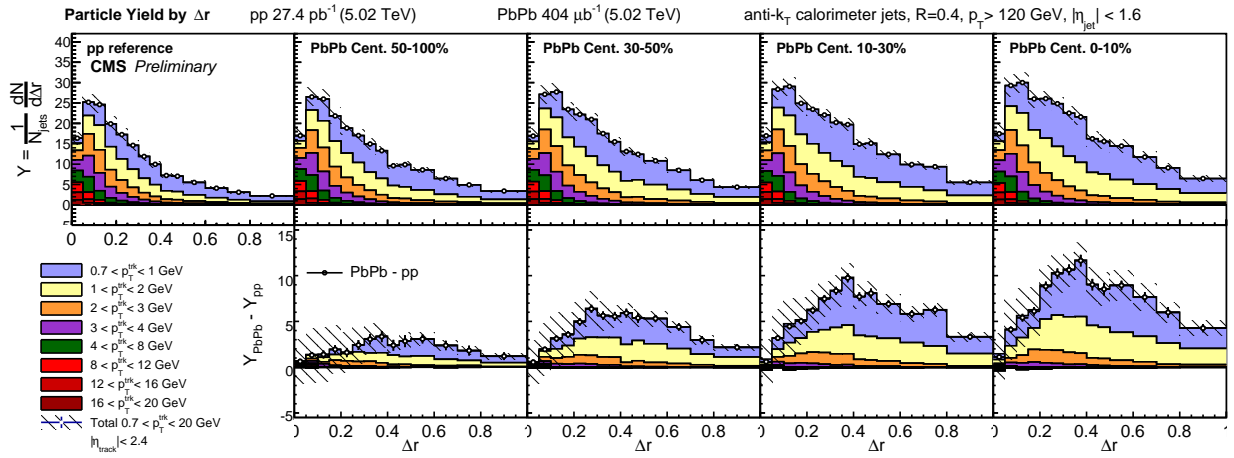


Figure 68. Top row: distributions of charged particle yields correlated to jets with  $p_T > 120$  GeV as a function of  $\Delta r$ , shown differentially for all  $p_T^{\text{trk}}$  bins. Bottom row: PbPb minus pp difference in these distributions. Hatched lines on  $p_T^{\text{trk}}$ -inclusive points show total systematic uncertainties.

To summarize the magnitude of the modifications to particle yields in PbPb relative to pp collisions, integrated yields as a function of  $p_T^{\text{trk}}$  are presented in the top panel of Fig. 69. The bottom panel of Fig. 69 shows differences PbPb–pp in total integrated particle yields in each  $p_T^{\text{trk}}$  class for results at 5.02 TeV compared to 2.76 TeV results. This quantifies the low- $p_T$  excess in central PbPb collisions to as many as 4 additional particles (in central PbPb relative to pp reference) per unit of  $p_T^{\text{trk}}$  in the lowest  $p_T^{\text{trk}}$  bin. This excess decreases smoothly with  $p_T^{\text{trk}}$  in each centrality bin, until the 4–8 GeV central PbPb bin is consistent with or slightly depleted relative to pp reference. For tracks with  $p_T^{\text{trk}} > 8$  GeV, there is no evident modification in PbPb compared to pp. Excess yields do not exhibit significant dependence on collision energies; particle yields at low- $p_T^{\text{trk}}$  are consistently larger at 5.02 TeV than at 2.76 TeV, but within the systematic uncertainties of the two measurements.

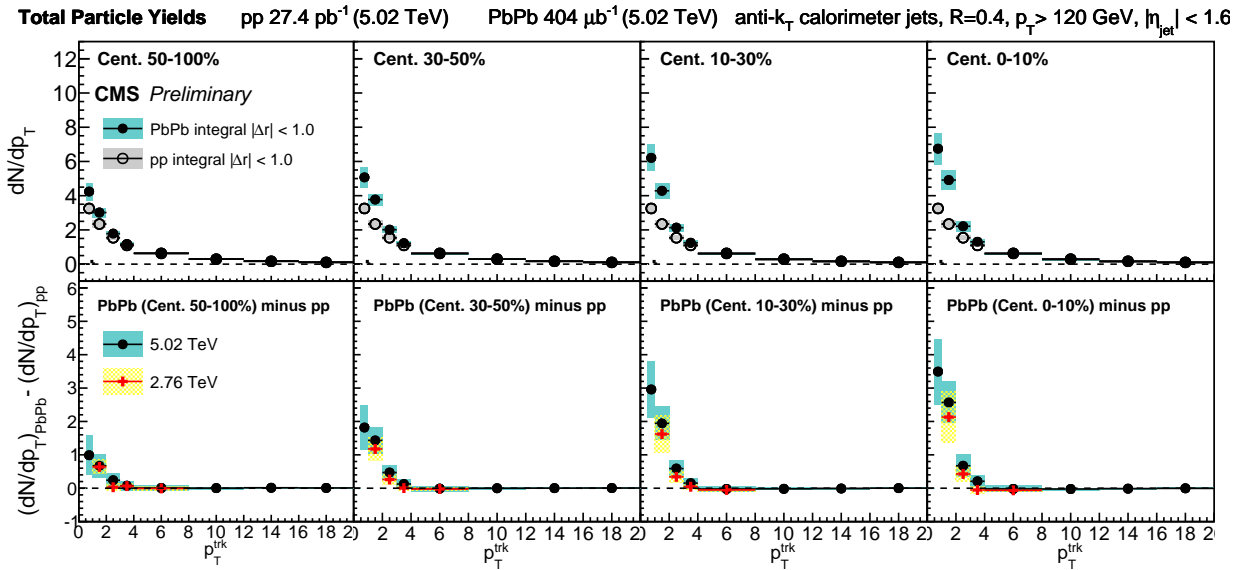


Figure 69. Top row: integrated yields of charged particle yields correlated to jets with  $p_T > 120$  GeV as a function of  $p_T^{\text{trk}}$  bins for PbPb data, compared to pp reference. Bottom row: integrated excess yield, PbPb minus pp. New measurements of excess yields at 5.02 TeV are compared to those measured at 2.76 TeV.

1546 **10.2 Dijet correlation results at 2.76 TeV**

1547 In the studies of charged-particle yields correlated to an inclusive sample of jets with  $p_T > 120$   
1548 GeV presented above, jet quenching is evident in the redistribution of  $p_T^{\text{trk}}$  from harder to softer  
1549 particles, and particularly in the observed centrality-dependent excess of low- $p_T^{\text{trk}}$  particle yields. Jet  
1550 quenching effects may be further probed by considering charged-particle yields correlated to each  
1551 jet axis in dijet events. Requiring events with two back-to-back jets (leading jet  $p_{T,1} > 120$  GeV,  
1552 subleading jet  $p_{T,2} > 50$  GeV,  $\Delta\phi_{1,2} > \frac{5\pi}{6}$ ), we construct separate correlations to the leading and  
1553 the subleading jet axes. In pp data, most dijets are balanced while in central PbPb a greater fraction  
1554 of dijet pairs are unbalanced (as discussed in Sec. 8.4), suggesting that central PbPb data contains  
1555 a significant fraction of dijet pairs in which the highest- and second-highest- $p_T$  hard-scattering  
1556 products had similar transverse momenta, but in which one jet experienced a greater path-length  
1557 through the medium and correspondingly greater quenching. This is expected to correspond to a  
1558 “surface-bias” toward leading jets with very short path-lengths through the medium, that might  
1559 be expected to cause minimal quenching in the leading jet sample. It is therefore interesting to  
1560 separately compare charged-particle distributions with respect to the leading and subleading jet  
1561 axes in PbPb and pp data to look for evidence of path-length dependence in jet quenching.

1562 Figures 70 and 71 show these correlation patterns in  $\Delta\eta$  and  $\Delta\phi$ , respectively, for the  
1563  $1 < p_T^{\text{trk}}$  GeV range in which the greatest quenching was evident in the 2.76 TeV inclusive jet  
1564 studies. As expected, quenching effects are greater for subleading than leading jets, as evident in  
1565 larger excesses of soft particles in subleading jet correlations (while retaining the same centrality  
1566 trends and gaussian-like distributions observed for the inclusive jet sample). However, leading jets  
1567 exhibit evidence of quenching as well, showing similar soft-particle excesses to those observed in  
1568 the inclusive sample. To quantitatively compare subleading and leading jet modifications to those  
1569 in the inclusive jet sample, Fig. 72 shows integrated particle yields for all three jet samples at 2.76  
1570 TeV. Here it is clear that leading jets show similar PbPb–pp modifications to those observed in the  
1571 inclusive sample, with approximately 2 excess particles in PbPb compared to pp data at lowest- $p_T^{\text{trk}}$ ,  
1572 while the subleading jet sample shows as many as 4 excess particles in PbPb compared to pp data  
1573 at lowest- $p_T^{\text{trk}}$ .

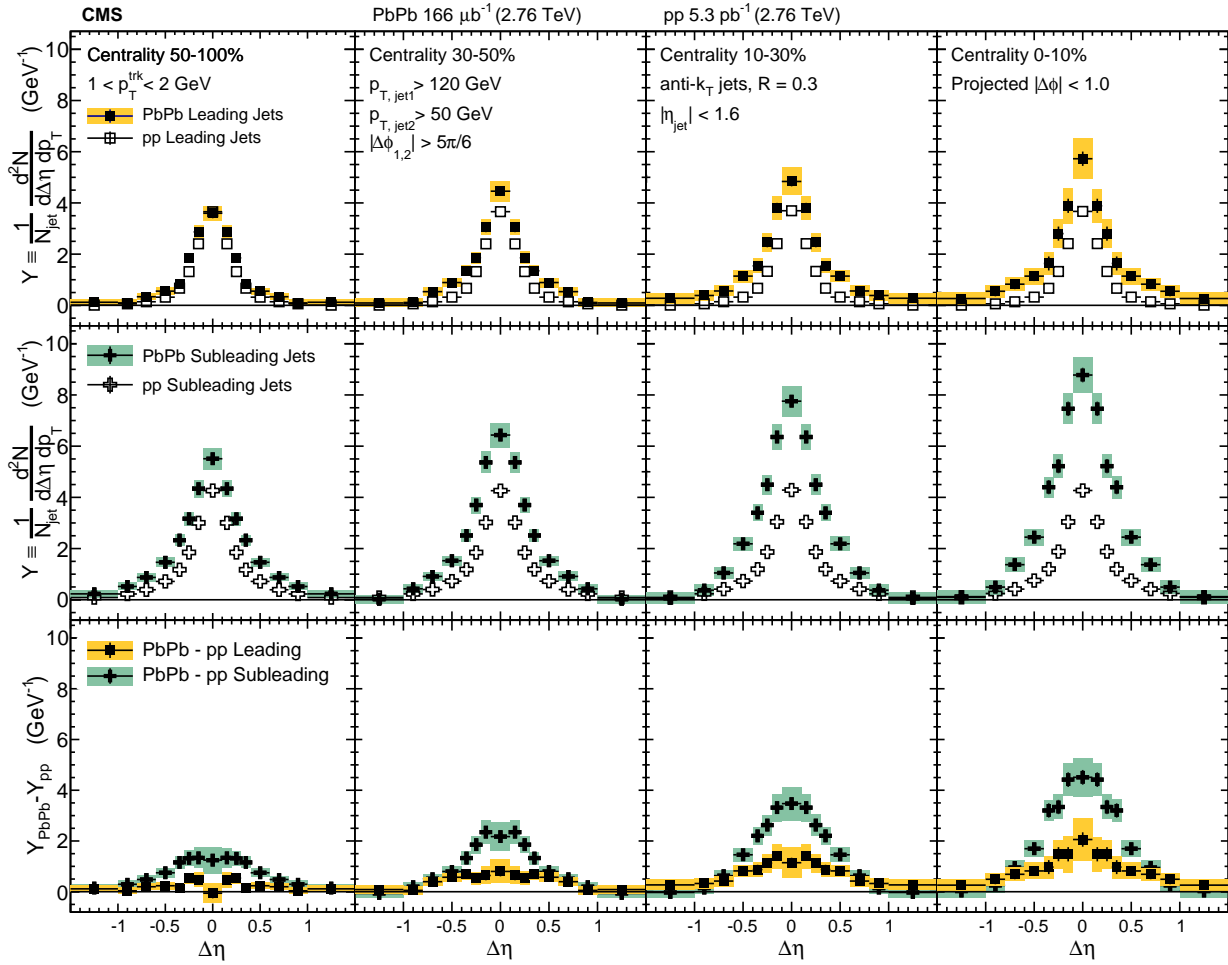


Figure 70. The top panels show the  $\Delta\eta$  distributions (projected over  $|\Delta\phi| < 1$ ) of charged-particle background-subtracted yields correlated to PbPb and pp leading jets with  $p_{T,\text{jet}1} > 120$  GeV. The middle panels show the same distributions for subleading jets with  $p_{T,\text{jet}2} > 50$  GeV, and the bottom panels show the difference PbPb minus pp for both leading and subleading jets. The total systematic uncertainties are shown as shaded boxes, and statistical uncertainties are shown as vertical bars (often smaller than the symbol size).

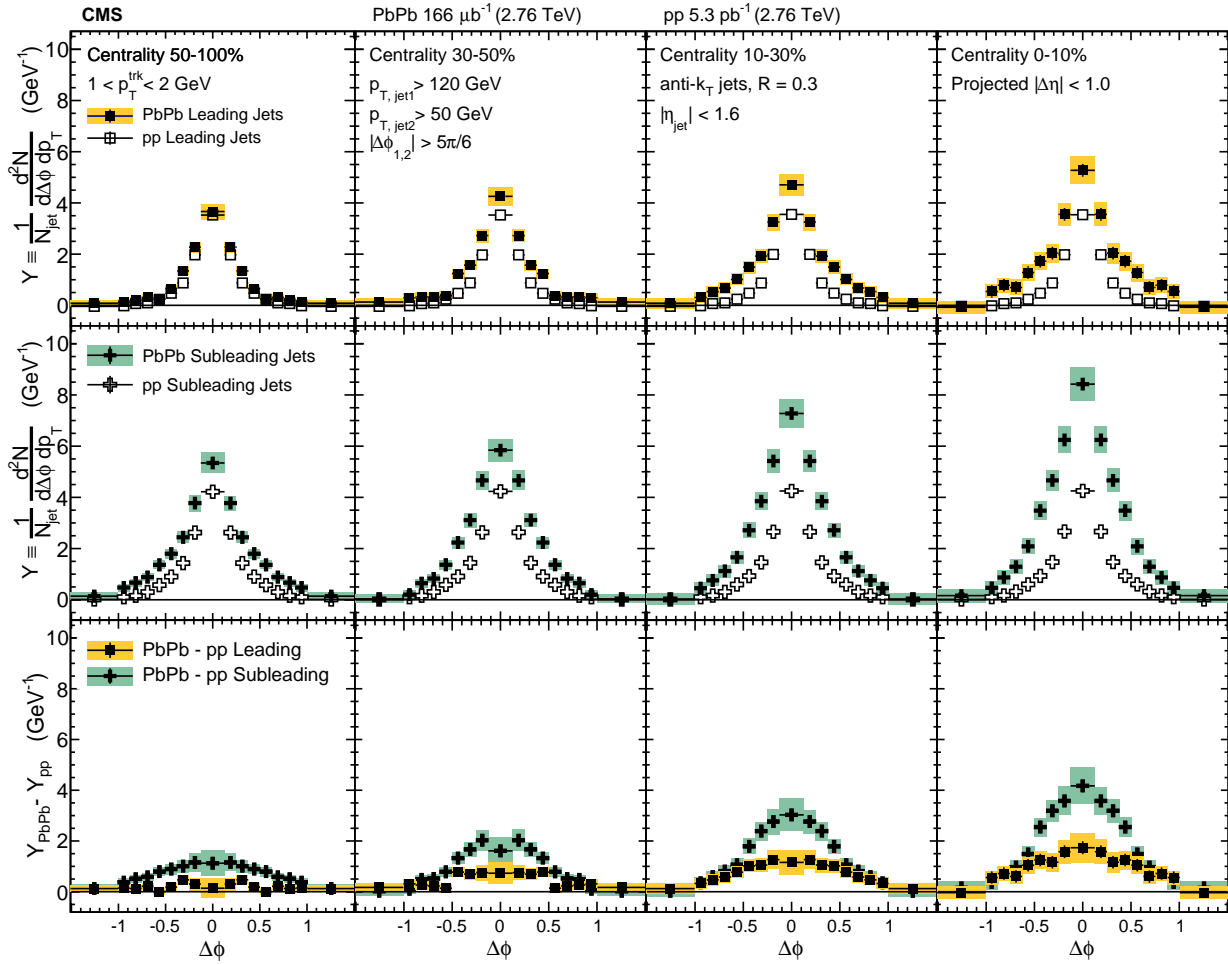


Figure 71. The top panels show the  $\Delta\phi$  distributions (projected over  $|\Delta\eta| < 1$ ) of charged-particle background-subtracted yields correlated to PbPb and pp leading jets with  $p_{T,\text{jet}1} > 120$  GeV. The middle panels show the same distributions for subleading jets with  $p_{T,\text{jet}2} > 50$  GeV, and the bottom panels show the difference PbPb minus pp for both leading and subleading jets. The total systematic uncertainties are shown as shaded boxes, and statistical uncertainties are shown as vertical bars (often smaller than the symbol size).

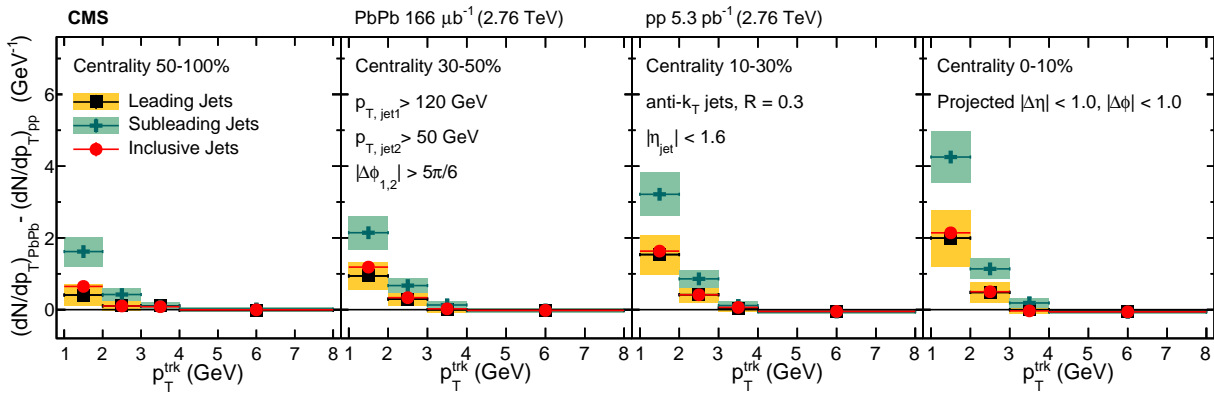


Figure 72. Total excess correlated yield observed in the PbPb data with respect to the reference measured in pp collisions, shown as a function of track  $p_T$  in four different centrality intervals (0–10%, 10–30%, 30–50%, 50–100%) for both leading jets with  $p_{T,\text{jet1}} > 120$  GeV and subleading jets with  $p_{T,\text{jet2}} > 50$  GeV. The total systematic uncertainties are shown as shaded boxes, and statistical uncertainties are shown as vertical bars (often smaller than the symbol size).

1574 In addition to characterizing the magnitude of jet quenching products (via the centrality-  
1575 dependent excess of low- $p_T^{trk}$  tracks greatest in correlations to subleading jets but also present in  
1576 leading jet correlations), modifications to charged-particle correlated yields may also be character-  
1577 ized by their widths. These studies are relevant to look for the presence and extent of jet peak  
1578 broadening due to medium interactions, and can be used to distinguish between different models  
1579 for jet-medium interaction and medium-modified jet radiation. In order to characterize correlation  
1580 widths, correlations are fit to double-gaussian functions (all  $\Delta\eta$  fits are shown in Appendix D for  
1581 illustration), and the width ( $\sigma$ ) of these fits is obtained as the range in  $|\Delta\eta|$  or  $|\Delta\phi|$  containing  
1582 67% of the total yield under the fit curve. To obtain systematic uncertainties on these fits, points  
1583 are varied up and down by their systematic uncertainties, and widths are re-calculated from these  
1584 varied distributions.

1585 Figures 73 and 74 show correlation widths in  $\Delta\eta$  and  $\Delta\phi$  for leading jets in PbPb and  
1586 pp data at 2.76 TeV. At low- $p_T^{trk}$  there is a significant broadening evident in central PbPb data  
1587 when compared to pp data, with this broadening decreasing in more peripheral collisions and with  
1588 increasing  $p_T^{trk}$  (with similar trends to those exhibited by correlated yield magnitudes). Widths  
1589 and width modifications are similar in  $\Delta\eta$  and  $\Delta\phi$ , but slightly broader in  $\Delta\phi$  for PbPb data.  
1590 These leading jet correlation widths and width modifications may also be compared to subleading  
1591 jet correlation widths and width modifications, shown in Figs. 75 and 76. In peripheral PbPb  
1592 data subleading and leading correlation widths are similar, but subleading jet PbPb correlation  
1593 widths exhibiting less centrality dependence than leading jet correlation widths so that leading jet  
1594 correlations in central PbPb data are slightly broader than subleading jet correlations (but  
1595 not significantly so, when taking into account the systematic uncertainties on both measurements).  
1596 Subleading jet peaks in pp data are, however, significantly broader than leading jet peaks in pp  
1597 data—as is to be expected since the kinematic selection defining subleading jet as that with lower- $p_T$ ,  
1598 also implies that subleading jets will on average have softer fragmentation than leading jets. Since  
1599 subleading pp jets are broader than leading pp jets while subleading and leading jets have similar  
1600 widths in PbPb, the jet peak broadening quantified as the PbPb–pp difference in widths is greater  
1601 for leading jets than for subleading jets.

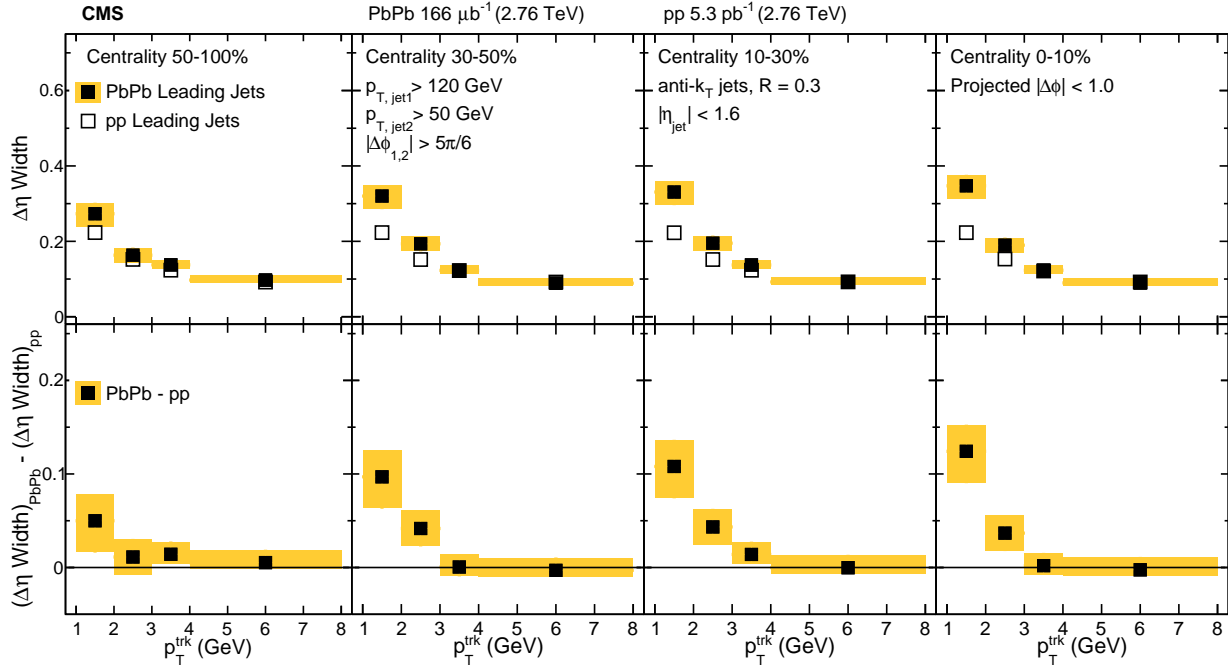


Figure 73. Comparison of the widths in PbPb and pp of the  $\Delta\eta$  charged-particle distributions correlated to leading jets with  $p_{T,\text{jet}1} > 120 \text{ GeV}$ , as a function of  $p_{T,\text{trk}}$ . The bottom row shows the difference of the widths in PbPb and pp data. The shaded band corresponds to systematic uncertainty, and statistical uncertainties are smaller than symbol size.

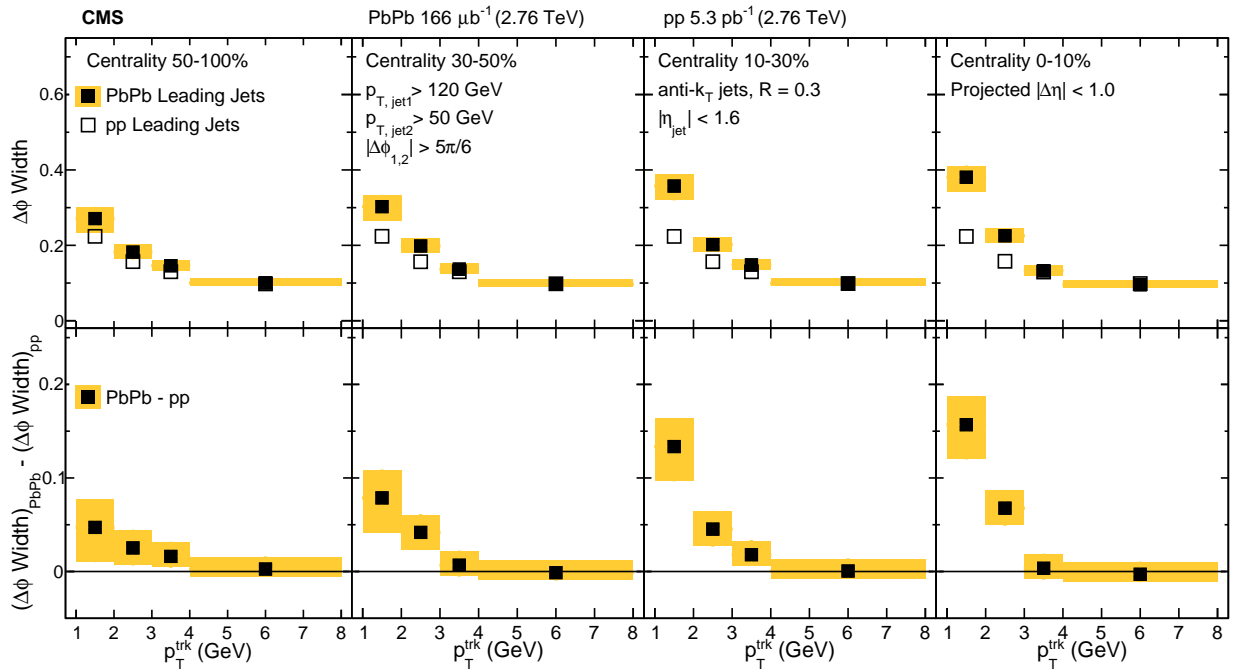


Figure 74. Comparison of the widths in PbPb and pp of the  $\Delta\phi$  charged-particle distributions correlated to leading jets with  $p_{T,\text{jet}1} > 120 \text{ GeV}$ , as a function of  $p_T^{\text{trk}}$ . The bottom row shows the difference of the widths in PbPb and pp data. The shaded band corresponds to systematic uncertainty, and statistical uncertainties are smaller than symbol size.

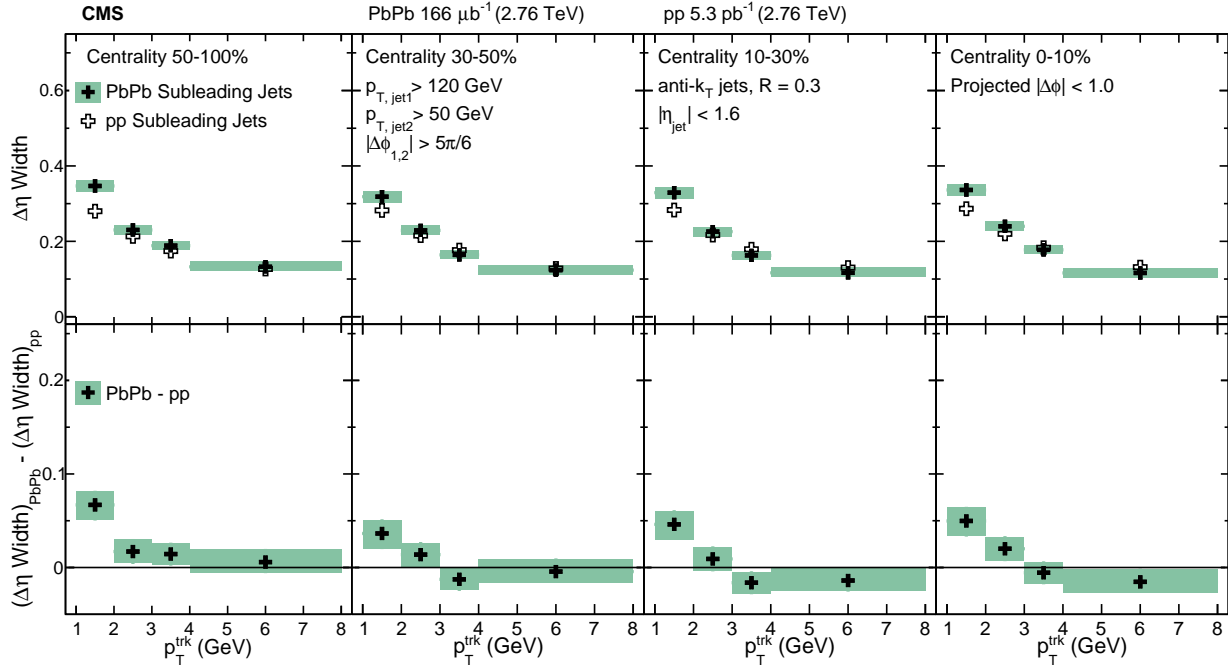


Figure 75. Comparison of the widths in PbPb and pp of the  $\Delta\eta$  charged-particle distributions correlated to leading jets with  $p_{T,\text{jet}2} > 50$  GeV, as a function of  $p_T^{\text{trk}}$ . The bottom row shows the difference of the widths in PbPb and pp data. The shaded band corresponds to systematic uncertainty, and statistical uncertainties are smaller than symbol size.

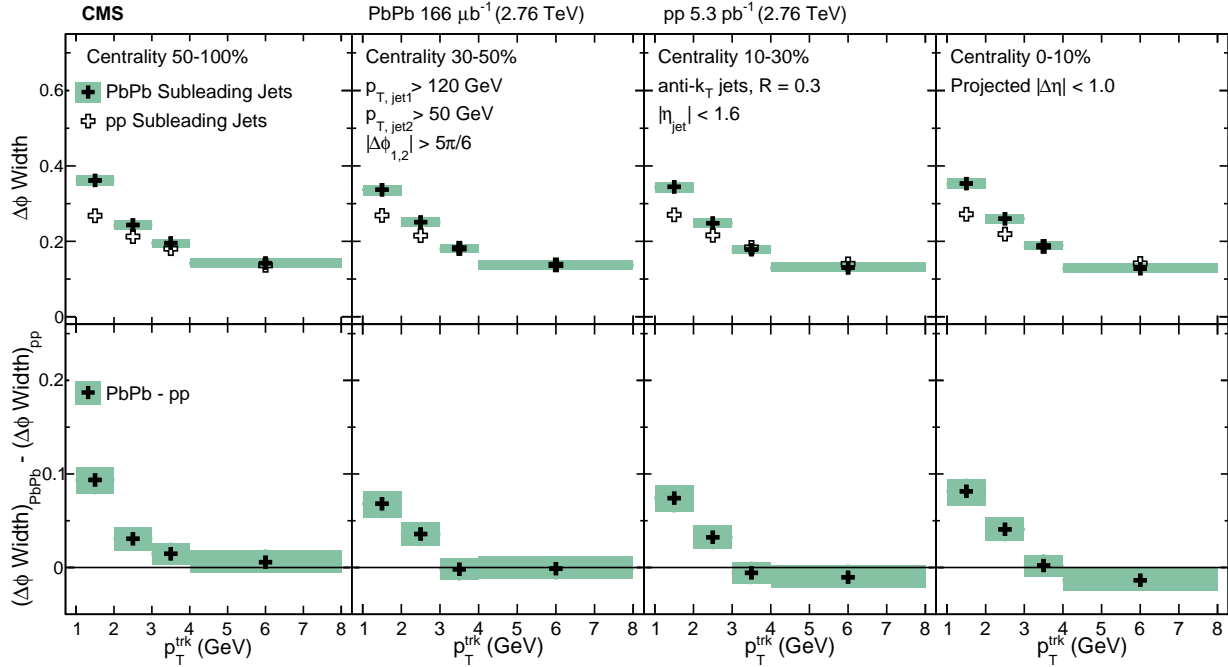


Figure 76. Comparison of the widths in PbPb and pp of the  $\Delta\phi$  charged-particle distributions correlated to leading jets with  $p_{T,\text{jet}2} > 50 \text{ GeV}$ , as a function of  $p_T^{\text{trk}}$ . The bottom row shows the difference of the widths in PbPb and pp data. The shaded band corresponds to systematic uncertainty, and statistical uncertainties are smaller than symbol size.

1602 **10.3 Jet shapes at 2.76 TeV and 5.02 TeV**

1603 A common observable to characterize and compare the widths of jet peaks is the jet shape  $\rho_{\Delta r}$ ,  
 1604 measuring the fraction of total jet transverse momentum as a function of distance  $\Delta r$  from the jet  
 1605 axis. As discussed in Sec. 4, previous CMS measurements of jet shape [31] have gained particular  
 1606 attention from the theoretical community in efforts to constrain models of jet energy loss. Jet shape  
 1607 measurements to large angles ( $\Delta r = 1$ , compared to previous measurements to only  $\Delta r = 0.3$ ) may  
 1608 be obtained from correlation studies, extending measurements to the full range of the jet peak  
 1609 and offering the capability of distinguishing between theoretical predictions based on earlier, more  
 1610 narrow, measurements.

1611 In the correlation technique, jet shapes are obtained by weighting correlations by  $p_T^{\text{trk}}$ , and  
 1612 integrating the resulting (background-subtracted) 2D jet-peak momentum distributions in annuli  
 1613 with radial width  $\Delta r = 0.05$ , where each has an inner radius of  $r_a = \Delta r - \delta r/2$  and an outer radius  
 1614 of  $r_b = \Delta r + \delta r/2$ . For this measurement, an inclusive high- $p_T^{\text{trk}}$  bin is included to capture particles  
 1615 with  $20 < p_T^{\text{trk}} < 300$  GeV. The resulting transverse momentum profile of the jet is defined as:

$$P(\Delta r) = \frac{1}{\delta r} \frac{1}{N_{\text{jets}}} \sum_{\text{jets}} \sum_{\text{tracks} \in (r_a, r_b)} p_T^{\text{trk}} \quad (28)$$

1616 This profile is then normalized to unity within  $\Delta r = 1$  to produce the jet shape  $\rho(\Delta r)$ :

$$\rho(\Delta r) = \frac{1}{\delta r} \frac{\sum_{\text{jets}} \sum_{\text{tracks} \in (r_a, r_b)} p_T^{\text{trk}}}{\sum_{\text{jets}} \sum_{\text{tracks}} p_T^{\text{trk}}} \quad (29)$$

1617 The top row of Fig. 77 presents the inclusive jet transverse momentum profile  $P(\Delta r)$  in pp  
 1618 and PbPb data at 5.02 TeV, while the middle row shows the jet shape  $\rho(\Delta r)$ , normalized to unity  
 1619 within  $\Delta r = 1$ . Here again redistribution of energy from small to large angles from the jet cone is  
 1620 evident in PbPb relative to pp reference, as seen in the dipping then rising trend in the jet shape  
 1621 ratio  $\rho(\Delta r)_{\text{PbPb}}/\rho(\Delta r)_{\text{pp}}$  presented in the bottom row.

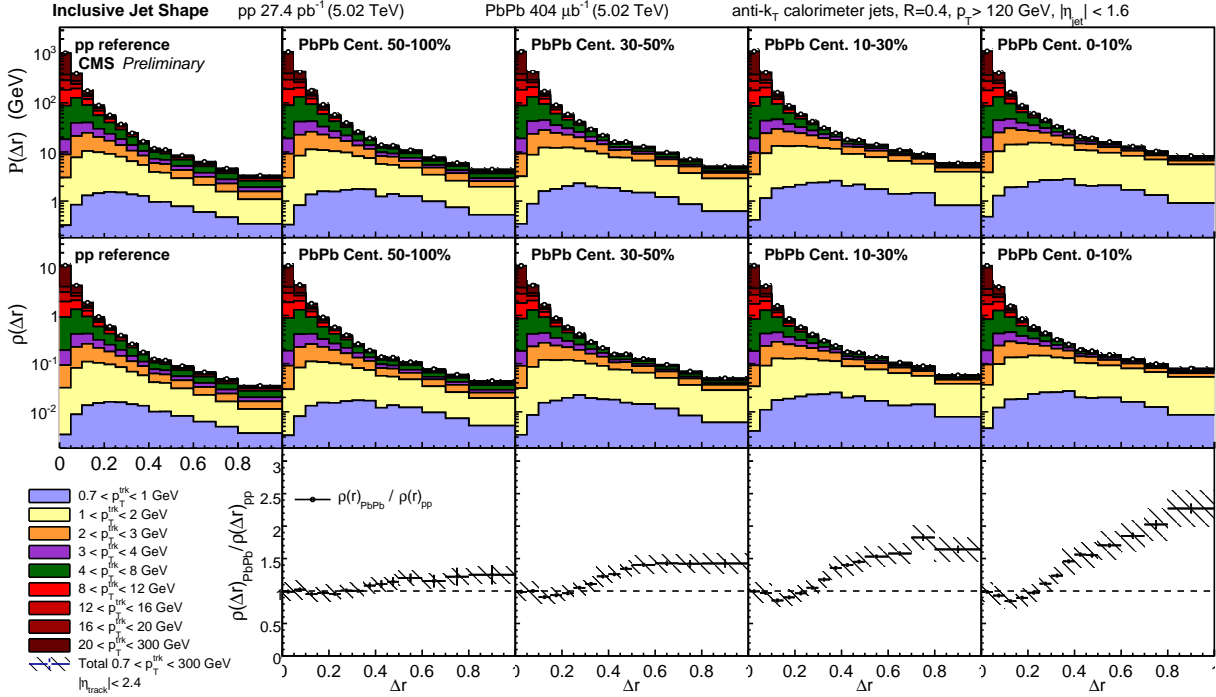


Figure 77. Top row: Transverse momentum profile of inclusive jets  $P(\Delta r)$  in pp and PbPb data at 5.02 TeV, shown differentially in  $p_T^{\text{trk}}$ . Middle row: jet shapes  $\rho(\Delta r)$  (normalized to unity over  $\Delta r < 1$ ) in PbPb and pp. Bottom row: jet shape ratio  $\rho(\Delta r)_{\text{PbPb}} / \rho(\Delta r)_{\text{pp}}$ . Hatched lines on  $p_T^{\text{trk}}$ -inclusive points show total systematic uncertainties.

In addition to studies of inclusive jet shapes, it is also interesting to consider the jet shapes and jet shape modifications of leading and subleading jets in dijet events. These studies are carried out with the same selection of 2.76 TeV dijet events used for the correlation studies presented in 10.2. In this case, for consistency with a previous CMS study measured the jet shape  $\rho(\Delta r)$  within the jet cone radius  $\Delta r = 0.3$  [31] at 2.76 TeV, these leading and subleading jet shape measurements at 2.76 TeV are normalized to integrate to unity with in the radius  $\Delta r < 0.3$ . In Fig. 78, the leading jet shape measured with this correlation technique is compared to the published CMS reference and extend this measurement to  $\Delta r = 1$ , noting that the leading jet shape is consistent within uncertainties with the previous measurement for an inclusive jet selection of all jets with  $p_T > 100 \text{ GeV}$ . A new measurement of subleading jet shape in Fig. 79 is then presented. As noted in the correlation width measurements discussed in Sec. 10.2, subleading jets in pp data are broader than leading jets in pp data. Therefore, although the PbPb-to-pp *modifications* are similar for leading and subleading jets, the more steeply falling pp leading jet shape results in a greater *relative*

1635 modification shown in the jet shape ratio  $\rho_{\text{PbPb}}(\Delta r)/\rho_{\text{pp}}(\Delta r)$  for leading than for subleading jets.  
 1636 Similarly, when comparing jet shape measurements at 2.76 TeV to those at 5.02 TeV, it is relevant  
 1637 to note that the pp reference is broader at 5.02 TeV than at 2.76 TeV, likely due to the greater  
 1638 fraction of gluon versus quark jets that pass the kinematic selections of the analysis at the higher  
 1639 center-of-mass energy.

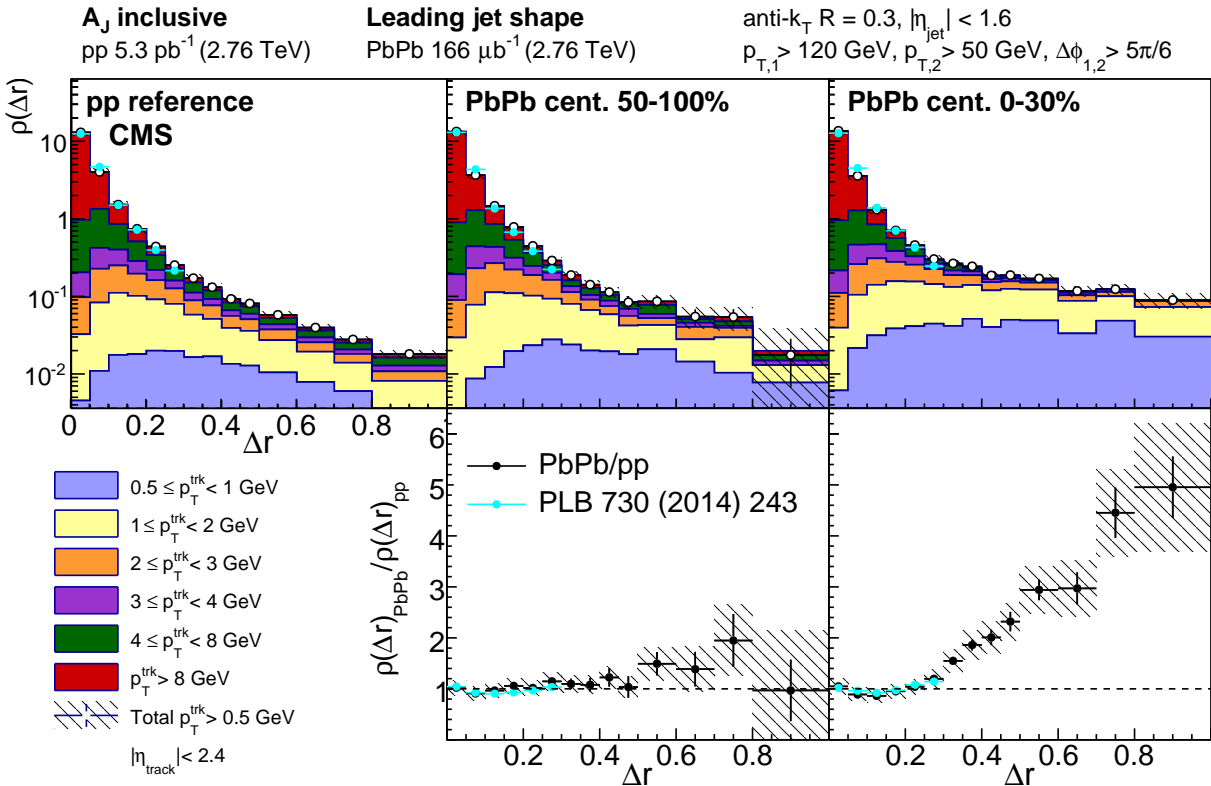


Figure 78. Top row: leading jet shape  $\rho(\Delta r)$  for pp reference and central and peripheral PbPb data, shown for all tracks with  $p_{T}^{\text{trk}} > 0.5 \text{ GeV}$  and decomposed by track transverse momentum. Shapes are normalized to unity over the region  $r < 0.3$  for consistency with the published reference shown (Ref. [31]). Bottom row: leading jet shape ratio  $\rho(\Delta r)_{\text{PbPb}}/\rho(\Delta r)_{\text{pp}}$ , again with published reference.

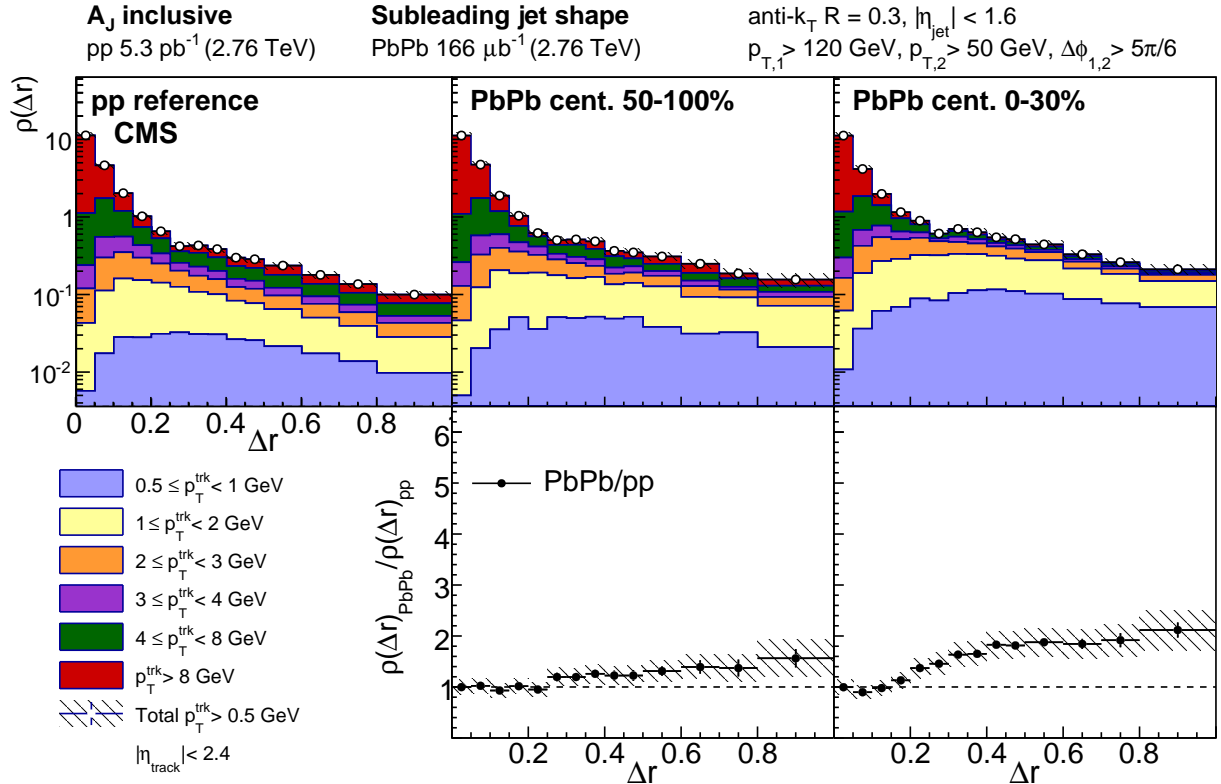


Figure 79. Top row: subleading jet shape  $\rho(\Delta r)$  for pp reference and central and peripheral PbPb data, shown for all tracks with  $p_T > 0.5$  GeV and decomposed by track transverse momentum, normalized to unity over the region  $\Delta r < 0.3$ . Bottom row: subleading jet shape ratio  $\rho(\Delta r)_{\text{PbPb}} / \rho(\Delta r)_{\text{pp}}$ .

1640 **10.4 Decomposition of hemisphere momentum balance in dijet events at 2.76 TeV**

1641 The dijet results at 2.76 TeV presented in this analysis are complimented by other CMS measure-  
1642 ments conducted on the same data using the “missing- $p_T$ ” hemisphere momentum balance method  
1643 presented in Ref. [36] and discussed in Secs. 3 and 4. In this analysis, a “dijet” axis is constructed  
1644 by averaging the leading jet and subleading jet axes (these are separated by  $\Delta\phi_{1,2} = \pi$  on average,  
1645 but are not necessarily parallel in each event due to 3-jet events) to construct a dijet axis, dividing  
1646 the event into leading and subleading hemispheres with respect to this axis, and comparing the  
1647 hemisphere-wide distributions of  $p_T^{\text{trk}}$  (projected, in this case, onto the combined dijet axis) to ob-  
1648 tain the subleading-to-leading balancing distribution as a function of distance from the dijet axis  
1649  $\Delta r$ . The jet track correlation technique may be used to obtain this same measurement (comparing  
1650 subleading-to-leading distributions on average rather than event-by-event, and making use of the  
1651 fact that the subleading and leading jet axes are *on average* perfectly back-to-back). When this  
1652 cross-check is performed *without background subtraction*, the two techniques yield consistent results,  
1653 despite methodological differences and differences in jet- $\eta$  cuts. This hemisphere-wide missing- $p_T$   
1654 technique is also used to extract differences in total particle yields between the leading and sublead-  
1655 ing hemispheres, and shows an average excess of 4–5 particles with  $p_T^{\text{trk}}$  in the subleading hemisphere  
1656 compared to the leading hemisphere [36]. In the dijet correlation studies presented in this analysis  
1657 *with background subtraction*, however, only approximately 2 additional particles were found cor-  
1658 related to the subleading jet peak compared to the leading jet peak, as shown in Sec. 10.2. This  
1659 apparent difference motivates a detailed examination and decomposition of the distribution of  $p_T^{\text{trk}}$   
1660 in dijet events in order to consider contributions to the hemisphere-wide momentum balance from  
1661 both the leading and subleading jet peaks, and from the long-range correlated underlying event.

1662 For this investigation, the dijet samples of 2.76 TeV PbPb and pp data are each divided  
1663 based on asymmetry parameter  $A_J$  to further illuminate quenching effects and to decompose the  
1664 contributions to the hemisphere  $p_T^{\text{trk}}$  balance studied in Ref. [36]: a balanced sample with  $A_J < 0.22$ ,  
1665 and an “unbalanced” sample with  $A_J > 0.22$ . Transverse momentum distributions for each sample  
1666 are constructed in  $\Delta\eta - \Delta\phi$  for each sample, and are corrected for pair-acceptance effects. Like all  
1667 particle density and  $p_T^{\text{trk}}$  correlations studied in this analysis, these show jet peaks on an underlying  
1668 event that shows significant  $\Delta\phi$  correlations but is flat in  $\Delta\eta$ . Correlations are therefore projected

1669 into  $\Delta\phi$  for further study in order to preserve this underlying event structure. Studies will begin  
1670 by considering the hemisphere-wide “missing- $p_T$ ” distribution as a function of  $\Delta\phi$ , and will then  
1671 decompose this distribution into jet peak and underlying event contributions, and finally consider  
1672 the relative contributions from jet peaks and from the underlying event to the overall hemisphere  
1673  $p_T^{\text{trk}}$  balance for balanced and unbalanced dijets.

1674 Figures 80 and 81 present the hemisphere-wide balancing distribution of transverse momen-  
1675 tum around the subleading versus the leading jet for balanced and unbalanced dijets respectively.  
1676 For both selections, a wide excess of soft particles in the subleading versus leading hemisphere in  
1677 central PbPb collisions relative to pp reference is evident, reflecting the greater quenching of the  
1678 subleading jet. In the unbalanced selection, as required by momentum conservation, the signal is  
1679 enhanced in both pp and PbPb data: in pp a large excess of particles with  $p_T > 3$  GeV long-range  
1680 is present on the subleading side, compensating for the lower momentum of the highest- $p_T$  particles  
1681 in the jet itself. In peripheral PbPb data the distribution is quite similar to pp reference, while  
1682 in central PbPb data this balancing distribution consists mostly of soft particles  $p_T < 3$  GeV,  
1683 consistent with the findings of a previous CMS study [36]. To better demonstrate these medium  
1684 modifications, the difference in yield between PbPb and pp collisions is shown in the bottom panels  
1685 of Fig. 80 and Fig. 81.

1686 To better understand the redistribution of transverse momentum within the QGP, the  
1687 distributions are then separated into three components as discussed above: the gaussian-like peaks  
1688 about the leading and subleading jet axes, plus a component accounting for overall subleading-  
1689 to-leading asymmetry in the  $\Delta\phi$ -correlated long-range underlying event (measured in the region  
1690  $1.5 < |\Delta\eta| < 2.5$ ). In Fig. 82 and Fig. 83, the jet peak components are shown for balanced and  
1691 unbalanced jets respectively, presenting subleading results positive and leading results negative (in  
1692 line with the hemisphere difference measurements in Fig. 81 and Fig. 80). Jet peak distributions  
1693 after decomposition are projected over the full range  $|\Delta\eta| < 2.5$ , again for consistency with the  
1694 hemisphere difference measurements. The top row of each panel first shows the overall distribution  
1695 of momentum carried by particles with  $p_T < 8$  GeV on about the jet peak. The middle two panels  
1696 then assess modifications to the subleading and leading jets, respectively. Here there is evidence  
1697 of quenching to both the subleading and the leading jet in central PbPb collisions relative to pp  
1698 reference, with an excess of low- $p_T^{\text{trk}}$  particles correlated to the jet axis in both the balanced and

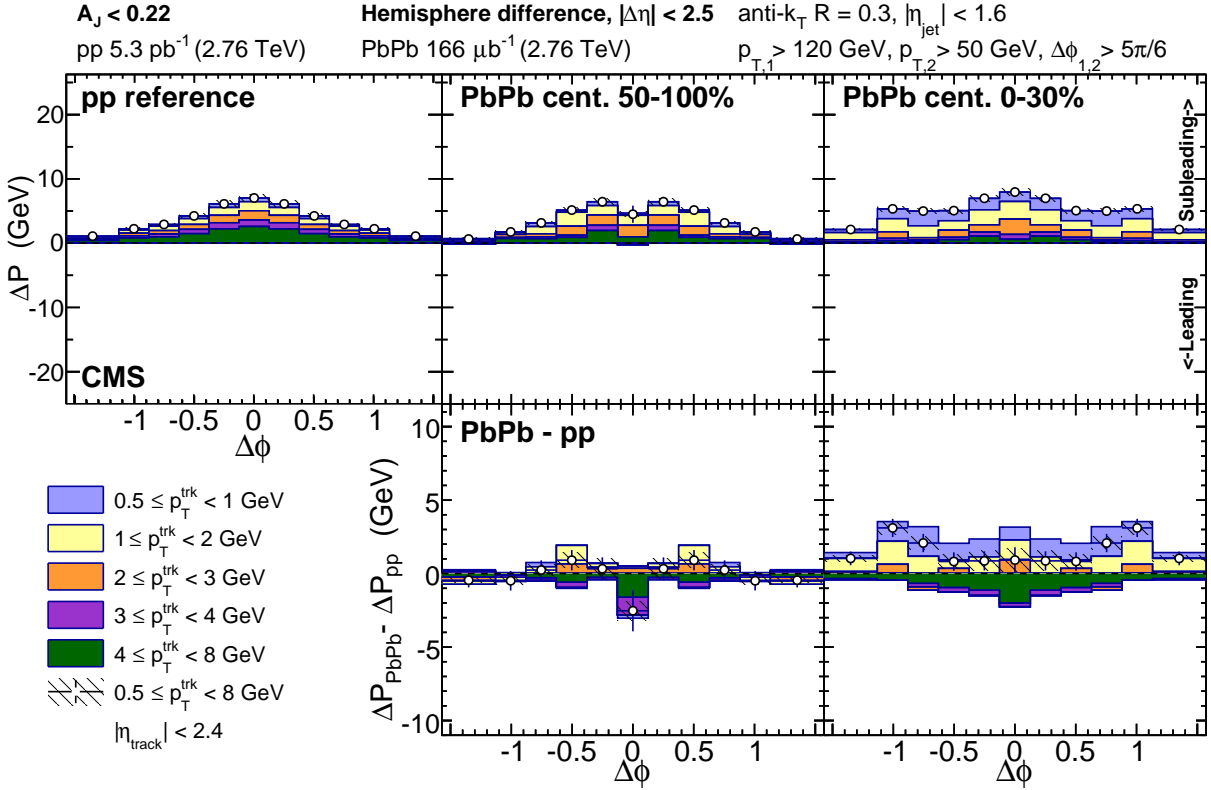


Figure 80. Top row: total hemisphere distribution in  $\Delta\phi$  of excess transverse momentum about the subleading relative to the leading jet for balanced dijets with  $A_J < 0.22$ , shown differentially by track transverse momentum for pp reference, peripheral PbPb, and central PbPb data. Bottom row: PbPb–pp difference in these  $\Delta\phi$  momentum distributions.

1699 unbalanced dijet selections, as observed in the charged particle density studies presented in Sec. 10.2.  
 1700 In unbalanced dijets this enhancement of soft- $p_T^{\text{trk}}$  particles turns into a depletion at higher- $p_T^{\text{trk}}$ , and  
 1701 is greater on the subleading than the leading side. To compare between hemispheres and assess the  
 1702 jet peak contribution to the overall hemisphere momentum balance, the double difference PbPb–pp,  
 1703 subleading–leading is presented in the bottom panel. Here it is evident that the low- $p_T^{\text{trk}}$  excess  
 1704 in central PbPb collisions is larger on the subleading than the leading side of the dijet system,  
 1705 but larger subleading-to-leading excess only accounts for only a portion of the total momentum  
 1706 redistribution in unbalanced dijet events.

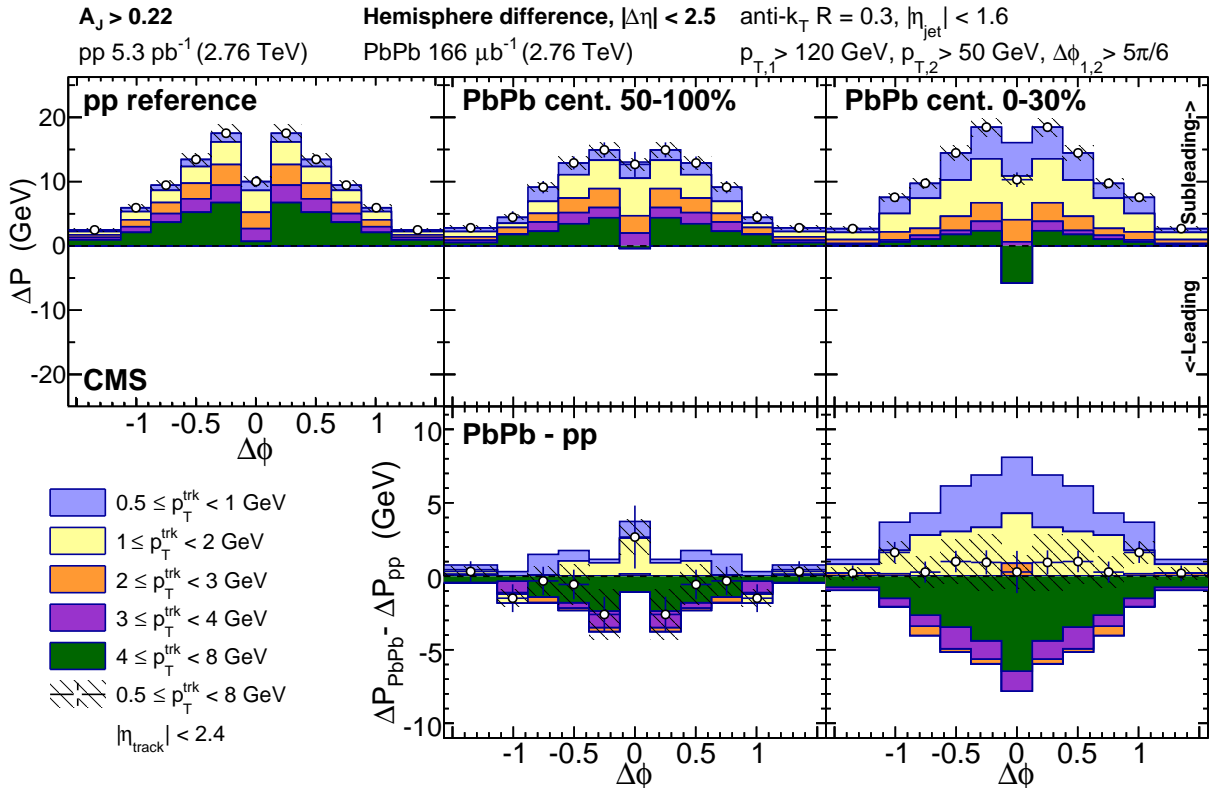


Figure 81. Top row: total hemisphere distribution in  $\Delta\phi$  of excess transverse momentum about the subleading relative to the leading jet for balanced dijets with  $A_J > 0.22$ , shown differentially by track transverse momentum for pp reference, peripheral PbPb, and central PbPb data. Bottom row: PbPb-pp difference in these  $\Delta\phi$  momentum distributions.

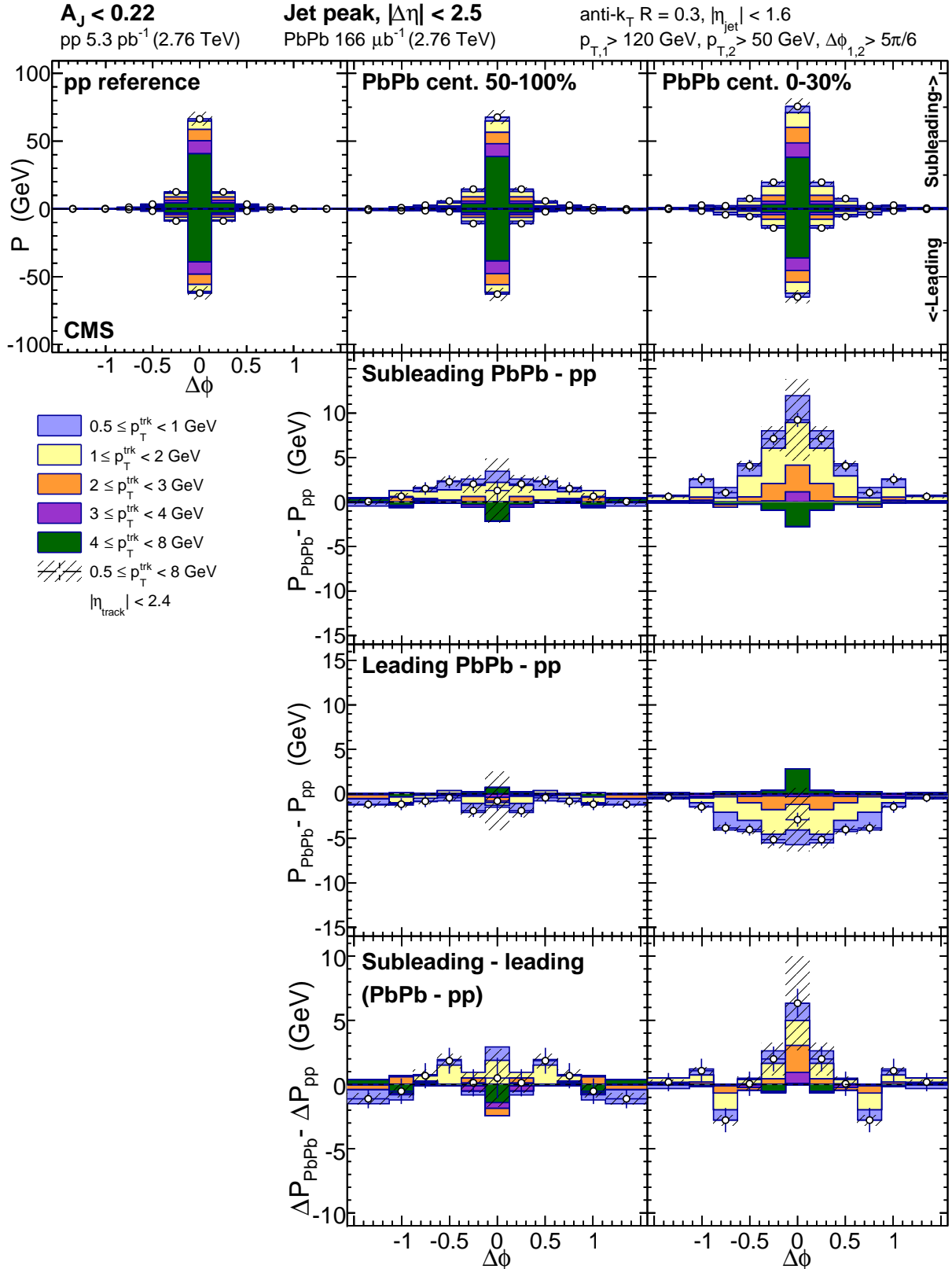


Figure 82. Top row: jet-peak (long-range subtracted) distribution in  $\Delta\phi$  of transverse momentum about the subleading (plotted positive) and leading (plotted negative) jets for balanced dijets with  $A_J < 0.22$ . Middle rows: PbPb–pp momentum distribution differences for subleading and leading jets. Bottom row: PbPb–pp, subleading–leading double difference in these  $\Delta\phi$  momentum distributions.

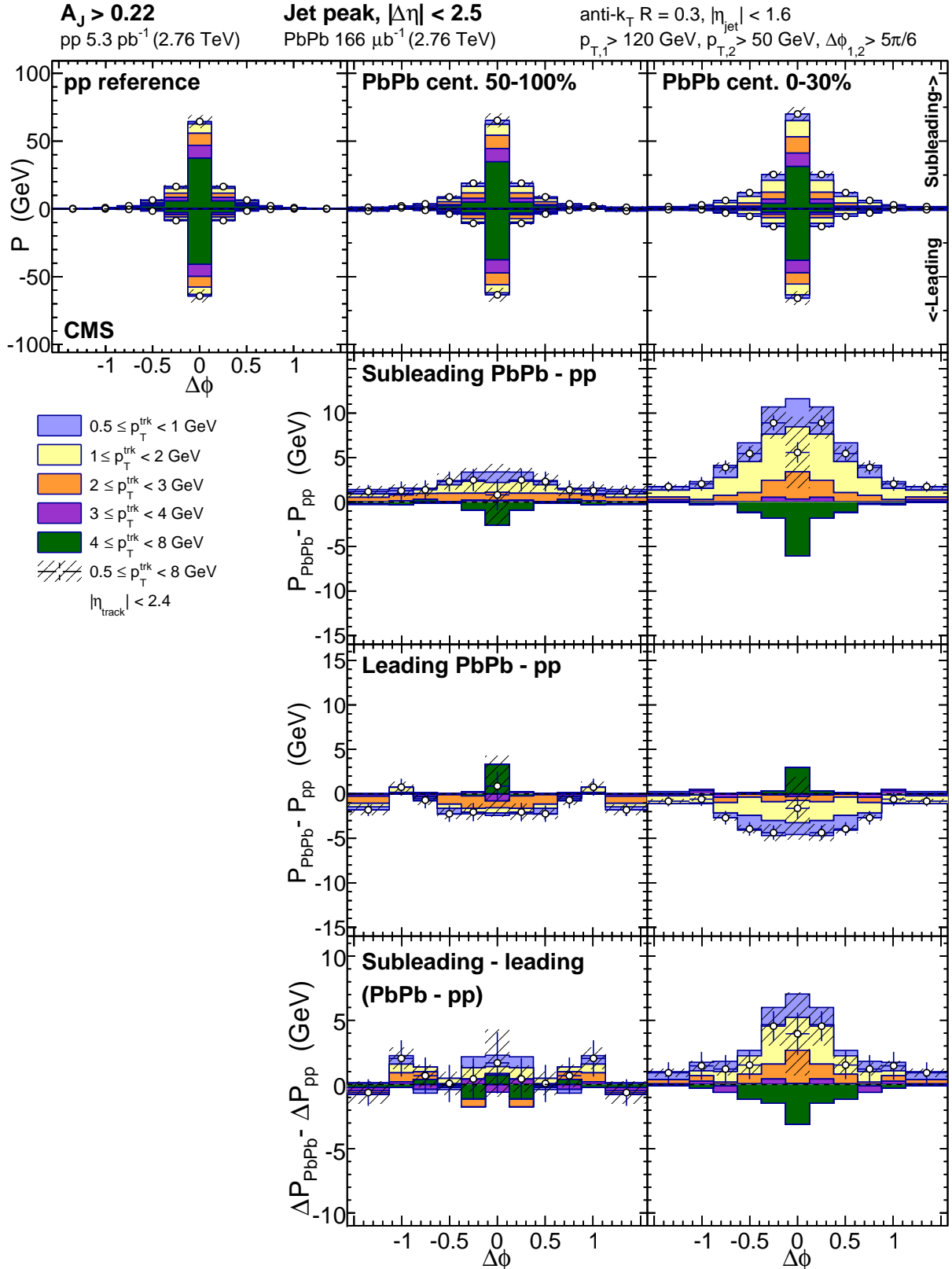


Figure 83. Top row: jet-peak (long-range subtracted) distribution in  $\Delta\phi$  of transverse momentum about the subleading (plotted positive) and leading (plotted negative) jets for balanced dijets with  $A_J > 0.22$ . Middle rows: PbPb-pp momentum distribution differences for subleading and leading jets. Bottom row: PbPb-pp, subleading-leading double difference in these  $\Delta\phi$  momentum distributions.

These jet-related studies are complemented by an analysis of the long-range subleading to leading asymmetry, presented in Fig. 84 and Fig. 85 for balanced and unbalanced jets respectively. The long-range correlated background in balanced dijet events is symmetric in pp and peripheral PbPb data, while in central PbPb data there is a small excess of low- $p_T^{\text{trk}}$  particles. In unbalanced dijets, however, there is significant asymmetry already in pp reference, with a large correlated excess of particles in all  $p_T$  classes less than 8 GeV on the subleading relative to leading side of the underlying event. This asymmetry reflects the presence of other hard-scattering products in the subleading hemisphere dijet event, as required by momentum conservation when selecting asymmetric dijets in vacuum-like collisions. In the presence of the strongly interacting medium; however, this underlying event asymmetry in asymmetric dijet events changes notably. In peripheral PbPb collisions there is already some depletion of momentum carried by high- $p_T^{\text{trk}}$  particles, and in central pp collisions subleading-to-leading underlying event excesses with  $p_T^{\text{trk}} > 2$  GeV vanish nearly completely. To assess the contribution of this long-range asymmetry to the total hemisphere imbalance, the double difference PbPb–pp, subleading–leading is plotted on the bottom panel as for (and on the same scale as) the double difference shown for the jet peaks. To assess the overall hemisphere momentum balance attributed to this long-range asymmetry, the hemisphere integral ( $|\Delta\phi| < \pi/2$  and  $|\Delta\eta| < 2.5$ ) is presented in Fig. 86 for balanced versus unbalanced dijets. For unbalanced dijets, the the overall asymmetry rises with track- $p_T$  pp reference, but falls with track- $p_T$  for central PbPb data.

Finally, to show the relative contributions to overall hemisphere momentum balance from the leading and subleading jet peaks as well as from the long-range underlying event asymmetry, a summary of hemisphere-integrated excess (PbPb–pp) yield for balanced and unbalanced dijets in central PbPb collisions is shown in Fig. 87 and Fig. 88 for central and peripheral collisions respectively. The top panels of Fig. 87 present total PbPb minus pp differences in transverse momentum associated with the subleading jet (plotted positive) and leading jet (plotted negative). Modifications to the distribution of tracks with  $p_T < 3$  GeV are evident for both the leading and subleading jet peaks, with a greater enhancement of low- $p_T^{\text{trk}}$  particles associated with the subleading jet. These total jet peak modifications in central PbPb collisions are not significantly different in unbalanced versus balanced dijets. The bottom panels of Fig. 87 present these jet-peak modifications together with the long-range modifications evident in Fig. 86 to show the decomposed

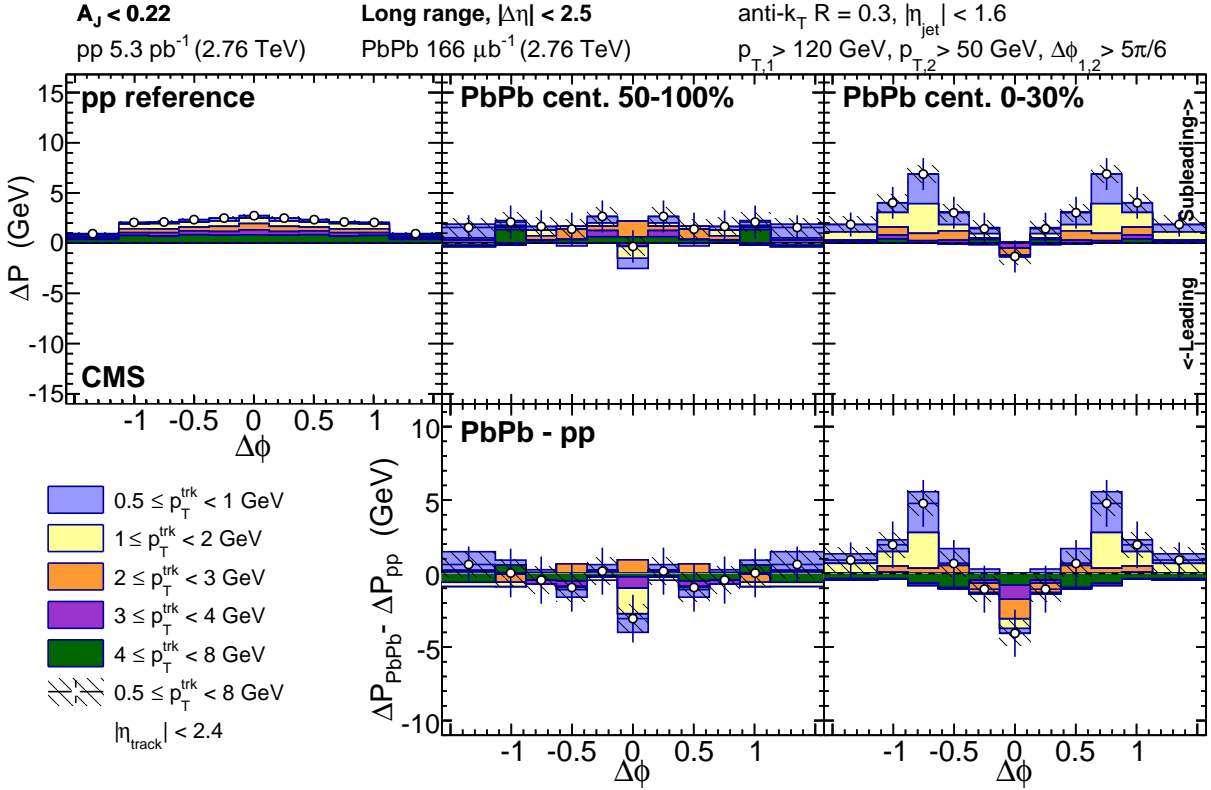


Figure 84. Top row: long-range distribution in  $\Delta\phi$  of excess transverse momentum in the subleading relative to leading sides for balanced dijets with  $A_J < 0.22$ . Bottom row: PbPb–pp difference in these  $\Delta\phi$  long-range momentum distributions.

hemisphere-wide differences in associated transverse momentum in each  $p_T^{\text{trk}}$  range. Unlike the jet peak contributions, the long-range PbPb versus modifications differ outside of uncertainties between balanced and unbalanced dijets: here the depletion of high- $p_T^{\text{trk}}$  particles in unbalanced PbPb versus pp dijets corresponds to the reduced contribution from third jets (which are prominently evident in the long-range distribution for pp unbalanced dijet events) in central PbPb unbalanced dijet events. Figure 88 presents the same hemisphere-integrated PbPb minus pp excess information for peripheral collisions for comparison to the central results shown in Fig. 87. Some possible small modifications are already evident in this 50-100% centrality range, but these differences between peripheral PbPb and pp results are in most cases smaller than systematic uncertainties.

The decomposition of integrated jet peak and long-range correlated  $p_T^{\text{trk}}$  shown in Fig. 87 and Fig. 88 clarify the relationship between the jet peak correlation studies presented in this analysis and the missing- $p_T$  measurements presented in Ref. [36]: as shown through this detailed decomposi-

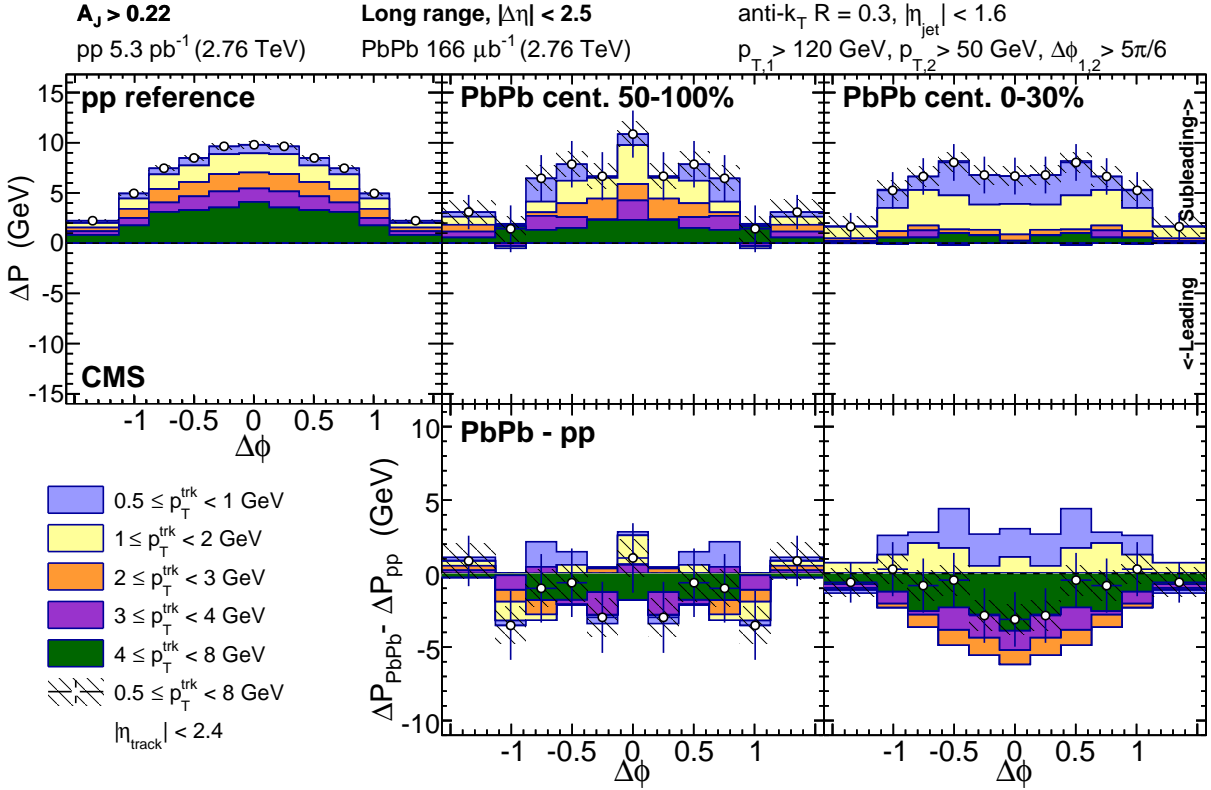


Figure 85. Top row: long-range distribution in  $\Delta\phi$  of excess transverse momentum in the subleading relative to leading sides for balanced dijets with  $A_J > 0.22$ . Bottom row: PbPb–pp difference in these  $\Delta\phi$  long-range momentum distributions.

1749 tion, comparing hemisphere distributions as a whole include contributions from the subleading and  
 1750 leading jet peaks studied in correlation studies, but also a contribution from the underlying event.  
 1751 In both PbPb and pp data, the underlying event partially cancels with hemisphere subtraction:  
 1752 contributions from combinatoric background and even flow harmonics ( $V_2$  etc.) will cancel, while  
 1753 contributions from 3rd jets and odd flow harmonics ( $V_1, V_3$  etc.) will not. As we have seen, in  
 1754 pp the non-cancelling underlying event is dominated by 3rd jets, especially in the unbalanced dijet  
 1755 selection in which their presence is kinematically required. In PbPb (where the contribution from  
 1756 3rd jet events is smaller), this underlying event has evident contributions from odd flow harmonics  
 1757 as well, reflecting coupling of jets to the event reaction plane.

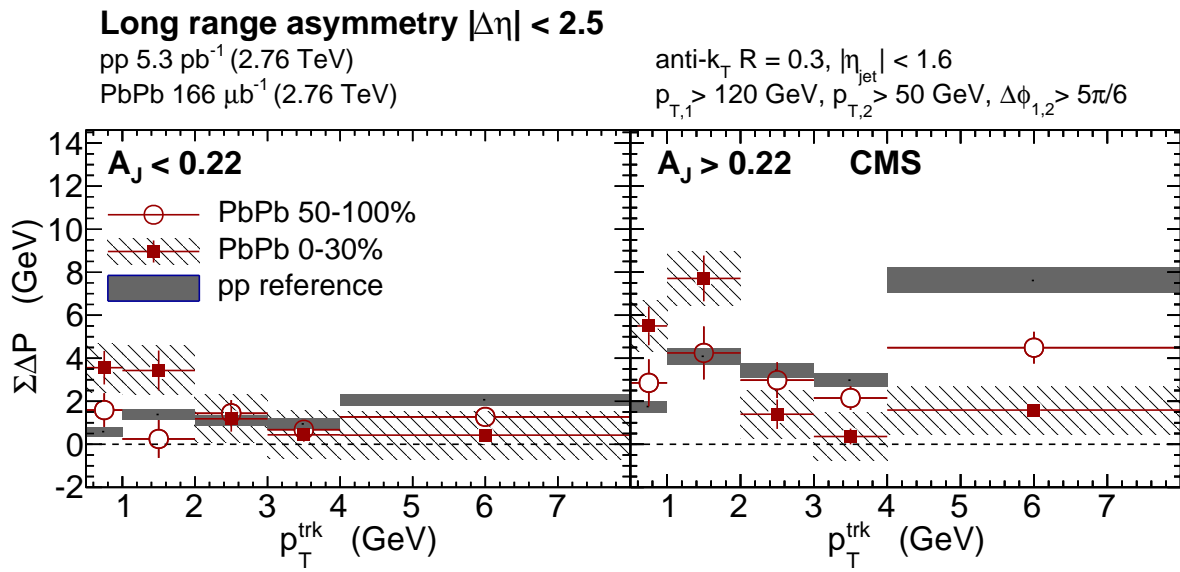


Figure 86. Integrated transverse momentum in the long-range  $\Delta\phi$ -correlated distribution as a function of track- $p_T$  integrated over  $|\Delta\phi| < \pi/2$  and  $|\Delta\eta| < 2.5$  and for pp reference, peripheral PbPb and central PbPb data for balanced compared to unbalanced dijets.

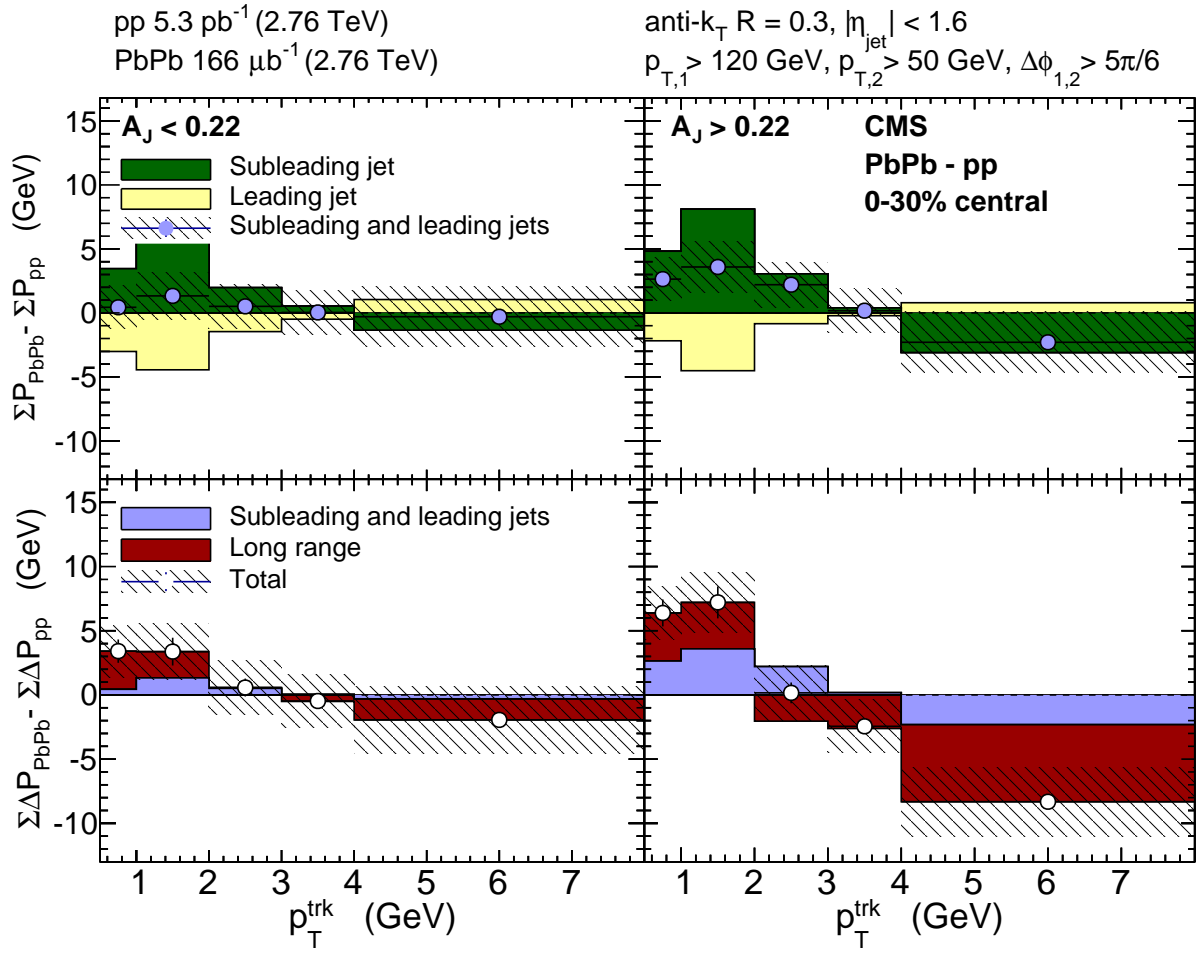


Figure 87. Modifications of jet-hadron correlated transverse momentum in central PbPb collisions with respect to pp reference, integrated  $|\Delta\phi| < \pi/2$ ,  $|\Delta\phi| < 2.5$ . Top row: subleading and leading jet peak PbPb-pp. Bottom row: relative contributions from jet peaks and long-range asymmetry to the double difference PbPb-pp, subleading-leading in total hemisphere transverse momentum.

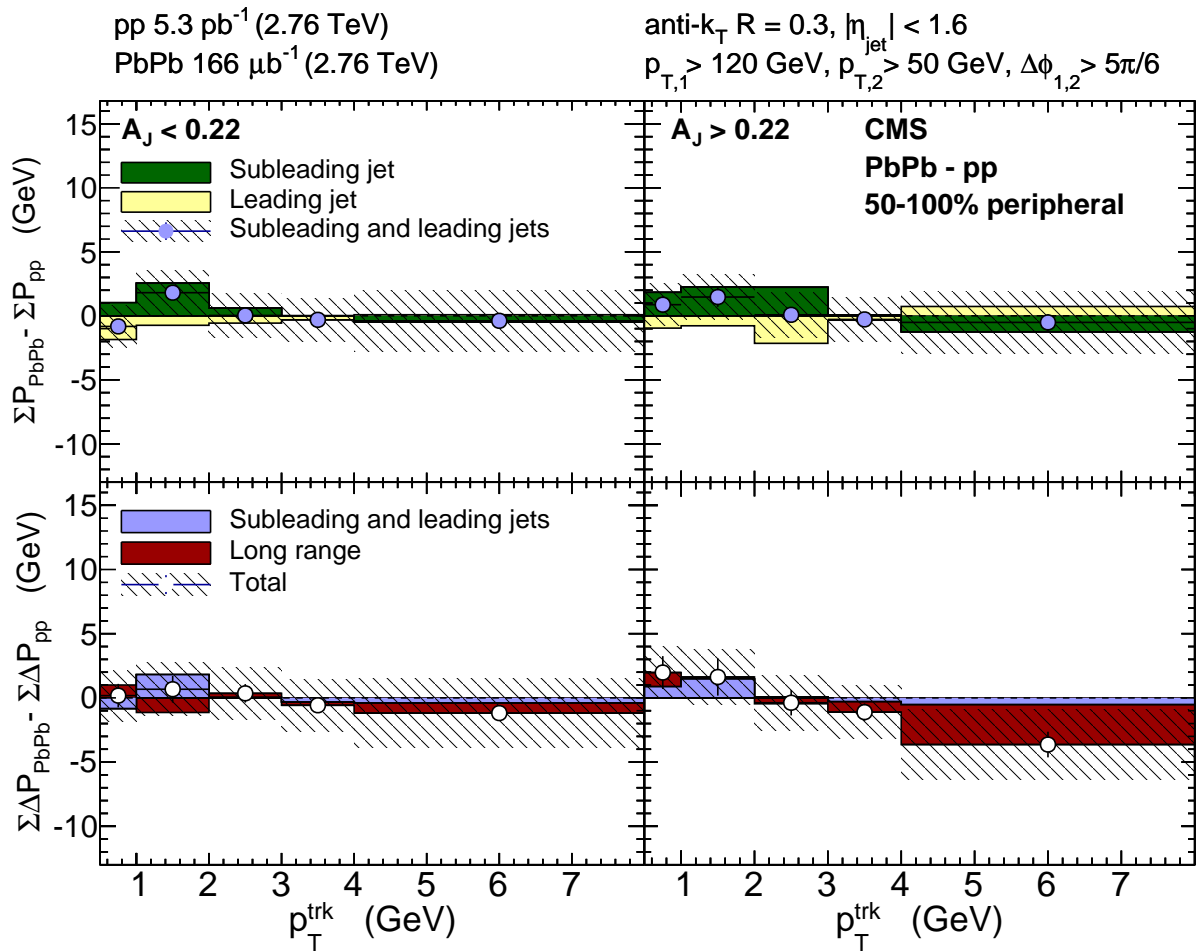


Figure 88. Modifications of jet-hadron correlated transverse momentum in peripheral PbPb collisions with respect to pp reference, integrated  $|\Delta\phi| < \pi/2$ ,  $|\Delta\phi| < 2.5$ . Top row: subleading and leading jet peak PbPb-pp. Bottom row: relative contributions from jet peaks and long-range asymmetry to the double difference PbPb-pp, subleading-leading in total hemisphere transverse momentum.

1758 **10.5 Theory implications of these results**

1759 <https://arxiv.org/abs/1707.01539>

**11 CONCLUSION**

## REFERENCES

- [1] O. K. Kalashnikov and V. V. Klimov. Phase transition in the quark-gluon plasma. *Physics Letters B*, 88:328–330, December 1979.
- [2] Edward V. Shuryak. Quantum Chromodynamics and the Theory of Superdense Matter. *Phys. Rept.*, 61:71–158, 1980.
- [3] Siegfried Bethke. World Summary of  $\alpha_s$  (2012). 2012. [Nucl. Phys. Proc. Suppl. 234, 229(2013)].
- [4] J. D. Bjorken. Highly relativistic nucleus-nucleus collisions: The central rapidity region. *Phys. Rev. D*, 27:140–151, Jan 1983.
- [5] Ulrich W. Heinz and Maurice Jacob. Evidence for a new state of matter: An Assessment of the results from the CERN lead beam program. 2000.
- [6] I. Arsene et al. Quark-gluon plasma and color glass condensate at RHIC? The perspective from the BRAHMS experiment. *Nucl. Phys. A*, 757:1, 2005.
- [7] K. Adcox et al. Formation of dense partonic matter in relativistic nucleus nucleus collisions at RHIC: Experimental evaluation by the PHENIX collaboration. *Nucl. Phys. A*, 757:184, 2005.
- [8] B. B. Back et al. The PHOBOS perspective on discoveries at RHIC. *Nucl. Phys. A*, 757:28, 2005.
- [9] John Adams et al. Experimental and theoretical challenges in the search for the quark gluon plasma: The STAR collaboration’s critical assessment of the evidence from RHIC collisions. *Nucl. Phys. A*, 757:102, 2005.
- [10] Miklos Gyulassy. Introduction to qcd thermodynamics and the quark-gluon plasma. *Progress in Particle and Nuclear Physics*, 15:403 – 442, 1985.
- [11] Sourav Sarkar, Helmut Satz, and Bikash Sinha. The physics of the quark-gluon plasma. *Lect. Notes Phys.*, 785:pp.1–369, 2010.
- [12] Helmut Satz. Extreme states of matter in strong interaction physics. An introduction. *Lect. Notes Phys.*, 841:1–239, 2012.

- 1786 [13] M. A. Stephanov. QCD phase diagram: An Overview. *PoS*, LAT2006:024, 2006.
- 1787 [14] Panagiota Foka and Małgorzata Anna Janik. An overview of experimental results from ultra-  
1788 relativistic heavy-ion collisions at the cern lhc: Bulk properties and dynamical evolution.  
1789 *Reviews in Physics*, 1:154 – 171, 2016.
- 1790 [15] Amaresh Jaiswal and Victor Roy. Relativistic hydrodynamics in heavy-ion collisions: general  
1791 aspects and recent developments. *Adv. High Energy Phys.*, 2016:9623034, 2016.
- 1792 [16] Ulrich Heinz, Chun Shen, and Huichao Song. The viscosity of quark-gluon plasma at RHIC  
1793 and the LHC. *AIP Conf. Proc.*, 1441:766–770, 2012.
- 1794 [17] Michael L. Miller, Klaus Reygers, Stephen J. Sanders, and Peter Steinberg. Glauber modeling  
1795 in high energy nuclear collisions. *Ann. Rev. Nucl. Part. Sci.*, 57:205, 2007.
- 1796 [18] David G. d'Enterria. Hard scattering cross-sections at LHC in the Glauber approach: From  
1797 pp to pA and AA collisions. 2003.
- 1798 [19] A. Majumder and M. Van Leeuwen. The Theory and Phenomenology of Perturbative QCD  
1799 Based Jet Quenching. *Prog. Part. Nucl. Phys. A*, 66:41, 2011.
- 1800 [20] Sergei A. Voloshin, Arthur M. Poskanzer, and Raimond Snellings. Collective phenomena in  
1801 non-central nuclear collisions. 2008.
- 1802 [21] Serguei Chatrchyan et al. Long-range and short-range dihadron angular correlations in central  
1803 PbPb collisions at a nucleon-nucleon center of mass energy of 2.76 TeV. *JHEP*, 07:076, 2011.
- 1804 [22] Serguei Chatrchyan et al. Multiplicity and transverse momentum dependence of two- and  
1805 four-particle correlations in pPb and PbPb collisions. *Phys. Lett.*, B724:213–240, 2013.
- 1806 [23] J. D. Bjorken. Energy loss of energetic partons in QGP: possible extinction of high  $p_t$  jets in  
1807 hadron-hadron collisions. FERMILAB-PUB-82-059-THY, 1982.
- 1808 [24] David d'Enterria. Jet quenching. *Landolt-Boernstein, Springer-Verlag*, Vol. 1-23A:99, 2010.
- 1809 [25] Nestor Armesto. Nuclear shadowing. *J. Phys.*, G32:R367–R394, 2006.

- 1810 [26] K. Aamodt. Suppression of Charged Particle Production at Large Transverse Momentum in  
 1811 Central PbPb Collisions at  $\sqrt{s_{\text{NN}}} = 2.76$  TeV. *Phys. Lett. B*, 696:30, 2011.
- 1812 [27] Vardan Khachatryan et al. Charged-particle nuclear modification factors in PbPb and pPb  
 1813 collisions at  $\sqrt{s_{\text{NN}}} = 5.02$  TeV. *JHEP*, 04:039, 2017.
- 1814 [28] Georges Aad et al. Measurements of the Nuclear Modification Factor for Jets in Pb+Pb  
 1815 Collisions at  $\sqrt{s_{\text{NN}}} = 2.76$  TeV with the ATLAS Detector. *Phys. Rev. Lett.*, 114(7):072302,  
 1816 2015.
- 1817 [29] Vardan Khachatryan et al. Measurement of inclusive jet cross-sections in pp and PbPb colli-  
 1818 sions at  $\sqrt{s_{\text{NN}}}=2.76$  TeV. *Phys. Rev. C*, 2016.
- 1819 [30] Serguei Chatrchyan et al. Measurement of jet fragmentation in PbPb and pp collisions at  
 1820  $\sqrt{s_{\text{NN}}} = 2.76$  TeV. *Phys. Rev. C*, 90:024908, 2014.
- 1821 [31] Serguei Chatrchyan et al. Modification of jet shapes in PbPb collisions at  $\sqrt{s_{\text{NN}}} = 2.76$  TeV.  
 1822 *Phys. Lett. B*, 730:243, 2014.
- 1823 [32] C. Adler et al. Disappearance of back-to-back high- $p_{\text{T}}$  hadron correlations in central Au+Au  
 1824 collisions at  $\sqrt{s_{\text{NN}}} = 200$  GeV. *Phys. Rev. Lett.*, 90:082302, 2003.
- 1825 [33] K. Aamodt et al. Particle-yield modification in jet-like azimuthal di-hadron correlations in  
 1826 Pb-Pb collisions at  $\sqrt{s_{\text{NN}}} = 2.76$  TeV. *Phys. Rev. Lett.*, 108:092301, 2012.
- 1827 [34] Georges Aad et al. Observation of a Centrality-Dependent Dijet Asymmetry in Lead-Lead  
 1828 Collisions at  $\sqrt{s_{\text{NN}}} = 2.76$  TeV with the ATLAS Detector at the LHC. *Phys. Rev. Lett.*,  
 1829 105:252303, 2010.
- 1830 [35] Serguei Chatrchyan et al. Observation and studies of jet quenching in PbPb collisions at  $\sqrt{s_{\text{NN}}}$   
 1831 = 2.76 TeV. *Phys. Rev. C*, 84:024906, 2011.
- 1832 [36] Vardan Khachatryan et al. Measurement of transverse momentum relative to dijet systems in  
 1833 PbPb and pp collisions at  $\sqrt{s_{\text{NN}}} = 2.76$  TeV. *JHEP*, 01:6, 2016.
- 1834 [37] Karen M. Burke et al. Extracting the jet transport coefficient from jet quenching in high-energy  
 1835 heavy-ion collisions. *Phys. Rev.*, C90(1):014909, 2014.

- 1836 [38] David d'Enterria. *Jet quenching*, volume 23: Relativistic Heavy Ion Physics of *Springer Materials - The Landolt-Börnstein Database*, chapter 6.4. Springer-Verlag, 2010.
- 1837
- 1838 [39] Shanshan Cao, Tan Luo, Guang-You Qin, and Xin-Nian Wang. Linearized Boltzmann trans-
- 1839 port model for jet propagation in the quark-gluon plasma: Heavy quark evolution. *Phys. Rev.*,
- 1840 C94(1):014909, 2016.
- 1841 [40] Shanshan Cao, Tan Luo, Guang-You Qin, and Xin-Nian Wang. Heavy and light flavor jet
- 1842 quenching at RHIC and LHC energies. 2017.
- 1843 [41] Yang-Ting Chien and Ivan Vitev. Jet Shape Resummation Using Soft-Collinear Effective
- 1844 Theory. *JHEP*, 12:061, 2014.
- 1845 [42] Yang-Ting Chien and Ivan Vitev. Towards the understanding of jet shapes and cross sections
- 1846 in heavy ion collisions using soft-collinear effective theory. *JHEP*, 05:023, 2016.
- 1847 [43] Ira Z. Rothstein and Iain W. Stewart. An Effective Field Theory for Forward Scattering and
- 1848 Factorization Violation. *JHEP*, 08:025, 2016.
- 1849 [44] Steven S. Gubser and Andreas Karch. From gauge-string duality to strong interactions: A
- 1850 Pedestrian's Guide. *Ann. Rev. Nucl. Part. Sci.*, 59:145–168, 2009.
- 1851 [45] Steven S. Gubser, Silviu S. Pufu, Fabio D. Rocha, and Amos Yarom. Energy loss in a strongly
- 1852 coupled thermal medium and the gauge-string duality. In Rudolph C. Hwa and Xin-Nian
- 1853 Wang, editors, *Quark-gluon plasma 4*, pages 1–59. 2010.
- 1854 [46] Jorge Casalderrey-Solana, Hong Liu, David Mateos, Krishna Rajagopal, and Urs Achim Wiede-
- 1855 mann. Gauge/String Duality, Hot QCD and Heavy Ion Collisions. 2011.
- 1856 [47] Jorge Casalderrey-Solana, Doga Gulhan, Guilherme Milhano, Daniel Pablos, and Krishna
- 1857 Rajagopal. Angular Structure of Jet Quenching Within a Hybrid Strong/Weak Coupling
- 1858 Model. *JHEP*, 03:135, 2017.
- 1859 [48] Yasuki Tachibana, Ning-Bo Chang, and Guang-You Qin. Full jet in quark-gluon plasma with
- 1860 hydrodynamic medium response. *Phys. Rev.*, C95(4):044909, 2017.

- 1861 [49] Raghav Kunnawalkam Elayavalli and Korinna Christine Zapp. Medium response in JEWEL  
1862 and its impact on jet shape observables in heavy ion collisions. *JHEP*, 07:141, 2017.
- 1863 [50] Lyndon Evans and Philip Bryant. LHC Machine. *JINST*, 3:S08001, 2008.
- 1864 [51] S. Chatrchyan et al. The CMS experiment at the CERN LHC. *JINST*, 3:S08004, 2008.
- 1865 [52] Tai Sakuma and Thomas McCauley. Detector and event visualization with sketchup at the  
1866 cms experiment. *Journal of Physics: Conference Series*, 513(2):022032, 2014.
- 1867 [53] Serguei Chatrchyan et al. Description and performance of track and primary-vertex recon-  
1868 struction with the CMS tracker. *JINST*, 9(10):P10009, 2014.
- 1869 [54] Vardan Khachatryan et al. Performance of photon reconstruction and identification with the  
1870 CMS detector in proton-proton collisions at  $\sqrt{s_{\text{NN}}} = 8$  TeV. *JINST*, 10:P08010, 2015.
- 1871 [55] Vardan Khachatryan et al. The CMS trigger system. *JINST*, 12:P01020, 2017.
- 1872 [56] CMS Collaboration. Momentum flow relative to dijets in pbpb collisions at 2.76 tev. *CMS*  
1873 *Analysis Note (Internal)*, AN-14-024, 2014.
- 1874 [57] CMS Internal. Study of high- $p_t$  charged particle suppression in pbpb compared to pp collisions  
1875 at 5.02 tev. 2016.
- 1876 [58] Gavin P. Salam. Towards Jetography. *Eur. Phys. J.*, C67:637–686, 2010.
- 1877 [59] Matteo Cacciari, Gavin P. Salam, and Gregory Soyez. The anti- $k_t$  jet clustering algorithm.  
1878 *JHEP*, 04:063, 2008.
- 1879 [60] Matteo Cacciari, Gavin P. Salam, and Gregory Soyez. FastJet user manual. *Eur. Phys. J. C*,  
1880 72:1896, 2012.
- 1881 [61] Olga Kodolova, I. Vardanian, A. Nikitenko, and A. Oulianov. The performance of the jet  
1882 identification and reconstruction in heavy ions collisions with CMS detector. *Eur. Phys. J. C*,  
1883 50:117, 2007.
- 1884 [62] Serguei Chatrchyan et al. Studies of jet quenching using isolated-photon+jet correlations in  
1885 PbPb and pp collisions at  $\sqrt{s_{\text{NN}}} = 2.76$  TeV. *Phys. Lett. B*, 718:773, 2013.

- 1886 [63] Serguei Chatrchyan et al. Measurement of jet fragmentation into charged particles in pp and  
1887 PbPb collisions at  $\sqrt{s_{\text{NN}}} = 2.76$  TeV. *JHEP*, 10:087, 2012.
- 1888 [64] CMS. Identification and Filtering of Uncharacteristic Noise in the CMS Hadron Calorimeter.  
1889 *JINST*, 5:T03014, 2010.
- 1890 [65] Torbjorn Sjöstrand, Stephen Mrenna, and Peter Skands. PYTHIA 6.4 physics and manual.  
1891 *JHEP*, 05:026, 2006.
- 1892 [66] S. Agostinelli et al. GEANT4—a simulation toolkit. *Nucl. Instrum. and Methods A*, 506:250,  
1893 2003.
- 1894 [67] I. P. Lokhtin and A. M. Snigirev. A model of jet quenching in ultrarelativistic heavy ion  
1895 collisions and high- $p_T$  hadron spectra at RHIC. *Eur. Phys. J. C*, 45:211, 2006.
- 1896 [68] S. Chatrchyan et al. Azimuthal anisotropy of charge particles at high transvere momenta in  
1897 pb-pb collisions at  $\sqrt{s_{\text{NN}}} = 2.76$  TeV. *Phys. Rev. Lett.*, 109:022301, 2012.
- 1898 [69] Serguei Chatrchyan et al. Centrality dependence of dihadron correlations and azimuthal  
1899 anisotropy harmonics in PbPb collisions at  $\sqrt{s_{\text{NN}}} = 2.76$  TeV. *Eur. Phys. J.*, C72:2012,  
1900 2012.
- 1901 [70] K. Aamodt et al. Harmonic decomposition of two-particle angular correlations in Pb-Pb  
1902 collisions at  $\sqrt{s_{\text{NN}}} = 2.76$  TeV. *Phys. Lett. B*, 708:249, 2012.

## APPENDICES

### 1904 A Jet kinematics

1905 The following sections summarize jet kinematics for inclusive jets and dijets at 2.76 TeV, for inclu-  
 1906 sive jets at 5.02 TeV, and for dijets in each asymmetry class at 2.76 TeV.

#### 1907 A.1 Jet kinematics at 2.76 TeV

1908 The kinematic observables of jets in pp and PbPb 2.76 TeV events (solid markers) are compared  
 1909 with Monte Carlo (hatched marks). All spectra have been normalized to unity. Comparing the jet  
 1910 spectra observed in PbPb data (pp data) and in PYTHIA+HYDJET (PYTHIA) samples, a reasonable  
 1911 agreement in the overall shape is found.

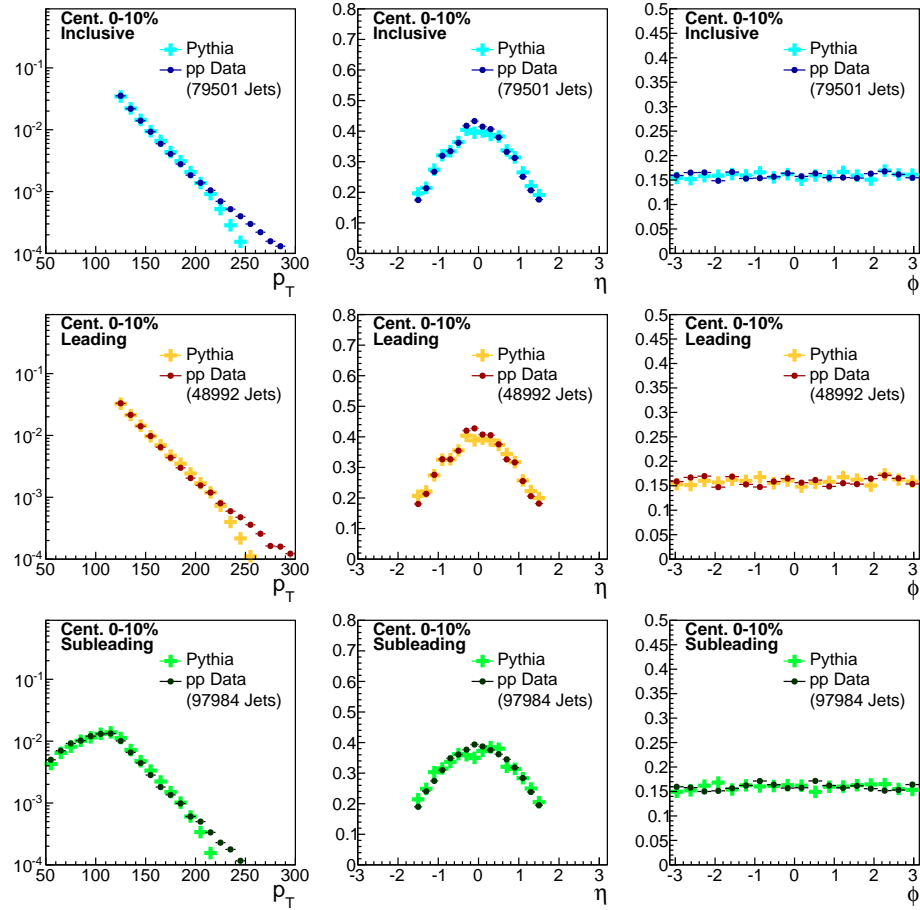


Figure 89. Distribution of transverse momentum, pseudorapidity, and azimuthal distribution of all jet selections for Pythia data compared to PYTHIA simulation.

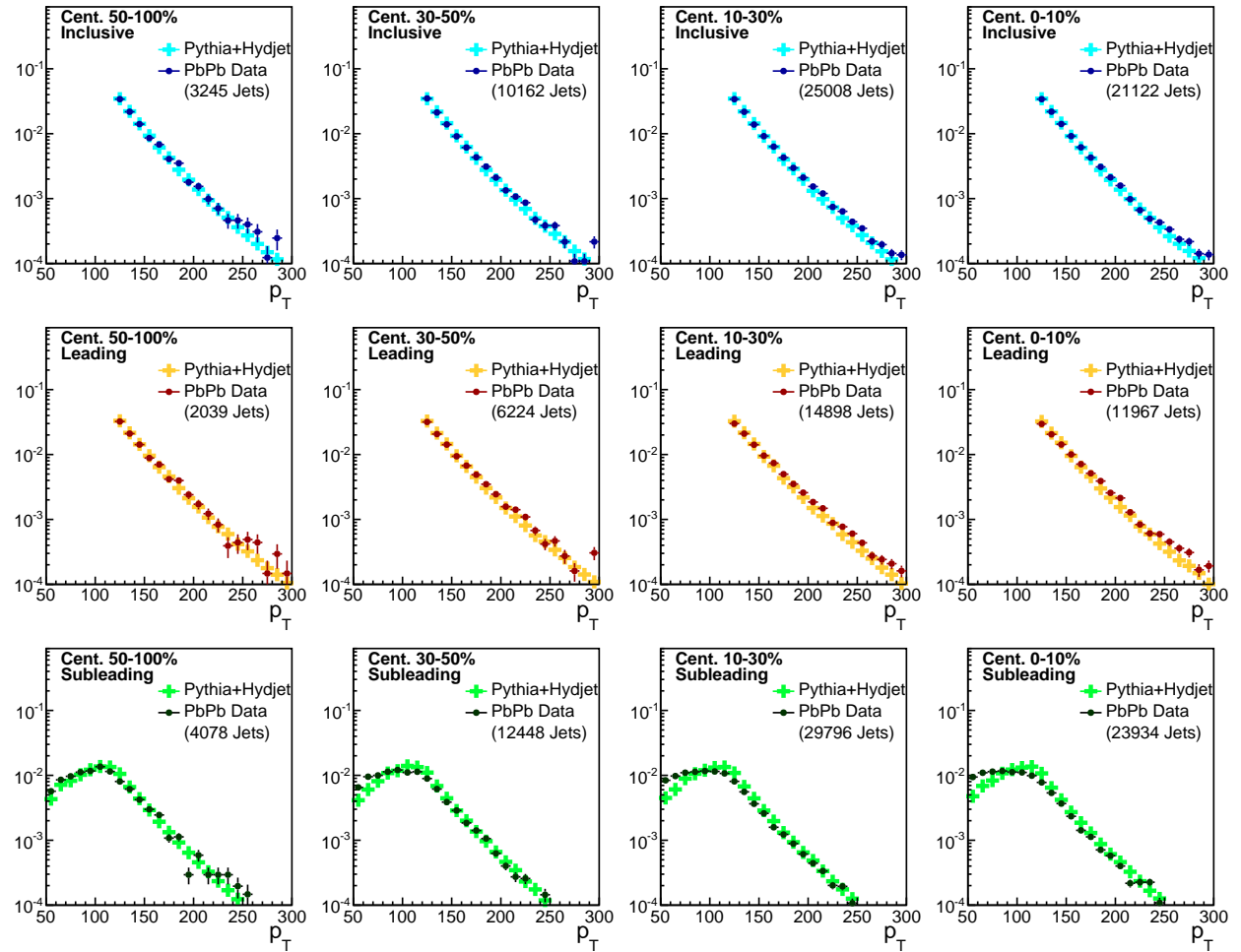


Figure 90. Transverse momentum distribution of all jet selections for PbPb data at 2.76 TeV compared to PYTHIA+HYDJET simulation.

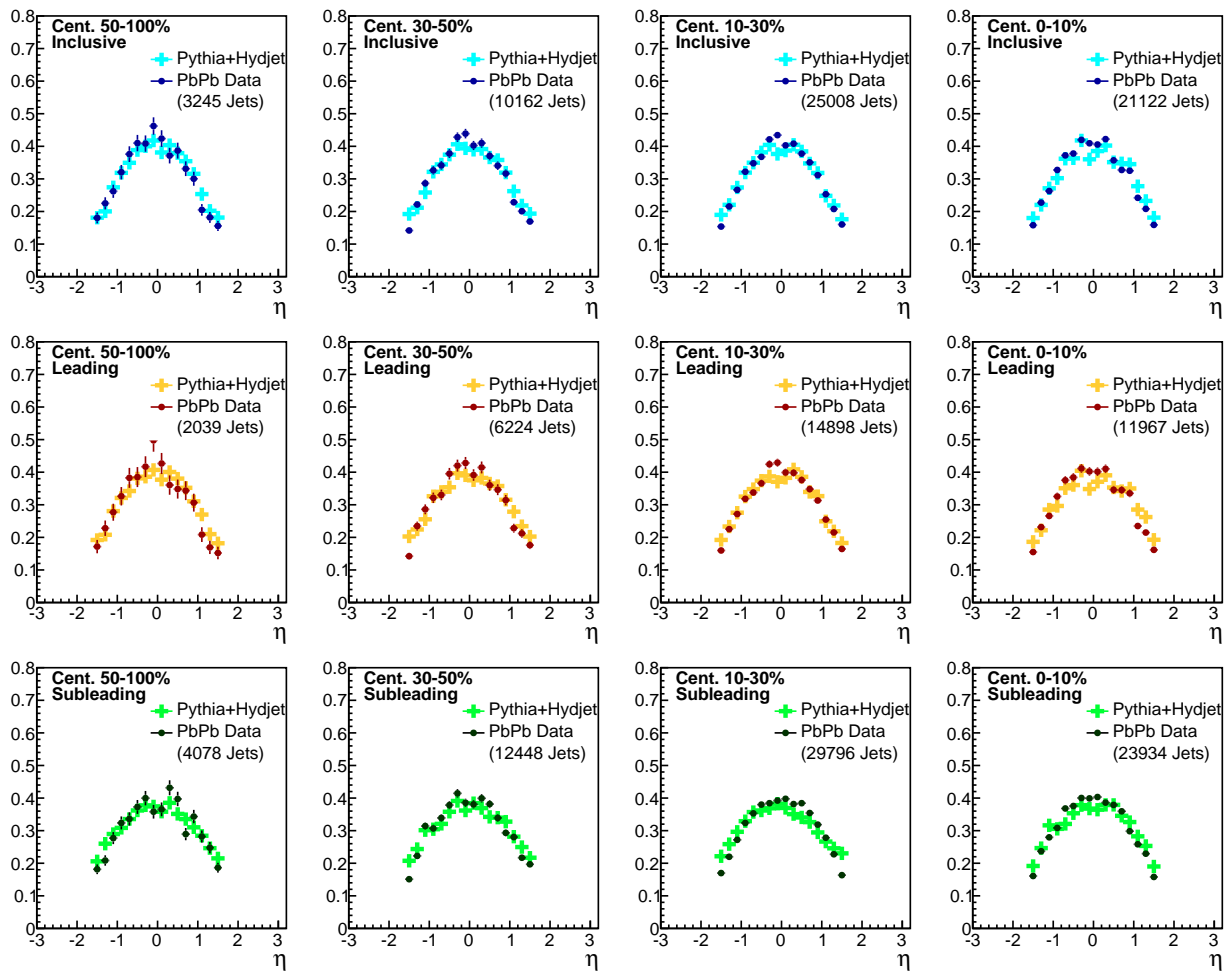


Figure 91. Pseudorapidity distribution of all jet selections for PbPb data at 2.76 TeV compared to PYTHIA + HYDJET simulation.

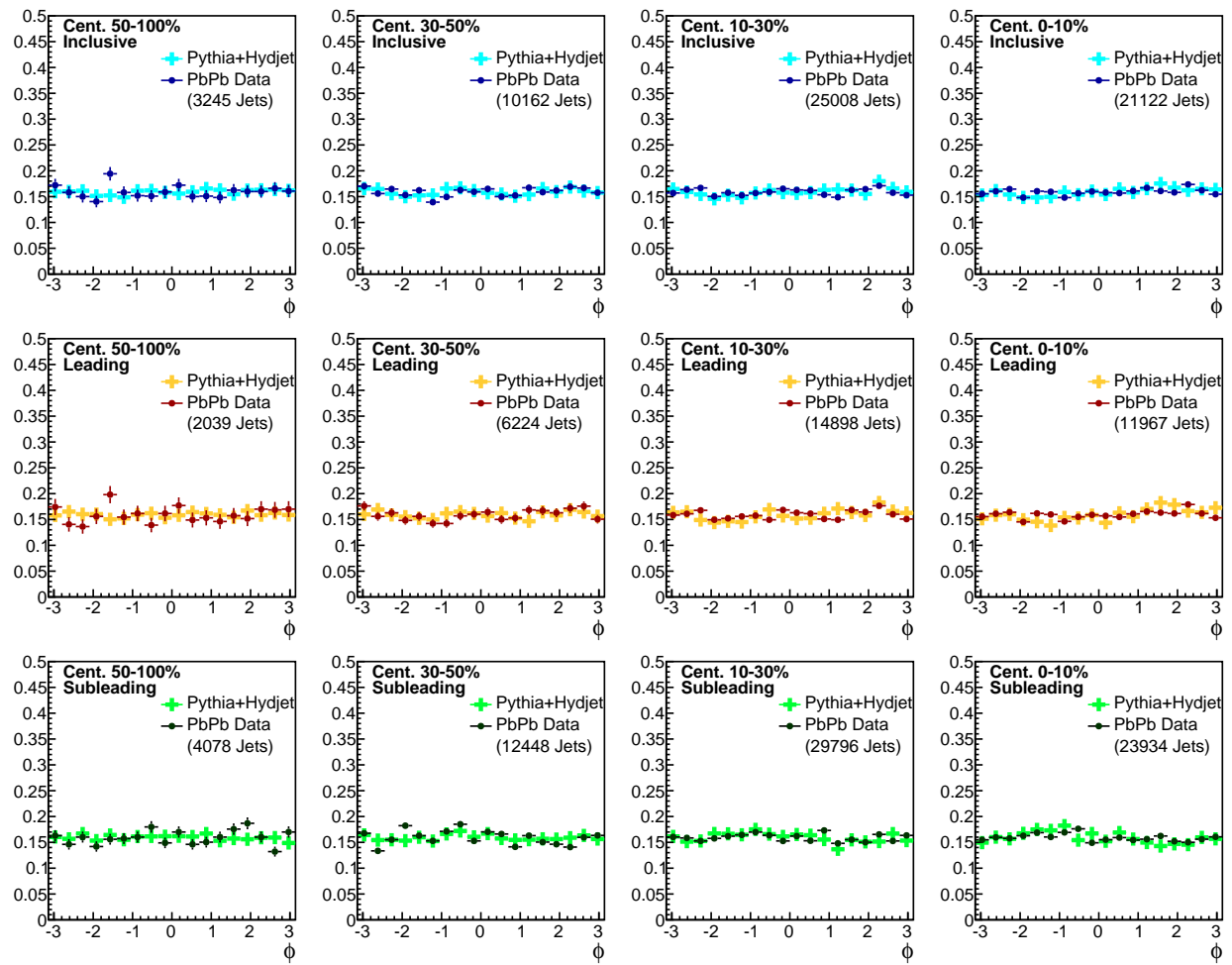


Figure 92. Azimuthal angle distribution of all jet selections for PbPb data at 2.76 TeV compared to PYTHIA+HYDJET simulation for each collision centrality bin.

1912 **A.2 Inclusive jet kinematics at 5.02 TeV**

1913 Jet  $p_T$ ,  $\eta$ , and  $\phi$  distributions for 5.02 TeV data, comparing PbPb data to PYTHIA+HYDJET and  
 1914 pp data to PYTHIA simulation.

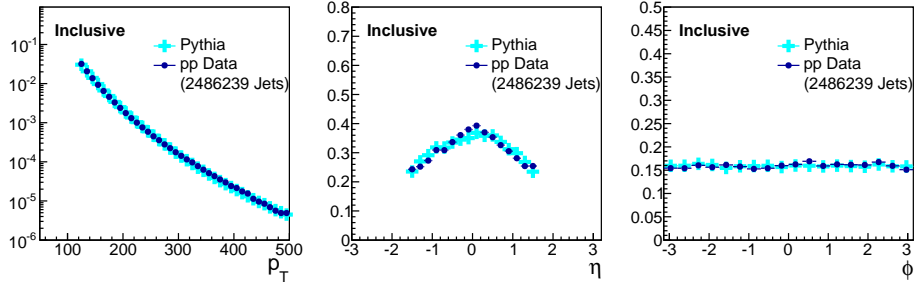


Figure 93. Distribution of pseudorapidity distribution of all jet selections for PbPb data compared to PYTHIA+HYDJet simulation for each collision centrality bin.

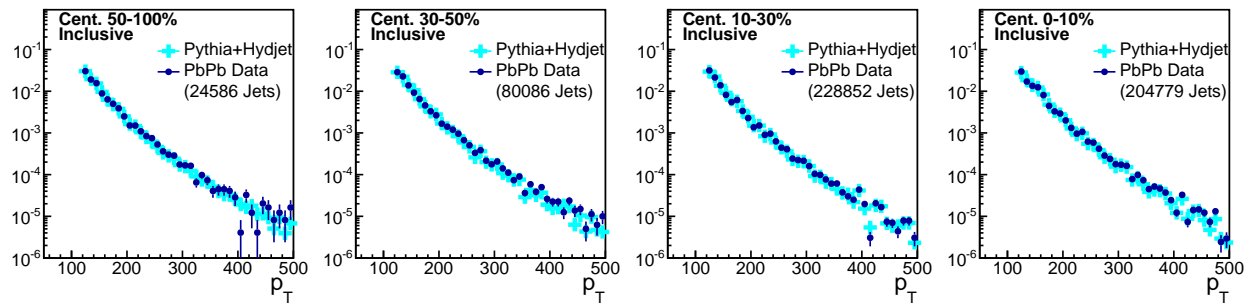


Figure 94. Transverse momentum distribution for PbPb data compared to PYTHIA+HYDJet simulation for each collision centrality bin.

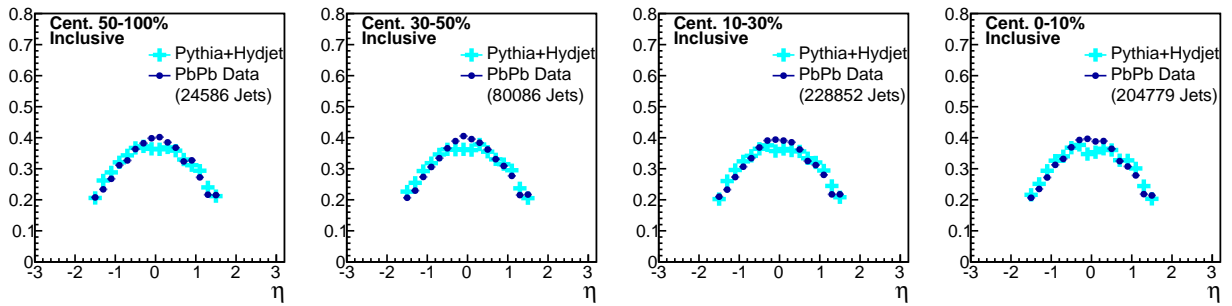


Figure 95. Jet  $\eta$  distribution for PbPb data compared to PYTHIA+HYDJet simulation for each collision centrality bin.

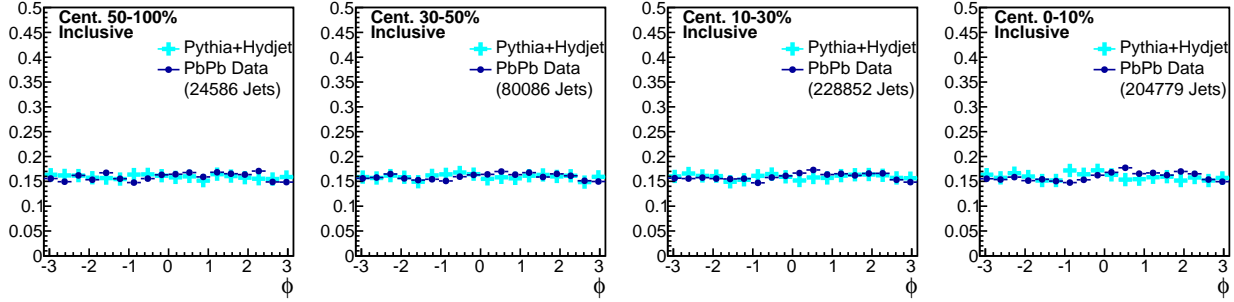


Figure 96. Jet  $\phi$  distribution for PbPb data compared to PYTHIA+HYDJET simulation for each collision centrality bin.

<sup>1915</sup> **A.3 Dijet kinematics in asymmetry classes at 2.76 TeV**

<sup>1916</sup> In the figures below, jet transverse momentum, pseudorapidity, and azimuth are shown for our  $A_J$ -  
<sup>1917</sup> inclusive sample, compared to each  $A_J$  selection in our analysis. Note that  $A_J$ -selection primarily  
<sup>1918</sup> affects the subleading jet spectrum, while the leading jet spectrum is nearly unchanged. Jet  $\eta$  and  
<sup>1919</sup> jet  $\phi$  exhibit no significant  $A_J$ -dependence for leading or subleading jets. Distributions are shown  
<sup>1920</sup> first for pp, and then for PbPb data at 2.76 TeV.

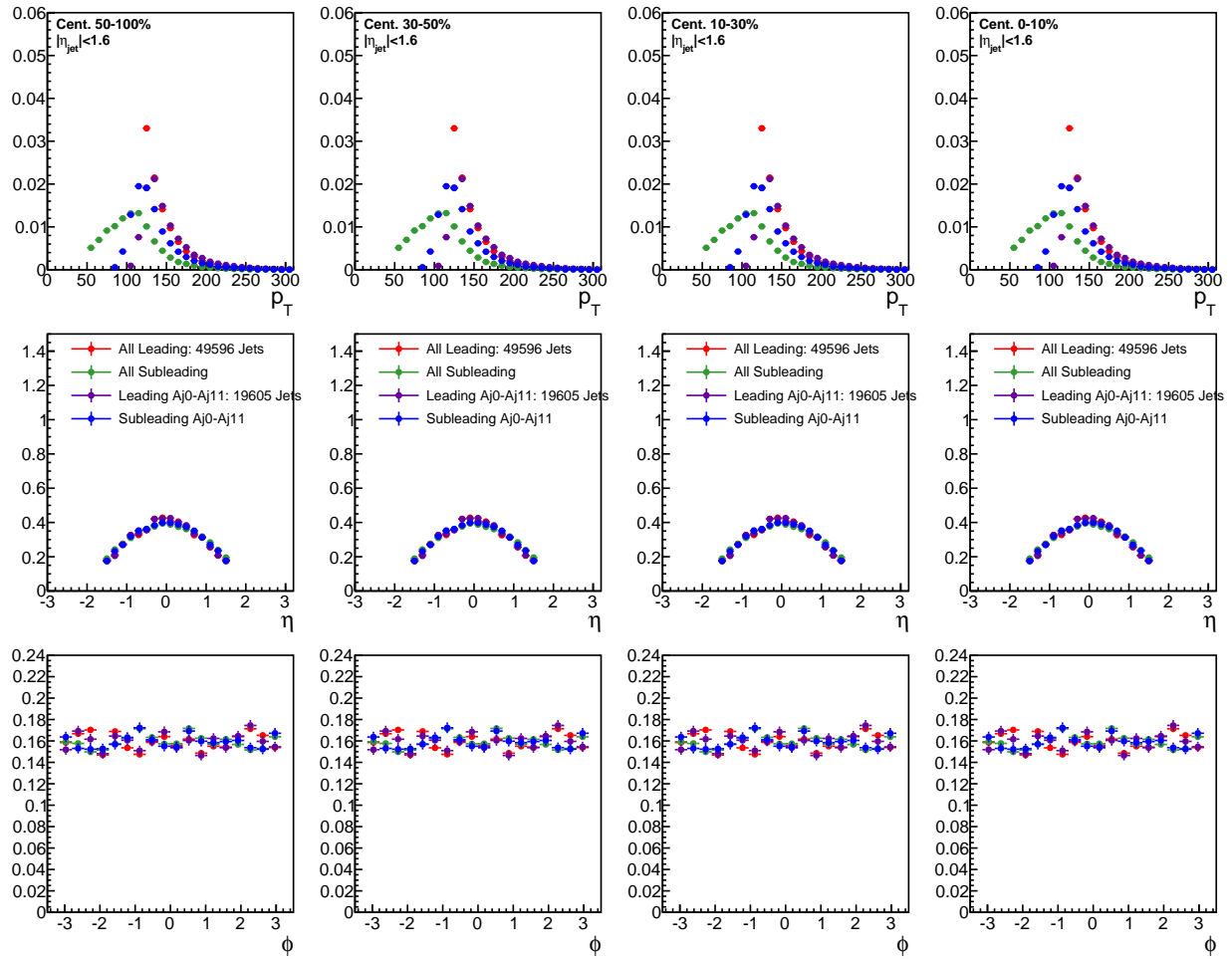


Figure 97. Jet  $p_T$ ,  $\eta$ , and  $\phi$  for all pp dijets and for pp dijets with  $A_J$ :  $0 < A_J < 0.11$ .

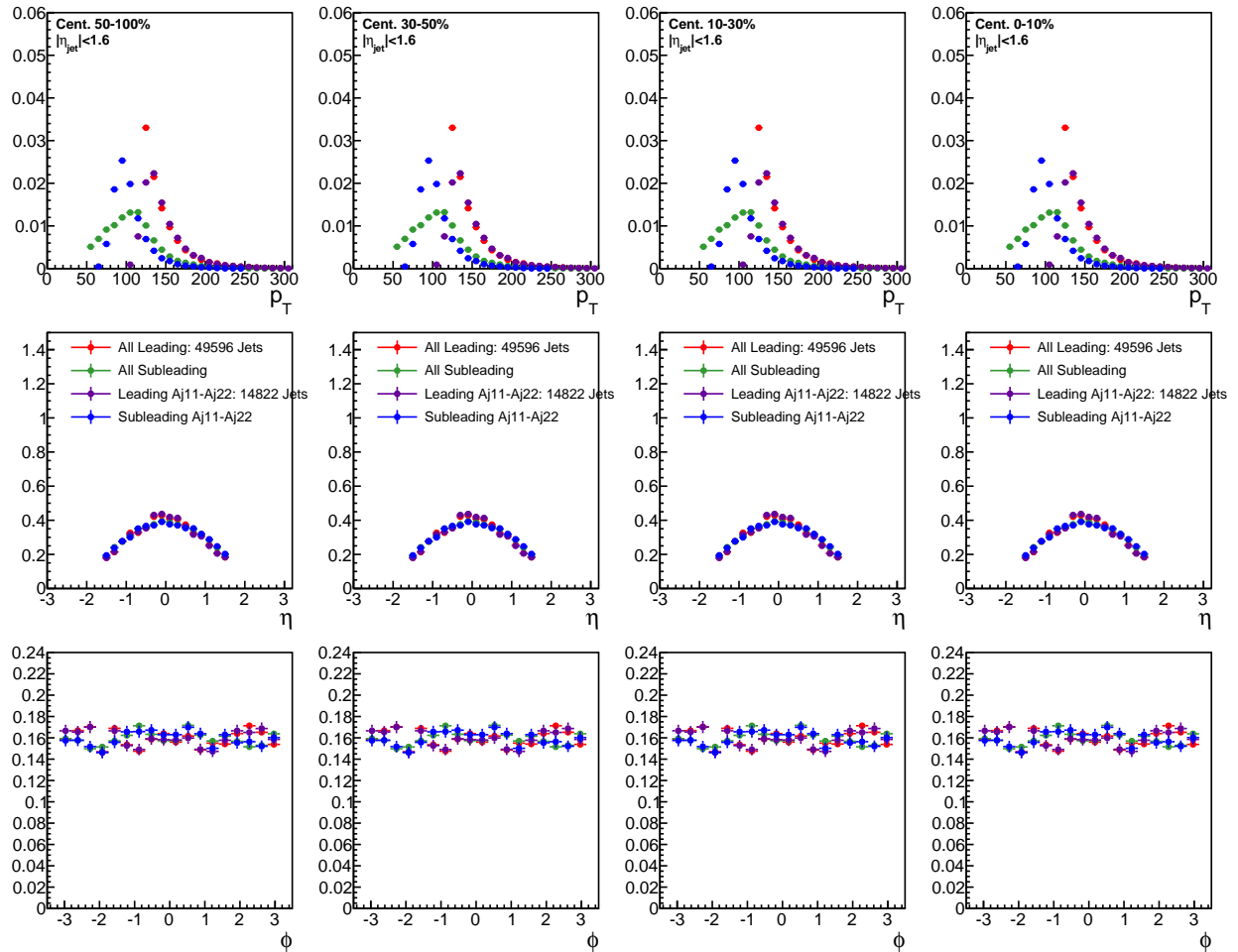


Figure 98. Jet  $p_T$ ,  $\eta$ , and  $\phi$  for all pp dijets and for pp dijets with  $A_J$ :  $0.11 < A_J < 0.22$ .

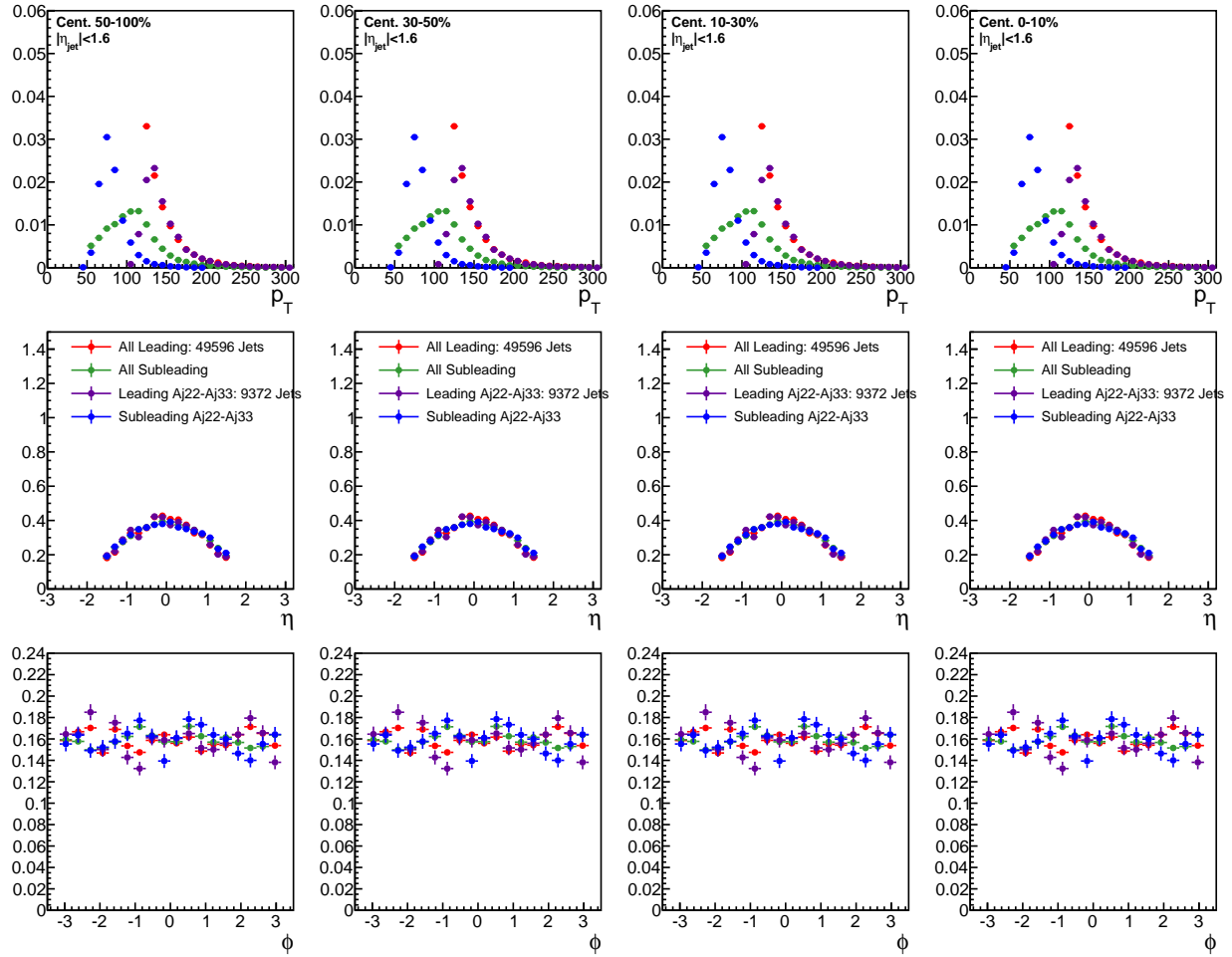


Figure 99. Jet  $p_T$ ,  $\eta$ , and  $\phi$  for all pp dijets and for pp dijets with  $A_J$ :  $0.22 < A_J < 0.33$ .

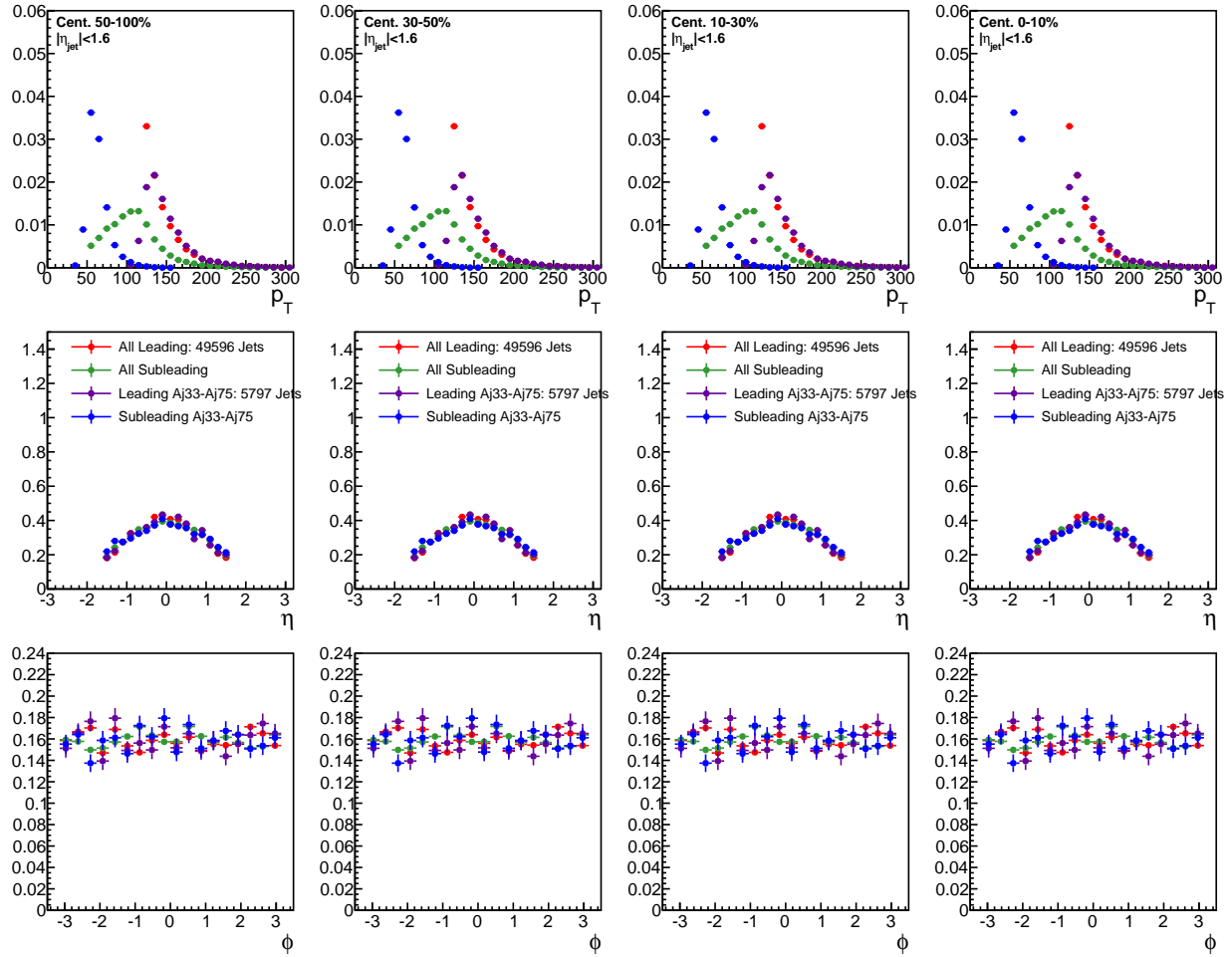


Figure 100. Jet  $p_T$ ,  $\eta$ , and  $\phi$  for all pp dijets and for pp dijets with  $A_J$ :  $A_J > 0.33$ .

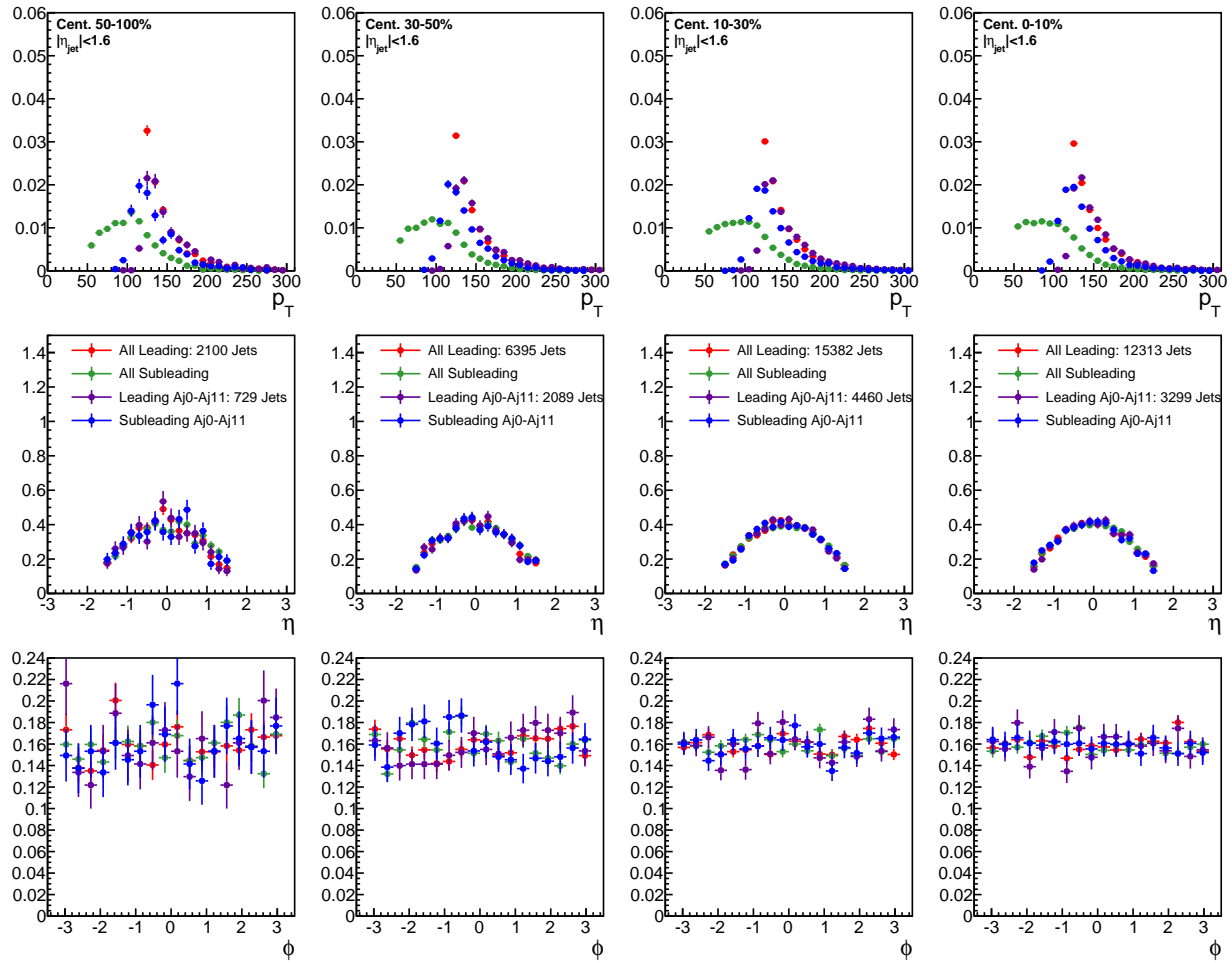


Figure 101. Jet  $p_T$ ,  $\eta$ , and  $\phi$  for all PbPb dijets and for PbPb dijets with  $0 < A_J < 0.11$ .

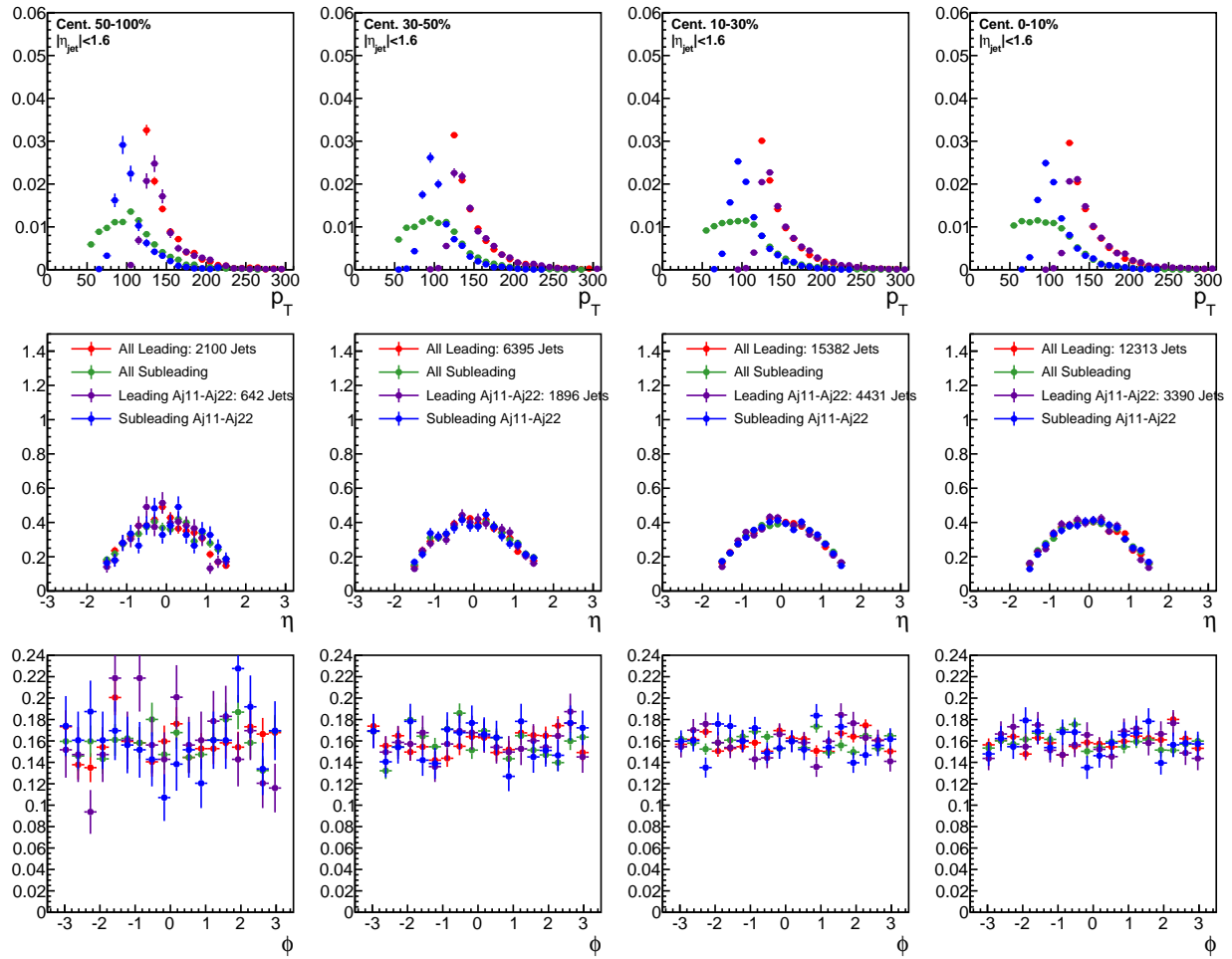


Figure 102. Jet  $p_T$ ,  $\eta$ , and  $\phi$  for all PbPb dijets and for PbPb dijets with  $0.11 < A_J < 0.22$ .

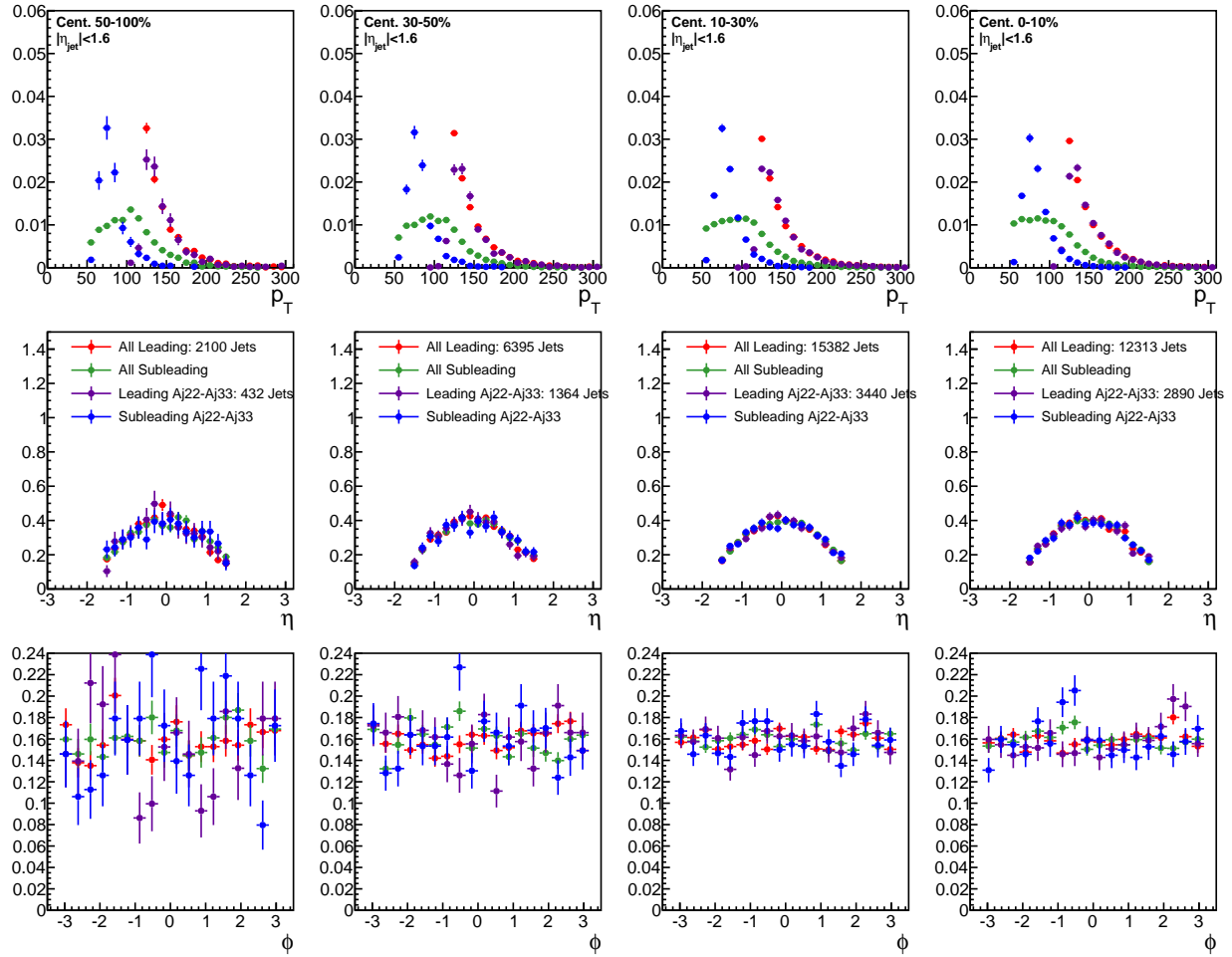


Figure 103. Jet  $p_T$ ,  $\eta$ , and  $\phi$  for all PbPb dijets and for PbPb dijets with  $0.22 < A_J < 0.33$ .

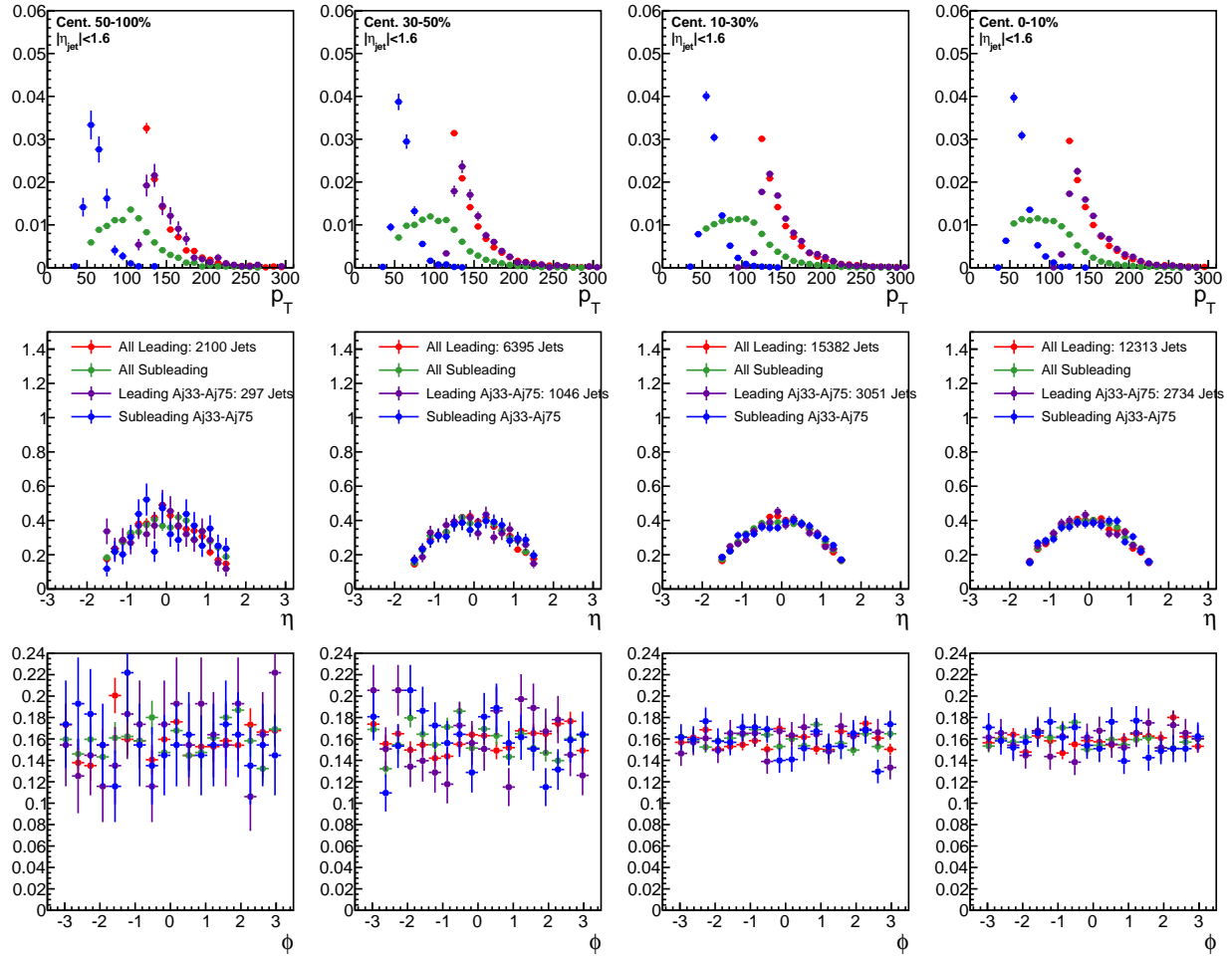


Figure 104. Jet  $p_T$ ,  $\eta$ , and  $\phi$  for all PbPb dijets and for PbPb dijets with  $A_J > 0.33$ .

1921 **B Background fitting details**

1922 Figures 105-108 show the two steps of fits involved in modeling the the background distribution in  
 1923  $\Delta\phi$ , as discussed in section 9.3.

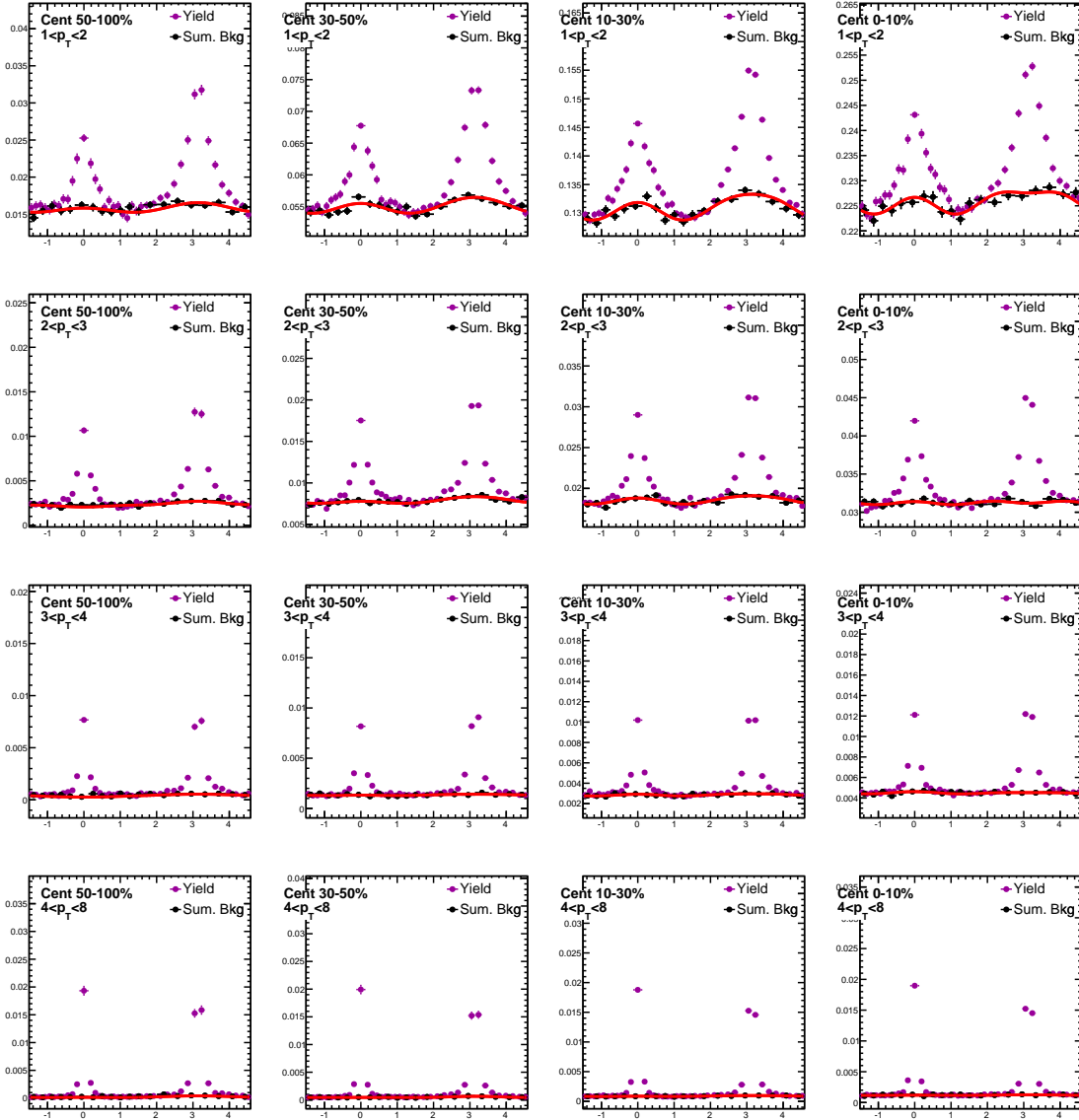


Figure 105. Dijet combined background  $\Delta\phi$  distributions, estimated by projection over the region  $1.5 < |\Delta\eta| < 3.0$ . Here the "near-side" region  $-\frac{\pi}{2} < \Delta\phi < \frac{\pi}{2}$  is taken from the leading jet correlation, while the "away-side"  $-\frac{\pi}{2} < \Delta\phi < \frac{\pi}{2}$  is taken from the subleading jet correlation. The resulting combined background distribution is fit with the function  $B^{dijet}(\Delta\phi) = B_0(1 + 2V_1\cos(\Delta\phi) + 2V_2\cos(2\Delta\phi) + 2V_3\cos(3\Delta\phi))$ .

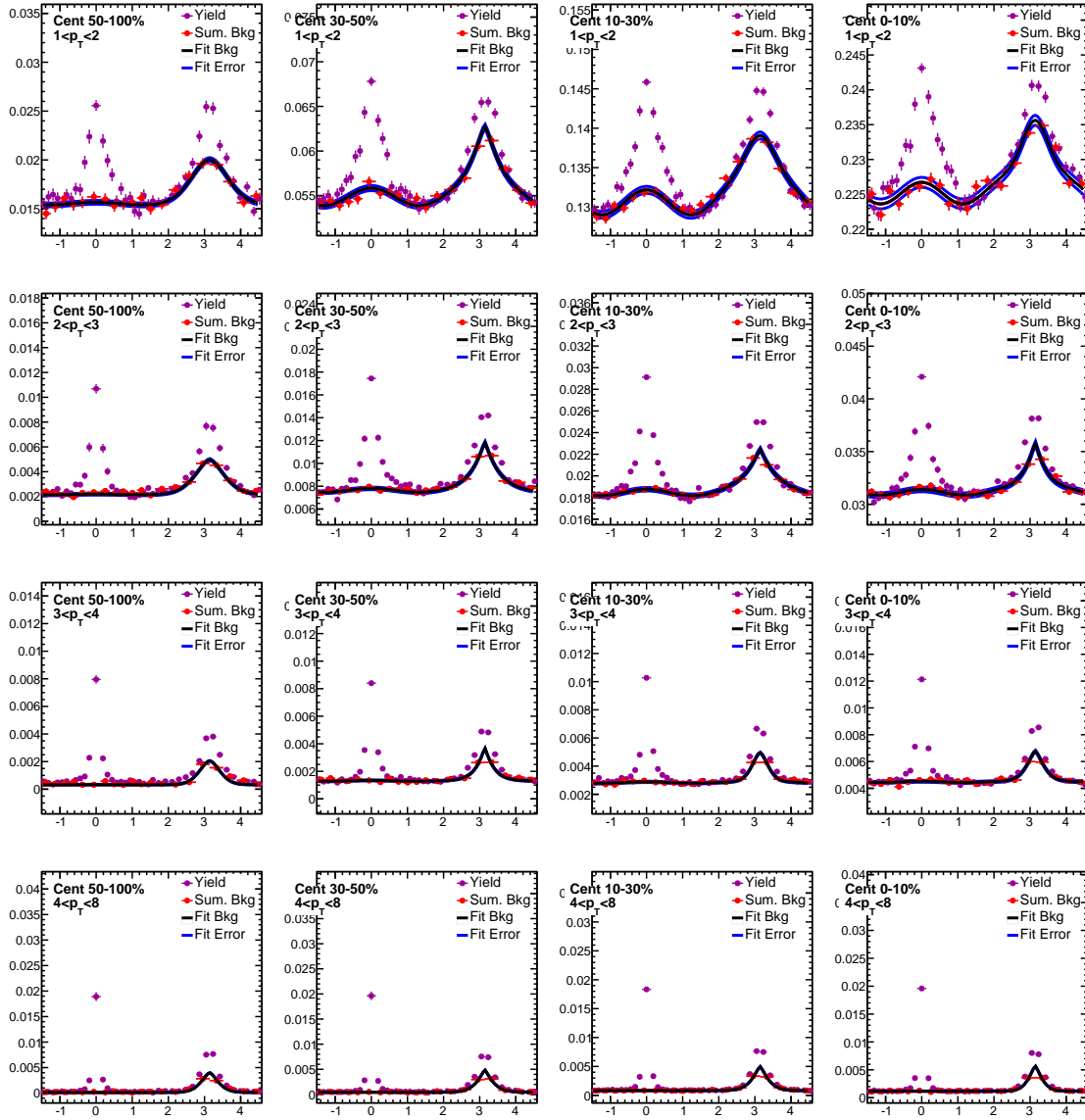


Figure 106. Background leading jet  $\Delta\phi$  distributions, estimated by projection over the region  $1.5 < |\Delta\eta| < 3.0$ , is fit as shown. The 2D background distribution is estimated by propagating the black fit line in  $\Delta\eta$ , with uncertainty assigned by varying fit parameters by the appropriate fit error as shown in the blue error band.

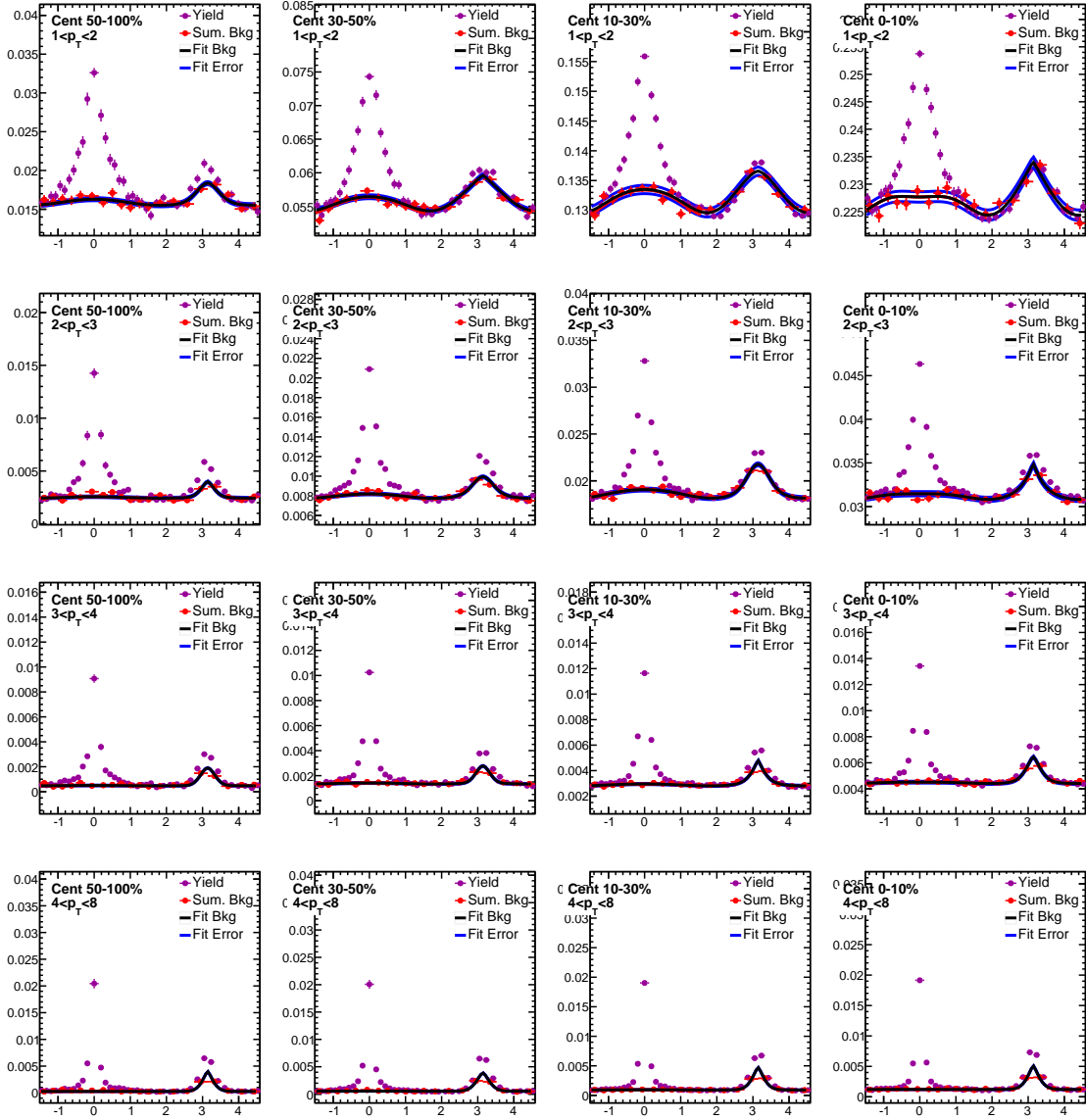


Figure 107. Background subleading jet  $\Delta\phi$  distributions, estimated by projection over the region  $1.5 < |\Delta\eta| < 3.0$ , is fit as shown. The 2D background distribution is estimated by propagating the black fit line in  $\Delta\eta$ , with uncertainty assigned by varying fit parameters by the appropriate fit error as shown in the blue error band.

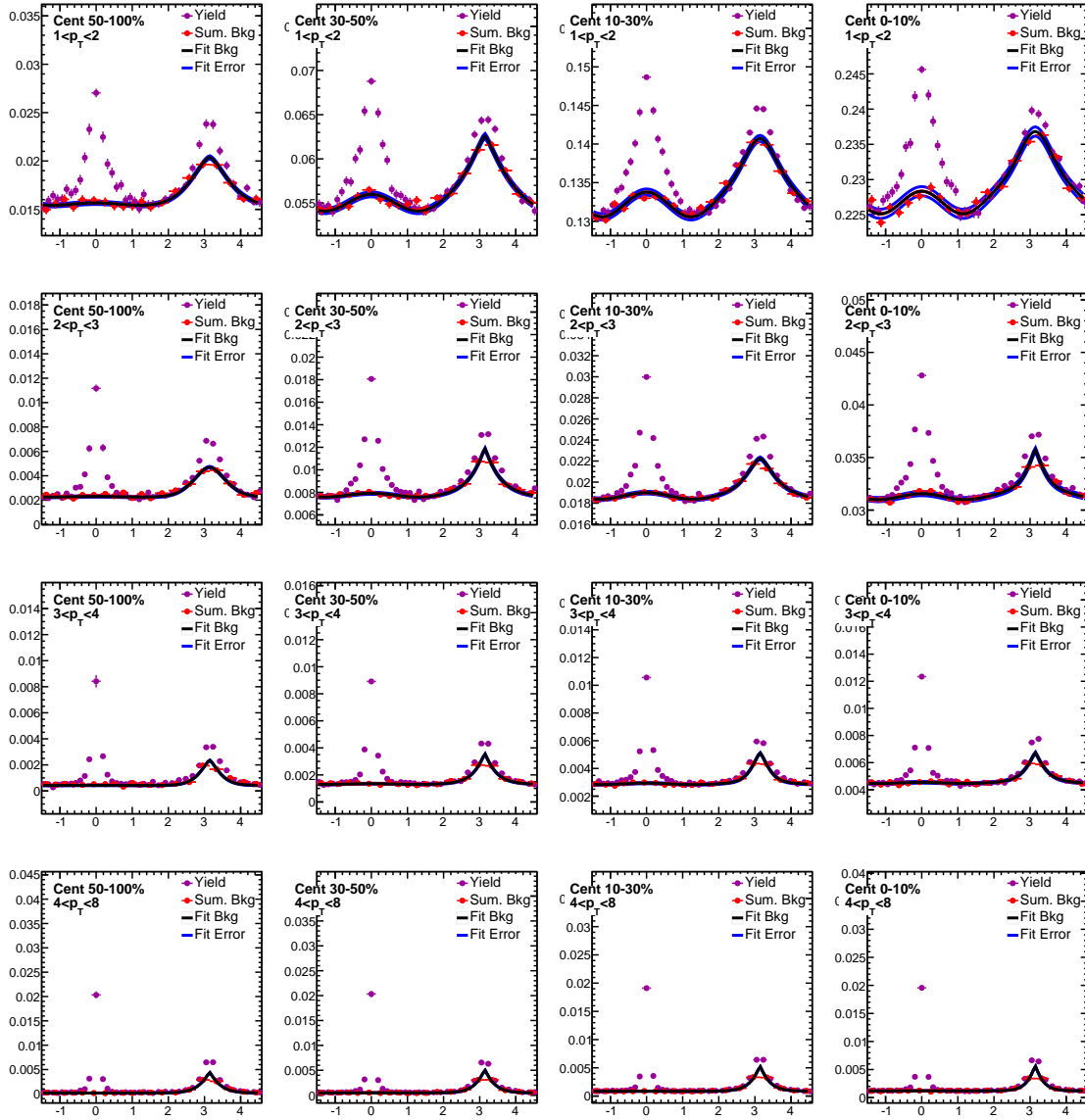


Figure 108. Background inclusive jet  $\Delta\phi$  distributions, estimated by projection over the region  $1.5 < |\Delta\eta| < 3.0$ , is fit as shown. The 2D background distribution is estimated by propagating the black fit line in  $\Delta\eta$ , with uncertainty assigned by varying fit parameters by the appropriate fit error as shown in the blue error band.

1924 **C Pair acceptance and event decomposition systematic uncertainties**

1925 Figure 109 illustrates the estimation of pair-acceptance uncertainty, determined by considering the  
 1926 sideband asymmetry in the  $\Delta\eta$  distributions of background subtracted yield.

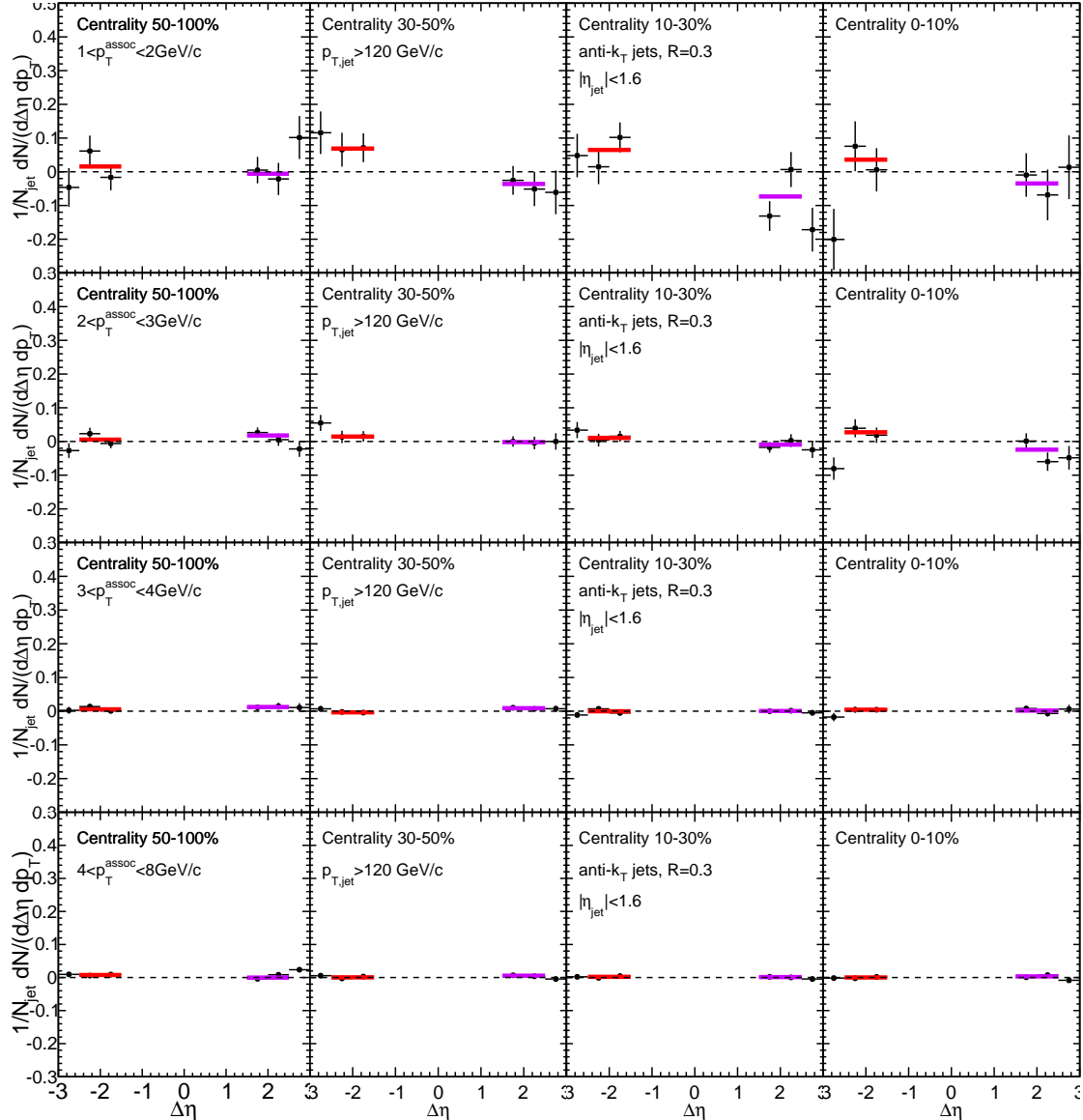


Figure 109. Background-subtracted inclusive jet  $\Delta\eta$  distribution is shown for sideband region  $1.5 < |\Delta\eta| < 3.0$  only. Each side is fit separately with a horizontal line, and the greater deviation from zero is assigned as systematic uncertainty arising from the pair-acceptance correction.

1927 Figure 110 illustrates the background-subtraction systematic uncertainty estimation: the average  
 1928 content of the two  $1.5 < \Delta\eta < 2.0$  bins is assigned as systematic uncertainty for each  $p_T$  and centrality  
 1929 bin.

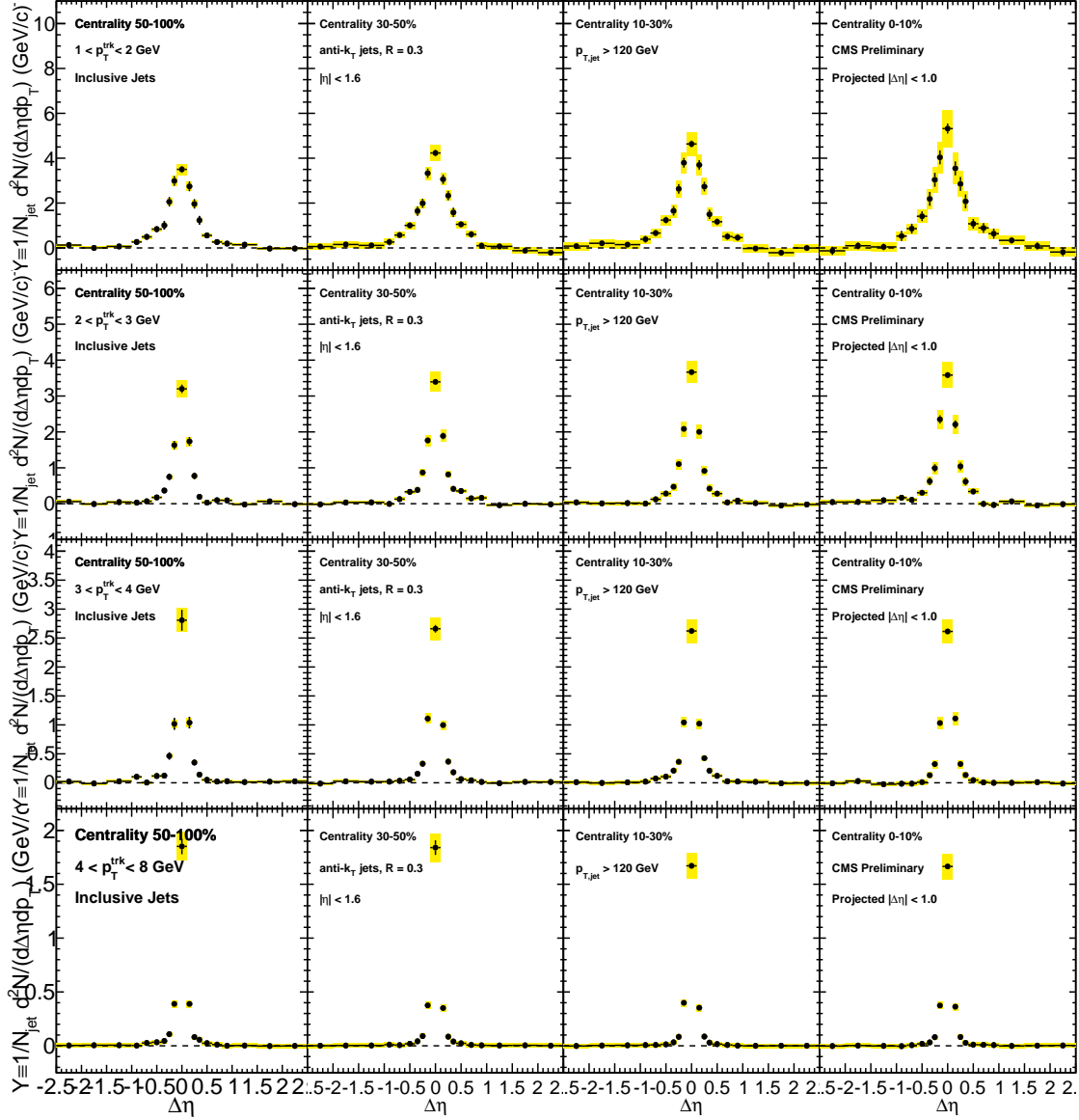


Figure 110. Inclusive jet correlated yield in  $\Delta\eta$ , shown to axis range  $|\Delta\eta| < 2.0$ . The deviation of the most peripheral points from zero is assigned as systematic uncertainty as discussed in the Systematic Uncertainty section above.

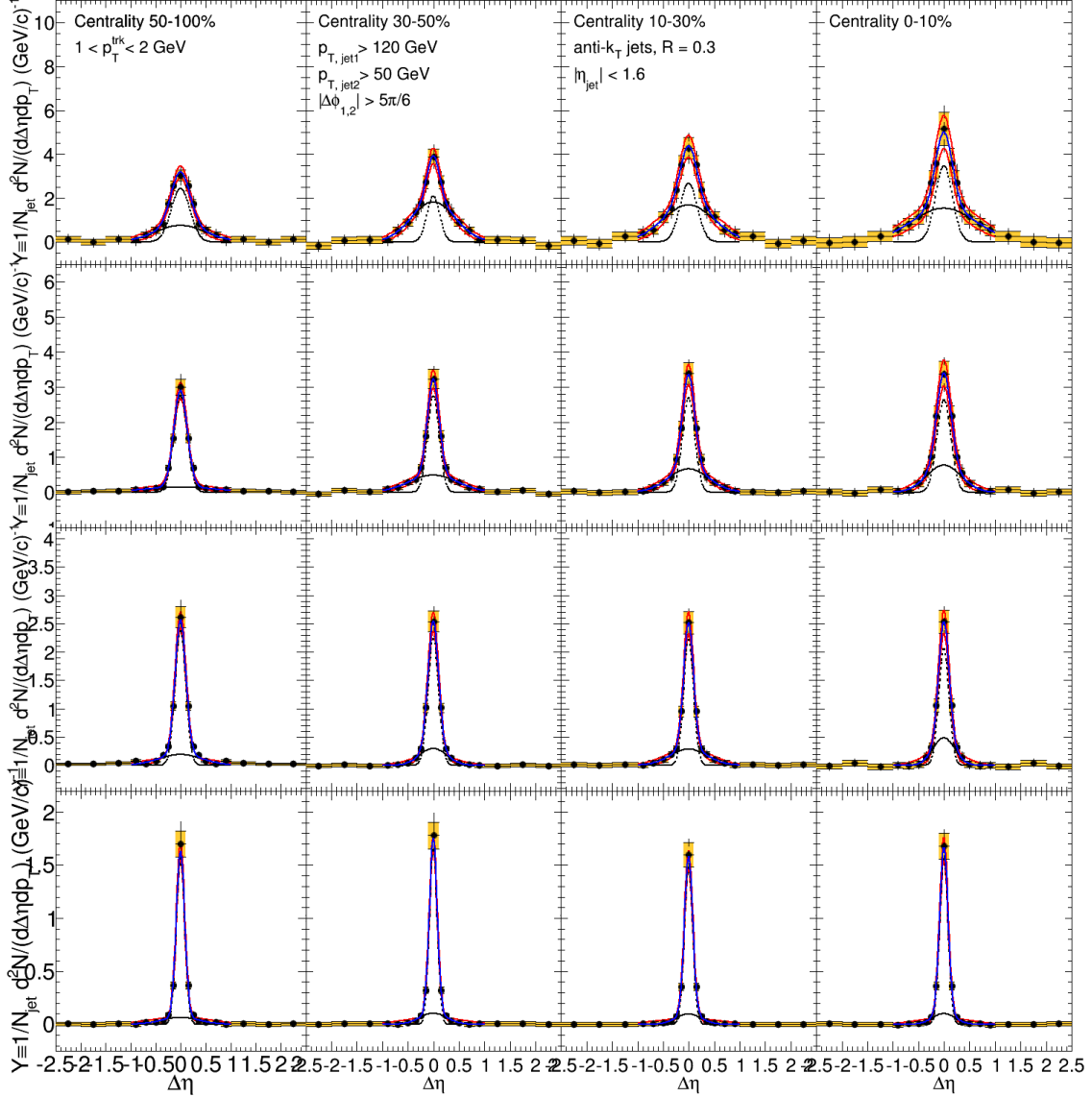


Figure 111. Illustration of the fits used to determine the distribution widths (shown here for leading jet PbPb  $\Delta\eta$  correlations). Correlations are fit to a double gaussian (shown in blue, with black dashed lines indicating constituent gaussians), and width is taken as the  $\Delta\eta$  value containing 67% of the total yield. Points are varied by their systematic errors and the fits are repeated (shown in red) to obtain the systematic error on the width.

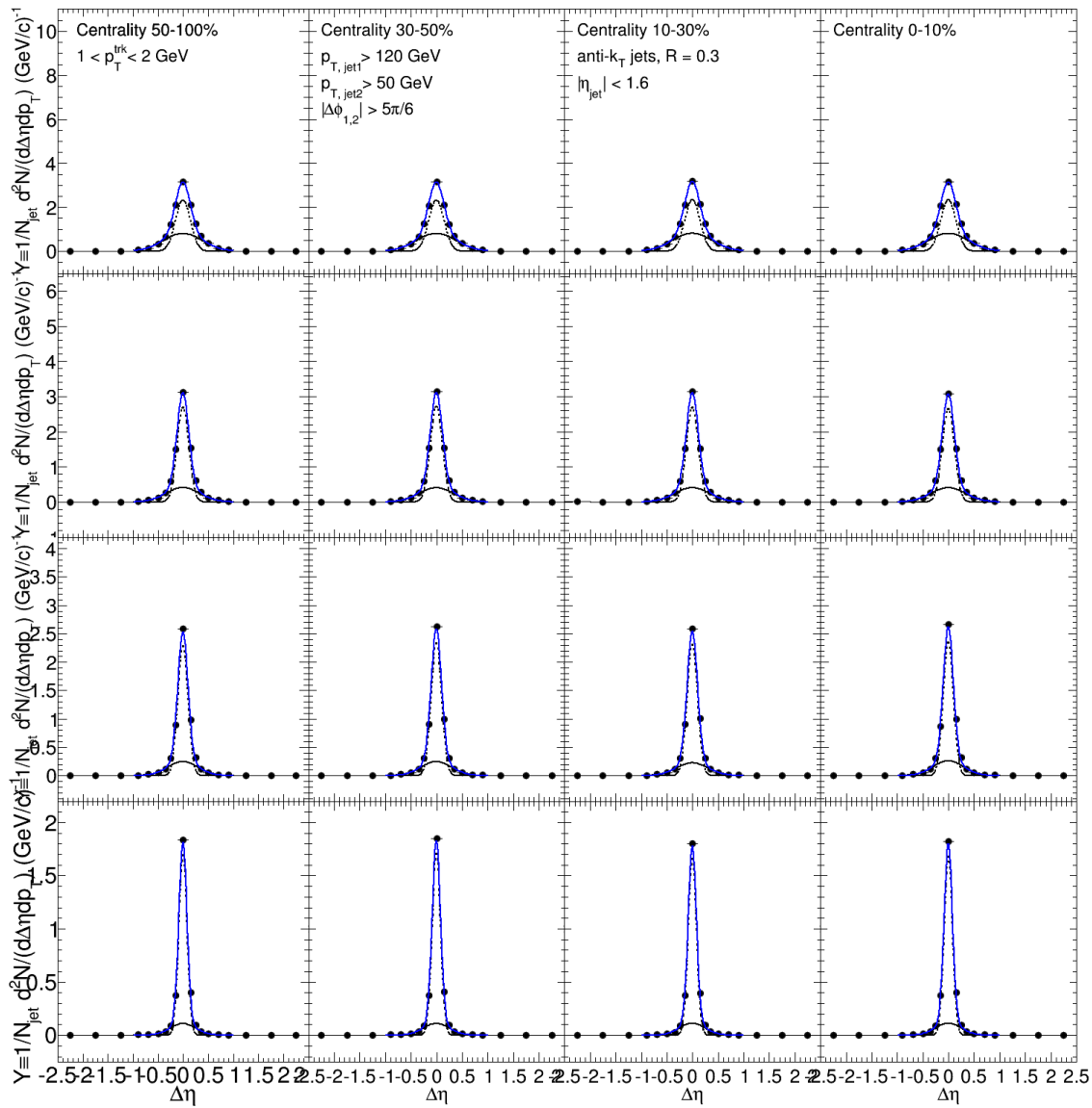


Figure 112. Illustration of the fits used to determine the distribution widths (shown here for leading jet pp  $\Delta\eta$  correlations). Correlations are fit to a double gaussian (shown in blue, with black dashed lines indicating constituent gaussians), and width is taken as the  $\Delta\eta$  value containing 67% of the total yield.

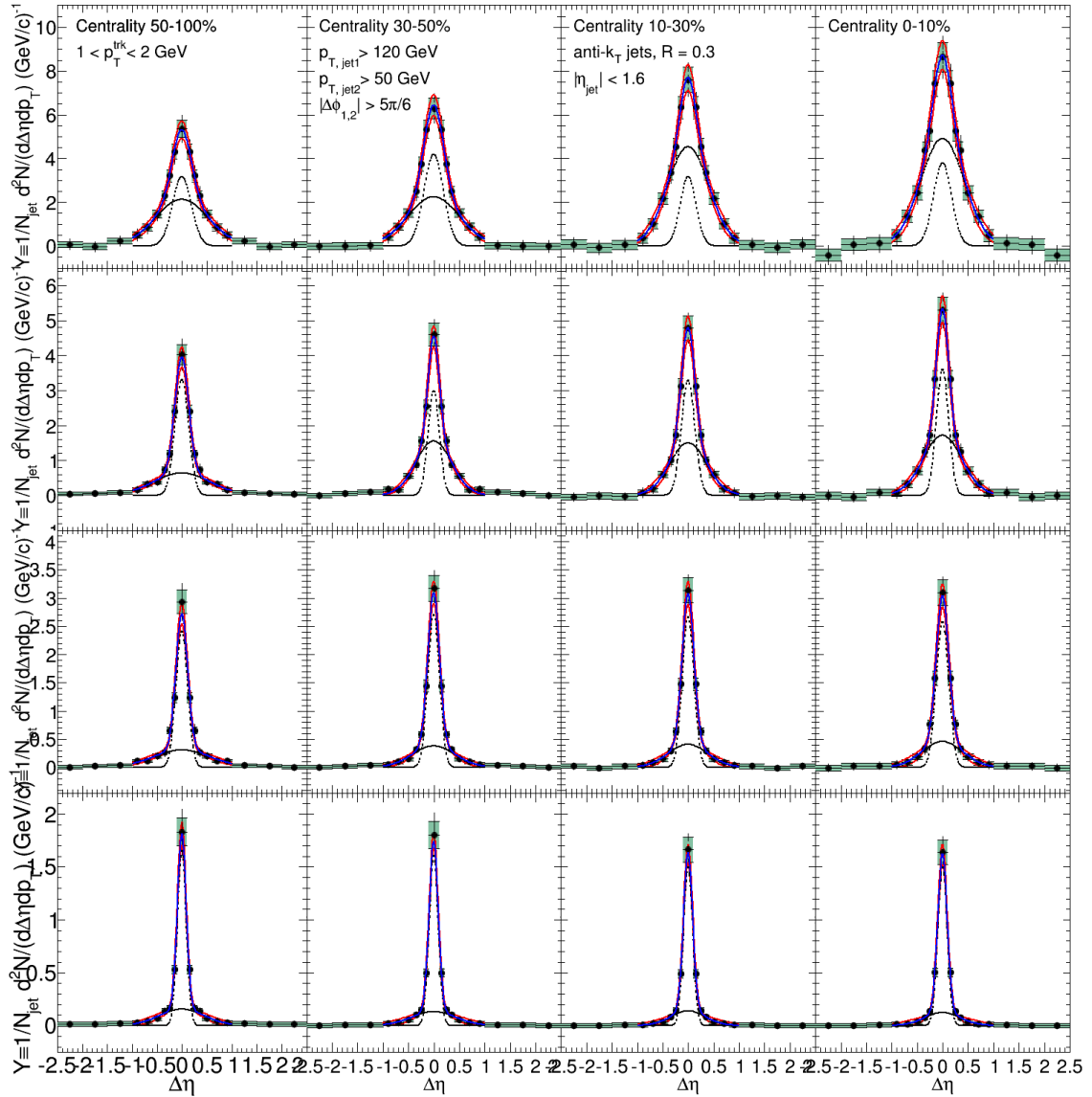


Figure 113. Illustration of the fits used to determine the distribution widths (shown here for subleading jet PbPb  $\Delta\eta$  correlations). Correlations are fit to a double gaussian (shown in blue, with black dashed lines indicating constituent gaussians), and width is taken as the  $\Delta\eta$  value containing 67% of the total yield. Points are varied by their systematic errors and the fits are repeated (shown in red) to obtain the systematic error on the width.

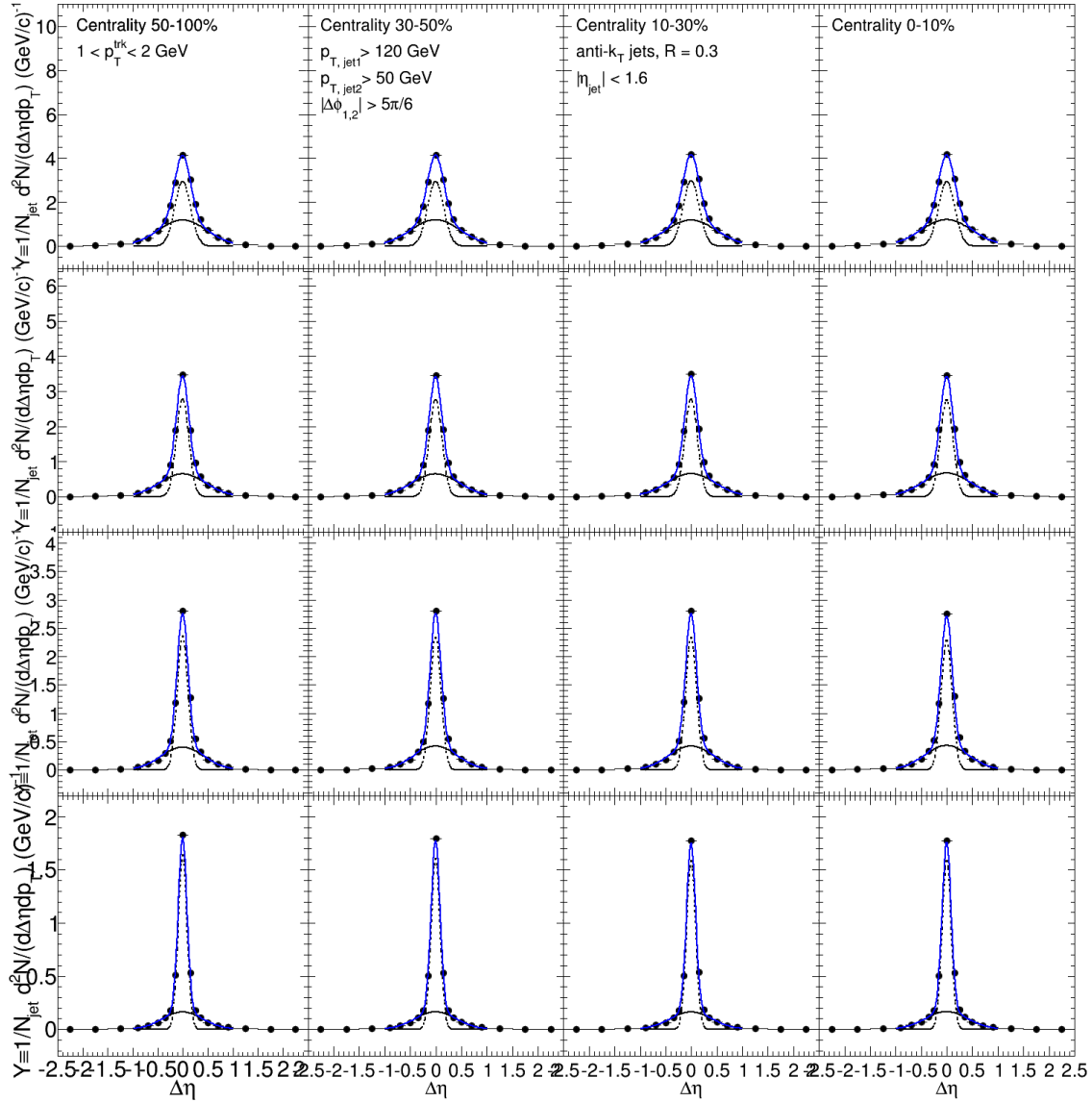


Figure 114. Illustration of the fits used to determine the distribution widths (shown here for subleading jet pp  $\Delta\eta$  correlations). Correlations are fit to a double gaussian (shown in blue, with black dashed lines indicating constituent gaussians), and width is taken as the  $\Delta\eta$  value containing 67% of the total yield.

**VITA**

NAME:	Hallie Causey Trauger
EDUCATION:	<p>Ph.D., Physics, University of Illinois at Chicago, 2017</p> <p>M.Ed., Secondary Science, University of Illinois at Chicago, 2015</p> <p>M.S., Physics, University of Illinois at Chicago, 2014</p> <p>B.A., Political Science, University of Chicago, 2010</p>
HONORS:	<p>Paul M. Raccah Award for the highest score on the Doctoral Qualifying Exam, University of Illinois at Chicago, 2014</p> <p>Student Marshal, highest academic honor at the University of Chicago, 2010</p>
TEACHING:	<p>12th Grade Computer Science, Back of the Yards College Preparatory High School, Chicago, IL 2016-2017</p> <p>9th Grade Physics, Back of the Yards College Preparatory High School, Chicago, IL 2014-2017</p> <p>Physics 104 (TA leading algebra-based mechanics workshop), University of Illinois at Chicago, 2013-2014</p> <p>Physics 108 (TA for algebra-based electricity &amp; magnetism discussions and labs), University of Illinois at Chicago, 2012-2013</p>
PUBLICATIONS:	<p>Khachatryan, Vardan et al. Decomposing transverse momentum balance contributions for quenched jets in PbPb collisions at <math>\sqrt{s_{NN}} = 2.76</math> TeV. JHEP 1611 (2016) 055.</p> <p>Khachatryan, Vardan et al. Correlations between jets and charged particles in PbPb and pp collisions at <math>\sqrt{s_{NN}} = 2.76</math> TeV. JHEP 1602 (2016) 156.</p>

- PRESENTATIONS:
- “Jet-track correlation studies in PbPb and pp collisions at 5.02 TeV,” at Quark Matter XVI, Chicago, IL, February 2017.
  - “Heavy ion jet results from CMS” at the 2015 US LHC Users Association Meeting, Batavia, IL, November 2015
  - “Heavy ion jet results from CMS and ATLAS” at the 12th Conference on the Intersections of Particle and Nuclear Physics, Vail, CO, May 2015
  - “Jet quenching studies in CMS” at the Winter Workshop on Nuclear Dynamics, Keystone, CO, January 2015. J.Phys.Conf.Ser. 636 (2015) no.1, 012012